TECHNISCHE
UNIVERSITÄT
MÜNCHEN

WALTHER-
MEISSNER-
INSTITUT

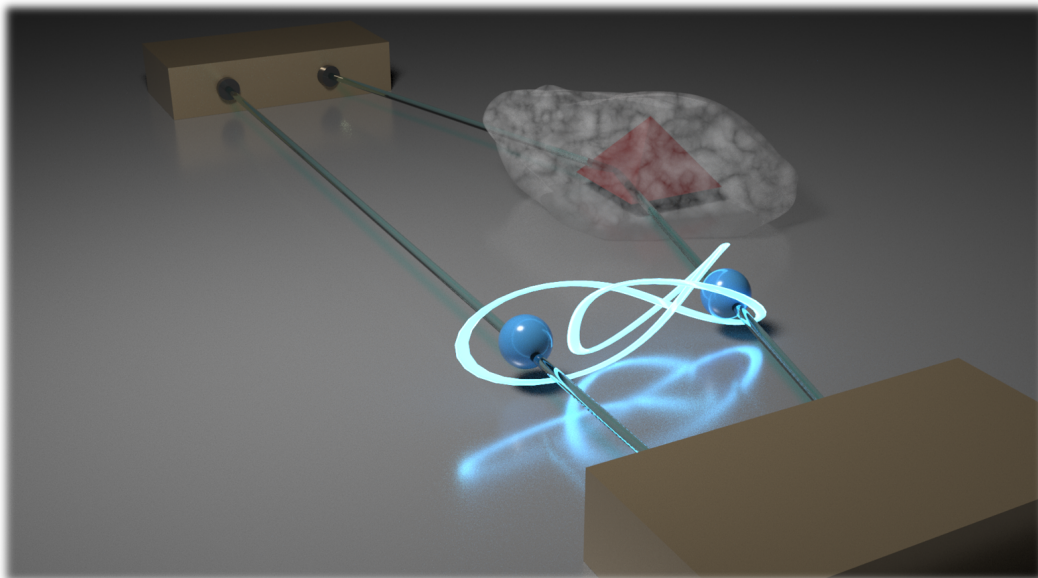BAYERISCHE
AKADEMIE DER
WISSENSCHAFTEN

A journey into quantum illumination

Dissertation

Fabian Johannes Kronowetter

TECHNISCHE UNIVERSITÄT MÜNCHEN

TUM School of Natural Sciences

A journey into quantum illumination

Fabian Johannes Kronowetter

Abstract

The second quantum revolution and the associated development of applications that exploit the distinct properties of individual quantum systems promise to redefine the limits of technology as we know it today. Along with quantum computing and quantum communication, quantum sensing is a central pillar of these recent developments. In quantum sensing, the quantum illumination (QI) scheme, which can be classified as part of the broader application segment of quantum radar, represents one of these advances and promises to outperform the best classical radar schemes. The unprecedented potential of QI relies on quantum-entangled probing states to push the well-known and established frontiers in object detection. To date, the only successful implementation of QI in the microwave domain relies on a specific mixing operation of the respective return and idler modes, followed by single-photon counting in one of the two mixer outputs. In this thesis, we present decisive advancements for a profound understanding of QI based on such a mixing scheme. As a first central result, we present a theoretical study on the robustness of the associated quantum advantage against imperfect detection of the return signals. We focus on realistic detection parameters in terms of detection efficiency and dark count probability, and quantify the trade-off between these two metrics in the framework of QI. We further unveil strongly asymmetric photon-number resolution requirements for detecting the two mixer outputs due to their largely different mean photon numbers. In addition, we extend the protocol to introduce correlated photon counting, which is based on counting photons from both mixer outputs, and identify an ideal weighting of the respective measurement outcomes in post-processing. Apart from these receiver characteristics, we identify rigorous requirements for the resource-state purity, which stem from an inherent fragility of the associated idler mode. The second main result is the experimental study of a nonlinear Josephson interferometer operating in the microwave regime. The architecture of our quantum microwave parametric interferometer (QUMPI) is based on superconducting Josephson parametric amplifiers as nonlinear quantum elements combined with linear microwave components. While the sensitivity of classical interferometers is intrinsically bound by shot noise, the usage of quantum input states or nonlinear quantum elements can push this fundamental bound to the Heisenberg limit. We find that the interferometric power of the QUMPI exceeds the shot-noise limit and observe sub-Poissonian photon statistics in the output modes. In addition, we identify a low-gain operation regime of the QUMPI which is essential for optimal quantum measurements in QI protocols with frequency-degenerate signal and idler modes. The novel insights based on these investigations are vital for a profound understanding of QI and successful experimental implementations approaching fundamental quantum limits.

Kurzzusammenfassung

Die zweite Quantenrevolution und die damit verbundene Entwicklung von Anwendungen, die sich die besonderen Eigenschaften einzelner Quantensysteme zunutze machen, eröffnen die Möglichkeit, die heute bekannten Grenzen der Technologie neu zu definieren. Neben dem Quantencomputing und der Quantenkommunikation stellt die Quantensensorik einen zentralen Pfeiler dieser jüngsten Entwicklungen dar. Im Bereich der Quantensensorik ermöglicht das Quantenbeleuchtungsverfahren (QI), das als Teil des breiteren Anwendungssegments des Quantenradars aufgefasst werden kann, die Empfindlichkeit der besten klassischen Radarverfahren zu übertreffen. Das beispiellose Potenzial von QI beruht auf der Verwendung von quantenverschränkten Abtastzuständen, um die Empfindlichkeitsgrenzen der klassischen Objekterkennung zu überwinden. Bislang beruht die einzige erfolgreiche Implementierung von QI im Mikrowellenbereich auf einer speziellen Mischoperation der jeweiligen zurückkehrenden und zurückgehaltenen Signalmoden, gefolgt von einer Einzelphotonenzählung in einem der beiden Mischerausgänge. In dieser Arbeit entwickeln wir ein tiefgreifendes Verständnis von QI-Verfahren, die auf einem solchen Mischschema basieren. Als erstes zentrales Ergebnis präsentieren wir eine theoretische Studie zur Robustheit des prinzipiell möglichen Quantenvorteils gegenüber einer nicht idealen Detektion der zurückkehrenden Signale. Unsere Studie verwendet realistische Detektionsparameter für die Detektionseffizienz und die Dunkelzählwahrscheinlichkeit der Mikrowellenphotonen, und quantifiziert den notwendigen Kompromiss zwischen diesen beiden Metriken im Rahmen von QI. Weiterhin zeigen wir stark asymmetrische Anforderungen an die Photonenzahlauflösung für die Detektion der beiden Mischerausgänge auf, die aus deren stark unterschiedlichen mittleren Photonenzahlen resultieren. Darüber hinaus erweitern wir das Protokoll für die Implementierung einer korrelierten Photonenzählung, die auf der Zählung von Photonen beider Mischerausgänge basiert, und identifizieren eine ideale Gewichtung der jeweiligen Messergebnisse in der Nachbearbeitung. Abgesehen von diesen Empfängereigenschaften definieren wir die notwendigen Anforderungen an die Reinheit des Ressourcenzustands, die sich aus der inhärenten Fragilität der zugehörigen zurückgehaltenen Mode ergibt. Das zweite Hauptergebnis ist eine experimentelle Studie eines nichtlinearen Josephson-Interferometers, das im Mikrowellenbereich betrieben wird. Die Architektur unseres parametrischen Quanten-Mikrowellen-Interferometers (QUMPI) basiert auf supraleitenden parametrischen Josephson-Verstärkern als nichtlineare Quantenelemente in Kombination mit linearen Mikrowellenkomponenten. Während die Empfindlichkeit klassischer Interferometer durch Schrotrauschen begrenzt ist, kann die Verwendung von Quantenzuständen anstelle von klassischen Signalen oder nichtlinearen Quantenelementen diese fundamentale Grenze bis zum Heisenberg-Limit verschieben. Wir stellen fest, dass

die interferometrische Leistung des QUMPI die Grenze des Schrotrauschens überschreitet und beobachten subpoissonische Photonenstatistiken in den Ausgangssignalen. Darüber hinaus identifizieren wir einen Betriebsmodus des QUMPI mit geringer Verstärkung, der für optimale Quantenmessungen in QI-Protokollen von grundlegender Bedeutung ist. Die neuen Erkenntnisse, die auf diesen Untersuchungen beruhen, sind entscheidend für ein tiefgehendes Verständnis von QI-Verfahren und ihre erfolgreiche experimentelle Implementierung nahe am fundamentalen Quantenlimit.

Contents

List of Figures

List of Tables

Chapter 1

Introduction

The second quantum revolution comes with a paradigm shift in our understanding and utilization of quantum phenomena, extending far beyond the theoretical realm into practical applications that could redefine technology fields, such as information processing, as we know them today [1–12]. The foundations for these impressive developments were laid by the first quantum revolution in the early 20th century, which culminated in the formulation of revolutionary theories like quantum mechanics and quantum electrodynamics [13–17]. The second quantum revolution has been enabled by our ability to design, control and manipulate quantum systems in unprecedented ways. This makes it possible to create artificial quantum systems and tailor them for specific applications. Based on this approach, a tremendous technological progress has been achieved in various fields, including quantum computing [18–28], quantum communication [29–34], and quantum sensing and metrology [35–39]. The basic ingredients for these advances are inherent quantum phenomena, such as quantum squeezing [40, 41], quantum superposition [42], and quantum entanglement [17]. In quantum sensing and metrology, novel approaches based on these phenomena enable an unprecedented level of precision and sensitivity [43]. The quantum illumination (QI) scheme, associated with the broad application segment of quantum radar, represents one of these approaches and can outperform the best classical radar schemes. Conventional radar architectures are based on sending a classical electromagnetic signal (e.g. microwave radiation) to an object and inferring information on the object by measuring and interpreting the reflected signal portions [43–46]. In general, the search for improved radar systems is ever-present for a wide range of applications, spanning from the medical sector to space exploration. QI relies on the use of entangled resource states to go beyond the state of the art in object detection. The QI protocol was first proposed in 2008 [47, 48] at optical frequencies for both discrete variable [47] and continuous variable (CV) quantum states [48]. As it turned out, the use of CV quantum states is compatible with classical radar architectures. Optical frequencies, however, are inherently incompatible with the requirement of a bright thermal background in QI [48, 49]. These findings led to a refocus of QI toward microwave frequencies that are naturally subject to a strong thermal background at ambient conditions. As a further limitation, the QI protocol only outperforms classical radar schemes for weakly reflecting objects and low

powers of the probing signals. Intuitively, the QI-based approaches excel where classical counterparts fail: in traditional sensing systems, the detection of weak signals is hindered by background noise, limiting their effectiveness in scenarios where precision is crucial. QI, however, leverages the highly correlated nature of the entangled probing signals to discriminate the faint signal from pure background noise with unprecedented sensitivity. The pioneering insights into QI propelled a plethora of theoretical and experimental studies exploring quantum object detection based on QI [50–64]. The ongoing efforts in QI exemplify the frontier of quantum technologies, marking a significant stride towards harnessing quantum principles for practical and impactful real-world applications.

Transferring quantum information protocols into the microwave realm poses numerous experimental hurdles. The comparatively low energy of single microwave quanta in the gigahertz range (1 GHz corresponds to about 50 mK) mandates cryogenic conditions - typically in the low tens of millikelvins range - to suppress the unwanted thermal noise. Furthermore, a general prerequisite for the operation of the employed superconducting circuits is a system temperature below the respective critical temperatures. Additionally, these superconducting circuits are based upon sophisticated fabrication techniques and tailor-made for operation at specific working frequencies. The cryogenic circuitry is interfaced by state-of-the-art microwave devices at room temperature, which enable control and readout of the quantum signals at the cryogenic stage. These measurement techniques require advanced signal recovery methods [65, 66]. The development and pioneering of such techniques have been undertaken at the Walther-Meißner-Institut (WMI) over the past decade [65, 67–74]. The corresponding central groundwork encompasses the development of advanced signal reconstruction techniques allowing for full Wigner tomography [67] and associated photon-number calibration methods [70]. The subsequent experimental realization of microwave squeezing [75], path entanglement with propagating quantum microwaves [65], and coherent displacement in phase space [76] complete the tool set for conducting advanced protocols, such as remote-state preparation [77], deterministic quantum teleportation [78], and microwave quantum key distribution [79].

The first main building block of this thesis is a theoretical discussion of different QI detection schemes [54]. In general, there are proposals for different QI schemes that all aim at harnessing remaining quantum correlations of an entanglement-based resource state. This two-mode quantum state is composed of a so-called signal mode, which is employed as a probe tone, and an idler mode, which is retained for a subsequent measurement in conjunction with the returned signal. To this date, the only successful implementation of QI in the microwave domain [55] relies on a specific mixing operation of the respective return and idler modes, followed by single-photon counting in one of the two mixer outputs. We investigate the performance of this scheme for realistic detection parameters regarding detection efficiency, dark count probability, and photon number resolution. Furthermore, we take into account the second mixer output and investigate the advantage of correlated photon counting (CPC) for a varying thermal background and optimum post-processing

weighting in CPC. We find that the requirements for photon number resolution in the two mixer outputs are highly asymmetric due to different associated photon number expectation values. In addition, we observe that the requirements regarding purity of the resource state are stringent, caused by high purity demands for the idler mode, while we observe a robustness against finite detection efficiencies of the single-photon detectors.

The second central component of this thesis is an experimental study of a nonlinear Josephson interferometer operating in the microwave regime [80]. While classical interferometers (operating with classical signals such as coherent light) are indispensable tools for the precise determination of various physical quantities, their accuracy is ultimately bound by the standard quantum limit. This limit can be overcome by using quantum states or nonlinear quantum elements. Our quantum microwave parametric interferometer (QUMPI) is based on superconducting flux-driven Josephson parametric amplifiers (JPAs) [81–83] as the nonlinear element combined with linear microwave elements. Such JPAs are established devices for various applications [84–87], such as quantum-limited phase-sensitive amplification [73] or generation of entangled two-mode squeezed (TMS) states [88]. We perform a systematic analysis of the implemented QUMPI. We find that its interferometric power exceeds the shot-noise limit and observe a sub-Poissonian photon statistics in the output modes. Furthermore, we identify a low-gain operation regime of the QUMPI which is essential for optimal quantum measurements in QI protocols.

The structure of this thesis is outlined as follows. First, we introduce some fundamental concepts of quantum information with propagating microwaves based on Gaussian-distributed states in chapter 2. In particular, we motivate continuous-variable (CV) states in quantum information and discuss Gaussian states of light with the most important single-mode and two-mode states. In addition, we briefly motivate different quantities of central importance for the analysis and categorization of such states, e.g., quantum entanglement and the degree of second-order coherence. Next, in chapter 3, we present a theory study on QI. After a brief discussion of classical radar and some basics on hypothesis testing, we present the Gaussian QI protocol that relies on entangled two-mode resource states. The additional information encoded into these quantum states, compared to the classical states used in the optimal classical radar scheme, needs to be harnessed by means of suitable detection schemes, which is an ongoing field of research [49]. We evaluate the most promising detection schemes in terms of performance and implementation. Next, we discuss the robustness of these QI schemes against unavoidable imperfections, such as a non-ideal purity of the resource states, an imperfect idler storage, and a realistic receiver performance. We conclude the chapter with a brief analysis of applications that go beyond binary detection in QI and a discussion of our findings. In chapter 4, we then motivate superconducting quantum technology as a platform for conducting experiments with propagating quantum microwaves. Here, we briefly introduce basic concepts of superconductivity, Josephson junctions, dc-SQUIDs and JPAs. Chapter 5 covers the experimental techniques used for conducting experiments with quantum microwaves at

millikelvin temperatures. Besides describing a cryogenic setup, we introduce the room-temperature electronics and important measurement techniques, such as the output line calibration and the experimental characterization of flux-driven JPAs. In chapter 6, we present an experimental realization of a quantum microwave parametric interferometer composed of balanced microwave beam splitters and JPAs. In a first step, we conduct a frequency-resolved network analysis, which is fundamental for a thorough understanding of the design requirements of our device. Next, we introduce a theory model for simulating the behavior of the interferometer at a fixed operation frequency. The main results of this chapter encompass a detailed study of the interferometer and its application potential in quantum information processing, and specifically, in the framework of QI. Finally, we summarize our key results and provide a brief outlook in chapter 7.

Chapter 2

Gaussian quantum information with propagating microwaves

In this chapter, we present some fundamental theoretical concepts that are necessary for a thorough understanding of the experimental results obtained within this thesis. In a first step, we introduce the concept of continuous variables in quantum information in Sec. 2.1. In Sec. 2.2, we discuss various Gaussian states and their corresponding characteristics. The intriguing concept of quantum entanglement, which lays the foundation for a plethora of quantum schemes and protocols, is addressed in Sec. 2.3. Finally, in Sec. 2.4 we introduce the second-order correlation function, which can be used to categorize the nature and underlying statistics of electromagnetic waves.

2.1 Continuous variables in quantum information

In quantum physics, intuitive concepts that are inherent to quantum phenomena, such as quantum superposition and entanglement, are often associated with discrete-variable (DV) states. In this context, quantum superposition can be nicely illustrated based on the two logical basis states of a qubit, $|0\rangle$ and $|1\rangle$ in Dirac notation, according to its wave function $|\psi\rangle = c_0|0\rangle + c_1|1\rangle$, where c_0 and c_1 are complex coefficients describing the weight of the corresponding basis state in the superposition [6]. Similarly, quantum entanglement between two parties A and B corresponds to a nonlocal wave function $|\psi_{\mathrm{AB}}\rangle = 1/\sqrt{2}\,(|0\rangle_{\mathrm{A}} \otimes |1\rangle_{\mathrm{B}} - |1\rangle_{\mathrm{A}} \otimes |0\rangle_{\mathrm{B}})$. The extension from discrete to continuous variables (CV), and hence to infinite dimensions, is a natural and logical approach for various applications in quantum information processing [6, 78, 89]. The preparation, unitary transformation, and measurement of quantum states is implementable in a straightforward manner with CVs, such as continuous quadrature amplitudes of the quantized electromagnetic field [6]. For example, squeezed electromagnetic fields enable the straightforward generation of CV entanglement, while homodyne detection represents an established measurement technique for accessing the information encoded in the continuous phase-space quadratures [6]. Next to these practical and efficiency-based considerations, schemes based on CVs stand out due to their unconditional character,

which is difficult to achieve in DV settings based on qubits or single-photon states [6]. The generation of squeezed states, and similarly of entangled states, unconditionally occurs at a timescale inversely proportional to the corresponding bandwidth [6]. However, the generated entangled states suffer from a finite degree of entanglement, and only converge to an equivalent of the maximally entangled EPR state in the threshold of very large squeezing [6]. Accordingly, CV approaches excel in terms of generation efficiency and deterministic character, but never reach perfect operation in realistic experimental settings. A variety of CV protocols can be fully described in the framework of Gaussian operations, i.e., interaction Hamiltonians that are at most quadratic in terms of the bosonic mode operators and maintain the Gaussian statistics of input states [6, 54, 78, 90, 91]. Throughout this work, we focus on Gaussian CV quantum information.

2.1.1 Quadrature operators of the quantized electromagnetic field

In quantum information, electromagnetic modes are quantized and, for a harmonic potential, can be well described by quantum harmonic oscillators with a Hamiltonian [92]

$$\hat{H}_k = \hbar\omega_k \left(\hat{a}_k^\dagger \hat{a}_k + \frac{1}{2} \right), \tag{2.1}$$

where $\hbar$ is the reduced Planck constant, k is the mode index, ω_k is the corresponding angular frequency, and $\hat{a}_k^\dagger$ and $\hat{a}_k$ are the bosonic creation and annihilation operators, respectively. The corresponding bosonic commutation relations are

$$[\hat{a}_k, \hat{a}_{k'}^\dagger] = \delta_{kk'} \qquad \text{and} \qquad [\hat{a}_k, \hat{a}_{k'}] = 0. \tag{2.2}$$

The Hamiltonian in Eq. (2.1) can also be expressed as

$$\hat{H}_k = \frac{1}{2}(\hat{p}_k^2 + \omega_k^2 \hat{x}_k^2), \tag{2.3}$$

where $\hat{p}_k$ and $\hat{x}_k$ are the momentum and position operators, which can be expressed via the creation and annihilation operators according to

$$\hat{x}_k = \sqrt{\frac{\hbar}{2\omega_k}}\, (\hat{a}_k + \hat{a}_k^\dagger), \tag{2.4}$$

$$\hat{p}_k = \frac{1}{i} \sqrt{\frac{\hbar\omega_k}{2}}\, (\hat{a}_k - \hat{a}_k^\dagger), \tag{2.5}$$

where i is the imaginary unit, and where we employ the commutation relation for position and momentum

$$[\hat{x}_k, \hat{p}_{k'}] = i\hbar\delta_{kk'}. \tag{2.6}$$

For the propagating electromagnetic modes, the quantum harmonic oscillators' position and momentum operators correspond to the quadrature operators, which we introduce as dimensionless, Hermitian quantities [93]

$$\hat{q}_k \equiv \sqrt{\frac{\omega_k}{2\hbar}} \; \hat{x}_k = \frac{\hat{a}_k + \hat{a}_k^\dagger}{2}, \tag{2.7}$$

$$\hat{p}_k \equiv \sqrt{\frac{1}{2\hbar\omega_k}} \; \hat{p}_k = \frac{\hat{a}_k - \hat{a}_k^\dagger}{2\mathrm{i}}, \tag{2.8}$$

with a commutation relation given by

$$[\hat{q}_k, \hat{p}_{k'}] = \frac{\mathrm{i}}{2}\delta_{kk'}. \tag{2.9}$$

From a classical viewpoint, these quadrature operators correspond to the real and imaginary part of the complex oscillator amplitude for a single mode k [6]. Importantly, the Heisenberg uncertainty relation for any arbitrary quantum state in terms of two non-commuting observables $\hat{O}_1$ and $\hat{O}_2$ is given by [94]

$$\langle(\Delta\hat{O}_1)^2\rangle\langle(\Delta\hat{O}_2)^2\rangle \geq \frac{1}{4}|\langle[\hat{O}_1,\hat{O}_2]\rangle|^2, \tag{2.10}$$

where the variance $(\Delta\hat{O})^2$ of an observable $\hat{O}$ is

$$\langle(\Delta\hat{O})^2\rangle = \langle(\hat{O} - \langle\hat{O}\rangle)^2\rangle = \langle\hat{O}^2\rangle - \langle\hat{O}\rangle^2. \tag{2.11}$$

As a consequence of Eq. (2.9) combined with Eq. (2.10), the propagating-field quadratures possess a finite variance

$$\langle(\Delta\hat{q})^2\rangle\langle(\Delta\hat{p})^2\rangle \geq \frac{1}{4}|\langle[\hat{q}_k,\hat{p}_k]\rangle|^2 = \frac{1}{16}. \tag{2.12}$$

The classical counterparts of the quadrature operators $\hat{q}$ and $\hat{p}$ are the in-phase (I) and quadrature (Q) components of the complex classical signal, respectively [95]. Since the global phase reference is arbitrary, one can define generalized quadratures [92]

$$\begin{pmatrix}\hat{q}_k^\theta \\ \hat{p}_k^\theta\end{pmatrix} = \begin{pmatrix}\cos\theta & \sin\theta \\ -\sin\theta & \cos\theta\end{pmatrix}\begin{pmatrix}\hat{q}_k \\ \hat{p}_k\end{pmatrix}, \tag{2.13}$$

which are rotated globally by a phase θ.

2.1.2 Representations of quantum states

An arbitrary pure state $|\Psi\rangle$ of the electromagnetic field is defined by a linear superposition of the products of photon-number states of the distinct modes [93]

$$|\Psi\rangle = \sum_{n_1} \ldots \sum_{n_m} \ldots C_{n_1 \cdots n_m \cdots} |n_1\rangle_1 \otimes \ldots \otimes |n_m\rangle_m \otimes \ldots, \tag{2.14}$$

where the summation runs over the entire set of photon numbers n_1 to n_m and $\otimes$ denotes the tensor product. Importantly, pure states are composed of photon-number states with the weight of the number states given by the complex coefficients $C_{n_1 \cdots n_m}$. For some fundamental pure states of the electromagnetic field, Eq. (2.14) reduces to a superposition of solely single-mode states, such as coherent states (see Sec. 2.2.3) or squeezed states (see Sec. 2.2.4). A two-mode example of a pure state is the photon pair state. Conversely, not all excitations of the electromagnetic field are encompassed by the description of pure states according to Eq. (2.14). In this case, one can only rely on a set of probabilities for the field to be characterized by a pure state according to Eq. (2.14). The corresponding quantum state is a statistical mixture of pure states and is often referred to as a mixed state. An important example of the statistical mixture is the thermal state characterized by its temperature T, introduced in Sec. 2.2.2. In the quantum description, statistical mixtures are described by the density operator

$$\hat{\rho} = \sum_k P_k |\psi_k\rangle\langle\psi_k|, \tag{2.15}$$

where P_k is the probability of the quantum state to be in the pure state $|\psi_k\rangle$, such that $\sum_k P_k = 1$ with $0 \leq P_k \leq 1$. Consequently, a pure state is a specific case of a mixed state for which one probability within the sum is unity, while all remaining sum elements are zero [56, 93]. Opposed to mixed states, pure states fulfill the relation

$$\hat{\rho}^2 = \hat{\rho}. \tag{2.16}$$

The expectation value of an operator $\hat{O}$ can be obtained via the trace operation

$$\langle\hat{O}\rangle = \mathrm{Tr}(\hat{O}\hat{\rho}) = \sum_k P_k \langle\psi_k|\hat{O}|\psi_k\rangle. \tag{2.17}$$

Thus, the density matrix formalism is especially convenient for the expectation value analysis in both, pure and mixed scenarios. For an alternative description of a general N-mode quantum state, we can define a vector operator

$$\hat{\boldsymbol{r}} = (\hat{q}_1, \hat{p}_1, \ldots, \hat{q}_N, \hat{p}_N), \tag{2.18}$$

composed of the set of single-mode quadrature operators, which enters in the operator

$$\hat{O}(\boldsymbol{\xi}) = \exp\left(i\hat{\boldsymbol{r}}^T \boldsymbol{\Omega}\,\boldsymbol{\xi}\right), \tag{2.19}$$

where $\boldsymbol{\Omega}$ is the symplectic form of dimension $2N \times 2N$

$$\boldsymbol{\Omega} = \oplus_{k=1}^{N}\boldsymbol{\omega} \quad \text{with} \quad \boldsymbol{\omega} = \begin{pmatrix} 0 & 1 \\ -1 & 0 \end{pmatrix}, \tag{2.20}$$

and $\boldsymbol{\xi} \in \mathbb{R}^{2N}$. The symmetrically ordered characteristic function χ of an arbitrary quantum state is linked to its density operator via [96]

$$\chi(\boldsymbol{\xi}) = \text{Tr}\left[\hat{\rho}\,\hat{O}(\boldsymbol{\xi})\right]. \tag{2.21}$$

The Fourier transform of the symmetrically ordered characteristic function, also known as the Wigner function W, can be written as [97, 98]

$$W(\boldsymbol{r}) = \int_{\mathbb{R}^{2N}} \frac{\mathrm{d}^{2N}\boldsymbol{\xi}}{(2\pi)^{2N}} \exp\left(-i\boldsymbol{r}^T\boldsymbol{\omega}\,\boldsymbol{\xi}\right)\chi(\boldsymbol{\xi}). \tag{2.22}$$

The Wigner function is a quasi-probability distribution that is normalized according to $\int_{-\infty}^{\infty} W(\boldsymbol{r})d\boldsymbol{r} = 1$. The continuous variables $\boldsymbol{r}$ constitute the quadrature operators eigenvalues [6]. In its general form, the Wigner function can be non-positive [6]. A marginal distribution of a subset m of the $2N$ field quadratures can be straightforwardly calculated by integration of $W(\boldsymbol{r})$ over the $2N - m$ residual field quadratures [6]. For instance, the marginal distribution of one local mode k of an N-mode state can be obtained via

$$W(q_k, p_k) =$$
$$\int_{-\infty}^{\infty}\ldots\int_{-\infty}^{\infty} W(q_1,\ldots,q_{k-1},p_{k-1},q_{k+1},p_{k+1},\ldots,p_N)\mathrm{d}q_1\ldots\mathrm{d}q_{k-1}\mathrm{d}p_{k-1}\mathrm{d}q_{k+1}\mathrm{d}p_{k+1}\ldots\mathrm{d}p_N. \tag{2.23}$$

The Wigner function is a versatile tool to obtain expectation values of arbitrary quantities that are symmetric in $\hat{a}$ and $\hat{a}^\dagger$, in particular the field quadratures [6]. Importantly, a variety of alternative quasi-probabilities is used in quantum information. Among these are the P-function [99, 100], which is particularly useful for calculating mean values of operators normally ordered in $\hat{a}$ and $\hat{a}^\dagger$. The Q-function [101], on the other hand, is well-suited for calculating mean values of operators anti-normally ordered in $\hat{a}$ and $\hat{a}^\dagger$ [6].

In the picture of a single-mode quantum state, the signal moments $\langle(\hat{a}^\dagger)^k \hat{a}^l\rangle$ with $k, l \in \mathbb{N}_0$ fully describe the corresponding state, similar to the density operator [102]. The signal moments can be analogously expressed for multimode states. For a two-mode state

they are given by $\langle (\hat{a}_1^\dagger)^k (\hat{a}_2^\dagger)^l \hat{a}_1^m \hat{a}_2^n \rangle$ with $k, l, m, n \in \mathbb{N}_0$. In general, such a full description requires knowledge of the infinite number of signal moments. There are, however, certain classes of states that can be fully described by a finite number of signal moments. One of such classes are Gaussian states, introduced in the next section [103].

2.2 Gaussian states of light

In this section, we discuss Gaussian states, a class of particularly useful quantum states of light that are fully characterized by signal moments up to second order, which allows for a straightforward mathematical description [104]. The uniqueness of these states lies in their versatility and simplicity, which is exploited in many quantum information processing and quantum communication protocols. Gaussian states follow a Gaussian probability distribution of their field quadratures with a positively defined Wigner function [6]. This class of states is of central importance for the theoretical study presented in Ch. 3 and for the experimental results presented in Ch. 6. A convenient approach to describe an arbitrary N-mode Gaussian state is given by the statistical moments of its quadratures. We introduce the displacement vector $\boldsymbol{d}$ as the first statistical moment

$$\boldsymbol{d} = \langle \hat{\boldsymbol{r}} \rangle, \tag{2.24}$$

which carries information on the mean field amplitude of all $2N$ quadratures of the N-mode electromagnetic state. We further define a covariance matrix $\boldsymbol{V}$, a $2N \times 2N$ real symmetric matrix, as the second statistical moment with

$$\boldsymbol{V} = \frac{\langle \hat{r}_k \hat{r}_l + \hat{r}_l \hat{r}_k \rangle}{2} - \langle \hat{r}_k \rangle \langle \hat{r}_l \rangle, \tag{2.25}$$

for $k, l = 1, ..., 2N$. Accordingly, any Gaussian state can be fully described by a suitable $\boldsymbol{d}$ and $\boldsymbol{V}$ [6, 7]. The associated purity can be directly obtained from the covariance matrix according to

$$\mu = \frac{1}{4^N \sqrt{\det(\boldsymbol{V})}}. \tag{2.26}$$

Pure Gaussian states are characterized by $\det(\boldsymbol{V}) = 4^{-2N}$, while mixed states satisfy $0 \leq \mu < 1$, where $\mu = 0$ corresponds to a maximally mixed state [105]. The Wigner function of an N-mode Gaussian state is given by

$$W(\boldsymbol{r}) = \frac{\exp\left[-\frac{1}{2}(\boldsymbol{r} - \boldsymbol{d})\boldsymbol{V}^{-1}(\boldsymbol{r} - \boldsymbol{d})^{\mathrm{T}}\right]}{(2\pi)^N \sqrt{\det(\boldsymbol{V})}}. \tag{2.27}$$

In this work, we focus on two-mode systems ($N = 2$) that are described by a 4×4
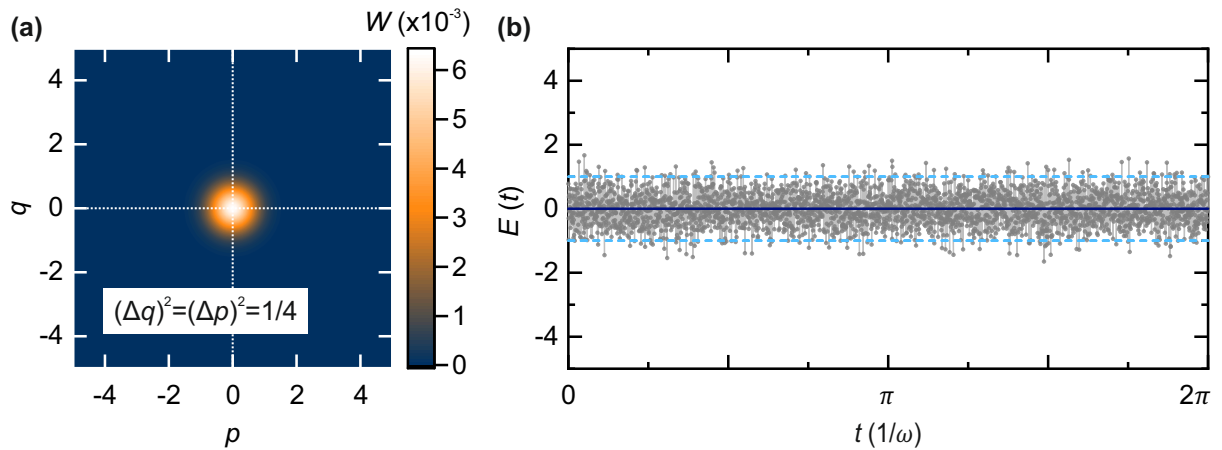
Figure 2.1: The vacuum state illustrated via (a) its Wigner function and (b) the associated electric field with an angular carrier frequency ω. The gray dots in (b) are 3000 randomly sampled points from the underlying Gaussian distribution, the light gray line is a guide to the eye. The solid dark blue line depicts the associated mean, whereas the dashed blue lines show the 2σ confidence interval of the vacuum fluctuations.

covariance matrix

$$V = \begin{pmatrix} A & C \\ C^{\mathrm{T}} & B \end{pmatrix}, \tag{2.28}$$

where A and B are 2×2 matrices that characterize the local properties of modes A and B, respectively. The associated cross-correlations between both local modes are captured in the 2×2 matrix C.

2.2.1 Vacuum state

The quantum-mechanical ground state is characterized by a finite, non-zero energy, which is a direct consequence of the bosonic commutation relation [106]. This lowest energy state is referred to as the vacuum state, $|0\rangle$, carrying an energy of half a photon, often referred to as the vacuum fluctuations [6]. These fluctuations manifest themselves, based on our convention, in a quadrature variance of $(\Delta q)^2 = (\Delta p)^2 = 1/4$. Consequently, for a single mode the vacuum state is characterized by

$$d_{\mathrm{vac}} = 0, \qquad V_{\mathrm{vac}} = \frac{\mathbb{I}_2}{4}, \tag{2.29}$$

where $\mathbb{I}_2$ is the 2×2 identity matrix. Figure 2.1(a) shows the corresponding Wigner function, Fig. 2.1(b) depicts the associated electric field in the time domain. Importantly, this vacuum variance is a direct consequence of the definition of the quadrature operators [cf. Eqs. (2.7) and (2.8)]. Since this definition is arbitrary, one needs to pay attention on the underlying reference when performing a quantitative analysis of electromagnetic states. Other vacuum variance definitions often found in literature are $1/2$ and 1 [6, 93, 97].
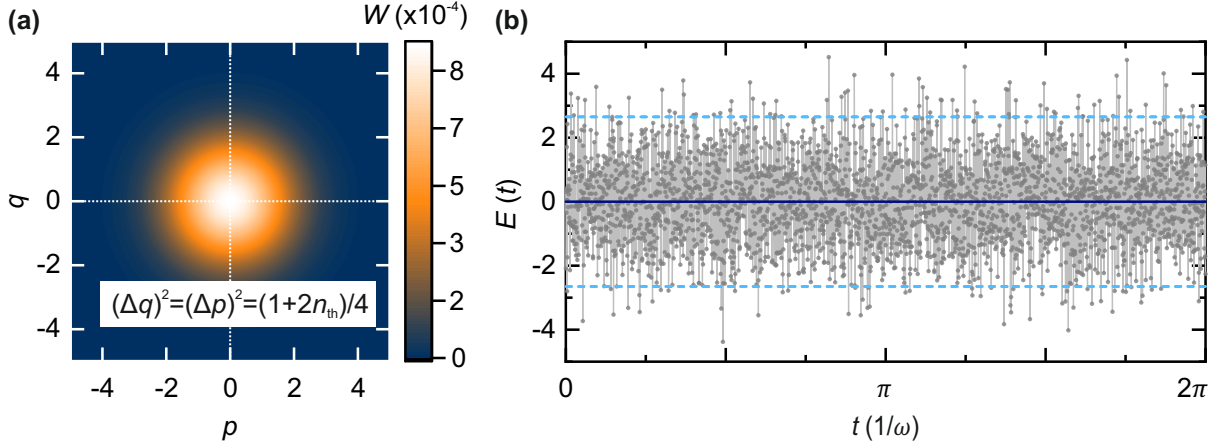
Figure 2.2: Thermal state with $n_{\mathrm{th}} = 3$ photons illustrated via (a) its Wigner function and (b) the associated electric field with an angular carrier frequency ω. The gray dots in (b) are 3000 randomly sampled points from the underlying Gaussian distribution, the light gray line is a guide to the eye. The solid dark blue line depicts the associated mean, whereas the dashed blue lines show the 2σ confidence interval of the thermal fluctuations.

2.2.2 Thermal state

The vacuum state can be understood as a thermal state with equilibrium temperature $T = 0$. At finite temperatures, $T > 0$, a thermal state is characterized by its density matrix operator

$$\hat{\rho}_{\mathrm{th}} = \sum_n \frac{n_{\mathrm{th}}^n}{(1 + n_{\mathrm{th}})^{n+1}} |n\rangle\langle n|, \tag{2.30}$$

where $|n\rangle$ is a Fock state of a single mode with frequency ω. The density matrix operator in Eq. (2.30) is fully described by the corresponding equilibrium photon number distribution that follows the Bose-Einstein statistics [107]

$$n_{\mathrm{th}} = \langle \hat{a}^\dagger \hat{a} \rangle = \frac{1}{\exp(\frac{\hbar\omega}{k_{\mathrm{B}}T}) - 1}, \tag{2.31}$$

where k_{B} is the Boltzmann constant and $\hbar$ is the reduced Planck constant. The normally ordered signal moments of a thermal state are given by

$$\langle (\hat{a}^\dagger)^m \hat{a}^n \rangle = n! n_{\mathrm{th}}^n \delta_{nm}. \tag{2.32}$$

The mean and covariance matrix of a thermal state are

$$\boldsymbol{d}_{\mathrm{th}} = 0, \qquad \boldsymbol{V}_{\mathrm{th}} = (1 + 2n_{\mathrm{th}})\frac{\mathbb{I}_2}{4}. \tag{2.33}$$

Figure 2.2(a) shows an exemplary Wigner function of a thermal state, Fig. 2.2(b) depicts the associated electric field distribution in the time domain with a clear broadening of its
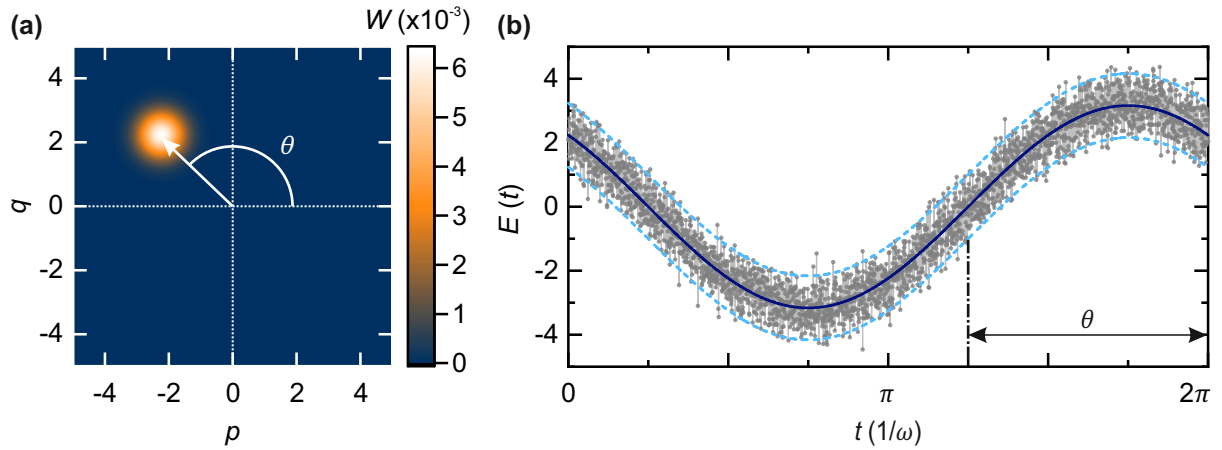
Figure 2.3: Coherent state with a displacement angle $\theta = 3\pi/4$ and displacement amplitude $|\alpha|^2 = 10$ illustrated via (a) its Wigner function and (b) the associated electric field with an angular carrier frequency ω. The gray dots in (b) are 3000 randomly sampled points from the underlying Gaussian distribution, the light gray line is a guide to the eye. The solid dark blue line depicts the associated mean, whereas the dashed blue lines show the 2σ confidence interval of the coherent state.

variance as compared to Fig. 2.1.

2.2.3 Coherent state

A coherent state $|\alpha\rangle$ can be generated by applying the displacement operator [104]

$$\hat{D}(\alpha) = \exp\left(\alpha\,\hat{a}^\dagger - \alpha^*\hat{a}\right) \tag{2.34}$$

to the vacuum state according to [99]

$$|\alpha\rangle = \hat{D}(\alpha)|0\rangle = \exp\left(-\frac{|\alpha|^2}{2}\right)\sum_n \frac{\alpha^n}{\sqrt{n!}}|n\rangle. \tag{2.35}$$

The complex displacement amplitude, $\alpha = |\alpha|\exp(\mathrm{i}(\pi/2-\theta)) = P+\mathrm{i}Q$, carries information about the average number of displacement photons, $n_\mathrm{d} = |\alpha|^2$, and the displacement angle θ, which we define with respect to the p-axis, as illustrated in Fig. 2.3(a). The coherent state is also an eigenstate of the annihilation operator

$$\hat{a}|\alpha\rangle = \alpha|\alpha\rangle. \tag{2.36}$$

Figure 2.3(a) illustrates the Wigner function of a coherent state with $|\alpha|^2 = 10$ and $\theta = 3\pi/4$. Figure 2.3(b) shows the corresponding electric field in the time domain with an identical variance as the vacuum state (cf. Fig. 2.1). Correspondingly, coherent states are minimum-uncertainty, pure states with $\mu = 1$. The expectation value and covariance
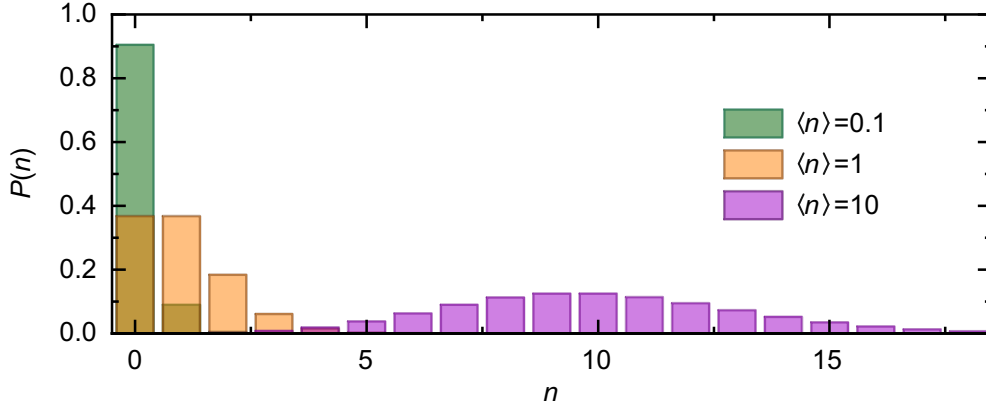
Figure 2.4: Photon-number probability distributions of coherent states with different mean photon numbers, according to Eq. (2.39).

matrix of a coherent state are

$$
\boldsymbol{d}_{\mathrm{coh}} = \begin{pmatrix} P \\ Q \end{pmatrix} = \begin{pmatrix} \mathrm{Re}\,\alpha \\ \mathrm{Im}\,\alpha \end{pmatrix}, \qquad \boldsymbol{V}_{\mathrm{coh}} = \frac{\mathbb{1}_2}{4}. \tag{2.37}
$$

From an intuitive point of view, the sinusoidal oscillations of strong coherent states, $\alpha \gg 1$, resemble the characteristics of a harmonic oscillator supplemented by the quantum mechanical vacuum noise. The relative uncertainty of the coherent state photon number is [93]

$$
\frac{\Delta n}{\langle n \rangle} = \frac{1}{|\alpha|} = \frac{1}{\sqrt{n}}, \tag{2.38}
$$

which decreases with increasing $|\alpha|$ and illustrates the vanishing quantum signatures in coherent states towards large mean photon numbers, $n \gg 1$. Figure 2.4 shows the Poisson-type photon-number probability distributions of coherent states for different mean photon numbers

$$
P(n) = |\langle n | \alpha \rangle|^2 = \exp\left(-|\alpha|^2\right) \frac{|\alpha|^{2n}}{n!} = \exp\left(-\langle n \rangle\right) \frac{\langle n \rangle^n}{n!}. \tag{2.39}
$$

2.2.4 Squeezed vacuum state

So far, we exclusively considered Gaussian states with a uniform variance in phase space. Single-mode squeezed (SMS) states break this rotational symmetry and exhibit a distorted, ellipsoidal probability distribution in phase space. Importantly, the minimal variance of such SMS states is lower than the vacuum variance. Consequently, the orthogonal, maximal variance of SMS states must be increased accordingly, hence the terminology

squeezed. The SMS vacuum state is defined as

$$|\xi\rangle = \hat{S}(\xi)|0\rangle, \tag{2.40}$$

where the squeeze operator is

$$\hat{S}(\xi) = \exp\left[\frac{1}{2}\xi^*\hat{a}^2 - \frac{1}{2}\xi\left(\hat{a}^\dagger\right)^2\right], \tag{2.41}$$

and $\xi = re^{\mathrm{i}\varphi}$ denotes the complex squeeze parameter with the squeeze factor r, and the corresponding phase φ that carries information on the squeezing orientation in phase space. The squeeze factor r encodes the squeezed (or minimum) variance, σ_s^2, as well as the anti-squeezed (or maximum) variance, σ_a^2, according to

$$\sigma_\mathrm{s}^2 = \frac{1}{4}e^{-2r} \qquad \text{and} \qquad \sigma_\mathrm{a}^2 = \frac{1}{4}e^{2r}. \tag{2.42}$$

Note that the prefactor of $1/4$ in Eq. (2.42) stems from our definition of the vacuum fluctuations [cf. Eq. (2.29)] and that Eq. (2.42) is only valid for pure states. The level of squeezing and anti-squeezing can be also expressed in decibel as [108]

$$S \equiv -10\log_{10}(4\,\sigma_\mathrm{s}^2) \qquad \text{and} \qquad A \equiv 10\log_{10}(4\,\sigma_\mathrm{a}^2), \tag{2.43}$$

respectively. While the definition of the SMS vacuum state in Eq. (2.40) is similar to its counterpart for coherent states [cf. Eq. (2.35)], the squeeze operator has a quadratic exponent in terms of the creation and annihilation operators in contrast to the linear displacement operator [cf. Eq. (2.34)]. The squeeze operator is a unitary operator with [109]

$$\hat{S}^\dagger\hat{S} = \hat{S}\hat{S}^\dagger = 1. \tag{2.44}$$

Analogous to coherent states, squeezed states can be expressed in the Fock basis as [97]

$$|\xi\rangle = \sqrt{\operatorname{sech} r} \sum_{n=0}^\infty (-1)^n \frac{\sqrt{(2n)!}}{n!} \left[\frac{\exp(\mathrm{i}\varphi)\tanh r}{2}\right]^n |2n\rangle. \tag{2.45}$$

This shows that an ideal SMS vacuum state is formed by even-numbered Fock states $|2n\rangle$. The photon-number expectation value of SMS vacuum states can be evaluated as [110]

$$\langle n\rangle = \langle\xi|\hat{a}^\dagger\hat{a}|\xi\rangle = \langle 0|\hat{S}^\dagger(\xi)\hat{a}^\dagger\hat{S}(\xi)\hat{S}^\dagger(\xi)\hat{a}\hat{S}(\xi)|0\rangle = \sinh^2 r, \tag{2.46}$$

which can be straightforwardly calculated via the squeezing operator transformation [97]

$$\hat{S}^\dagger(\xi)\hat{a}^\dagger\hat{S}(\xi) = \hat{a}\cosh r - \hat{a}^\dagger e^{\mathrm{i}\varphi}\sinh r, \tag{2.47}$$
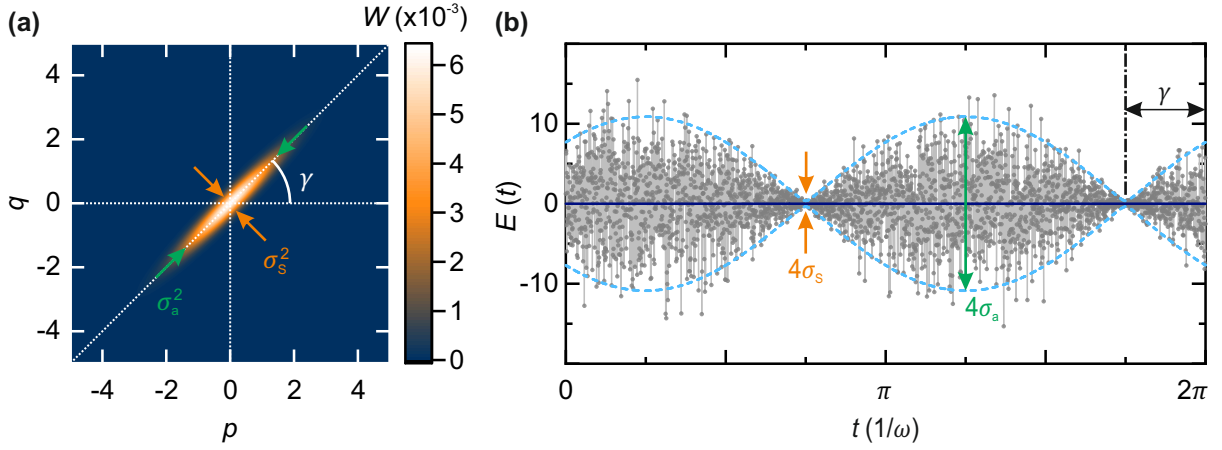
Figure 2.5: Squeezed vacuum state with a squeeze factor $r = 1$ and squeeze angle $\gamma = \pi/4$ illustrated via (a) its Wigner function and (b) the associated electric field with an angular carrier frequency ω. The gray dots in (b) are 3000 randomly sampled points from the underlying Gaussian distribution, the light gray line is a guide to the eye. The solid dark blue line depicts the associated mean, whereas the dashed blue lines show the 2σ confidence interval of the squeezed vacuum fluctuations.

and its Hermitian conjugate

$$\hat{S}^\dagger(\xi)\hat{a}\hat{S}(\xi) = \hat{a}^\dagger \cosh r - \hat{a}\,e^{-i\varphi}\sinh r. \tag{2.48}$$

The corresponding photon-number variance is

$$(\Delta n)^2 = 2\langle n\rangle(\langle n\rangle + 1). \tag{2.49}$$

Equation (2.46) yields zero in the case of no squeezing, $r = 0$, coinciding with the vacuum state, and increases with increasing r. The average field amplitude and covariance matrix of the SMS state are given by

$$\boldsymbol{d}_{\mathrm{sq}} = 0, \qquad \boldsymbol{V}_{\mathrm{sq}} = \frac{1}{4}\begin{pmatrix} e^{-2r}\cos^2\frac{\varphi}{2} + e^{2r}\sin^2\frac{\varphi}{2} & -\sinh 2r\,\sin\varphi \\ -\sinh 2r\,\sin\varphi & e^{2r}\cos^2\frac{\varphi}{2} + e^{-2r}\sin^2\frac{\varphi}{2} \end{pmatrix}. \tag{2.50}$$

Similar to the phase convention of coherent states, we introduce the squeeze angle, $\gamma = -\varphi/2$, as the angle between the anti-squeezed quadrature direction and the p-axis, illustrated in Fig. 2.5(a).

2.2.5 Squeezed coherent state

A central question for applications relying on squeezed states is how one can leverage the reduced quadrature noise in practical scenarios. While a wide range of classical communication and sensing applications relies on coherent resource states combined
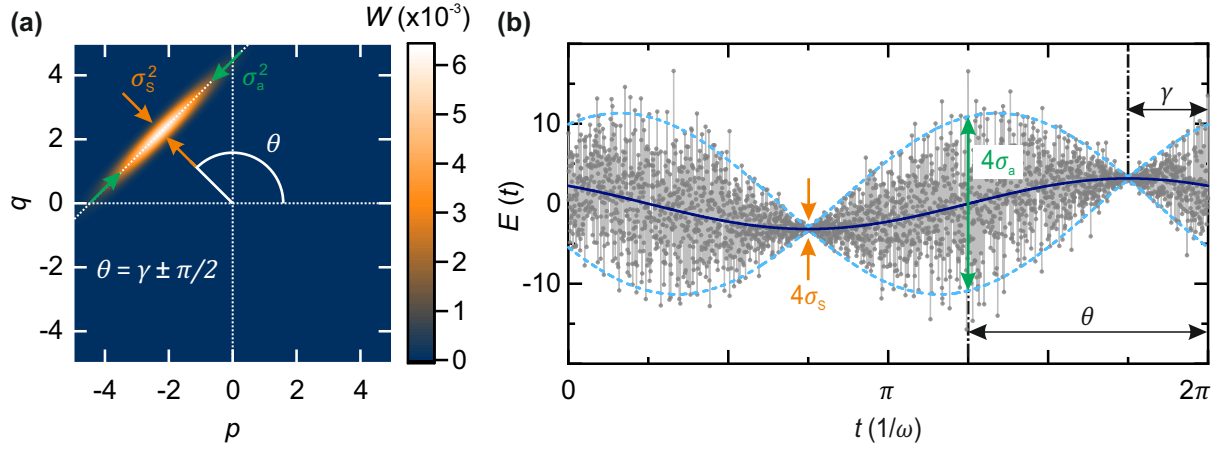
Figure 2.6: Amplitude-squeezed state with squeeze factor $r = 1$, squeeze angle $\gamma = \pi/4$, displacement
angle $\theta = 3\pi/4$ and $|\alpha|^2 = 10$ illustrated via (a) its Wigner function and (b) the associated
electric field with an angular carrier frequency ω. The gray dots in (b) are 3000 randomly
sampled points from the underlying Gaussian distribution, the light gray line is a guide to
the eye. The solid dark blue line depicts the associated mean, whereas the dashed blue lines
show the 2σ confidence interval of the squeezed vacuum fluctuations.

with homodyne detection, the zero mean of SMS vacuum states hinders their use in
these protocols. We introduce the displaced squeezed state $|\alpha, \xi\rangle$, which overcomes
this restriction. This class of states is generated by squeezing the vacuum state and
subsequently applying the displacement operation [97]

$$|\alpha, \xi\rangle = \hat{D}(\alpha)\hat{S}(\xi)|0\rangle. \tag{2.51}$$

Accordingly, this state has unit purity and is characterized by

$$\boldsymbol{d}_{\text{disp,sq}} = \begin{pmatrix} \text{Re}\,\alpha \\ \text{Im}\,\alpha \end{pmatrix}, \quad \boldsymbol{V}_{\text{disp,sq}} = \frac{1}{4} \begin{pmatrix} e^{-2r}\cos^2\frac{\varphi}{2} + e^{2r}\sin^2\frac{\varphi}{2} & -\sinh 2r \sin\varphi \\ -\sinh 2r \sin\varphi & e^{2r}\cos^2\frac{\varphi}{2} + e^{-2r}\sin^2\frac{\varphi}{2} \end{pmatrix}, \tag{2.52}$$

and the photon-number properties

$$\langle n \rangle = |\alpha|^2 + \sinh^2 r, \tag{2.53}$$

$$(\Delta n)^2 = |\alpha \cosh r - \alpha^* e^{-i\varphi}\sinh r|^2 + 2\cosh^2 r \sinh^2 r. \tag{2.54}$$

As can be seen from Eq. (2.52), the squeezed coherent state carries the same coherent
information α as a coherent state in the first statistical moment, while the underlying
phase-dependent noise (or variance) can be suppressed below the vacuum limit. The
SNR of squeezed coherent states depends on the distinct phase angles θ and φ and can
exceed the coherent-state reference by a factor of $\exp(2r)$ [93]. This maximized SNR is
achieved with *amplitude-squeezed* states, where the displacement angle is orthogonal to
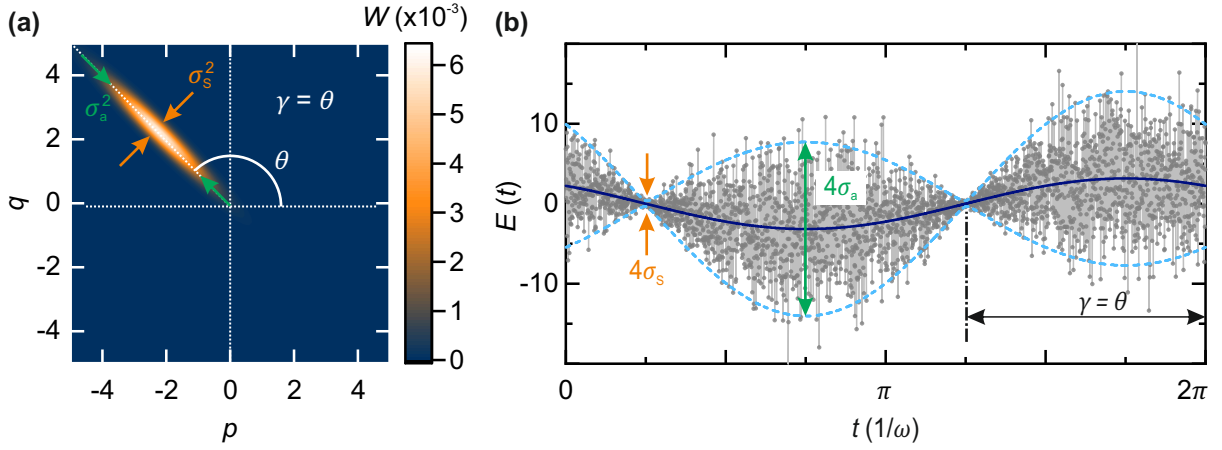
Figure 2.7: Phase-squeezed state with squeeze factor $r = 1$, squeeze angle $\gamma = 3\pi/4$, displacement angle $\theta = 3\pi/4$ and $|\alpha|^2 = 10$ illustrated via (a) its Wigner function and (b) the associated electric field with an angular carrier frequency ω. The gray dots in (b) are 3000 randomly sampled points from the underlying Gaussian distribution, the light gray line is a guide to the eye. The solid dark blue line depicts the associated mean, whereas the dashed blue lines show the 2σ confidence interval of the squeezed vacuum fluctuations.

the squeeze angle, i.e., $\theta = \gamma \pm \pi/2$ [cf. Fig. 2.6(a)]. This family of states is characterized by a reduced photon-number uncertainty compared to coherent states, while the associated phase uncertainty is increased [97]. Figure 2.6(b) shows the time-dependent electric field of the amplitude-squeezed state in Fig. 2.6(a) with a reduction in the amplitude uncertainty, illustrated by its standard deviation coinciding with σ_s, and an enlarged phase uncertainty, σ_a. The orthogonal ensemble of states with $\theta = \gamma \, (\pm\pi$, because of the symmetry of the squeezed state) is called *phase-squeezed* states, shown in Fig. 2.7. In contrast to amplitude-squeezed states, these states are characterized by reduced phase uncertainties at the cost of magnified amplitude noise, illustrated in Fig. 2.7(b).

Figure 2.8 can be understood as a phase diagram of the introduced single-mode Gaussian states as a function of quadrature variances. The global threshold for the entire family of minimum-uncertainty states, defined by Eq. (2.12), is illustrated in orange and encompasses all squeezed states with unit purity. The coherent state, shown as the dark blue dot can be interpreted as the minimum uncertainty state with symmetric variance $(\Delta q)^2 = (\Delta p)^2 = 1/4$. Note that since Fig. 2.8 does not reflect the average field amplitude, the vacuum state coincides with the coherent states. The class of thermal states corresponds to the blue line over the main diagonal. The purple horizontal and vertical lines illustrate the vacuum variance threshold for $(\Delta q)^2$ and $(\Delta p)^2$, respectively. Hence, all states that can be found below this limit (in the purple-shaded areas) correspond to non-pure, or noisy, squeezed states. These states are highly relevant in experiment, since realistic squeezed states always carry a finite amount of noise. States that do not follow a uniform variance distribution in phase space, but exhibit a minimum variance larger than the vacuum fluctuations are called *squashed* states (green color).
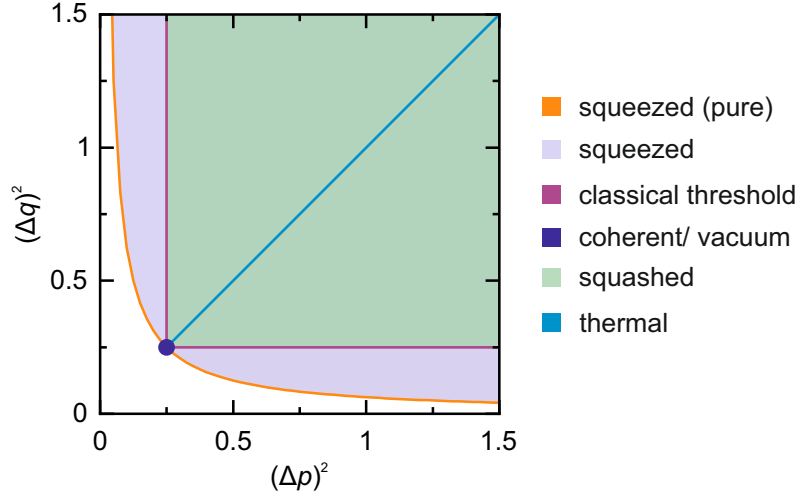
Figure 2.8: Phase diagram of single-mode Gaussian states. The white region corresponds to unphysical states that violate the Heisenberg uncertainty relation in Eq. (2.12).

2.2.6 Two-mode squeezed vacuum state

In the following, we expand the picture from the fundamental Gaussian single-mode states $[k = 1$ in Eq. (2.1)] to a two-mode case $(k = 2)$ by introducing a unitary two-mode squeezing (TMS) operator [1, 6]

$$\hat{S}_{\mathrm{TMS}}(\xi) = \exp(\xi^* \hat{a}_1 \hat{a}_2 - \xi \hat{a}_1^\dagger \hat{a}_2^\dagger), \tag{2.55}$$

where $\xi = r \exp(\mathrm{i}\varphi)$ is the two-mode squeezing parameter analogous to the single-mode case, and $\hat{a}_k$ $(k = 1, 2)$ refer to the two distinct vacuum modes. Similar to the single-mode transformation, the operator implements the transformations

$$\hat{S}_{\mathrm{TMS}}^\dagger(\xi) \hat{a}_1 \hat{S}_{\mathrm{TMS}}(\xi) = \hat{a}_1 \cosh r + \hat{a}_2^\dagger e^{\mathrm{i}\varphi} \sinh r, \tag{2.56}$$

$$\hat{S}_{\mathrm{TMS}}^\dagger(\xi) \hat{a}_2 \hat{S}_{\mathrm{TMS}}(\xi) = \hat{a}_2 \cosh r + \hat{a}_1^\dagger e^{\mathrm{i}\varphi} \sinh r. \tag{2.57}$$

The TMS vacuum state generated by the TMS operator in Eq. (2.55) has unit purity and is identical to a sequence (illustrated in Fig. 2.9) of generating two orthogonal single-mode squeezed vacuum states with equal squeeze amplitude r,

$$\hat{b}_1 = \hat{a}_1 \cosh r + \hat{a}_1^\dagger e^{\mathrm{i}\varphi} \sinh r, \tag{2.58}$$

$$\hat{b}_2 = \hat{a}_2 \cosh r + \hat{a}_2^\dagger e^{\mathrm{i}(\varphi \pm \pi)} \sinh r, \tag{2.59}$$
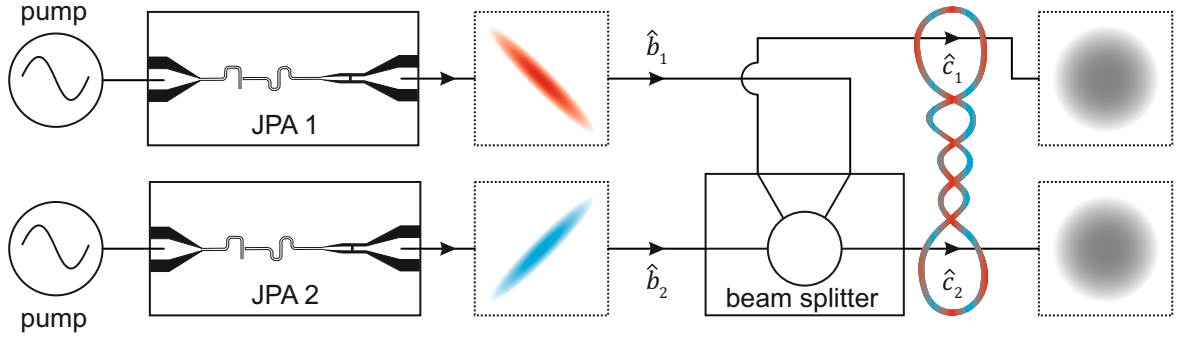
Figure 2.9: Scheme for the generation of TMS vacuum states. JPA 1 and JPA 2 generate two single-mode squeezed states, $\hat{b}_1$ and $\hat{b}_2$, with identical squeeze amplitude and orthogonal amplification orientation, illustrated by the red and blue ellipses, respectively. Superposition of these states in a balanced beam splitter (depicted as a 180° hybrid ring) results in TMS vacuum states with entangled local modes $\hat{c}_1$ and $\hat{c}_2$ that locally resemble thermal states, illustrated by the uniformly distributed gray circles.

where $\hat{a}_1$ and $\hat{a}_2$ are the initial vacuum modes, followed by a superposition of these states in a balanced $50:50$ beam splitter

$$\hat{c}_1 = \frac{\hat{b}_1 + \hat{b}_2}{\sqrt{2}} = \hat{d}_1 \cosh r + \hat{d}_2^\dagger e^{i\varphi} \sinh r, \tag{2.60}$$

$$\hat{c}_2 = \frac{\hat{b}_1 - \hat{b}_2}{\sqrt{2}} = \hat{d}_2 \cosh r + \hat{d}_1^\dagger e^{i\varphi} \sinh r, \tag{2.61}$$

where we define $\hat{d}_1 = 1/\sqrt{2}(\hat{a}_1 + \hat{a}_2)$ and $\hat{d}_2 = 1/\sqrt{2}(\hat{a}_1 - \hat{a}_2)$ as two further vacuum modes. The generated states, $\hat{c}_1$ and $\hat{c}_2$, are identical to the ones from Eqs. (2.56) and (2.57). In the Fock basis, the TMS vacuum state can be written as a superposition state by applying the TMS squeeze operator to the vacuum according to [93]

$$\hat{S}_{\mathrm{TMS}}(\xi)|0,0\rangle = \frac{1}{\cosh r} \sum_{n=0}^{\infty} (-e^{i\varphi} \tanh r)^n |n,n\rangle. \tag{2.62}$$

The reduced density matrix of one mode of the TMS vacuum state coincides with that of a thermal state [97]

$$\hat{\rho}_{\mathrm{th}} = \sum_n \frac{n_{\mathrm{th}}^n}{(1+n_{\mathrm{th}})^{n+1}} |n\rangle\langle n|, \tag{2.63}$$

with the mean photon number $n_{\mathrm{th}} = \sinh^2 r$. The nonlocal correlations encoded in the family of TMS vacuum states become apparent by the statistical moments

$$\boldsymbol{d}_{\mathrm{TMS}} = 0 \text{ and } \boldsymbol{V}_{\mathrm{TMS}} = \frac{1}{4} \begin{pmatrix} \cosh 2r \, \mathbb{1}_2 & \sinh 2r \, (\sigma_z \cos\varphi + \sigma_x \sin\varphi) \\ \sinh 2r \, (\sigma_z \cos\varphi + \sigma_x \sin\varphi) & \cosh 2r \, \mathbb{1}_2 \end{pmatrix}, \tag{2.64}$$
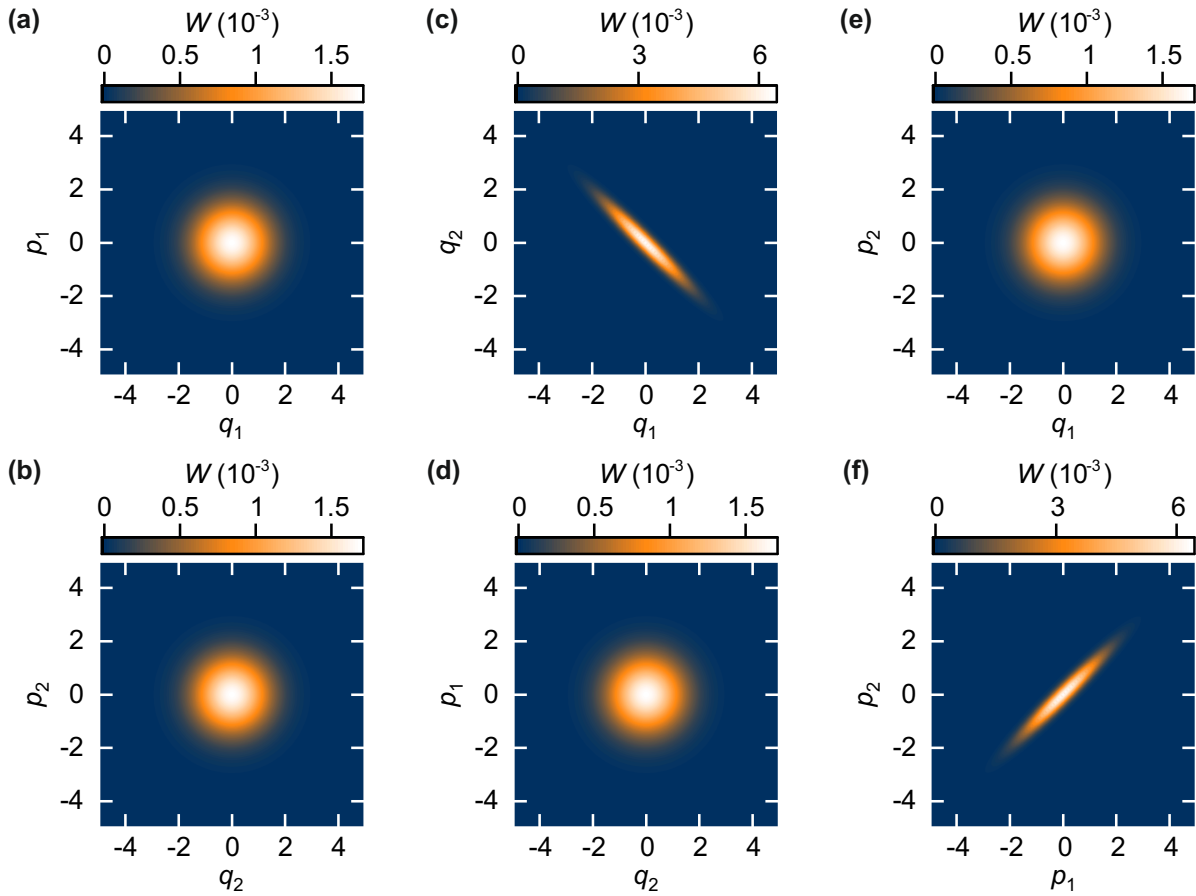
Figure 2.10: Marginal distributions of the Wigner function W for the TMS vacuum. The local marginal distributions of modes 1 and 2 resemble thermal states and are depicted in panels (a) and (b), respectively. Panels (c) to (f) show the nonlocal phase-space correlations. For the employed parameters of $r = 1$ and $\varphi = \pi$ [cf. Eq. (2.55)], the quadrature pair (q_1, q_2) is anti-correlated, as shown in panel (c), while another pair (p_1, p_2) is correlated, as depicted in panel (f).

where $\mathbb{I}_2$ is the (2×2) unity matrix and σ_z (σ_x) are the Pauli-z (x) matrices, respectively [1]. Figure 2.10 shows the Wigner marginal distributions of the TMS vacuum. The correlations of the nonlocal q- and p-quadrature pairs become ideal in the limit $r \to \infty$ [111]. In this limit, the Wigner function converges to $W(\boldsymbol{r}) \propto \delta(q_1 + q_2)\delta(p_1 - p_2)$, which is the continuous-variable equivalent to the EPR state.

2.3 Quantum entanglement

Nonclassical correlations in propagating signals provide an essential ingredient for various protocols in quantum communication and sensing, such as quantum teleportation, Heisenberg-limited precision measurements, and quantum cryptography [54, 78, 88, 89, 112, 113]. Quantum entanglement is an intriguing and purely quantum phenomenon [114, 115].

At the same time, quantum entanglement is inherently fragile and can easily be destroyed by losses and noise [116]. In the Fock basis, an entangled Gaussian state can be expressed as [93]

$$|\psi\rangle_{\mathrm{AB}} = \sum_{n=0}^{\infty} \sqrt{\frac{N^n}{(N+1)^{n+1}}} |n\rangle_{\mathrm{A}} |n\rangle_{\mathrm{B}}, \tag{2.65}$$

where A and B are the indices denoting two distinct modes and N is the average photon number per mode. The associated wave function, $|\psi\rangle_{\mathrm{AB}}$, corresponds to a zero-mean Gaussian state, the TMS vacuum state. In general, quantum entanglement can be expressed via a separability criterion of the associated density operator, $\hat{\rho}_{\mathrm{AB}}$. If the state $\hat{\rho}_{\mathrm{AB}}$ can be described by a sum of product states

$$\hat{\rho}_{\mathrm{AB}} = \sum_k p_k \, \hat{\rho}_{k,\mathrm{A}} \otimes \hat{\rho}_{k,\mathrm{B}}, \tag{2.66}$$

this state is separable and, therefore, not entangled [6, 108]. For bipartite Gaussian states, the negativity $\mathcal{N}$ provides a useful entanglement monotone. To this end, it is useful to introduce local symplectic invariants of the covariance matrix [117]

$$\boldsymbol{V} = \begin{pmatrix} \boldsymbol{A} & \boldsymbol{C} \\ \boldsymbol{C}^{\mathrm{T}} & \boldsymbol{B} \end{pmatrix}, \tag{2.67}$$

where $\boldsymbol{A}$, $\boldsymbol{B}$ and $\boldsymbol{C}$ are 2×2 matrices, which fully describe the local states A, B, and corresponding cross-correlations, respectively. The associated symplectic invariants are given by

$$I_1 = \det(\boldsymbol{A}), \quad I_2 = \det(\boldsymbol{B}), \quad I_3 = \det(\boldsymbol{C}), \quad I_4 = \det(\boldsymbol{V}). \tag{2.68}$$

The symplectic eigenvalues of $\boldsymbol{V}$ are [118]

$$\nu_{\pm} = \sqrt{\frac{\Delta \pm \sqrt{\Delta^2 - 4I_4}}{2}}, \tag{2.69}$$

where $\Delta = I_1 + I_2 + 2I_3$. Accordingly, we can express the negativity as [119]

$$\mathcal{N} = \max\left[0, \frac{1 - 4\nu_-}{8\nu_-}\right] = \max\left[\mathcal{N}_{\mathrm{k}}\right], \tag{2.70}$$

where $\mathcal{N}_{\mathrm{k}} = (1 - 4\nu_-)/(8\nu_-)$ is the negativity kernel. The bipartite state is separable for $\mathcal{N}_{\mathrm{k}} \leq 0$, i.e., $\nu_- \geq 1/4$. A positive $\mathcal{N}_{\mathrm{k}} > 0$ is indicative of non-zero quantum entanglement and $\mathcal{N}_{\mathrm{k}} \to \infty$ corresponds to maximally entangled states in the limit of $r \to \infty$ [108, 117]. Quantum entanglement is related to a subset of a more general class of quantum correlations, which can be captured by the quantum discord [120, 121]. From a conceptual point of view, quantum discord is a measure of nonclassicality of a

corresponding system. The quantum discord can be written as [120]

$$D_{\mathrm{A}} = I(A : B) - J(A|B), \tag{2.71}$$

where $I(A : B)$ is the quantum mutual information and $J(A|B)$ denotes the one-way classical correlations. The quantum mutual information encompasses the whole of the correlations in the bipartite system, both classical and quantum. For two-mode Gaussian states we can express it as [117]

$$I(A : B) = f\left(\sqrt{I_1}\right) + f\left(\sqrt{I_2}\right) - \left(f\left(\nu_+\right) + f\left(\nu_-\right)\right), \tag{2.72}$$

where

$$f(x) = \left(2x + \frac{1}{2}\right)\log\left(2x + \frac{1}{2}\right) - \left(2x - \frac{1}{2}\right)\log\left(2x - \frac{1}{2}\right). \tag{2.73}$$

The one-way classical correlations are closely linked to the entropy of the system, which leads to a nontrivial task of minimizing the conditional entropy of the bipartite quantum state to find an analytical solution for the associated quantum discord [122–124]. For the class of bipartite Gaussian states, however, there exists an analytical expression [125, 126]

$$D_{\mathrm{A}} = f\left(\sqrt{I_2}\right) - \left(f\left(\nu_+\right) + f\left(\nu_-\right)\right) + f\left(\sqrt{E_{\mathrm{A|B}}^{\min}}\right), \tag{2.74}$$

where [108, 123]

$$E_{\mathrm{A|B}}^{\min} = \begin{cases} \left(\frac{1}{4}\dfrac{|I_3| + \sqrt{I_3^2 - (I_1 - 16I_4)(I_2 - 1/16)}}{I_2 - 1}\right)^2, & \text{if } \dfrac{(I_1 I_2 - I_4)^2}{(I_1 + 16I_4)(I_2 + 1/16)I_3^2} \leq 1 \\ \dfrac{I_1 I_2 + I_4 - I_3^2 - \sqrt{I_1 I_2 + I_4 - I_3^2 - 4I_1 I_2 I_4}}{3I_2}, & \text{otherwise.} \end{cases} \tag{2.75}$$

The quantum discord is not symmetric with respect to the associated subsystems A and B, i.e., $D_{\mathrm{A}} \neq D_{\mathrm{B}}$. Furthermore, a finite quantum discord is a necessary but not sufficient criterion for bipartite correlations to be strictly nonclassical [127]. The role of quantum entanglement and more general quantum correlations in the framework of entanglement-based quantum radar are discussed in Ch. 3.

2.4 Second-order correlation function

Intensity fluctuations represent a powerful tool to categorize light in its most general sense. Accordingly, chaotic light exhibits different photon statistics compared to coherent light or single photons [104]. The second-order correlation function, $g^{(2)}(\tau)$, is the central figure of merit in this scope and captures the distinct nature of photon statistics. This correlation function is typically expressed in a normalized form, also called the degree of

second-order temporal coherence [104], which can be expressed in classical terms as [93]

$$g^{(2)}(\tau) = \frac{\langle E^*(t)E^*(t+\tau)E(t+\tau)E(t)\rangle}{\langle E^*(t)E(t)\rangle^2} = \frac{\langle I(t)I(t+\tau)\rangle}{\langle I(t)\rangle^2}, \qquad (2.76)$$

where $E(t)$ is the time-dependent electrical field amplitude, $I(t)$ corresponds to the associated field intensity, τ denotes a finite time delay and the light is assumed to follow stationary statistical properties. Application of the Cauchy-Schwartz inequality to Eq. (2.76) shows that for classical light $1 \leq g^{(2)}(0)$ and $g^{(2)}(\tau) \leq g^{(2)}(0)$ [93]. Accordingly, from a classical point of view, the degree of second-order coherence is upper bounded by its zero time delay value. The first experimental efforts to investigate the correlation between two optical intensities were conducted by Hanbury Brown and Twiss in 1956 [128]. Their pioneering work builds the foundation for a plethora of studies on the correspondence between the classical and quantum nature of light [104]. For single-mode light, the quantum description of the degree of second-order temporal coherence can be expressed as

$$g^{(2)}(0) = \frac{\langle \hat{a}^\dagger \hat{a}^\dagger \hat{a} \hat{a} \rangle}{\langle \hat{a}^\dagger \hat{a} \rangle^2}. \qquad (2.77)$$

With the commutation relation of the creation and annihilation operators, $[\hat{a}, \hat{a}^\dagger] = 1$, and the definition of the photon number operator, $\hat{n} = \hat{a}^\dagger \hat{a}$, we can express Eq. (2.77) in terms of the mean and mean-square photon numbers as [104]

$$g^{(2)}(0) = \frac{\langle \hat{n}(\hat{n}-1)\rangle}{\langle \hat{n}\rangle^2} = \frac{\langle \hat{n}^2 \rangle - \langle \hat{n}\rangle}{\langle \hat{n}\rangle^2} = 1 + \frac{\langle (\Delta\hat{n})^2 \rangle - \langle \hat{n}\rangle}{\langle \hat{n}\rangle^2}. \qquad (2.78)$$

Since $\langle (\Delta\hat{n})^2 \rangle \geq 0$, we can infer the inequality [97]

$$g^{(2)}(0) \geq 1 - \frac{1}{\langle \hat{n}\rangle} \quad \text{for} \quad \langle \hat{n}\rangle \geq 1. \qquad (2.79)$$

From an intuitive point of view, the degree of second-order temporal coherence provides information on the likeliness to find one or more photons at a time delay τ, when there is a photon present at $\tau = 0$ [97]. Note that in Eq. (2.79), $g^{(2)}(0) \to 0$ for $\langle \hat{n}\rangle \ll 1$, which is evident since a very weak source of quantum light (e.g. a single photon source) has a very small probability that more than one photon is emitted at a time.

For coherent light, the photon-number variance is $\langle (\Delta\hat{n})^2 \rangle = |\alpha|^2 = \langle \hat{n}\rangle$, which yields a degree of second-order temporal coherence of $g^{(2)}(\tau) = g^{(2)}(0) = 1$. Consequently, this class of states is unconditionally second-order coherent. In other terms, the photons in the coherent state are evenly distributed in time [93]. Thermal states are characterized by the photon-number variance $\langle (\Delta\hat{n})^2 \rangle = \langle \hat{n}\rangle^2 + \langle \hat{n}\rangle$, which results in $g^{(2)}(0) = 2$. Thermal states belong to the class of bunched light, characterized by $g^{(2)}(\tau) < g^{(2)}(0)$, i.e., photons

Degree of second-order coherence for single-mode states

	$\langle\hat{n}\rangle$	$\left\langle(\Delta\hat{n})^2\right\rangle$	$g^{(2)}(0)$	statistics
coherent	$|\alpha|^2$	$|\alpha|^2 = \langle\hat{n}\rangle$	1	Poissonian
thermal	$\frac{1}{\exp(\frac{\hbar\omega}{k_\mathrm{B}T})-1}$	$\langle\hat{n}\rangle^2 + \langle\hat{n}\rangle$	2	super-Poissonian
squeezed	$\sinh^2 r$	$2\langle\hat{n}\rangle(\langle\hat{n}\rangle+1)$	$3 + 1/\langle\hat{n}\rangle$	super-Poissonian
phase-sq.	$|\alpha|^2 + \sinh^2 r$	$\langle\hat{n}\rangle\,e^{2r}$	$1 - 1/\langle\hat{n}\rangle + \frac{e^r}{\langle\hat{n}\rangle^{3/2}}$	super-Poissonian
amplitude-sq.	$|\alpha|^2 + \sinh^2 r$	$\langle\hat{n}\rangle\,e^{-2r}$	$1 - 1/\langle\hat{n}\rangle + \frac{e^{-r}}{\langle\hat{n}\rangle^{3/2}}$	sub-Poissonian
Fock	n	0	$1 - 1/\langle\hat{n}\rangle$	sub-Poissonian

Table 2.1: Overview of the mean photon number $\langle\hat{n}\rangle = \langle\hat{a}^\dagger\hat{a}\rangle$ and photon-number variance $\langle(\Delta\hat{n})^2\rangle$ for different classes of single-mode states, which enable an evaluation of the second-order coherence degree, $g^{(2)}(0)$, and the associated photon statistics.

tend to bunch in time, which leads to an enhanced probability of finding more than one photon within a characteristic time scale. Squeezed vacuum states also exhibit bunched-light characteristics, as dictated by their photon-number variance $\left\langle(\Delta\hat{n})^2\right\rangle = 2\langle\hat{n}\rangle(\langle\hat{n}\rangle+1)$, which yields $g^{(2)}(0) = 3 + 1/\langle\hat{n}\rangle$. Accordingly, the photon-number fluctuations in the squeezed vacuum exceed those of the thermal states for a given mean photon number [93]. The opposite behavior occurs for anti-bunched light, characterized by $g^{(2)}(\tau) > g^{(2)}(0)$. Typical sources of such light are quantum two-level systems that emit single quanta of light within a characteristic time scale. In a more general approach, the entire class of number states show anti-bunched characteristics, since they have a zero photon-number uncertainty, $\left\langle(\Delta\hat{n})^2\right\rangle = 0$, which gives $g^{(2)}(0) = 1 - 1/\langle\hat{n}\rangle < 1$ for all $n \geq 1$. This result for the number states satisfies the lower bound for Eq. (2.79) and violates the classical limit of $g^{(2)}(0) \geq 1$. Interestingly, the squeezed coherent states can also go below this classical limit [129]. These states have a photon-number variance

$$\left\langle(\Delta\hat{n})^2\right\rangle = |\alpha|^2 \left[e^{2r}\sin^2\left(\theta - \frac{1}{2}\varphi\right) + e^{-2r}\cos^2\left(\theta - \frac{1}{2}\varphi\right)\right] + 2\sinh^2(r)\left[\sinh^2(r) + 1\right], \tag{2.80}$$

which yields

$$g^{(2)}(0) = 1 + \frac{|\alpha|^2\left(\cosh(2r) - \cos(2\theta - \varphi)\sinh(2r) - 1\right) + \sinh^2(r)\cosh(2r)}{\left(|\alpha|^2 + \sinh^2(r)\right)^2}. \tag{2.81}$$

The variance in Eq. (2.80) for the amplitude-squeezed states, i.e., $\theta = \varphi/2$ (cf. Fig. 2.6),
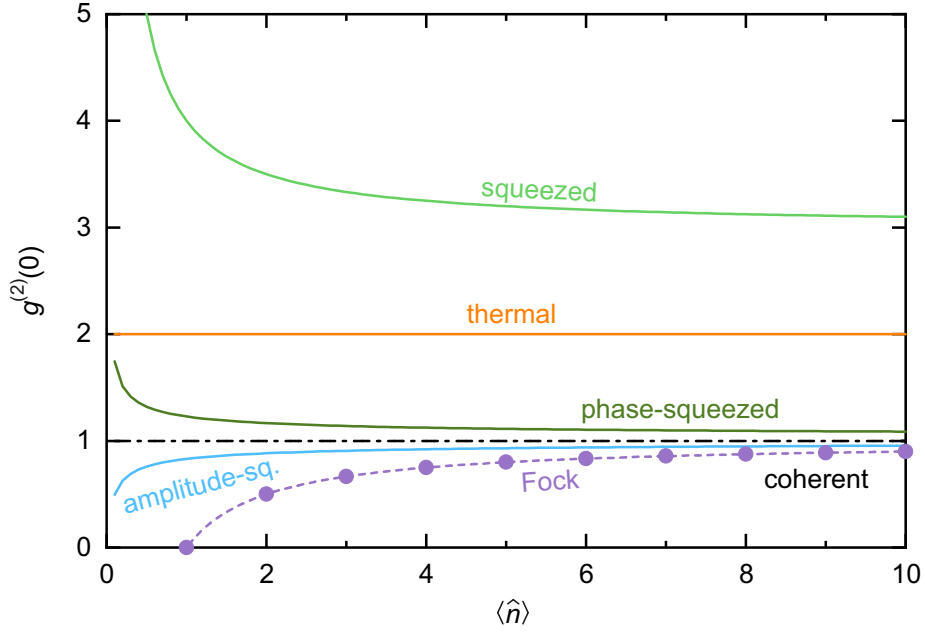
Figure 2.11: Second-order correlation function $g^{(2)}(0)$ for various single-mode states. The dot-dashed black line represents the boundary between sub- and super-Poissonian statistics, which is saturated by the coherent state. The dashed purple line for the Fock states illustrates the lower limit from Eq. (2.79), the discrete purple points correspond to the integer number states with $\langle n \rangle = n$.

simplifies to

$$\left\langle (\Delta \hat{n})^2 \right\rangle = \left(\sqrt{\langle \hat{n} \rangle} + \frac{1}{4} e^{-r} \right)^2 - \left(\sqrt{\langle \hat{n} \rangle} - \frac{1}{4} e^{-r} \right)^2 = \sqrt{\langle \hat{n} \rangle} e^{-r}, \tag{2.82}$$

which is valid for the case when the coherent portion of the mean photon number is much larger than that of the squeezing, i.e., $|\alpha| \gg e^r$ [93]. Accordingly, amplitude-squeezed states have a reduced uncertainty compared to the coherent states and follow a sub-Poissonian statistics, characterized by $g^{(2)}(0) < 1$ [129, 130].

In general, Poissonian statistics are reflected by $g^{(2)}(0) = 1$, while super-Poissonian light exhibits $g^{(2)}(0) > 1$. Phase-squeezed states, i.e., $\theta = \varphi/2 + \pi/2$ (cf. Fig. 2.7) are characterized by an increased photon-number variance

$$\left\langle (\Delta \hat{n})^2 \right\rangle = \sqrt{\langle \hat{n} \rangle} e^r, \tag{2.83}$$

for the identical threshold given in Eq. (2.82). A summary of various single-mode characteristics is provided in Tab. 2.1 and is also illustrated in Fig. 2.11. The investigation of intensity correlations can be expanded from the single-mode picture to multiple modes, which might exhibit non-vanishing cross-correlations. The two-mode second-order correlation function, also known as the second-order cross-correlation function, is of central

importance for the results presented in Ch. 6 and can be expressed as

$$g_{\mathrm{C}}^{(2)}(0) = \frac{\langle \hat{a}^\dagger \hat{a}^\dagger \hat{a} \hat{a} \rangle + \langle \hat{b}^\dagger \hat{b}^\dagger \hat{b} \hat{b} \rangle + 2 \langle \hat{a}^\dagger \hat{a} \hat{b}^\dagger \hat{b} \rangle}{\left(\langle \hat{a}^\dagger \hat{a} \rangle + \langle \hat{b}^\dagger \hat{b} \rangle \right)^2}, \tag{2.84}$$

where $\hat{a}$ and $\hat{b}$ represent the two distinct modes. For TMS states with finite individual displacements, theory predicts a parameter region where $g_{\mathrm{C}}^{(2)}(0) < 1$ for orthogonal squeeze angles [131]. These sub-Poissonian characteristics are maximal for symmetric configurations, i.e., identical displacement amplitudes of the respective modes. Although the non-classical regime is shallow with $g_{\mathrm{C,min}}^{(2)}(0) \simeq 0.9$ for experimentally accessible squeeze levels and displacement amplitudes, this non-classical footprint shows a robustness against finite noise in the signal [131]. In Ch. 6, we experimentally realize such non-local photon anti-bunching, $g_{\mathrm{C}}^{(2)}(0) < 1$, with noisy and displaced TMS states [80].

Chapter 3

Quantum illumination

In this chapter, we first introduce the concept of quantum illumination (QI) and present established knowledge in the field. Later sections of this chapter discuss our own advancements in this thriving area of research, with a focus on the signal detection in QI and the robustness of the protocol against realistic imperfections. These findings are based on a collaboration with *M. Würth* and *Prof. Dr. W. Utschick* from the Technical University of Munich, TUM School of Computation, Information and Technology within the project "Quantum Radar Team" (QuaRaTe).

The fundamental paradigm of QI is based on quantum-entangled resource states, which are employed in a radar-type scheme. One mode of the entangled resource state is sent as a probe signal to interrogate a region of interest for the presence or absence of an object. The other mode, conventionally labeled as the idler, is preserved for the round-trip time of the signal. In case the object is present, the probe signal is partially reflected and propagates back to a detection unit. The signal is entirely lost if the object is not present. Irrespective of the object being present or absent, thermal background noise enters the detector. Here, a joint measurement on the idler and the received signal fraction lays the foundation for a statistics-based analysis, which corresponds to hypothesis testing in order to discriminate, based on the measurement data, between the two cases [48, 49]. Most importantly, QI is robust against an entanglement-breaking background noise, which results in an enhanced performance compared to the ideal classical reference scheme based on coherent resource states [48]. In this framework, remaining non-classical correlations in the propagating modes provide the essential ingredient for QI [47, 48].

Although the two terms are not interchangeable, the term quantum radar is often used as a synonym for quantum illumination. Importantly, quantum radar encompasses *any target detection scheme that employs any non-classical part for the purposes of enhanced capabilities* [49]. Accordingly, the scope of quantum radar clearly goes beyond QI, i.e., any radar scheme based on QI can be classified as a quantum radar, but not vice versa. The quantum feature in quantum radar may be based on using: a quantum transmitter and/or a quantum receiver [64]. Here, the realm of quantum sensing provides a useful classification of sensors into three distinct quantum types, based on their application and non-classical properties [132]:
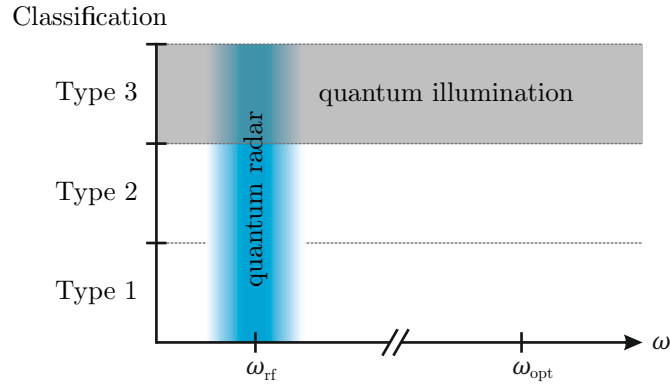
Figure 3.1: Classification of quantum radar (blue) into the three different quantum sensor types [132] at microwave frequencies compared to the concept of quantum illumination (gray), which can be viewed as a type 3 quantum sensor independent of the operating frequency.

- **Type 1:** Transmission of non-classical quantum states of light that are not entangled with the receiver,

- **Type 2:** Transmission of classical states of light combined with a quantum receiver,

- **Type 3:** Transmission of non-classical quantum states of light that are initially entangled with the receiver.

Here, a quantum receiver may be any type of receiver that goes beyond classical limits, e.g., regarding its noise temperature or non-classical detection techniques. In this framework, QI schemes may be understood as type-3 quantum sensors, since they intrinsically rely on quantum-entangled resource states. Note that from another point of view, it can also be argued that the term quantum radar implies microwave frequencies, while the general concept of QI is independent of the operating frequency, as illustrated in Fig. 3.1.

In this chapter, we shed light on the paradigm of quantum illumination, starting with a brief summary of the classical radar basics in Sec. 3.1. In Sec. 3.2, we introduce the concept of hypothesis testing, which represents a central component in the analysis of general radar schemes. The widely considered quantum illumination protocol based on Gaussian states is discussed in Sec. 3.3. Here, various different detection schemes have been proposed, which all aim towards harnessing remaining quantum correlations of the initially entangled states. We introduce and discuss various such detection schemes in Sec. 3.4. Next, we focus on a particular QI scheme that relies on a parametric mixing (PM) of the return and idler signal, followed by single-photon detection. We evaluate this PM scheme in terms of robustness against finite purity of the resource states in Sec. 3.5 and briefly address challenges related to the idler storage in in Sec. 3.6. We continue with a thorough study on practical receiver characteristics in Sec. 3.7. Finally, we introduce various accuracy-enhancing protocols that go beyond binary hypothesis testing and conclude the chapter with a concise discussion. The results presented in this chapter have been published in Ref. [54]. Parts of the text and figures are adapted from this
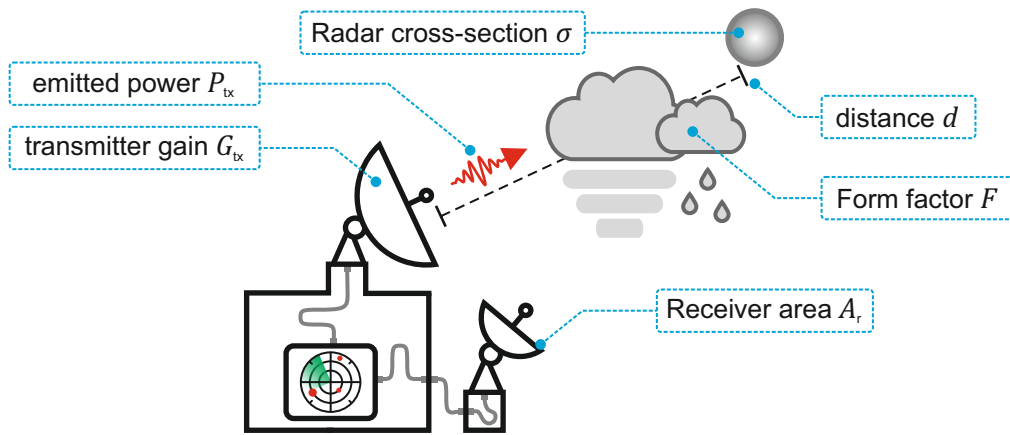
Figure 3.2: Schematic depiction of a classical radar scheme with all relevant quantities for the radar equation [see Eq. (3.3)].

reference.

3.1 Fundamentals of classical radar

The first steps toward classical radar technology were taken by Heinrich Hertz in 1886, when he demonstrated that radio waves could be reflected from solid objects [133]. Sophisticated radar applications emerged during the first half of the 20th century and have continuously evolved and improved since then. Today, classical radar use cases are highly diverse, ranging from ocean monitoring, to self-driving vehicles, meteorological precipitation monitoring, flight control, and outer space surveillance.

In its simplest form, a radar system emits electromagnetic radiation toward an object and records the fraction of the transmitted power that is reflected back from that object, implying a co-located transmitter and receiver unit. In this case, we can evaluate the power density incident on the object as [49, 95]

$$S_\text{o} = \frac{1}{4\pi R^2} P_\text{tx} G_\text{tx} F^2, \tag{3.1}$$

where R is the distance between the transceiver and the object, which is connected to the signal round-trip time $t = 2R/c$, where c is the speed of light in vacuum. The power emitted by the transmitter is denoted by P_tx, G_tx is the transmitter gain, and $0 \leq F \leq 1$ is a form factor that incorporates the transmissivity of the path along which the signal propagates. The radar cross-section, σ, is a measure for the effective reflectivity of the object and linearly enters the expression for the power density of the reflected signal portion incident on the receiver [49]

$$S_\text{r} = \frac{1}{(4\pi)^2 R^4} \sigma P_\text{tx} G_\text{tx} F^4 = \frac{P_\text{r}}{A_\text{r}}, \tag{3.2}$$

where the quantity P_r denotes the total power incident on the receiver and A_r is the effective area of the receiver. Solving Eq. (3.2) for P_r yields the famous radar equation

$$P_r = \frac{1}{(4\pi)^2 R^4} \sigma A_r P_{tx} G_{tx} F^4,$$ (3.3)

which is illustrated in Fig. 3.2 and represents the conceptual core behind classical radar technology. A corresponding signal-to-noise (SNR) ratio can be defined as [134, 135]

$$\text{SNR} = \frac{P_r}{k_B T B_r F_n} = \frac{\sigma A_r P_{tx} G_{tx} F^4}{(4\pi)^2 R^4 k_B T B_r F_n} = \frac{\sigma P_{tx} G_{tx} G_r \lambda^2 F^4}{(4\pi)^3 R^4 k_B T B_r F_n},$$ (3.4)

where k_B is the Boltzmann constant, T is the radar unit operating temperature, B_r is the receiver bandwidth, F_n is a dimensionless quantity that corrects for deviations of the actual noise characteristics from a perfect black-body radiator, and $G_r = 4\pi A_r/\lambda^2$ is the receiver gain [49]. Note that $k_B T B_r F_n$ is the effective noise power withing the detection bandwidth. For a given minimum detectable signal and an associated minimum SNR_{min}, we can express the maximum radar range as [135]

$$R_{max} = \left[\frac{\sigma P_{tx} G_{tx} G_r \lambda^2 F^4}{(4\pi)^3 \text{SNR}_{min} k_B T B_r F_n} \right]^{1/4},$$ (3.5)

which represents a central quantity in the world of radar engineering. For the binary detection task of radar applications, one aims for inferring the presence or absence of an object based on a detected signal. The associated analysis relies on hypothesis testing and an optimal decision strategy, which we introduce in the next section.

3.2 Decision strategy and hypothesis testing

The task of testing for the presence or absence of an object, or in other terms discriminating between two hypotheses, coincides with sampling from two distinct probability distributions and distinguishing between them based on the sampling routine [56]. Here, the conditional probability distributions $p_0(\boldsymbol{R})$ and $p_1(\boldsymbol{R})$ for a random variable $\boldsymbol{R}$ carry information on the hypotheses H_0 (target absent) and H_1 (target present), respectively. In the most general case, $\boldsymbol{R}$ spans the real space Z, shown in Fig. 3.3(a). A decision strategy separates this decision space into the sub-spaces Z_0 and Z_1 [136]. Accordingly, we assume that H_0 is true for $\boldsymbol{R} \in Z_0$ and decide that H_1 is true for $\boldsymbol{R} \in Z_1$. The decision strategy aims toward optimizing this task, or equivalently, minimizing the associated error [56]. This binary hypothesis scenario encompasses four distinct outcomes of a hypothesis test [56], which can be divided into correct decisions

(i) declare H_0, when H_0 is true,
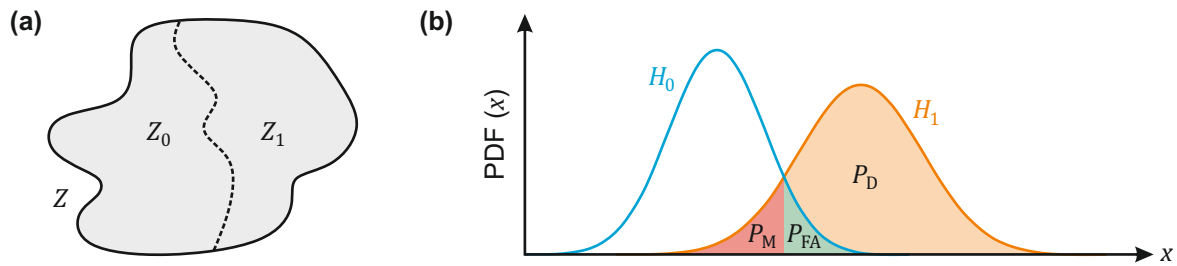
Figure 3.3: (a) Illustration of a decision space Z. In a binary decision task, a suitable decision strategy separates Z into the subspaces Z_0 and Z_1 to minimize associated error probabilities. (b) Exemplary probability density functions (PDFs) that depend on a statistical observable x for a radar scenario, where H_0 corresponds to an object being absent and H_1 denotes an object being present. The associated miss probability P_M, false-alarm probability P_{FA}, and detection probability P_D are highlighted in red, green, and orange, respectively.

(ii) declare H_1, when H_1 is true,

and wrongful decisions

(iii) declare H_1, when H_0 is true,

(iv) declare H_0, when H_1 is true.

Figure 3.3(b) illustrates the associated probabilities for the radar scenario, where we set the intersection between the two probability density functions as the decision threshold. Accordingly, decision (iii) corresponds to the false alarm probability $P_{FA} = P(H_1|H_0)$, i.e., the probability of a target falsely being declared present. We label decision (iv) as the miss probability $P_M = P(H_0|H_1)$, which corresponds to the probability of a target falsely being declared absent [136, 137]. The detection probability P_D can be straightforwardly defined as $P_D = P(H_1|H_1) = 1 - P_M$ [56, 133, 138]. The optimization of such a set of probabilities decisively depends on the considered scenario and a suitable decision rule must be constructed for given boundary conditions. In typical radar applications, the Neyman-Pearson approach is a common decision criterion. Here, the detection probability is maximized for a given tolerable false alarm probability [49]. The receiver operating characteristic (ROC) represents the central figure of merit for Neyman-Pearson-based considerations. The ROC evaluates P_D versus a fixed P_{FA}, and can be interpreted as the relation between sensitivity and specificity $(1 - P_{FA})$ [49]. We focus on the Bayesian decision strategy, i.e., minimizing the mean error probability $P_e = w_0 P_{FA} + w_1 P_M$, where w_0 and w_1 are the prior probabilities of the respective hypothesis to occur. For the Bayesian strategy, a likelihood test represents an optimal testing approach and can be written as [138]

$$\Lambda(\boldsymbol{R}) = \frac{p_1(\boldsymbol{R})}{p_0(\boldsymbol{R})} \gtrless \lambda, \tag{3.6}$$

where $\Lambda(\boldsymbol{R})$ is the likelihood ratio, $\lambda = w_0/w_1$ is the decision threshold, the case of $\Lambda(\boldsymbol{R}) > \lambda$ is given under H_1 and $\Lambda(\boldsymbol{R}) < \lambda$ is given under H_0. The corresponding decision

space is delimited by [56]

$$Z_1 = \left\{ \boldsymbol{R} \ s.t. \ \frac{p_1(\boldsymbol{R})}{p_0(\boldsymbol{R})} > \frac{w_0}{w_1} \right\}, \tag{3.7}$$

and

$$Z_0 = \left\{ \boldsymbol{R} \ s.t. \ \frac{p_0(\boldsymbol{R})}{p_1(\boldsymbol{R})} > \frac{w_1}{w_0} \right\}, \tag{3.8}$$

where *s.t.* is an abbreviation for the expression *such that*. Customarily, one assumes that both hypotheses are equally likely, $w_0 = w_1 = 1/2$, when no prior knowledge on the scenario is accessible [56]. In this case, we observe $\lambda = 1$, which corresponds to the intersection of two probability density functions (cf. Fig. 3.3(b)). The mean error probability can be written as [136]

$$P_e = w_0 \, P_{FA} + w_1 \, P_M =$$
$$= \int_{Z_1} w_0 \, p_0(\boldsymbol{R}) \mathrm{d}\boldsymbol{R} + \int_{Z_0} w_1 \, p_1(\boldsymbol{R}) \mathrm{d}\boldsymbol{R} = \int_Z \min\left[w_0 \, p_0(\boldsymbol{R}), w_1 \, p_1(\boldsymbol{R})\right] \mathrm{d}\boldsymbol{R}, \tag{3.9}$$

which we also express as

$$P_e \leq \min_{0 \leq s \leq 1} w_0^s w_1^{1-s} \int_Z p_0^s(\boldsymbol{R}) p_1^{1-s}(\boldsymbol{R}) \mathrm{d}\boldsymbol{R}, \tag{3.10}$$

by inserting $\min(a, b) \leq x^s y^{1-s}$ ($0 \leq s \leq 1$), which is valid for any positive numbers x and y [56]. Under the assumption of equally probable hypotheses, $w_0 = w_1 = 1/2$, Eq. (3.10) simplifies to the Chernoff bound (CB) [56]

$$P_e \leq \frac{1}{2} \min_{0 \leq s \leq 1} \int_Z p_0^s(\boldsymbol{R}) p_1^{1-s}(\boldsymbol{R}) \mathrm{d}\boldsymbol{R} = \frac{1}{2} e^{-M\xi_{CB}}, \tag{3.11}$$

were M is the number of test samples, which are independent and identically distributed, and ξ_{CB} is the error probability exponent. Importantly, the Chernoff bound is asymptotically tight for a large number of test samples M according to [139]

$$\xi_{CB} = -\lim_{M \to \infty} \frac{\log P_e}{M}. \tag{3.12}$$

The Battacharyya bound (BB)

$$P_e \leq \frac{1}{2} e^{-M\xi_{CB}} \leq \frac{1}{2} e^{-M\xi_{BB}} = \frac{1}{2} \int_Z \sqrt{p_0(\boldsymbol{R}) p_1(\boldsymbol{R})} \mathrm{d}\boldsymbol{R} \tag{3.13}$$

represents a simplified version of the Chernoff bound with $s = 1/2$. While the Battacharyya bound does not require the potentially cumbersome minimization over s, this bound is not exponentially tight, and therefore only represents a strict upper bound on the respective

error probabilities.

In the quantum case, the error probability for a binary decision task can be expressed as

$$P_{\mathrm{e}} = w_0 \, \mathrm{tr}(\hat{O}_1 \hat{\rho}_0) + w_1 \, \mathrm{tr}(\hat{O}_0 \hat{\rho}_1), \tag{3.14}$$

where $\hat{\rho}_0$ ($\hat{\rho}_1$) is the density operator of the associated system under hypothesis H_0 (H_1), and $\hat{O}_0$ ($\hat{O}_1$) is the measurement operator that minimizes the error probability [140]. For $w_1 = w_2 = 1/2$, we can formulate the quantum Chernoff bound (QCB) and the quantum Battacharyya bound (QBB) as [56, 141, 142]

$$P_{\mathrm{e}} \leq \frac{1}{2} e^{-M \xi_{\mathrm{QCB}}} \leq \frac{1}{2} e^{-M \xi_{\mathrm{QBB}}}, \tag{3.15}$$

similar to the classical counterparts in Eqs. 3.11 and 3.13. The corresponding error exponents are given by [56]

$$\xi_{\mathrm{QCB}} = -\log\left(\min_{0 \leq s \leq 1} \mathrm{tr}\left(\hat{\rho}_0^s \hat{\rho}_1^{1-s}\right)\right), \tag{3.16}$$

and

$$\xi_{\mathrm{QBB}} = -\log\left(\mathrm{tr}\left(\sqrt{\hat{\rho}_0}\sqrt{\hat{\rho}_1}\right)\right). \tag{3.17}$$

Note that the quantum Chernoff bound and the quantum Battacharyya bound can be analytically evaluated for Gaussian states.

3.3 Gaussian quantum illumination protocol

The QI scheme relies on quantum-enhanced remote sensing by exploiting quantum correlations between M spatially separated pairs of signal and idler modes, described by the bosonic operators $\hat{a}_{\mathrm{S}}$ and $\hat{a}_{\mathrm{I}}$, respectively [6, 7, 48, 143]. The first proposal of QI by Seth Lloyd in 2008 [47] relies on discrete variables and associated non-classical states for enhanced sensitivity in quantum radar under the following conditions:

- Low number of signal photons, $N_{\mathrm{S}} \ll 1$,

- Low-brightness of thermal background, $N_{\mathrm{B}} \ll 1$,

- Low target reflectivity, $\kappa \ll 1$,

- Large measurement time-bandwidth product, $M = TW \gg 1$.

In his study, Lloyd considers resource states for the QI protocol that are formed by entangled pairs of qubits, while the classical reference scheme relies on transmission of unentangled discrete states, characterized by N_{S} photons per mode. The performances of both schemes can be divided into a 'good' and a 'bad' regime, respectively. Note that the thresholds for the distinction between 'good' and 'bad' are different for the QI

scheme and the classical reference, for details we refer the reader to Refs. [47, 50]. While the error exponents in the 'good' regimes coincide, the QI scheme achieves an M-fold enhancement of the error exponent with respect to the discrete-variable reference in the 'bad' case [47, 50]. This enormous improvement in performance caused a hype in the community, suggesting that QI could revolutionize radar technology [50].

However, Tan *et al.* [48] soon after proved that the discrete-variable reference scheme does not correspond to the optimal classical scheme and, correspondingly, that the M-fold enhancement of the error exponent is not a legit QA. Their work extends the scope to the entire family of Gaussian states and proves that a coherent-state transmitter represents the ideal classical reference [48]. For the parameters considered by Lloyd [47], most importantly for $N_B \ll 1$, the QI protocol yields a performance that is at best as good as the coherent-state system, dampening the initial hopes and promises of QI [50]. At the same time, Tan *et al.* [48] identified a more conservative 6 dB improvement of the error exponent with respect to the ideal classical reference for the bright-background regime of $N_B \gg 1$, while the remaining parameters are identical to the initial proposal by Lloyd. This promise for a 6 dB QA has inspired a plethora of theoretical and experimental efforts [50–64]. Based on these pioneering theory works, the focus of QI has shifted to Gaussian states with a parameter space restricted to [48, 49]:

- Low number of signal photons, $N_S \ll 1$,

- Large number of thermal background photons, $N_B \gg 1$,

- Low target reflectivity, $\kappa \ll 1$,

- Large measurement time-bandwidth product, $M = TW \gg 1$.

While initial studies [47] focused on optical wavelengths, the condition of a bright thermal background, $N_B \gg 1$, is not naturally fulfilled for ambient room-temperature settings with $N_B^{\text{opt}} \simeq 10^{-6}$ per mode [49]. This absence of noise results in a QI performance similar to its classical counterpart in the optical regime [144]. Microwave frequencies, however, intrinsically fulfill this bright background condition, making the microwave domain a natural candidate for QI implementations.

For Gaussian states, the resource states are pure quantum-entangled zero-mean states which are fully characterized by the corresponding covariance matrix

$$\boldsymbol{V}_{\text{SI}} = \langle [\hat{a}_S \, \hat{a}_I \, \hat{a}_S^\dagger \, \hat{a}_I^\dagger]^{\text{T}} [\hat{a}_S^\dagger \, \hat{a}_I^\dagger \, \hat{a}_S \, \hat{a}_I] \rangle \tag{3.18}$$

$$= \begin{bmatrix} (N_S + 1)\, \mathbb{1}_2 & C_q\, \boldsymbol{\sigma}_X \\ C_q\, \boldsymbol{\sigma}_X & N_S\, \mathbb{1}_2 \end{bmatrix}, \tag{3.19}$$

where N_S is the mean photon number of the respective signal and idler modes, $\mathbb{1}_2$ is the two-dimensional identity matrix, the quantity $C_q = \sqrt{N_S(N_S + 1)}$ encodes the strength of quantum correlations, and $\boldsymbol{\sigma}_X$ is the Pauli-X matrix. In this framework, the signal

mode interrogates a region of interest, while the idler mode is retained and stored for a round-trip time of the signal.

For the task of a binary decision between hypothesis H_0 (target absent) and hypothesis H_1 (target present), the return modes entering the receiving unit are given by

$$\hat{a}_{\mathrm{R}}|_{H_0} = \hat{a}_{\mathrm{B}}, \tag{3.20}$$

$$\hat{a}_{\mathrm{R}}|_{H_1} = e^{\mathrm{i}\theta}\sqrt{\kappa}\,\hat{a}_{\mathrm{S}} + \sqrt{1-\kappa}\,\hat{a}_{\mathrm{B}}, \tag{3.21}$$

where $\hat{a}_{\mathrm{B}}$ represents a thermal state with mean photon number $N_{\mathrm{B}} = \langle \hat{a}_{\mathrm{B}}^{\dagger}\hat{a}_{\mathrm{B}}\rangle \gg 1$, θ is the overall phase shift and $\kappa \ll 1$ is the round-trip signal loss. Note that, under H_1, $N_{\mathrm{B}}/(1-\kappa)$ thermal photons are encoded in $\hat{a}_{\mathrm{B}}$ under both hypotheses [145]. Since we focus on QI and do not consider quantum phase estimation, we set $\theta = 0$ [58]. The resulting joint return-idler state is again characterized by zero-mean Gaussian states with

$$\boldsymbol{V}_{\mathrm{RI}} = \langle[\hat{a}_{\mathrm{R}}\,\hat{a}_{\mathrm{I}}\,\hat{a}_{\mathrm{R}}^{\dagger}\,\hat{a}_{\mathrm{I}}^{\dagger}]^{\mathrm{T}}[\hat{a}_{\mathrm{R}}^{\dagger}\,\hat{a}_{\mathrm{I}}^{\dagger}\,\hat{a}_{\mathrm{R}}\,\hat{a}_{\mathrm{I}}]\rangle \tag{3.22}$$

$$\stackrel{H_0}{=} \begin{bmatrix} N_{\mathrm{B}}+1 & 0 & 0 & 0 \\ 0 & N_{\mathrm{S}}+1 & 0 & 0 \\ 0 & 0 & N_{\mathrm{B}} & 0 \\ 0 & 0 & 0 & N_{\mathrm{S}} \end{bmatrix} \tag{3.23}$$

$$\stackrel{H_1}{=} \begin{bmatrix} \kappa N_{\mathrm{S}}+N_{\mathrm{B}}+1 & 0 & 0 & \sqrt{\kappa}C_{\mathrm{q}} \\ 0 & N_{\mathrm{S}}+1 & \sqrt{\kappa}C_{\mathrm{q}} & 0 \\ 0 & \sqrt{\kappa}C_{\mathrm{q}} & \kappa N_{\mathrm{S}}+N_{\mathrm{B}} & 0 \\ \sqrt{\kappa}C_{\mathrm{q}} & 0 & 0 & N_{\mathrm{S}} \end{bmatrix}. \tag{3.24}$$

Notably, the entanglement is not only lost under H_0, but also under H_1, which can be expressed by the relative correlation enhancement [64]

$$\chi = \frac{|\langle \hat{a}_{\mathrm{R}}\hat{a}_{\mathrm{I}}\rangle|}{N_{\mathrm{S}}} \leq \frac{\sqrt{\kappa}C_{\mathrm{q}}}{C_{\mathrm{c}}} < 1. \tag{3.25}$$

Note that the presence of finite entanglement is quantified by $\chi > 1$ and $C_{\mathrm{c}} = N_{\mathrm{S}}$ denotes the maximally obtainable correlations by classical means, and $[\hat{a}_{\mathrm{R}}, \hat{a}_{\mathrm{S}}] = \left[\hat{a}_{\mathrm{R}}^{\dagger}, \hat{a}_{\mathrm{S}}^{\dagger}\right] = 0$. The expression in Eq. (3.25) is valid for $\kappa \ll 1$ and an identical photon number N_{S} in the signal and idler mode, respectively. The ideal TMSV resource states are always entangled, $\chi = C_{\mathrm{q}}/N_{\mathrm{S}} = \sqrt{N_{\mathrm{S}}(N_{\mathrm{S}}+1)}/N_{\mathrm{S}} > 1$ [see Eq. (3.18)]. However, the relative correlation enhancement, as captured by χ, decreases with increasing N_{S} and vanishes towards large N_{S}, as shown in Fig. 3.4. This dependence leads to the intuition that a larger quantum advantage (QA) in QI may be expected for low $N_{\mathrm{S}} \ll 1$.

The minimum error probability, $P_{\mathrm{e,min}}$, for the binary decision task between H_0 and H_1 has an upper bound given by the quantum Chernoff bound (QCB), $P_{\mathrm{e,min}} \leq 0.5\exp(-\xi_{\mathrm{QCB}}M)$, as introduced in the previous paragraph. Note that we only consider
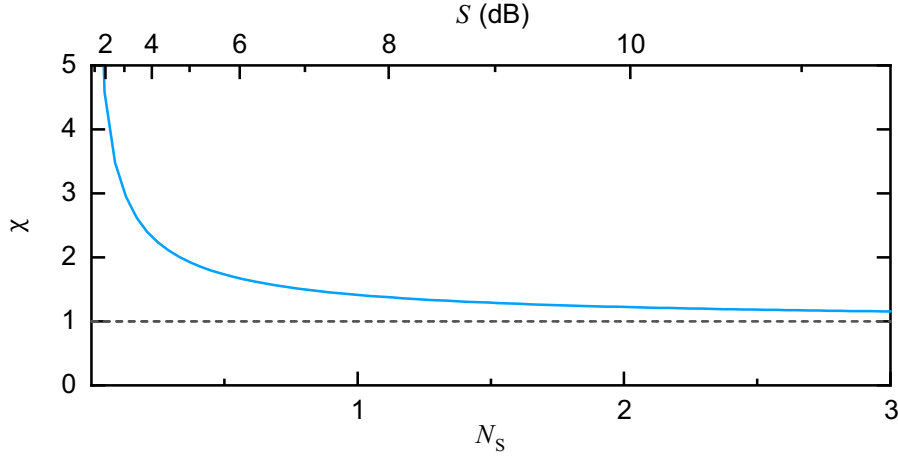
Figure 3.4: Relative correlation enhancement χ [solid blue line, see Eq. (3.25)] as a function of the signal photon number N_S per mode of a TMSV state. The top x-axis shows the corresponding squeezing level. The dashed gray line illustrates the classical limit, $\chi = 1$, above which correlated states are quantum-entangled.

the particular case $w_0 = w_1 = 0.5$. A typical classical reference scheme is a coherent state (CS) transmitter with a mean photon number N_S per mode, combined with a homodyne detector. This classical reference achieves an error exponent

$$\xi_C = \kappa N_S \left(\sqrt{1 + N_B} - \sqrt{N_B} \right)^2 , \tag{3.26}$$

which converges to

$$\xi_C = \kappa N_S/(4N_B), \tag{3.27}$$

for the QI limitations introduced above, i.e., in the weak transmission ($N_S \ll 1$), bright background ($N_B \gg 1$), and high loss ($\kappa \ll 1$) limit. Since Eq. (3.27) coincides with the classical Chernoff bound, this error exponent represents the ideal case for classical illumination, which also holds for classical two-mode states characterized by classical correlations $C \leq C_c = N_S$ [48, 56].

In the same parameter space, the QI protocol has an error exponent

$$\xi_{QI} = \kappa N_S/N_B = \xi_{QCB}, \tag{3.28}$$

which is 6 dB, or a factor of four in linear units, larger than ξ_C [48]. Theory shows that this 6 dB enhancement is optimal and coincides with the quantum Chernoff bound [146].

The QI paradigm is closely related to the task of quantum parameter estimation, e.g., when the object reflectivity κ is of interest [147]. In the realm of quantum parameter estimation, the quantum Fisher information (QFI) represents the central figure of merit and is connected to the Cramér-Rao bound, which gives an upper limit for the obtainable

precision of the unbiased estimator $\hat{\kappa}$

$$\Delta\hat{\kappa}^2 \geq \frac{1}{M\mathcal{F}}, \tag{3.29}$$

where $\mathcal{F}$ denotes the QFI for a number of M independent measurements. The QFI is a quantum analogue to its classical counterpart, which is defined as [148]

$$\mathcal{I}_X(\kappa) = \int_{\mathcal{X}} \left(\frac{\mathrm{d}}{\mathrm{d}\kappa}\log f(x|\kappa)\right)^2 p_\kappa(x)\mathrm{d}x, \tag{3.30}$$

where X is a continuous random variable, $f(x|\kappa)$ is the probability density function for a measurement outcome x conditioned on an unknown parameter κ, and $\mathcal{X}$ is the possible outcome space of x. The derivative $\frac{\mathrm{d}}{\mathrm{d}\kappa}\log f(x|\kappa)$ is called the score function, which describes how sensitive f is to changes in κ at a particular value of κ. The classical Fisher information provides a metric for the overall sensitivity of f to changes of κ by weighting the score function for each point $x \in \mathcal{X}$ in the possible outcome space with the chance $p_\kappa(x) = f(x|\kappa)$ [148]. Similarly, the QFI grants access to the amount of information that a quantum state $\hat{\rho}_\kappa$ conveys about an unknown parameter κ upon which the quantum state depends [149]. From an intuitive point of view, the QFI is large if $\hat{\rho}_\kappa$ exhibits a large gradient with respect to κ. In contrast, the associated QFI is small for a shallow gradient, since a change in κ only weakly affects $\hat{\rho}_\kappa$. For Gaussian-distributed states, the QFI can generally be expressed analytically [147, 150–152]. The QFI is closely linked to various other important quantities, such as the Bures distance [153] between two quantum states.

In the framework of QI, the enhancement of the QFI with respect to the optimal classical case is limited to $3\,\mathrm{dB}$, i.e., $\mathcal{F}_{\mathrm{QI}}/\mathcal{F}_{\mathrm{C}} \leq 2$, where $\mathcal{F}_{\mathrm{QI}}$ denotes the QFI associated with the QI protocol and $\mathcal{F}_{\mathrm{C}}$ represents the classical counterpart [147]. For Gaussian QI, the QFI can be expressed as [147]

$$\mathcal{F}_{\mathrm{QI}} = \frac{4N_{\mathrm{S}}}{(N_{\mathrm{B}} + 1)\left(1 + \frac{N_{\mathrm{S}}}{N_{\mathrm{S}}+1}\frac{N_{\mathrm{B}}}{N_{\mathrm{B}}+1}\right)}. \tag{3.31}$$

In principle, the QI task can be mapped onto quantum parameter estimation via a corresponding error probability [147, 154]

$$P_{\mathrm{e}} \simeq \exp(-\kappa^2 \mathcal{F}_{\mathrm{QI}} M/8), \tag{3.32}$$

which is valid for pairwise joint measurements, as realized in the PM-type receiver (cf. Sec. 3.4). For large M, Eq. (3.32) converges toward the $3\,\mathrm{dB}$ QA for $N_{\mathrm{S}} \ll 1$, $N_{\mathrm{B}} \gg 1$, and $\kappa \ll 1$, in accordance with the QI theory for this class of receivers [145, 155]. In this work, we are interested in the binary target detection problem, as opposed to the continuous-valued parameter estimation. Accordingly, we use the QCB for the performance evaluation of various receiver schemes. Nonetheless, Eq. (3.32) provides a useful general

illustration on the connection between the QFI and the QCB.

3.4 Detection schemes

In the following, we first discuss the detection scheme for the classical reference method, followed by an evaluation of various detection schemes for the QI protocol. In principle, achieving the 6 dB advantage in QI is theoretically possible with optimal collective quantum measurements throughout all M transmitted mode pairs [49]. The corresponding experimental implementation is challenging, which promotes more practical detection schemes that typically rely on pairwise joint measurements and yield a 3 dB QA [49, 53, 64].

For the classical reference scheme based on coherent-state transmission, the information is exclusively encoded in the first-order signal moments. Accordingly, each received mode is in a thermal state characterized by the background photon number N_B and a mean field of $\langle \hat{a}_R \rangle = 0$ under H_0, versus a mean field of $\langle \hat{a}_R \rangle = \sqrt{\kappa N_S}$ under H_1. Homodyne detection grants access to this information and results in sampling from a Gaussian distribution with variance $(2N_B + 1)/4$ and zero mean (H_0), or a mean of $\sqrt{\kappa N_S}$ (H_1) [145]. The individual measurement results Y_k ($k = 1, \ldots, M$) for a set of M mode copies can be summed up $Y = \sum_{k=1}^{M} Y_k$ and evaluated according to the decision rule:

(i) declare H_0, if $Y < (M \sqrt{\kappa N_S})/2$,

(ii) declare H_1, if $Y > (M \sqrt{\kappa N_S})/2$.

The associated detection error probability is given by [145]

$$P_e^{CS} = \frac{1}{2} \mathrm{erfc} \left(\sqrt{\frac{\kappa N_S M}{4N_B + 2}} \right) \simeq \frac{1}{2 \sqrt{\pi M \xi_{C,hom}}} e^{-M \xi_{C,hom}}, \qquad (3.33)$$

where $\mathrm{erfc}(x) = (2/\sqrt{\pi}) \int_x^\infty \exp(-t^2) \mathrm{d}t$ is the complementary error function and $\xi_{C,hom} = \kappa N_S/(4N_B + 2)$ denotes the corresponding error exponent. For a bright thermal background, $N_B \gg 1$, we can approximate $\xi_{C,hom} \simeq \kappa N_S/(4N_B)$, which coincides with the classical Chernoff bound in Eq. (3.27). This serves as a proof that coherent resource states in combination with homodyne detection represent an optimal classical radar scheme in the asymptotic regime. Note that the approximation in Eq. (3.33) is valid for $\kappa N_S M/(4N_B + 2) \gg 1$ [145].

The setting in quantum illumination is decisively different due to the zero-mean resource states, which makes basic homodyne detection obsolete. The goal of various proposed receiver schemes is to reach the theoretical 6 dB QA. From Eq. (3.23) and Eq. (3.24), it is obvious that the potential of the entanglement-assisted protocol does not originate from local properties of the individual modes (i.e., the diagonal $\boldsymbol{V}_{RI}$ entries), but rather from remaining non-local correlations (i.e., the anti-diagonal $\boldsymbol{V}_{RI}$ entries) characterized by $\langle \hat{a}_R \hat{a}_S \rangle = \langle \hat{a}_R^\dagger \hat{a}_S^\dagger \rangle = \sqrt{\kappa} C_q$ with $[\hat{a}_R, \hat{a}_S] = \left[\hat{a}_R^\dagger, \hat{a}_S^\dagger \right] = 0$. This fundamental result leads
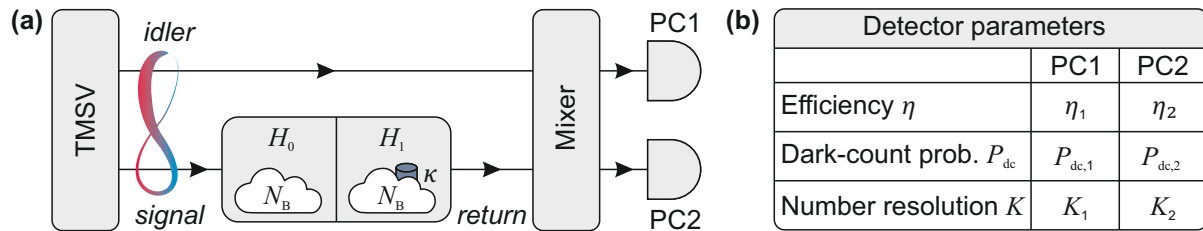
Figure 3.5: (a) Illustration of the considered quantum illumination scheme [155]. One mode of a two-mode squeezed vacuum state (TMSV), characterized by N_S photons per entangled mode, serves as a signal source. While the idler mode can directly pass to the PM receiver, the signal propagates through a bright thermal background characterized by the noise photon number N_B. Under hypothesis H_0 (no target present), the entire signal is lost and only N_B thermal photons enter the receiver via the signal path. Under H_1 (target present), the signal is weakly reflected from the target (with reflectivity $\kappa \ll 1$) and $N_B + \kappa N_S$ photons enter the receiver via the signal path. The receiver consists of a mixer, implementing an interaction between the retained idler and return signal modes, followed by two single-photon counters, PC1 and PC2. (b) The PCs can be characterized by their detection efficiency η, dark count probability P_{dc}, and photon number resolution K. We analyze the performance of the overall scheme in terms of error probabilities for realistic values of η, P_{dc}, and K in order to test robustness of the QI quantum advantage in presently accessible experimental settings in Sec. 3.7.

to the intuition that a joint measurement of $\hat{a}_R$ and $\hat{a}_I$ is a prerequisite for achieving the QA [48, 145, 155]. A potential workaround for this joint measurement might be implemented with a feed-forward heterodyne scheme, which also avoids using single-photon detectors or counters [57]. Moreover, a variant of this scheme exploiting re-programmable beam splitters promises the full 6 dB QA [58]. However, its experimental implementation remains very challenging in the microwave regime due to the absence of required components.

Parametric mixer

As of today, the only successful experimental implementation of a microwave quantum radar relies on the PM-type receiver, schematically shown in Fig. 3.5(a) [55]. In this approach, the return and idler modes interact non-linearly to form the input-output relations

$$\hat{b}_1 = \sqrt{G}\,\hat{a}_I + \sqrt{G-1}\,\hat{a}_R^\dagger, \tag{3.34}$$

$$\hat{b}_2 = \sqrt{G}\,\hat{a}_R + \sqrt{G-1}\,\hat{a}_I^\dagger, \tag{3.35}$$

where $G = 1 + \varepsilon^2$ is the mixer gain and $\varepsilon \ll 1$. Originally, it was proposed to use an optical parametric amplifier for implementing this input-output relation [145]. In the microwave domain, a Josephson ring modulator or a degenerate Josephson mixer realizes the same transformation [55, 73, 80]. The optimal mixer gain, G^*, has been derived in
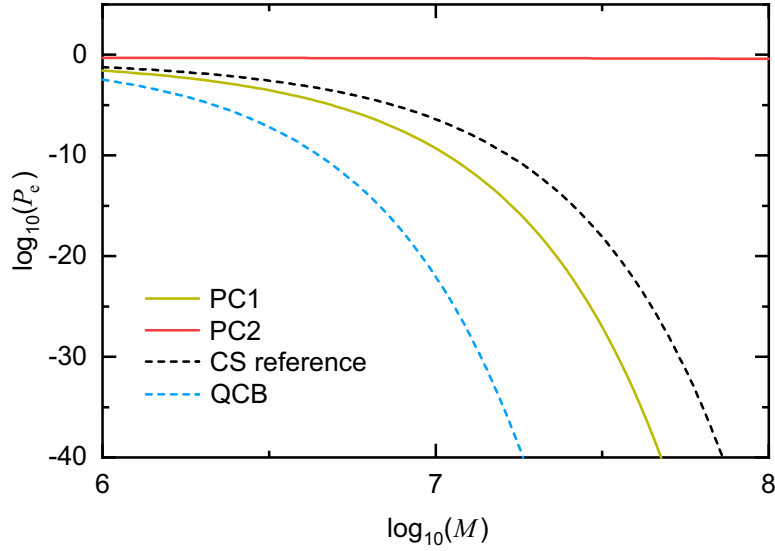
Figure 3.6: Error probability P_e as a function of the number of transmitted modes M for individual single-photon counting with PC1 (olive green) and PC2 (red) in an PM-type QI scheme. The dashed black line represents the error probability of the ideal classical reference radar (CS transmitter with a coherent photon number N_S in combination with a homodyne detector), which coincides with the Helstrom (lower) bound for classical state transmitters [56]. The dashed blue line depicts the quantum Chernoff (upper) bound for entanglement-based QI schemes. The employed system parameters are $N_S = 0.01$, $N_B = 20$, $\kappa = 0.01$, and $G = G^*$.

Ref. [58] as a function of the system parameters, N_S, N_B, and κ. The mixer is followed by single-photon counters, PC1 and PC2, with

$$N_1 = \langle \hat{b}_1^\dagger \hat{b}_1 \rangle = G\langle \hat{a}_I^\dagger \hat{a}_I \rangle + \sqrt{G(G-1)} \left(\langle \hat{a}_R^\dagger \hat{a}_I^\dagger \rangle + \langle \hat{a}_R \hat{a}_I \rangle \right) + (G-1)\langle \hat{a}_R \hat{a}_R^\dagger \rangle, \qquad (3.36)$$

and

$$N_2 = \langle \hat{b}_2^\dagger \hat{b}_2 \rangle = G\langle \hat{a}_R^\dagger \hat{a}_R \rangle + \sqrt{G(G-1)} \left(\langle \hat{a}_R^\dagger \hat{a}_I^\dagger \rangle + \langle \hat{a}_R \hat{a}_I \rangle \right) + (G-1)\langle \hat{a}_I \hat{a}_I^\dagger \rangle, \qquad (3.37)$$

as the respective detected photon numbers. As it can be seen from Eq. (3.23) and Eq. (3.24), the return mode $\hat{a}_R$ is characterized by $\langle \hat{a}_R^\dagger \hat{a}_R \rangle = N_B$ under H_0 and $\langle \hat{a}_R^\dagger \hat{a}_R \rangle = N_B + \kappa N_S$ under H_1. The non-local correlations, $\langle \hat{a}_R^\dagger \hat{a}_I^\dagger \rangle = \langle \hat{a}_R \hat{a}_I \rangle = 0$ vanish for H_0 and are given by $\langle \hat{a}_R^\dagger \hat{a}_I^\dagger \rangle = \langle \hat{a}_R \hat{a}_I \rangle = \sqrt{\kappa} C_q$ for H_1.

Within the scope of this work, all detection protocols perform a maximum likelihood analysis of the photon number statistics, which is based on photon counting through M return-idler transmitted modes. Irrespective of the detection scheme (individual or correlated photon counting, introduced in the next paragraph), it is assumed that for both hypotheses the conditional photon number distributions are given by

$$P_N|_{H_m} = \binom{n+M-1}{n} \frac{N_m^n}{(1+N_m)^{n+M}}, \qquad (3.38)$$

where N is the total photon count, $n \in \mathbb{N}_0$ and $m = 0, 1$. They converge to a normal distribution for $M \gg 1$ according to the central limit theorem. The decision threshold for the maximum likelihood test is given by [56]

$$N_{\text{th}} = M \frac{\sigma|_{H_1} \mu|_{H_0} + \sigma|_{H_0} \mu|_{H_1}}{\sigma|_{H_0} + \sigma|_{H_1}}, \tag{3.39}$$

where $\mu|_{H_{0,1}}$ and $\sigma^2|_{H_{0,1}}$ are the mean and variance of the photon number distribution under the two hypotheses, respectively. The obtained overlap of the two distributions defines the error probability of the scheme. This overlap depends on the difference of the means $\Delta \mu_k = |N_k|_{H_1} - N_k|_{H_0}|$ $(k = 1, 2)$, as well as on the respective variances $\sigma_k^2|_{H_{0,1}} = N_k(N_k + 1)|_{H_{0,1}}$, where both quantities scale linearly with the total number of transmitted modes [145]. Since $N_1|_{H_{0,1}} \ll 1$, it follows that $\sigma_1^2|_{H_{0,1}} \simeq N_1 \ll 1$, which results in a small overlap of the two distributions and a low resulting error probability (cf. Fig. 3.6). Conversely, for the same parameters, $N_2 \simeq 20.104|_{H_0}$ $(N_2 \simeq 20.105|_{H_1})$ is dominated by $G\langle \hat{a}_{\text{R}}^\dagger \hat{a}_{\text{R}} \rangle \simeq N_{\text{B}}$ and yields photon number distributions with variances $\sigma_2^2|_{H_{0,1}} \simeq N_2^2 \gg 1 \gg \sigma_1^2|_{H_{0,1}}$, while $\Delta N_2 \simeq \Delta N_1$. The associated error probability of N_2 is much larger than that of N_1 and clearly inferior to the ideal classical reference scheme, as shown in Fig. 3.6. Note that the considered maximum likelihood test yields the minimum possible error probability in a scenario where the prior distribution of the two hypotheses is unknown and is thus optimal [156]. To conclude, the PM-type receiver shows a strong asymmetry of the detection performance in individual detection, where only PC1 (in our convention) shows a QA.

From a theoretical point of view, the error probability for PC1 is bounded by the classical Bhattacharyya bound [cf. Eq. (3.13)] according to

$$P_{\text{e}}^{\text{PC1}} \leq \frac{1}{2} e^{-M\xi_{\text{CB}}}, \tag{3.40}$$

where the corresponding error exponent is given by [145]

$$\xi_{\text{CB}} = \frac{\varepsilon^2 \kappa N_{\text{S}}(N_{\text{S}} + 1)}{2N_{\text{S}}(N_{\text{S}} + 1) + 2\varepsilon^2 \kappa(2N_{\text{S}} + 1)(N_{\text{S}} + N_{\text{B}} + 1)} \simeq \frac{\kappa N_{\text{S}}}{2N_{\text{B}}}, \tag{3.41}$$

for $N_{\text{S}} \ll 1$, $\kappa \ll 1$, and $N_{\text{B}} \gg 1$. Accordingly, individual detection with PC1 converges towards the 3 dB QA in the asymptotic regime.

(Un)balanced difference detection

Las Heras *et al.* [155] consider the PM-type receiver exploiting both PCs by analyzing the operator $\hat{O} = G\hat{N}_1 - (G - 1)\hat{N}_2$. Note that this difference detector (correlated photon counting, CPC, in our convention) is unbalanced with weights G and $G - 1$, such that the decisive non-local correlations persist in $\hat{O}$ [cf. Eq. (3.36) and Eq. (3.37)]. The phase-
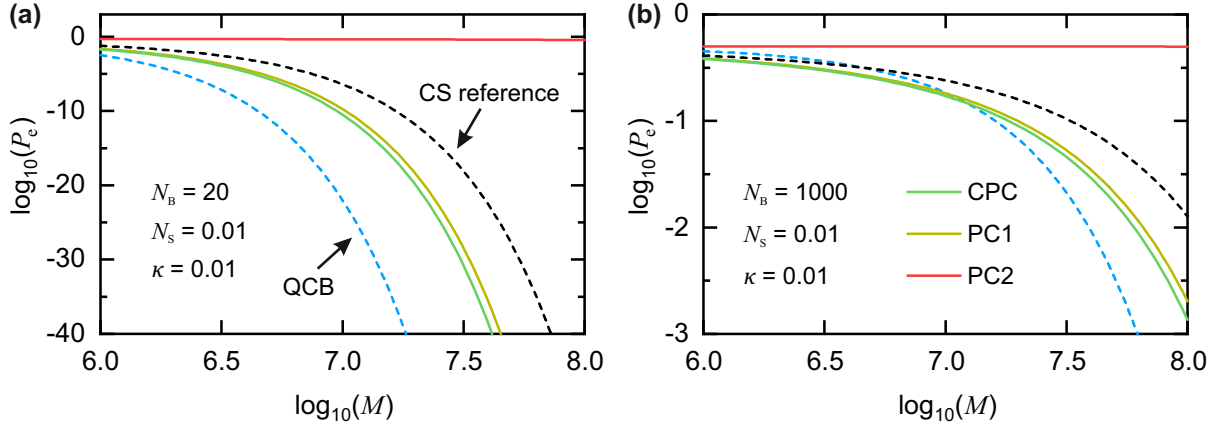
Figure 3.7: Error probability P_e as a function of transmitted modes M for individual single-photon detection and correlated photon counting with $w_1 = G$ and $w_2 = G - 1$ for (a) $N_B = 20$ coupled background photons and (b) $N_B = 1000$. The black dashed line represents the error probability of the ideal CS radar. The blue dashed line depicts the corresponding QCB. The green line depicts the ideal CPC performance, the olive green (red) line shows the results for individual detection with PC1 (PC2). The employed system parameters are $N_S = 0.01$, $\kappa = 0.01$, and $G = G^*$.

conjugate receiver scheme, discussed further below, also utilizes the measurement outcome of both single-photon counters in a balanced difference detector with $\hat{N} = \hat{N}_1 - \hat{N}_2$ [145]. In the following, we compare the performance of the PM-type scheme for individual photon counting with the CPC approach which relies on the operator $\hat{O}$ (see Fig. 3.7). The error probability of the CPC in comparison with individual detection (PC1) is very similar for both $N_B = 20$ [see Fig. 3.7(a)] and $N_B = 1000$ [see Fig. 3.7(b)]. Note that for $\log_{10}(M) < 7$ in Fig. 3.7(b), the QCB lies above the performances of CPC and PC1 and can only be interpreted as an upper bound to the associated error probabilities [48, 145]. Similarly, we observe a second crossing of the QCB and the CS reference at an even lower $\log_{10}(M) \simeq 6.5$. These features can be explained by the QCB reaching the asymptotic regime only when $M \gg N_B/(\kappa N_S)$, corresponding to the error probability converging towards zero, which occurs for $M \gg 10^7$ in Fig. 3.7(b) [48]. For Fig. 3.7(a), this criterion yields $M \gg 2 \cdot 10^5$ and is fulfilled for the entire range of M. Large correlations between individual photon counting events of PC1 and PC2, illustrated by Eqs. (3.45) and (3.46), result in the enhanced performance of the CPC. The operator $\hat{O}$ can be more generally described as

$$\hat{O} = w_1 \hat{N}_1 - w_2 \hat{N}_2, \tag{3.42}$$

where w_1 and w_2 are the artificial weights of the measured photon numbers in post-processing, such that they are not constricted by experimental conditions. The expectation value and variance of $\hat{O}$ are given by

$$\langle \hat{O} \rangle = w_1 \langle \hat{N}_1 \rangle - w_2 \langle \hat{N}_2 \rangle, \tag{3.43}$$

and

$$\mathrm{Var}\left(\hat{O}\right) = w_1^2\,\mathrm{Var}\left(\hat{N}_1\right) + w_2^2\,\mathrm{Var}\left(\hat{N}_2\right) - 2w_1w_2\mathrm{Cov}\left(\hat{N}_1, \hat{N}_2\right), \qquad (3.44)$$

where $\mathrm{Var}(\hat{N}_k) = N_k\left(N_k + 1\right)$ for $k = 1, 2$. Under the hypotheses H_0 and H_1, the corresponding covariances yield

$$\mathrm{Cov}\left(\hat{N}_1, \hat{N}_2\right)\Big|_{H_0} = G\left(G - 1\right)\left(N_\mathrm{S} + N_\mathrm{B} + 1\right)^2, \qquad (3.45)$$

$$\mathrm{Cov}\left(\hat{N}_1, \hat{N}_2\right)\Big|_{H_1} = \left((2G - 1)\,C_\mathrm{q} + \sqrt{G\left(G - 1\right)}\left(N_\mathrm{S}\left(\kappa + 1\right) + N_\mathrm{B} + 1\right)\right)^2, \qquad (3.46)$$

the corresponding derivation is provided in Appendix A. Figure 3.8(a) shows the QA of the CPC approach as a function of w_1 and w_2. Here, the conventional weighting according to Ref. [155], $w_1 = G$ and $w_2 = G - 1$ (solid red line), has a large gradient with respect to the optimal working regime (blue), such that a small change or misestimation of G can lead to a complete loss of the QA [white star versus black star, see also Fig. 3.8(b)]. We identify an optimal weighting according to

$$
\begin{aligned}
w_2 &= \left(\frac{\sqrt{N_\mathrm{S}(N_\mathrm{S} + 1)(N_\mathrm{B} + \kappa N_\mathrm{S})(N_\mathrm{B} + \kappa N_\mathrm{S} + 1)}}{(N_\mathrm{B} + (\kappa - 1)N_\mathrm{S})(N_\mathrm{B} + (\kappa + 1)N_\mathrm{S} + 1)}\right.\\
&\quad \left.+\frac{N_\mathrm{S}(N_\mathrm{S} + 1)}{(N_\mathrm{B} + (\kappa - 1)N_\mathrm{S})(N_\mathrm{B} + (\kappa + 1)N_\mathrm{S} + 1)}\right) w_1\\
&= (G^* - 1)\,w_1,
\end{aligned}
\qquad (3.47)
$$

shown as the dashed white line in Fig. 3.8(a), which relaxes the requirements in terms of parameter precision and introduces a degree of freedom in the choice of the post-processing weights.

Phase-conjugate receiver

Similar to the PM scheme, the phase-conjugate receiver (PCR) relies on mixing the return signal with the retained idler and a subsequent photon-number measurement [145]. As can be seen from Eqs. (3.34), (3.36) and (3.37), the transformation of the non-local correlations into observables is mediated by the phase-conjugating properties of the input-output relations in the parametric mixer. In the PCR scheme, this phase-conjugation is established by a receiver that implements [145]

$$\hat{a}_\mathrm{PCR} = \hat{a}_\mathrm{R}^\dagger + \sqrt{2}\hat{a}_\mathrm{vac} \qquad (3.48)$$

for each return mode, where $\hat{a}_\mathrm{vac}$ is the vacuum-state operator that is required in order to fulfill the bosonic commutation relation. Subsequently, the phase-conjugated modes are superimposed with the corresponding retained idler modes in a symmetric beam splitter
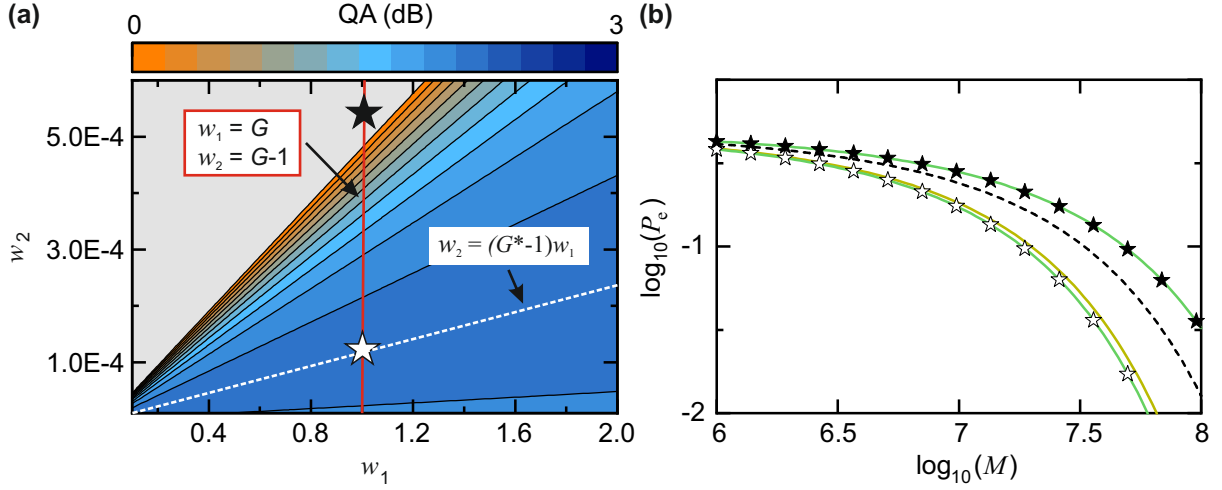
Figure 3.8: (a) QA as a function of weights w_1 and w_2. The solid red line represents weighting according to $w_1 = G$ and $w_2 = G - 1$ [155]. While this relation (white star) can yield the full $3\,\mathrm{dB}$ QA (blue color code), a slight variation or misestimation of G on the order of 0.05% (black star) leads to inferior results with respect to the CS reference. The dashed white line represents an optimal weighting according to Eq. (3.47). (b) Resulting error probability as a function of transmitted modes for the optimal weighting (green line with white stars) versus a misestimated weighting (green line with black stars) in comparison with individual detection (PC1, olive green) and the CS reference (dashed black). The system parameters are $N_\mathrm{S} = 0.01, \kappa = 0.01, N_\mathrm{B} = 1000$, and $G = G^*$.

to form two output modes [49]

$$\hat{a}_\pm = \frac{\hat{a}_\mathrm{PCR} \pm \hat{a}_\mathrm{I}}{\sqrt{2}}. \tag{3.49}$$

The final measurement operator is given by [145]

$$\hat{N} = \hat{N}_+ - \hat{N}_-, \tag{3.50}$$

where $\hat{N}_+ = \hat{a}_+^\dagger \hat{a}_+$ and $\hat{N}_- = \hat{a}_-^\dagger \hat{a}_-$. The associated error probability of the PCR scheme can be approximated as [145]

$$P_\mathrm{e}^\mathrm{PCR} \simeq \frac{1}{2}\mathrm{erfc}\left(\sqrt{\xi_\mathrm{PCR}M}\right) \simeq \frac{e^{-M\xi_\mathrm{PCR}}}{2\sqrt{\pi M \xi_\mathrm{PCR}}}, \tag{3.51}$$

where the corresponding error exponent is given by [145]

$$\xi_\mathrm{PCR} = \frac{\kappa N_\mathrm{S}(N_\mathrm{S} + 1)}{2N_\mathrm{B} + 4N_\mathrm{S}N_\mathrm{B} + 6N_\mathrm{S} + 4\kappa N_\mathrm{S}^2 + 3\kappa N_\mathrm{S} + 2} \simeq \frac{\kappa N_\mathrm{S}}{2N_\mathrm{B}}, \tag{3.52}$$

for $N_\mathrm{S} \ll 1$, $\kappa \ll 1$ and $N_\mathrm{B} \gg 1$. Accordingly, the PCR scheme also converges toward the $3\,\mathrm{dB}$ QA in the asymptotic regime. Similar to the CPC approach, the PCR scheme exploits the entire information carried by the two outputs of the phase conjugator, which

reflects in a slight performance advantage over individual detection with PC1 in the PM scheme [145]. Nevertheless, the full potential of the QI protocol is beyond reach for these receiver schemes, which belong to the class of local operations plus classical communication (LOCCs) and are known to perform not optimally for such a type of state discrimination [157, 158].

Sum-frequency generation receiver

The sum-frequency generation (SFG) architecture was the first proposed receiver to saturate the QCB in QI [159]. Here, the return and idler pairs are upconverted to a single mode at the sum frequency $\omega_P = \omega_S + \omega_I$. Conceptually, SFG relies on pairwise return-idler input states which are converted into a single-mode output state that is initially vacuum and evolves into either a weak thermal state (under H_0) or a weak coherent state embedded in a weak thermal state (under H_1). Here, the coherent footprint is a direct consequence of the non-zero cross-correlations of the return and idler modes under H_1. Such an output state evolution is only valid for low photon numbers $\langle \hat{a}_R^\dagger \hat{a}_R \rangle$ of the return state, which is not the case for the typical QI parameter restrictions, specifically $N_B \gg 1$. A feedforward (FF) mechanism employing a series of pairwise low-transmissivity beam splitters, combined with conditional two-mode squeezing operations complement the SFG building block to form the FF-SFG, which saturates the Helstrom minimum probability of error, i.e., the 6 dB QA for $N_S \ll 1$ [140, 159]. This adapted scheme is also valid for $N_B \gg 1$ due to the low transmissivity of the employed beam splitters and an associated small photon number entering the SFG per cycle [159]. For each cycle, two photon number measurements with expectation values that are conditioned on the respective hypothesis are fed forward to the next pairwise modes and converge to a final hypothesis assumption after K cycles of the scheme [159]. Despite the optimum discrimination potential of this architecture for multimode mixed Gaussian states, an experimental realization is out of reach with the currently available technology. The main challenges are the stringent requirements for high-fidelity cascaded idler storage and finite efficiencies of each of the manifold operations in the scheme [49, 159].

Correlation-to-displacement conversion

Another interesting conversion module to capture quantum correlations and transform those into a coherent quadrature displacement was proposed in Ref. [58]. Its working principle can be divided into several steps. First, the module conducts a heterodyne measurement of each of the M return modes, which yields on average a zero-mean measurement distribution with a variance governed by the system parameters N_S, N_B and κ. For the favorable bright-background $N_B \gg 1$, weak-signal $N_S \ll 1$ regime of QI, the heterodyne measurement outcomes are on the order of $\sqrt{N_B}$. As a consequence, the corresponding idler states collapse into conditional, weakly displaced thermal states with

a mean photon number on the order of $\sqrt{\kappa N_{\mathrm{S}}/N_{\mathrm{B}}}$ [58]. The corresponding SNR $\simeq \kappa/N_{\mathrm{B}}$ of the individual, weakly displaced thermal states is extremely small. In a second step, a programmable beam splitter array of dimension M constructively combines the mean fields of the individual idler modes. The matched, complex weights of the beam splitters are adapted based on the respective heterodyne measurement outcomes and result in a constructive interference of the ensemble of means throughout all M modes. For uncorrelated noise, the SNR of the correlation-to-displacement module steadily grows with increasing M and yields an error exponent that saturates the QCB and the associated full 6 dB QA in the asymptotic regime [58]. The adaptive programming of the beam splitter array relies on the outcomes of each of the individual heterodyne measurements, which provide classical control signals as an input to the beam splitter array. Accordingly, the ensemble of $M \gg 1$ idler states needs to be reliably stored in a quantum memory, which represents a major experimental hurdle. The programmable beam splitter array of length $M \gg 1$ represents another technological challenge, which is highly nontrivial with currently available technology.

Hetero-homodyne receiver and sequential detection

The correlation-to-displacement conversion served as an inspiration for a simplified scheme of the hetero-homodyne receiver proposed in Ref. [57]. Here, the return modes undergo a heterodyne detection in order to extract the in-phase (I) and quadrature (Q) components, which resemble thermal states. In contrast to the correlation-to-displacement scheme, this first step is conducted sequentially, i.e., only one return mode is measured at a time. The extracted $+I$ and $-Q$ components are used to modulate a strong local oscillator tone that provides a reference for homodyning the associated idler modes, which have been stored for the signal round-trip time. This routine is repeated M times. Naturally, the information for these conditioned sequential homodyne measurements is encoded in the first signal moments [144]. Under H_0, the associated mean is zero, whereas under H_1, the measured mean values scale as $M\sqrt{\kappa N_{\mathrm{S}}}$ [57, 160]. Under both hypotheses, the measurement variances are approximately $MN_{\mathrm{B}}/4$. The corresponding decision threshold γ is based on the mean values extracted from these conditioned sequential homodyne measurements and scales as $\gamma = M\sqrt{\kappa N_{\mathrm{S}}/2}$ [57]. The error probability of this scheme converges toward the 3 dB QA in the asymptotic regime [57]. In principle, the hetero-homodyne receiver realizes an effective phase-conjugation that is required to convert the remaining signal and idler cross-correlations into a measurable quantity [57]. The employed heterodyne techniques in Refs. [57, 58], including their intrinsic finite added noise, can be applied to the return signals without loss of the QA due to the noisy character of the return modes for $N_{\mathrm{B}} \gg 1$. In contrast, the idler modes remain ideally pure during storage and require quantum-limited homodyne detection for a persistent QA [57].

3.5 Purity requirements for the resource states

Propagating TMS vacuum states represent an ideal resource for QI and can be routinely generated with various superconducting parametric circuits [65, 72, 78, 161, 162]. In experiment, however, these states [cf. Eq. (3.18)] are subject to finite added noise. In this section, we investigate the influence of such added noise on the performance of the QI protocol. In more detail, we focus on the PM scheme for individual detection with PC1. We assume the detection unit to operate in an optimal manner in order to gain a quantitative understanding of the robustness of the QA against noise in the resource states. The noise contribution for a TMS state can be quantified by the purity $\mu = 1/(16\sqrt{\det \boldsymbol{V}})$ of the associated 4×4 covariance matrix $\boldsymbol{V}$, according to Eq. (2.26). Similar to single-mode states, the purity is unity for states that saturate the Heisenberg uncertainty relation.

In experiment, we generate the TMS states by first creating two single-mode squeezed states with an orthogonal orientation in phase space and subsequently superimposing these states in a beam splitter, as illustrated in Fig. 2.9. For the case of a finite purity, $\mu_{\mathrm{SMS}} < 1$, of these initial single-mode squeezed states and an ideal, lossless beam splitter, we obtain the TMS purity of $\mu_{\mathrm{TMS}} = \mu_{\mathrm{SMS}}^2$. Here, we assume identical purities of the two initial single-mode states. In general, the purity decreases for increasing squeezing levels (and pump powers) due to non-idealities of the JPAs, as shown later in Ch. 5 (see Fig. 5.13). This pump-power dependence is linked to the highly nonlinear character of JPAs, which is based on associated Josephson junctions. While the lowest-order nonlinearity is used for parametric amplification, the unwanted higher-order nonlinearities play a detrimental role in the JPA dynamics with increasing pump powers [108]. Large pump powers also result in non-negligible microwave fields inside the JPA resonators, which may lead to increased coupling to various loss channels. In general, these effects lead to a deviation from an ideal parametric amplification and degrade the quality of the produced squeezed states [75, 108, 163]. In QI, we consider very low signal levels, where these pump-induced effects are expected to play a minor role. Here, the goal is to minimize a persisting noise floor in the generated JPA states, stemming, e.g., from finite internal quality factors of the JPAs. This ensemble of typically unwanted factors results in a decreased purity of the quantum states.

In order to test the robustness of the PM scheme against finite purities of the resource states, we investigate the following scenario: for a given photon number N_{TMS} per mode, which stems purely from squeezing according to $N_{\mathrm{TMS}} = \sinh^2(r)$, we analyze how pure such a state needs to be in order to outperform the associated classical reference scheme. In QI, we aim for a typical number of signal photons of $N_{\mathrm{S}} = N_{\mathrm{TMS}} = 0.01$ per mode, which corresponds to a squeeze factor of $r \simeq 0.1$ and an associated squeezing level $S = 20\,r\log_{10}(e) = 0.87\,\mathrm{dB}$. Importantly, the finite purity in this consideration is reflected in added noise of the QI resource states and a resulting enhanced photon number per mode, $N_{\mathrm{S}}' = N_{\mathrm{TMS}} + N_{\mathrm{N}}$, where N_{N} denotes the number of added noise photons in the

resulting state. Note that in order to maintain a fair comparison, the classical reference scheme can resort to an increased coherent resource photon number N_S'. We consider the case of an identical added noise for both JPAs, which we model according to

$$(\hat{S}')^\dagger \begin{pmatrix} \hat{a}_1 \\ \hat{a}_2 \end{pmatrix} \hat{S}' = \begin{pmatrix} (\hat{a}_1 + \zeta)\cosh r - \left(\hat{a}_1^\dagger + \zeta^*\right)e^{-2\mathrm{i}\gamma_1}\sinh r \\ (\hat{a}_2 + \zeta)\cosh r - \left(\hat{a}_2^\dagger + \zeta^*\right)e^{-2\mathrm{i}\gamma_2}\sinh r \end{pmatrix}, \tag{3.53}$$

where we set $r_1 = r_2 = r$, and restrict the squeezing angles to $|\gamma_1 - \gamma_2| = \pi/2$. The classical complex random variable ζ models the added noise and satisfies $\langle|\zeta|^2\rangle = N_N$. In the PM scheme, these noisy resource states result in adapted photon numbers, N_1' and N_2', as compared to Eqs. (3.36) and (3.37), given by

$$N_1' = G\langle(\hat{a}_I')^\dagger\hat{a}_I'\rangle + \sqrt{G(G-1)}\left(\langle(\hat{a}_R')^\dagger(\hat{a}_I')^\dagger\rangle + \langle\hat{a}_R'\hat{a}_I'\rangle\right) + (G-1)\langle\hat{a}_R'(\hat{a}_R')^\dagger\rangle, \tag{3.54}$$

and

$$N_2' = G\langle(\hat{a}_R')^\dagger\hat{a}_R\rangle + \sqrt{G(G-1)}\left(\langle(\hat{a}_R')^\dagger(\hat{a}_I')^\dagger\rangle + \langle\hat{a}_R'\hat{a}_I'\rangle\right) + (G-1)\langle\hat{a}_I'(\hat{a}_I')^\dagger\rangle. \tag{3.55}$$

Here, the return mode $\hat{a}_R' = \hat{a}_R$ is characterized by $\langle(\hat{a}_R')^\dagger\hat{a}_R'\rangle = N_B$ under H_0 and $\langle(\hat{a}_R')^\dagger\hat{a}_R'\rangle = N_B + \kappa N_S' = N_B + \kappa(N_{\mathrm{TMS}} + N_N)$ under H_1. The non-local correlations, $\langle(\hat{a}_R')^\dagger(\hat{a}_I')^\dagger\rangle = \langle\hat{a}_R'\hat{a}_I'\rangle = 0$ vanish for H_0 and are given by

$$\langle(\hat{a}_R')^\dagger(\hat{a}_I')^\dagger\rangle = \langle\hat{a}_R'\hat{a}_I'\rangle = \sqrt{\kappa}C_q = \sqrt{N_{\mathrm{TMS}}(N_{\mathrm{TMS}} + 1)} \tag{3.56}$$

for H_1. Based on Eqs. (3.54) and (3.55), we perform a maximum likelihood analysis, analogous to Sec. 3.4, and compare the resulting error probabilities to an ideal coherent-state transmitter that relies on sending N_S' photons per mode. Figure 3.9 shows the QA of the PM scheme for individual detection with PC1 as a function of the squeezing level S, which corresponds to a photon number N_{TMS} per mode of the resource state, and an associated two-mode purity level of these states. The QA is evaluated in the asymptotic regime with respect to the classical Chernoff bound of the classical reference, characterized by $P_e^{\mathrm{CS}} = 0.5\exp(-M\kappa N_S/(4N_B))$. Accordingly, the QA in decibel is given by

$$\mathrm{QA} = 10\log_{10}\left(\frac{\kappa N_S M}{4N_B}\frac{1}{\ln\left(2\Delta P_e(M) + \exp(-M\kappa N_S/(4N_B))\right)}\right), \tag{3.57}$$

where $\Delta P_e(M) = P_e^{\mathrm{CS}}(M) - P_e^{\mathrm{PC1}}(M)$. We observe stringent requirements on the purity, with a vanishing QA at a threshold value of approximately $98\,\%$ for $N_{\mathrm{TMS}} = 0.01$. The $0\,\mathrm{dB}$-threshold value relaxes slightly with increasing squeezing level, while at the same, the overall QA monotonously decreases, in accordance with theory [145]. Importantly, we only enter the realm of a QA greater than $2\,\mathrm{dB}$ for purities close to unity and squeezing levels on the order of $1\,\mathrm{dB}$ or smaller. The identical analysis for $N_B = 1000$ yields very
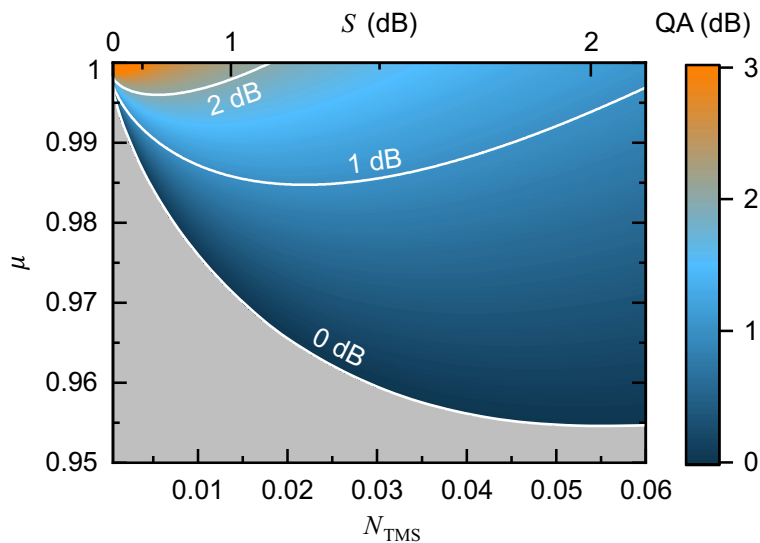
Figure 3.9: QA for individual detection with PC1 as a function of the TMS photon number, $N_{\text{TMS}} = \sinh^2(r)$ (bottom x-axis), the associated squeeze level S (top x-axis) and purity of the TMS resource states. The other employed system parameters are $N_{\text{B}} = 20$, $\kappa = 0.01$, and $G = G^*$.

similar results. This finding strongly suggests that the stringent purity requirements of the scheme stem predominantly from the idler part of the entangled resource state. From a conceptual point of view, this intuition is analogous to the argumentation why heterodyne measurements of the return mode do not impact the QA, while the idler mode requires quantum-limited homodyning in the hetero-homodyne receiver with sequential detection [57].

In summary, the required purities for a persistent QA greater than 1 dB are challenging from an experimental point of view. While purities close to unity can be routinely achieved with JPAs at low pump powers, the beam splitter that superimposes the single-mode squeezed states also suffers from finite losses and associated added noise to the TMS states [108]. However, the requirements in order to achieve a finite QA between 0.5 dB and 1 dB seem realistic based on our study shown in Fig. 3.9, which matches with the experimentally demonstrated microwave quantum radar QA of 0.8 dB [55]. Notably, the authors of Ref. [55] further improved the purity of the idler mode by sideband cooling down to a noise temperature of 29 mK, which corresponds to a thermal population of $N_{\text{th}} = 2.5 \times 10^{-3}$ at an idler frequency of $\omega/(2\pi) \simeq 3.75$ GHz.

3.6 Considerations on the idler storage

In comparison with the classical reference, storing the idler for the round-trip time of the propagating signal represents a major challenge in QI. In principle, proof-of-principle experiments can resort to using delay lines and rely on a finite temporal length of the signal and idler modes, which creates a certain flexibility for the exact timing of the joint

measurements [55]. A practical QI scheme, however, requires versatile idler storage [164–167]. Such a deterministic and reliable idler storage is specifically demanding for the full 6 dB QA schemes that rely on an optimal joint measurement of the entire signal and idler ensemble. A finite idler storage efficiency η_I results in a deteriorated performance of the associated signal-idler measurements and an increased detection error. Correspondingly, the QCB from Eq. (3.28) changes to [49, 56]

$$\xi_\mathrm{QCB}(\eta_\mathrm{I}) = \eta_\mathrm{I}\kappa N_\mathrm{S}/N_\mathrm{B}. \tag{3.58}$$

Since the quantity η_I enters the error exponent linearly, we observe that the maximally obtainable QA by means of QI, expressed in linear units, is reduced to $\mathrm{QA} \leq 4/\eta_\mathrm{I}$. This implies that we require $\eta_\mathrm{I} > 1/4$ for a persisting QA with respect to a 6 dB scheme. For the more practical 6 dB schemes, this threshold tightens to $\eta_\mathrm{I} > 1/2$.

3.7 Practical receiver characteristics

As introduced in Sec. 3.4, an optimal detector layout for QI remains an open question, because the full 6 dB QA in the error exponent requires very cumbersome and demanding experimental setups [58, 159]. At the same time, the 3 dB QA over the ideal classical radar can be achieved by using more practically accessible schemes. However, realistic quantum illumination implementations may contain detection imperfections [55, 59]. In this section, we analyze the practical limitations of microwave PCs and their impact on the PM-type receiver, which represents the detector layout that is best studied to date [55]. We investigate the PM-receiver performance with non-unity detection efficiencies, non-zero dark count probabilities, and finite photon number resolution [cf. Fig. 3.5(b)]. Furthermore, we consider the effects of these imperfections on the correlated photon counting (CPC) results of both PCs [155].

Although single-photon detection for propagating microwaves is challenging due to the low photon energies, which are approximately 6 orders of magnitude smaller than for optical photons, various theoretical concepts [168–178] have paved the road to successful experimental implementations [179–185]. Here, the most advanced schemes exploit Ramsey interferometry to implement quantum non-demolition detection, or counting, of incident microwave photons by measuring a photon-induced phase perturbation of an ancilla qubit [181, 182]. Since the qubit coherence time directly correlates with the dark count rate, the performance of Ramsey-based detectors strongly depends on a sufficiently long qubit lifetime. Apart from the dark count rate and detection efficiency, the photon-number resolution is another key parameter in single-photon detection. Dassonneville *et al.* [185] have realized a photon counter with a photon-number resolution of up to three photons, which we consider as a reference in Sec. 3.7. The dead time of single-photon detectors [186] represents a further important quantity, which we do not discuss in detail in this work.
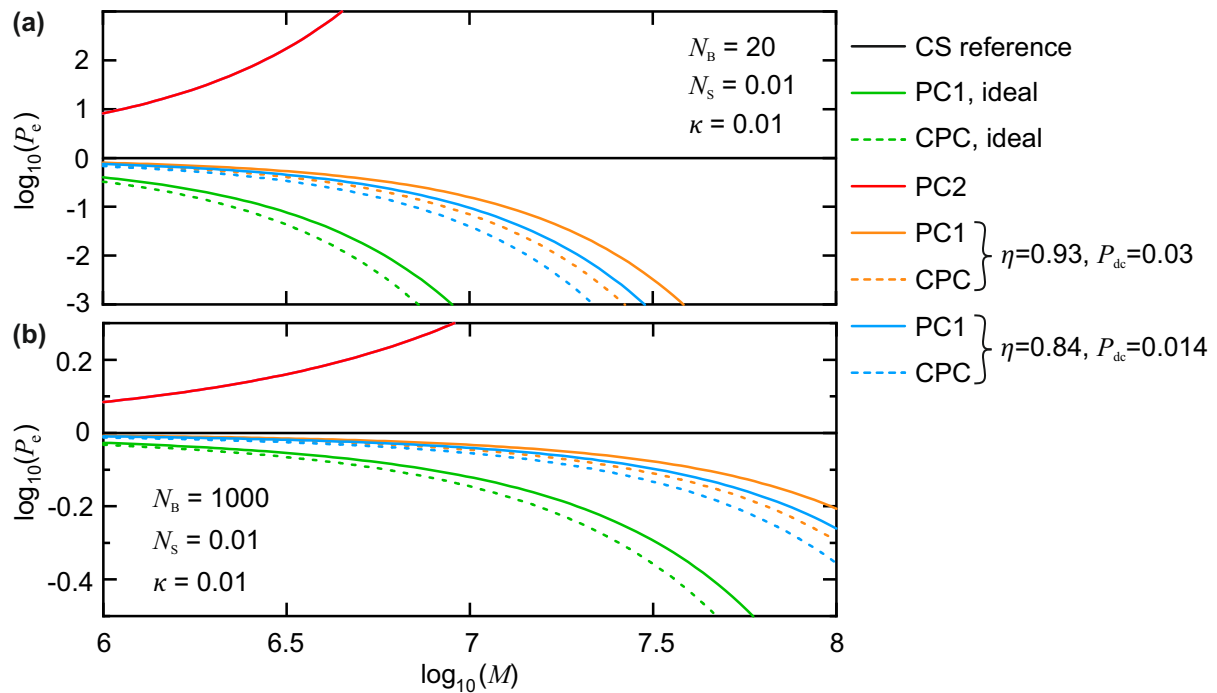
Figure 3.10: Error probability difference $\Delta\log_{10}(P_e) = \log_{10}(P_e) - \log_{10}(P_{e,CS})$ as a function of the number of transmitted modes M for individual photon counting (solid lines) and optimal [according to Eq. (3.47)] correlated photon counting (dashed lines) for (a) $N_B = 20$ coupled background photons and (b) $N_B = 1000$. The black line represents the error probability of the CS reference. Green lines depict ideal detectors, orange lines correspond to $\eta = 0.93$ and $P_{dc} = 0.03$, blue lines show the performance for $\eta = 0.84$ and $P_{dc} = 0.014$. The red line shows the results for PC2 which are close to $P_e = 0.5$ in each of the three considered cases. The mixer gain is set to $G = G^*$.

Modern microwave detection schemes achieve dead times between $100\,\text{ns}$ [181] and several microseconds [185, 187].

Finite detection efficiencies

State-of-the art microwave single-photon detectors (SPDs) achieve a click probability $P_c = 0.93$ for an incoming single photon with a dark count probability $P_{dc} = 0.03$ [185]. The dark count probability can be computed as the dark count rate times the duration of the detection window. Moreover, $P_c = 1 - P_{|1\rangle}(0)$, where $P_{|1\rangle}(0)$ is the probability of measuring no click for an impinging single photon. To this date, the quality of photon-number resolved measurements, expressed by the conditional probabilities $P_{|k\rangle}(l)$ of realizing a measurement outcome $l = \{0, \ldots, 3\}$ for an incoming Fock state $|k\rangle$ strongly depends on k, with $P_{|1\rangle}(1) = 76\%$, $P_{|2\rangle}(2) = 71\%$ and $P_{|3\rangle}(3) = 54\%$ [185]. For simplicity, we assume a photon number resolution corresponding to the SPD click probability, i.e., $P_{|k\rangle}(k) = P_c = 0.93$ for all $k = 1, 2, \ldots$ which effectively gives an upper performance bound. We model the influence of finite dark count probabilities and a finite detection efficiency
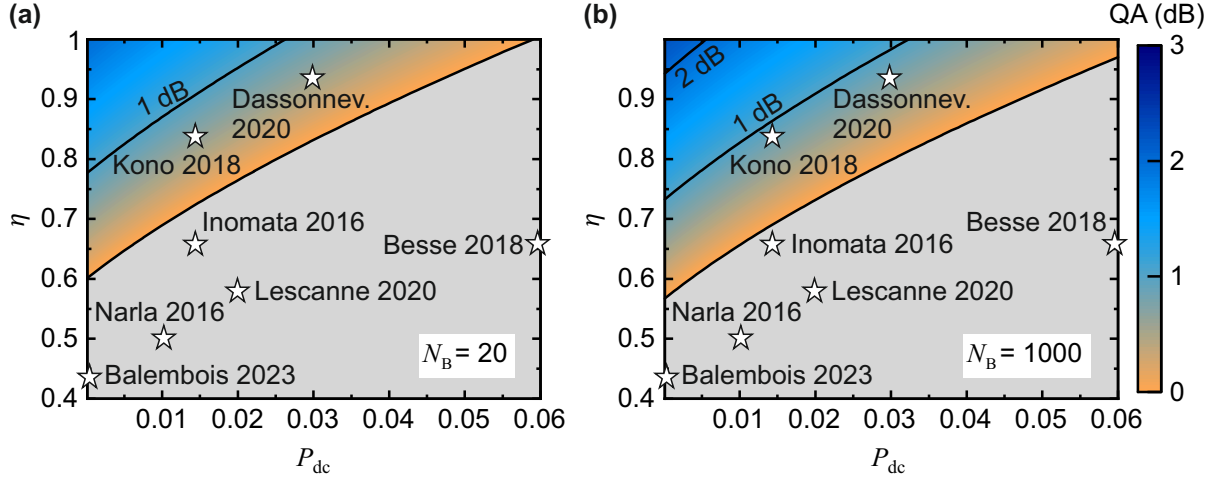
Figure 3.11: QA for individual detection with PC1 as a function of the dark count probability P_{dc} and detection efficiency η for (a) $N_B = 20$ and (b) $N_B = 1000$. The white stars indicate the performances of microwave single-photon detector implementations from Refs. [180–185, 187]. The gray color code illustrates a region without any QA. The other employed system parameters are $N_S = 0.01$, $\kappa = 0.01$ and $G = G^*$.

$P_{|k\rangle}(k) < 1$ with a beam splitter before an ideal PC

$$\hat{c}_j = \sqrt{\eta}\,\hat{b}_j + \sqrt{1-\eta}\,\hat{b}_{c,j}, \tag{3.59}$$

where $j = 1, 2$, $\eta = P_{|k\rangle}(k)$ is the beam splitter transmissivity, the dark count probability is modeled with a coupled mode $\hat{b}_{c,j} = 1/\sqrt{1-\eta}\,\hat{a}_{th,j}$ characterized by $\langle \hat{a}^\dagger_{th,j}\hat{a}_{th,j}\rangle = (1/(1-P_{dc})-1) \simeq P_{dc}$ for $P_{dc} \ll 1$. Accordingly, we do not take into account the influence of $P_{|k\rangle}(l)$ for $k \neq l$.

In Fig. 3.10, we plot the error probability difference for $N_B = 20$ [see Fig. 3.10(a)] and for $N_B = 1000$ [see Fig. 3.10(b)]. We compare the ideal performance of individual and CPC detection for a given CS reference in two realistic scenarios: high efficiency and moderate dark count probability [185] versus moderate efficiency and low dark count probability [182]. For $N_B = 20$, both scenarios yield clearly inferior results compared to the ideal case. We observe that the scenario with low dark count probability outperforms the high-efficiency counterpart, which underlines that for a realistic implementation, minimizing dark count probabilities plays a decisive role for the photon detection in QI. Additionally, the CPC approach only marginally beats individual detection for all three scenarios in the low-noise case of $N_B = 20$. The high-noise regime, $N_B = 1000$, shows similar results with the low dark count detector performing slightly better than the high efficiency case and a consistent performance enhancement for the CPC. In both noise regimes, PC2 does not exhibit a strong dependence on the non-idealities, since $P_e \simeq 0.5$ already in the ideal case.

Figure 3.11 illustrates the projected performance of various already demonstrated mi-

crowave single-photon detectors, in terms of P_{dc} and η, for achieving a QA in individual detection with PC1. In accordance with the successful microwave quantum radar realization [55], the underlying device investigated by Dassonneville *et al.* [185] is situated in the region of a robust QA. Importantly, the QA vanishes rapidly with increasing P_{dc}, even for an ideal detection efficiency of $\eta = 1$. Conversely, the scheme is robust against finite efficiencies, $\eta < 1$, down to $\eta \simeq 0.6$ for $N_{\text{B}} \gg 1$ (see Fig. 3.11). These findings suggest that the minimization of P_{dc} in combination with a reasonably high η is desirable in order to achieve the QA, in agreement with our results from Fig. 3.10. In accordance with the theory, the maximally reachable QA increases with increasing N_{B}, as it also can be seen in Fig. 3.11(a) and (b). As a consequence, the area of QA > 0 increases and, e.g., the 1 dB and 0 dB QA lines lean towards lower values of P_{dc} and η. We would like to mention that our mapping of existing single-photon detectors onto the QA problem in Fig. 3.11 may be limited to various simplifications of our theoretical model and should not be considered as a complete evaluation of those detectors' performance.

Finite detection resolution

In principle, photon counters can provide full access to the photon number operator in Eq. (3.36) and Eq. (3.37). However, existing state-of-the-art microwave single-photon counters exhibit a rather limited photon number resolution [182, 184, 185]. To analyze the impact of this finite resolution, we restrict the PCs in Fig. 3.5 to a resolution up to K photons. Therefore, a single measurement has possible outcomes of measuring $0, 1, \ldots, K$ photons. We assume that the measurement yields K if the number of photons in the probe is larger or equal K. Under both hypotheses the state at the output of the mixer is a thermal state with mean photon number $N_j, j \in \{1, 2\}$, given by Eqs. (3.36, 3.37) [145]. This yields a photon number distribution at the output of the photon counter

$$p(n) = \begin{cases} (1 - q_j)q_j^n, & 0 \le n < K, \\ 1 - (1 - q_j)\sum_{k=0}^{K-1} q_j^k, & n = K, \end{cases} \tag{3.60}$$

with $q_j = \frac{N_j}{N_j + 1}$. For this distribution, the expectation value is given by

$$\mu_j^{(K)} = \frac{q_j(1 - q_j^K)}{1 - q_j}, \tag{3.61}$$

and the respective variance can be written as

$$\sigma_j^{2,(K)} = \frac{q_j}{1 - q_j}\left(1 - (2K + 1)q_j^K + 2q_j\frac{1 - q_j^K}{1 - q_j}\right) - \left(\frac{q_j(1 - q_j^K)}{1 - q_j}\right)^2. \tag{3.62}$$
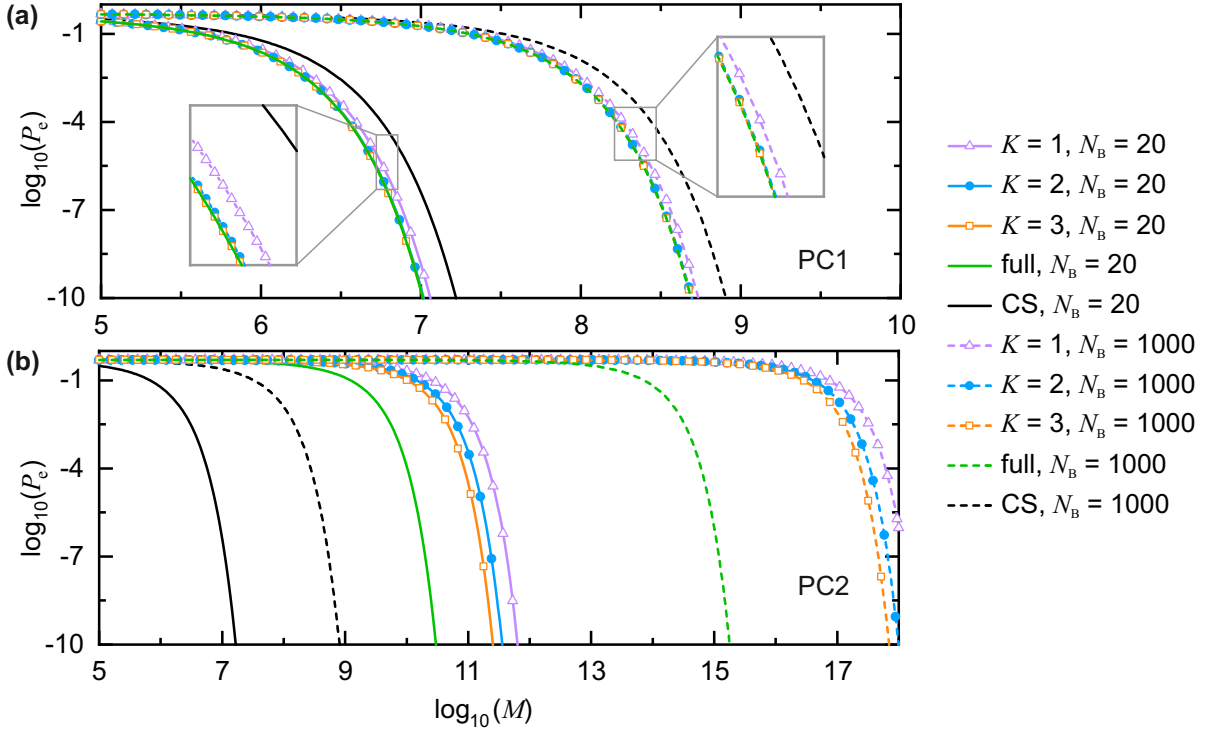
Figure 3.12: Error probability P_e as a function of the number of transmitted modes M for different resolutions K for individual detection with (a) PC1 and (b) PC2. The solid lines show the performance for the low-noise regime, $N_B = 20$, and dashed lines for the high-noise regime, $N_B = 1000$. The mean signal photon number is $N_S = 0.01$ and reflectivity $\kappa = 0.01$ in both cases. The mixer gain is set to $G = G^*$.

Analogous to the analysis of the ideal PM scheme, the assumption of a large number of transmitted modes, i.e. $M \gg 1$, leads to the threshold given in Eq. (3.39) but with mean and standard deviation from Eqs. (3.61, 3.62).

In Fig. 3.12, we plot the error probability for individual detection with PC1 and PC2 in panels (a) and (b), respectively. We compare ideal photon counters with a photon number resolution of $K = 1, 2, 3$. For PC1 and both background scenarios of $N_B = 20$ and $N_B = 1000$, all variants clearly outperform the CS reference and for a resolution of $K \geq 2$, the resulting error coincides with the full-resolution counter. The associated low average photon number $N_1 \simeq 0.11 \ll 1$ under both hypotheses and for both background scenarios explains why a binary SPD is close to being optimal. The reason why a higher resolution does not become more relevant in more noisy scenarios is that the optimal mixer gain, G^*, decreases with increasing N_B, such that N_1 stays similar for varying N_B. This finding is important for real-world applications with naturally high number of noise photons. Conversely, detection with PC2 alone is always inferior in comparison to the optimum classical scheme due to the large value of N_2, which is governed by strong background noise coupled to the return mode [see Eq. (3.37)].

3.8 Quantum illumination beyond binary detection

The binary detection task for the presence or absence of an object at a fixed distance represents the most fundamental challenge associated with radar technology. State-of-the-art classical radar applications go far beyond these capabilities and are able to infer the distance of an object by means of the signal round-trip time, and gain information on the velocity and direction by the associated Doppler shifts. A corresponding extension of the basic QI protocol is not straightforward, mainly due to the idler storage and the phase dependent correlations between the pairwise return and idler states. These hurdles are persisting for all varieties of the QI scheme, for pairwise detection schemes, as well as for global joint measurements [188].

The authors of Ref. [189] discuss quantum target ranging in a continuous-time setting and compare the associated performance to that of a classical radar scheme employing pulse compression. In order to implement the ranging functionality, both considered schemes are based on time-of-flight measurements [64]. The quantum radar approach yields an SNR threshold which is 6 dB better than that of the classical scheme. Here, the SNR threshold is defined as the crossover below which the range-delay accuracy is inferior to the associated Cramer-Rao bound limit [64]. Operation of the quantum radar scheme at its SNR threshold results in a mean-squared range-delay accuracy that can be tens of dB higher than the classical one with the same pulse bandwidth and an identical number of transmitted photons [64, 189]. The proposed protocol faces two main challenges in terms of implementation: first, a long pulse duration and integration time is needed, which is a major drawback for moving targets and in terms of idler storage. Second, a suitable receiver design has yet to be identified and developed, making the whole concept of a quantum-enabled range-delay accuracy advantage difficult to implement [189].

The deduction of an object's velocity based on the Doppler effect in the framework of QI is discussed in Ref. [190]. The quantum resource states yield a improved precision in the estimation of the velocity of an object, where a QA greater than 3 dB in the variance of the estimator is observed if the path transmissivity is larger or equal to 50 % [190]. Here, the authors propose frequency-resolved photon counting as an optimal measurement for the idealized scenario of no losses [190], which is difficult from an experimental point of view. Note that, in this scope, there is a lower limit for the precision of simultaneous estimation of both velocity and range, as imposed by Heisenberg's uncertainty principle [64, 112, 154, 191].

In Ref. [192], the authors propose an entanglement-based protocol for the localization of a point-like target in three-dimensional space. The corresponding scheme relies on N entangled photons that are all employed to interrogate a region of interest, while no idler photons are considered. On the receiving side, the individual positions of impact in combination with the respective arrival times allow for deduction of the position of the target by means of electromagnetic scattering relations [49, 192]. For an N-partite

entangled system, such an approach yields a $\sqrt{N}$ precision enhancement for locating the target [192]. However, from an experimental point of view it is highly challenging to generate such maximally entangled states with $N \gg 1$ for considerable precision enhancements. Moreover, this protocol is very susceptible to photon loss, i.e., already loosing one single mode of the N-mode ensemble results in a complete loss of information for the remaining $N-1$ modes [49]. The detector requirements are also demanding, since the proposed $\sqrt{N}$ precision enhancement is based on an infinite detector size and an infinite integration time [49]. These two requirements are a result of the assumed random times of arrival of each of the N modes, combined with a full randomness of their spatial point of impact on a planar receiver [192].

3.9 Discussion and summary

The general scope of quantum illumination can be expanded from two-mode entangled resource states to multimode (> 2) entanglement for a potentially improved sensitivity. The case of three entangled modes in the framework of Gaussian QI is discussed for both possible approaches: two modes are employed as a probing signal, while one idler mode is retained [193]; and a single signal mode in combination with two idler modes [194]. The expansion towards a higher number of entangled modes leads to an increased robustness of the protocol with respect to tolerable noise and losses [49]. For the single-mode probing case, the authors observe an improved error exponent of the three-mode protocol with respect to the typical two-mode Gaussian QI up to $N_\mathrm{S} = 0.295$ signal photons per mode [194]. The experimental exploration of two-mode QI is still at the proof-of-principle level, which renders an added complexity, such as three-mode entanglement and associated detector layouts, difficult to implement as of today. Interestingly, Ref. [43] widens the scope of the three-mode approach to non-Gaussian states. It is important to note that typically, Gaussian states are convenient to work with, both in theory and in experiment [6]. However, the community actively explores ways to boost the performance of the basic two-mode QI by exploiting non-Gaussian states, e.g., by means of photon addition or photon subtraction with the probe signals [49, 195, 196].

In the framework of QI, one typical assumption is the large number of employed modes, $M \gg 1$, which can lead to issues with the overall detection time. For a carrier frequency of $5\,\mathrm{GHz}$, which matches with conventional operating frequencies of state-of-the-art superconducting circuits [cf. Ch. 4 and Ch. 6], typical JPA bandwidths are on the order of $10\,\mathrm{MHz}$. For this bandwidth, the resulting time length per mode is $100\,\mathrm{ns}$. In our studies, we mainly focus on $10^6 \leq M \leq 10^8$, which coincides with previous studies [48, 145] and yields representative results especially for moderate background noise levels around $N_\mathrm{B} = 20$. In order to acquire such high M, typical integration times correspond to $0.1\,\mathrm{s}$ ($M = 10^6$) and $10\,\mathrm{s}$ ($M = 10^8$). For an increasingly bright thermal background ($N_\mathrm{B} = 1000$), we observe that an enhanced number of transmitted modes is necessary

to enter the asymptotic regime, which leads to even longer integration times. These associated time scales are clearly too slow for detecting moving targets [49].

In conclusion, QI and quantum radar are expected to have significant impact on radar applications [64]. Over the last two decades, the fascination behind QI has generated a great progress in theoretical studies and experimental efforts [47, 48, 55, 145]. The first successful experiments towards a QI implementation were conducted in the optics domain in 2013 by Lopaeva *et al.* [51]. This experiment, however, lacks an optimal classical reference setup and does not implement a joint measurement, leading to a complete loss of any QA. The first genuine experimental realization of a QI-based quantum radar scheme was carried out at optical frequencies in 2015 by Zhang *et al.* [59]. This implementation relies on the initial QI protocol [48] combined with the PC receiver [54, 145]. In this work, Zhang *et al.* demonstrate a QA of 0.8 dB. Various different researchers have tried to close the gap to the microwave domain, but the corresponding experiments often lack some basic requirements that are crucial for a genuine QA [60, 61, 63, 197]. For details, we refer the reader to Ref. [56]. The first, and so far the only, realization of a quantum microwave radar experiment with a finite QA was conducted by Assouly *et al.* [55] in 2023. In their approach, the signal mode of a TMSV state propagates along a delay line that is connected to a tunable notch filter, which allows for switching between the two hypotheses. The required bright thermal background is artificially generated and coupled to the return mode. The idler is stored in a long-lived mode for the round-trip time of the signal. The detector scheme is based on the PC scheme to parametrically mix the return and idler modes, followed by individual detection with PC1 (according to our convention). The demonstrated QA is 0.8 dB, on par with the experiments at optical frequencies. Note that in Ref. [55], the classical reference is evaluated only theoretically, not implemented in experiment.

In this chapter, we have thoroughly discussed the manifold facets of quantum illumination in terms of general concepts, concrete implementations, and the robustness against realistic experimental imperfections. In this context, we have focused on the performance of single-photon counters, which represent one of the central elements of QI protocols. With a focus on the PM scheme, we have compared individual single-photon detection to correlated difference detection, and have found that the latter performs slightly better for different noise regimes. We have analyzed the role of respective weighting of the individual detector outcomes and identified the adjusted ratio for the optimal QI performance [cf. Eq.(3.47)]. While large $N_B \simeq 1000$ theoretically gives access to a larger QA and matches realistic noise values at gigahertz frequencies, the detection unit needs to be able to handle corresponding return signal powers. Respectively, the mixer needs to operate at input signal powers on the order of $N_B \cdot \hbar\omega$ without suffering from compression effects; the same applies to PC2 [cf. Eq. (3.37)]. We find that the respective expectation values of the two photon number operators are highly asymmetric. This is due to the fact that the photon number expectation value at PC1 is governed by the number of

signal photons per mode, $N_S \ll 1$, while the average photon number at PC2 is dictated by the number of thermal background photons, $N_B \gg 1$. As a consequence, currently available PCs with a photon number resolution of up to three photons yield a clearly deteriorated performance of PC2 already for small $N_B \simeq 10$, such that CPC does not seem to be suitable for near-term implementations. In contrast, individual detection with PC1 and limited photon number resolution, $K \leq 3$, reaches a reasonable QA even for large $N_B \simeq 1000$. As we have noted, the maximum achievable QA with PM-type receivers increases with increasing N_B and saturates at $3\,\mathrm{dB}$ for large N_B, which imposes further restrictions on low-N_B implementations [55]. Therefore, individual detection with PC1 for large N_B may be the simplest route towards the practical $3\,\mathrm{dB}$ QA with the currently available technology. Finally, our presented results provide valuable insights also to neighboring research fields, such as quantum communication [90, 198, 199].

While the fundamental task of transmitting quantum signals at microwave frequencies over free-space channels remains to be an ongoing challenge, careful analysis of suitable operation scenarios represents a very important step towards experimental realization. There exist various further hurdles to overcome in order to push this technology towards field applications. More specifically, QI proves to be inherently fragile against a variety of unwanted effects, such as finite purities of the resource states, finite detection efficiencies, and persisting dark-count probabilities during detection [54]. Challenges with respect to ranging and long integration times pose further limitations which remain to be solved. Accordingly, long-range QI applications seem out of reach with the currently available technology, while short-range scenarios without a need for ranging capabilities represent promising candidates for initial QI use cases [49]. Especially, the detection of objects with a low speed or fixed in space could benefit from the discussed QI schemes. As such, applications like an airport body scanner searching for the presence or absence of metallic objects, or low-energy medical use cases show a great potential. Finally, it is important to keep in mind that research on QI and quantum radar is evolving fast, and new developments can drastically change the currently known limits.

Chapter 4

Superconducting quantum technology

In physics, phase transitions are usually characterized by the appearance of a new kind of order (described by an order parameter in the Ginzburg-Landau theory of phase transitions) on varying some control parameter such as temperature, pressure or magnetic field and the breaking of a particular symmetry. Numerous discoveries of the properties of matter trace back to studies executed under extreme conditions. Superconductivity is a prominent example in this context. The achievement of helium liquefaction in 1908 expanded the experimentally available temperature range close to absolute zero [200]. During this period, experimentalists had investigated the electrical conductivity of metals at varying temperatures and had observed a linear decrease in resistance as a function of decreasing temperature [201]. At this time, researchers speculated on three different concepts of the resistance evolution towards zero temperature [200]:

(i) A finite resistance persists.

(ii) The resistance converges towards zero.

(iii) At a certain temperature, the resistance shows a minimum and increases thereafter, diverging towards infinity.

Figure 4.1(a) conceptually shows the corresponding resistance curves as a function of temperature. Due to the intuition that the thermal motion of electrons may be frozen out at sufficiently low temperatures, the third concept was the most common at that time [200]. However, experiments with gold and platinum suggested that a small residual resistance at low temperatures was connected to purity imperfections in the studied materials [203]. This suspicion led to the investigation of mercury, which was available with very high purity and, therefore, should show a vanishingly small resistance at low temperatures. While the resistance below $4.2\,\text{K}$ indeed became too small to measure, the observed resistance change was not continuous, but showed a sudden drop, as illustrated in Fig. 4.1(b). Kammerlingh-Onnes described his observation as *"Mercury had passed into a new state, which on account of its extraordinary electrical properties may be called the superconductive state"* [204]. Today, we know a plethora of superconducting elements and compounds. The superconducting compounds encompass the high-temperature superconductors based on copper oxides, e.g., $YBa_2Cu_3O_7$ ("YBCO") and $Bi_2Sr_2CaCu_2O_8$
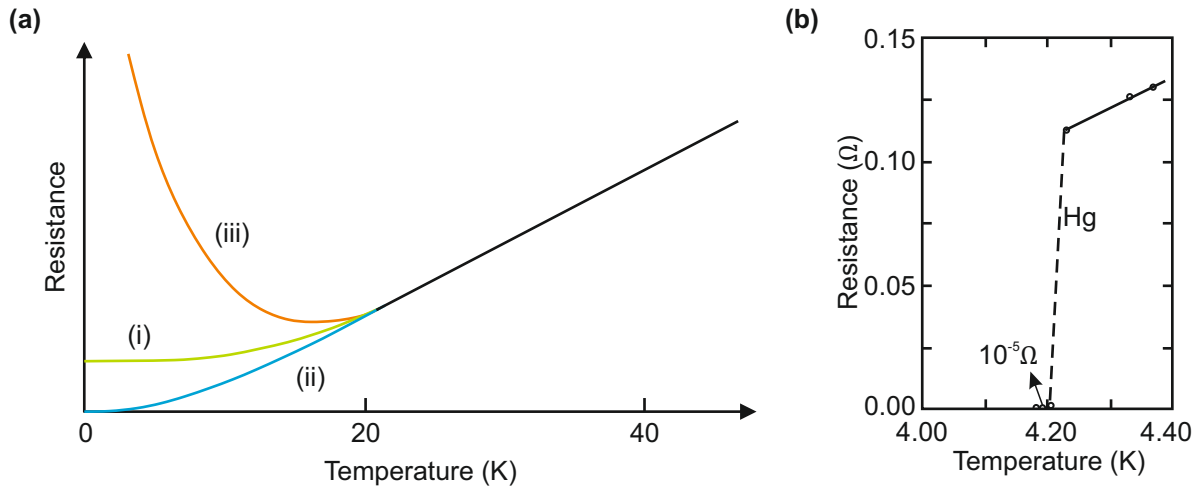
Figure 4.1: (a) Illustration of the historically expected resistance evolution in metals towards low temperatures (adapted from Ref. [200]). The three different concepts are discussed in the main text. (b) Discovery of the superconductivity by the sudden resistance drop of mercury at liquid helium temperatures (adapted from Ref. [202]).

("BsCCO"). In the following, we introduce some basics of superconductivity and discuss the related Josephson effects, which are important building blocks for various quantum devices, such as superconducting qubits and Josephson parametric amplifiers (JPAs). These JPAs represent a fundamental component of the experimental results presented in Ch. 6.

4.1 Superconductivity

The fascinating characteristics of superconductors encompass the phenomena of ideal diamagnetism, vanishing electrical resistance, and quantization of magnetic flux [200]. Importantly, the vanishing resistance is a necessary, but not a sufficient requirement for ideal diamagnetism, which has been discovered only in 1933 by Walther Meißner and Robert Ochsenfeld and therefore is known as the the Meißner-Ochsenfeld effect today. Accordingly, we extend the focus to fundamental magnetic considerations, which can be understood by treating the superconducting state as a macroscopic coherent quantum state [200]. In 1933, Meißner and Ochsenfeld observed that superconductors expel an applied flux density from the interior, except for a thin surface layer, even if they are cooled down a constant applied flux density [205]. This observation clearly showed that the superconducting state is a true thermodynamic phase with its properties depending only on the coordinates within the phase diagram but not the path used to arrive at these coordinates. This is visualized in Fig. 4.2: Fig. 4.2(a) shows a normal conductor (NC) that we first cool down ($T \downarrow$) to form a perfect conductor (PC). Subsequently we switch on an external magnetic field ($B_{\text{ext}} \uparrow$). Then, we switch the order of these

Figure 4.2: Evolution of a (a) perfect conductor (PC) and (b) superconductor (SC) for a two-step sequence consisting of cooling ($T \downarrow$) and then applying an external magnetic field ($B_{\text{ext}} \uparrow$), o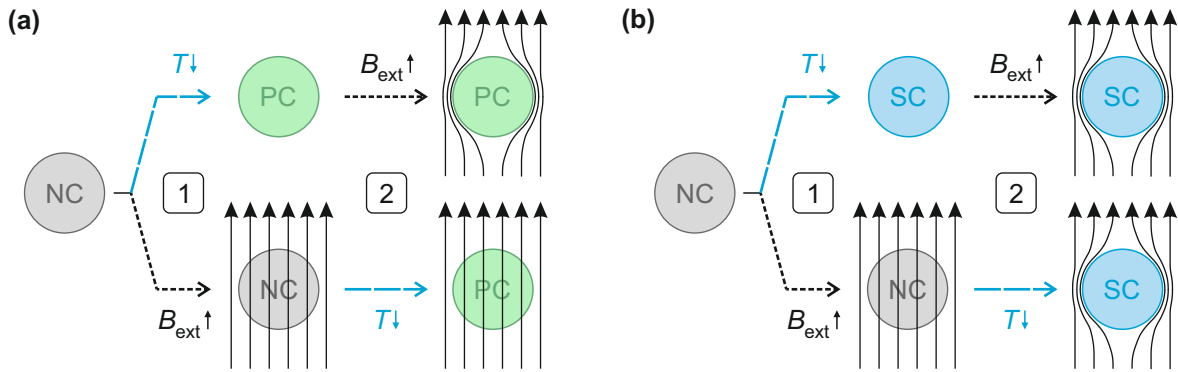r, alternatively, reversing the order of these steps. These two sequences are illustrated at the top and bottom of the two panels, respectively. We observe path-dependent final states for the perfect conductor in (a), while the superconductor exhibits a path-independent final state. Both, PC and SC, start in the normal-conducting (NC) state (adapted from Ref. [201]).

operations, i.e., first apply an external magnetic field and then cool down the material. We observe that the resulting final state depends on the path we choose. The perfect conductor only expels the external flux in the case where we first cool down the system, which can be straightforwardly explained by classical electromagnetism [201]. Ohm's law $\boldsymbol{J} = \sigma \boldsymbol{E}$ shows that for a given current density, perfect conductivity results in a vanishing electric field inside the conductor. Consequently, the magnetic flux density shows no time dependence, $\partial \boldsymbol{B} / \partial t = 0$, according to the Maxwell-Faraday equation, $-\partial \boldsymbol{B} / \partial t = \nabla \times \boldsymbol{E}$, with $\boldsymbol{E} = 0$ [201].

Application of the magnetic field in the normal-conducting state leads to eddy currents because of induction [200]. However, these currents disappear exponentially fast with time after the flux density reaches its steady state, so that the flux density inside and outside the normal conductor become homogeneous. The flux distribution remains constant when cooling this normal conductor to the perfectly conducting state, due to $\partial \boldsymbol{B} / \partial t = 0$ [200]. This flux density inside the perfect conductor remains preserved if the external magnetic field is switched off. In summary, we observe a path-dependent final state of a perfect conductor for the same position in the magnetic flux-temperature phase diagram.

In the same scenario, a superconductor shows strikingly different characteristics, as illustrated in Fig. 4.2(b). Starting again from the normal-conducting state, we observe an expulsion of the magnetic flux from the interior of the superconductor, independent of the temporal order with respect to cooling and application of the external magnetic field. Here, a similar argument as for the perfect conductor applies to the path consisting of first cooling the system down and, then, applying the magnetic field. Importantly, the superconductor also expels magnetic flux in the reversed scenario, when first the magnetic field is switched on and then the system is cooled down at constant magnetic flux. This

evolution represents a decisive difference compared to the behavior of a perfect conductor. Note that these observations only hold for magnetic field values up to a critical value known as the critical field. As a result, we observe a path-independent final state of the superconductor, which corresponds to the behavior of a true thermodynamic phase [201].

Flux quantization was first observed in 1961 nearly at the same time by two independent research groups, Doll and Näbauer [206] from the Walther-Meißner-Institut in Munich and Deaver and Fairbank [207] from Stanford University. Their studies were based on the measurement of the magnetic flux trapped within superconducting hollow cylinders. They demonstrated that the magnetic flux trapped in the cylinders at a continuously varied cooling field solely occurs in integer multiples of the flux quantum, $\Phi_0 = h/(2e)$. In order to trap only a few flux quanta by a magnetic cooling field $B_{\rm f}$ on the order of the Earth's magnetic field, $B_{\rm earth} \simeq 2.5 \times 10^{-5}$ T (at its surface), the cross-sectional area of the cylinder $\pi r^2 \simeq \Phi_0/B_{\rm f}$, and consequently a very small cylinder radius on the order of $r \simeq 10\,\mu{\rm m}$ has to be chosen. Note that for $r \simeq 1\,{\rm cm}$ millions of flux quanta are trapped by $B_{\rm f} \simeq B_{\rm earth}$, such that a very high resolution is required to measured changes of a single flux quantum on the huge background.

Doll and Näbauer used superconducting lead cylinders to study trapping of magnetic flux. For details on these experiments, we refer the reader to Refs. [200, 201, 206, 207]. For many decades, the phenomenon superconductivity was described by phenomenological models due to the absence of a microscopic theory [201]. The London brothers proposed a first phenomenological model that could explain the perfect conductivity and ideal diamagnetism of superconductors by introducing the two London equations [208]. Later on, they showed that the London equations can be derived in a straightforward way from the current-phase and energy-phase relations obtained by assuming that the entirety of superconducting charge carrier can be described by a macroscopic wave function with amplitude and phase, $\psi(\boldsymbol{r}, t) = \psi_0 \exp(\mathrm{i}\theta(\boldsymbol{r}, t))$, with the absolute square of the wave function given by the density $n_{\rm s} = |\psi_0|^2$ of the superconducting charge carriers. A drawback of the macroscopic quantum model was the fact that it could not describe situations with a spatially varying density of the superconducting charge carriers. This problem was solved by the Ginzburg-Landau (GL) theory. Within the GL theory [209] the transition into the superconducting state is described in terms of the Landau theory of phase transitions by introducing a complex, spatially varying order parameter $\Psi(\boldsymbol{r})$. Key achievements of GL-theory have been the description of the spatially inhomogeneous flux distribution in the mixed state of type-II superconductors and the prediction of the coherence length. The latter describes the minimum length scale over which spatial variations of the order parameter can occur. Finally, Bardeen, Cooper and Schrieffer [210, 211] provided the first microscopic theory of superconductivity in 1957, explaining the transition into the superconducting state by an instability of the Fermi sea of electrons in a metal due to an attractive electron-electron interaction mediated by phonons. The attractive electron-electron interaction leads to the formation of Cooper pairs, which form a coherent,
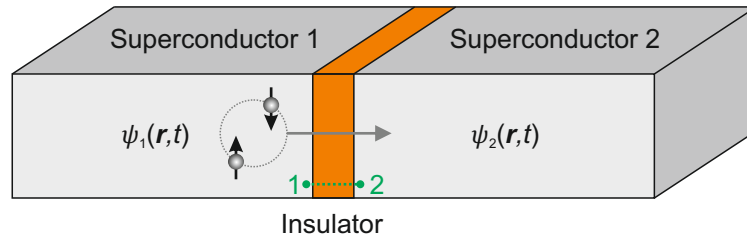
Figure 4.3: Schematic illustration of a Josephson junction. The two superconductors characterized by the respective macroscopic wave functions ψ_k ($k = 1, 2$) are coupled through a tunnel barrier, depicted in orange.

macroscopic many-body state [211]. This macroscopic quantum state can be described by a macroscopic wave function, $\psi(\boldsymbol{r}, t) = \sqrt{n_{\mathrm{s}}(\boldsymbol{r}, t)} \exp(\mathrm{i}\theta(\boldsymbol{r}, t))$, where $n_{\mathrm{s}}(\boldsymbol{r}, t)$ denotes the density of superconducting electrons and $\theta(\boldsymbol{r}, t)$ corresponds to the global phase of the many-body state. For details on the theory of superconductivity, we refer the reader to Refs. [200, 201, 208–211].

4.2 Josephson junctions

A Josephson junction is obtained by weakly coupling two superconductors, where the weak coupling is usually realized by placing a thin layer of a non-superconducting material, such as an insulator, between two layers of bulk superconducting material, schematically illustrated in Fig. 4.3. Each of the two superconductors is characterized by its macroscopic wave function $\psi_k(\boldsymbol{r}, t) = \sqrt{n_{\mathrm{s},k}(\boldsymbol{r}, t)} \exp(\mathrm{i}\theta_k(\boldsymbol{r}, t))$, where $k = 1, 2$ corresponds to superconductor 1 and 2. The two wave functions can have a finite spatial overlap if the layer of the non-superconducting material is thin enough. In the most general case, the phases θ_1 and θ_2 are not equal, leading to a phase difference across the Josephson junction. In the presence of a finite flux density threading the barrier region, the gauge-invariant phase difference can be expressed as [201]

$$\varphi(\boldsymbol{r}, t) = \theta_2(\boldsymbol{r}, t) - \theta_1(\boldsymbol{r}, t) - \frac{2\pi}{\Phi_0} \int_1^2 \boldsymbol{A}(\boldsymbol{r}, t) d\boldsymbol{l}, \tag{4.1}$$

with the path integration oriented from superconductor 1 across the barrier to superconductor 2 (illustrated in green in Fig. 4.3), and the vector potential $\boldsymbol{A}(\boldsymbol{r}, t)$. Josephson showed that the finite coupling of the two superconductors yields a finite supercurrent I_{s} flowing without any voltage drop across the insulator, which is given by

$$I_{\mathrm{s}} = I_{\mathrm{c}} \sin \varphi. \tag{4.2}$$

Here, I_{c} denotes the maximum Josephson current, or critical current, which is determined by the coupling strength of the two superconductors, and φ is the phase difference given by

Eq. (4.1). This current-phase relation is referred to as the first Josephson equation [201]. For the case of a non-vanishing voltage across the Josephson junction, the time derivative of the phase difference, $\varphi(t)$, is given by

$$\frac{\partial \varphi}{\partial t} = \frac{2\pi}{\Phi_0} U(t). \tag{4.3}$$

This voltage-phase relation is also known as the second Josephson equation. If a constant voltage is applied across the junction, the gauge-invariant phase difference evolves linearly with time. This results in an alternating current with Josephson frequency

$$f_{\mathrm{J}} = \frac{U}{\Phi_0} = \frac{2eU}{h}, \tag{4.4}$$

which corresponds to a ratio of approximately $484\,\mathrm{GHz}$ per mV of applied voltage [200]. Interestingly, Eq. (4.4) relates frequency and voltage to each other by using only the fundamental constants h and e, which allows for building robust voltage standards based on Josephson junctions [200]. In the framework of superconducting quantum computing, the nonlinear, lossless inductance of Josephson junctions introduces the anharmonicity to various superconducting circuits, allowing one to build quantum bits (qubits). The corresponding nonlinear Josephson junction inductance is given by

$$L_{\mathrm{J}}(\varphi) = \frac{U}{\dot{I}(\varphi)} = \frac{\Phi_0}{2\pi I_{\mathrm{c}} \cos\varphi} = \frac{L_{\mathrm{c}}}{\cos\varphi}, \tag{4.5}$$

where the Josephson inductance L_{c} represents the minimum inductance of the junction [201]. In the energy picture, the finite wave function overlap results in a Josephson coupling energy [201]

$$E_{\mathrm{J}}(\varphi) = \frac{1}{2\pi}\Phi_0 I_{\mathrm{c}}(1 - \cos\varphi) = E_{\mathrm{J},0}(1 - \cos\varphi), \tag{4.6}$$

where $E_{\mathrm{J},0} = \Phi_0 I_{\mathrm{c}}/(2\pi)$. An externally applied bias current I through the junction yields a tilted washboard potential with the potential energy of the system given by

$$E_{\mathrm{pot}}(\varphi) = E_{\mathrm{J}}(\varphi) - \left(\frac{\Phi_0\,\varphi}{2\pi}\right) I = E_{\mathrm{J},0}\left(1 - \cos\varphi - \frac{I\,\varphi}{I_{\mathrm{c}}}\right). \tag{4.7}$$

In this framework, the phase difference φ can be considered as a classical particle moving in this potential. Accordingly, the zero voltage state corresponds to the particle resting in one of the local potential minima. This state is accessible only for $|I| < I_{\mathrm{c}}$. The voltage state of the junction can be viewed as the particle moving down the tilted washboard potential, as for $|I| > I_{\mathrm{c}}$ there is no longer a local potential minimum [108].

The maximum value of the Josephson supercurrent can be varied by applying an
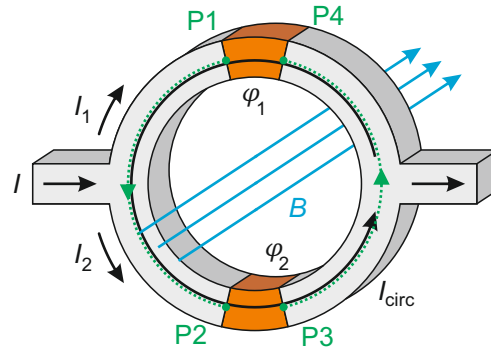
Figure 4.4: Schematic of a dc-SQUID biased by an external current I getting split into two paths, I_1 and I_2. Each path hosts one Josephson junction, shown in orange, characterized by the respective critical currents $I_{c,1}$ and $I_{c,1}$, and phase differences φ_1 and φ_2.

external magnetic field parallel to the barrier layer, resulting in the well-known Fraunhofer pattern $I_s(B_{ext})$ [201]. The magnetic field sensitivity can be drastically enhanced by employing superconducting loops, or hollow cylinders, which contain one or more Josephson junctions. The term superconducting quantum interference device (SQUID) encompasses all such kinds of systems containing superconducting loops intercepted by one or more Josephson junctions [201]. As of today, SQUIDs are used in a variety of applications and represent the most sensitive detectors for magnetic flux and all quantities that can be transformed into magnetic flux by suitable antenna structures. In most applications, SQUIDs are operated as flux-to-voltage converters, converting tiny flux changes at the input into large voltage changes at the output [201].

A superconducting loop hosting a single Josephson junction, which is driven by a time-dependent external flux, is called an rf-SQUID [201, 212, 213]. A parallel connection of two Josephson junctions in a superconducting loop is known as a dc-SQUID [201, 214–216]. The dc-SQUID, discussed in the next section, is a central component of the Josephson parametric amplifier, which we introduce in Sec. 4.4.

4.3 Dc-SQUIDs

Figure 4.4 illustrates the general layout of a dc-SQUID. We consider the case of equal critical currents $I_{c,1} = I_{c,2} = I_c$ for the two Josephson junctions, described by their respective current-phase relations $I_{s,k} = I_c \cos \varphi_k$, with $k = 1, 2$. The total supercurrent I_s through the dc-SQUID can be evaluated using Kirchhoff's law according to

$$I_s = I_{s,1} + I_{s,2} = 2\,I_c \cos\left(\frac{\varphi_1 - \varphi_2}{2}\right) \sin\left(\frac{\varphi_1 + \varphi_2}{2}\right) = 2\,I_c \cos\varphi_- \sin\varphi_+, \quad (4.8)$$

where the quantities $\varphi_- = (\varphi_2 - \varphi_1)/2$ and $\varphi_+ = (\varphi_1 + \varphi_1)/2$ correspond to new relative phase differences. The circulating current in the dc-SQUID loop, I_{circ}, is given by

$$I_{\mathrm{circ}} = \frac{I_{\mathrm{s,1}} - I_{\mathrm{s,2}}}{2} = I_{\mathrm{c}} \cos\left(\frac{\varphi_1 + \varphi_2}{2}\right) \sin\left(\frac{\varphi_1 - \varphi_2}{2}\right) = -I_{\mathrm{c}} \cos\varphi_+ \sin\varphi_- . \tag{4.9}$$

Since the overall phase change $\Delta\theta$ along the closed loop of the dc-SQUID needs to fulfill $\Delta\theta = n\,\pi$ with $n \in \mathbb{N}_0$, the gauge invariant phase differences φ_1 and φ_2 are not independent of each other [201]. The resulting relation between φ_1 and φ_2 is given by

$$\varphi_1 - \varphi_2 = -\frac{2\pi}{\Phi_0}\left(\oint_C \boldsymbol{A}dl + \int_{P1}^{P2} \Lambda \boldsymbol{J}_{\mathrm{s}} dl + \int_{P3}^{P4} \Lambda \boldsymbol{J}_{\mathrm{s}} dl\right), \tag{4.10}$$

where Λ is the London parameter, $\boldsymbol{J}_{\mathrm{s}}$ corresponds to the supercurrent density, and $\boldsymbol{A}$ is the vector potential. The corresponding integration path is highlighted in green in Fig. 4.4. Equation (4.10) is evaluated by using Eq. (4.1) in combination with the expression for the gauge-invariant phase gradient [200]

$$\boldsymbol{\nabla}\theta = \frac{2\pi}{\Phi_0}(\Lambda\,\boldsymbol{J}_{\mathrm{s}} + \boldsymbol{A}). \tag{4.11}$$

The integral over the closed contour C in Eq. (4.10) yields the total flux Φ. For the remaining two integrals over $\boldsymbol{J}_{\mathrm{s}}$, we choose an integration path deep inside the superconducting leads, where $\boldsymbol{J}_{\mathrm{s}} = 0$ and, thus, the corresponding integrals vanish [201]. This assumption is only valid for a superconductor with lateral dimensions much larger than the London penetration depth [201]. Note that the integration paths P_1 to P_2, and P_3 to P_4 in Eq. (4.10) cover the entire superconducting loop except for the two barriers. We obtain the relation

$$\varphi_2 - \varphi_1 = 2\pi\frac{\Phi}{\Phi_0}, \tag{4.12}$$

which we can insert into Eq. (4.8) to obtain

$$I_{\mathrm{s}} = 2\,I_{\mathrm{c}} \cos\left(\pi\frac{\Phi}{\Phi_0}\right) \sin\left(\varphi_1 + \pi\frac{\Phi}{\Phi_0}\right). \tag{4.13}$$

The total flux through the dc-SQUID is given by the sum of the external flux, Φ_{ext}, and the current-induced loop flux, $\Phi_{\mathrm{L}} = L_{\mathrm{L}}\,I_{\mathrm{circ}}$, according to $\Phi = \Phi_{\mathrm{ext}} + \Phi_{\mathrm{L}}$, where L_{L} is the self-inductance of the SQUID loop. The associated screening parameter of the loop is defined as

$$\beta_{\mathrm{L}} = \frac{L_{\mathrm{L}}\,I_{\mathrm{c}}}{\Phi_0/2}, \tag{4.14}$$
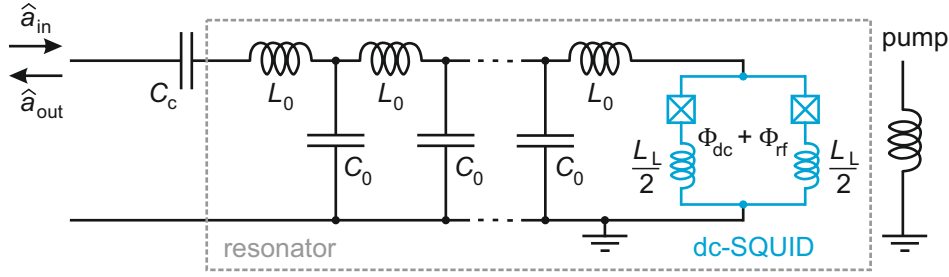
Figure 4.5: JPA circuit diagram. The central element is a quarter-wavelength resonator with characteristic inductance L_0 and capacitance C_0. Incoming modes $\hat{a}_{\text{in}}$ couple to the resonator via the coupling capacitance C_c.

and relates the induced flux, $L_L I_c$, to half a flux quantum, $\Phi_0/2$. Accordingly, the total loop flux, normalized to a flux quantum, can be expressed as

$$\frac{\Phi}{\Phi_0} = \frac{\Phi_{\text{ext}}}{\Phi_0} - \frac{\beta_L \cos\varphi_+ \sin\varphi_-}{2}. \tag{4.15}$$

For small loop inductances, we can approximate $\Phi \simeq \Phi_{\text{ext}}$ and write the maximal dc-SQUID supercurrent as [214]

$$I_s^{\text{max}} = 2I_c \left| \cos\left(\pi \frac{\Phi_{\text{ext}}}{\Phi_0} \right) \right|. \tag{4.16}$$

We see that for a small loop inductance the dc-SQUID can be viewed as a single Josephson junction with flux-tunable critical current and flux-tunable inductance [217]

$$L_{\text{SQ}}(\Phi_{\text{ext}}) = \frac{\Phi_0}{2\pi I_s^{\text{max}}} = \frac{\Phi_0}{4\pi I_c \left| \cos\left(\pi \frac{\Phi_{\text{ext}}}{\Phi_0} \right) \right|}. \tag{4.17}$$

This underlines the versatility of the device that can serve as a non-linear, flux-tunable lossless inductance in superconducting quantum circuits [108].

4.4 Josephson parametric amplifiers

In this section, we discuss the Josephson parameter amplifier (JPA) that constitutes an important building block for the experimental results presented in Ch. 6. The JPA consists of a quarter-wavelength coplanar waveguide (CPW) resonator in combination with a dc-SQUID, which connects the CPW to the ground plane. As the dc-SQUID can be viewed as a flux-tunable nonlinear inductance, a nonlinear, flux-tunable LC-resonator with potentially high quality factor is obtained. In the following, we first introduce the most important basics on CPWs, followed by a brief analysis of the flux-dependent JPA resonance frequency. Finally, we address parametric amplification with flux-driven JPAs

and discuss the standard quantum limit.

Coplanar waveguide resonators   Planar transmission lines encompass a broad range of implementations, such as striplines, microstrip lines, slotlines, and coplanar waveguides (CPWs). These types of transmission lines are compact and, importantly, compatible for integration with active circuit devices, forming microwave integrated circuits [95]. The telegrapher's equations are typically employed for describing the wave propagation through such linear transmission lines [95]. In general, CPWs form effective one-dimensional transmission lines, which do not impose any spectral restrictions on a propagating signal. In this work, we focus on superconducting CPWs which, in the ideal case, can be modeled as a lossless transmission line with characteristic impedance

$$Z = \sqrt{\frac{L_0}{C_0}}, \tag{4.18}$$

where L_0 and C_0 are the characteristic inductance and capacitance per unit length, respectively [95]. In a next step, we impose boundary conditions in the form of a coupling capacitance at one end of the CPW, combined with a short to ground at the other CPW end. The coupling capacitance C_c acts an effective line break and introduces a voltage antinode and current node. Correspondingly, the short to ground is reflected in a voltage node and current antinode. This combination of boundary conditions is used for creating quarter-wavelength resonators [95]. The resulting fundamental angular resonance frequency depends on the CPW length l according to [218]

$$\omega_0 = \frac{2\pi c}{\sqrt{\varepsilon_{\text{eff}}}} \frac{1}{4l} = \frac{1}{4l \sqrt{L_0 C_0}}, \tag{4.19}$$

where c denotes the velocity of light, $\varepsilon_{\text{eff}} = c^2/v_{\text{ph}}^2$ is the CPW permittivity, and $v_{\text{ph}} = 1/\sqrt{L_0 C_0}$ is the phase velocity. The loaded resonator quality factor, Q_l, provides information on the associated loss rates and is considered as the central figure of merit for resonators

$$Q_l = 2\pi \frac{\text{average energy stored}}{\text{energy loss/cycle}} = \frac{\omega_0}{\kappa_{\text{tot}}}, \tag{4.20}$$

with the total loss rate as the sum of the internal loss rate, κ_{int}, and the external loss rate, κ_{ext}, according to $\kappa_{\text{tot}} = \kappa_{\text{int}} + \kappa_{\text{ext}}$. The internal loss rate stems from typically unwanted loss channels, such as two-level fluctuators, surface resistance, or quasiparticles [219, 220]. The external loss rate is determined by the coupling capacitance and can be regarded as an adaptive design parameter. Accordingly, we can relate Q_l to the internal quality factor, $Q_{\text{int}} = \omega_0/\kappa_{\text{int}}$, and the external quality factor, $Q_{\text{ext}} = \omega_0/\kappa_{\text{ext}}$, via

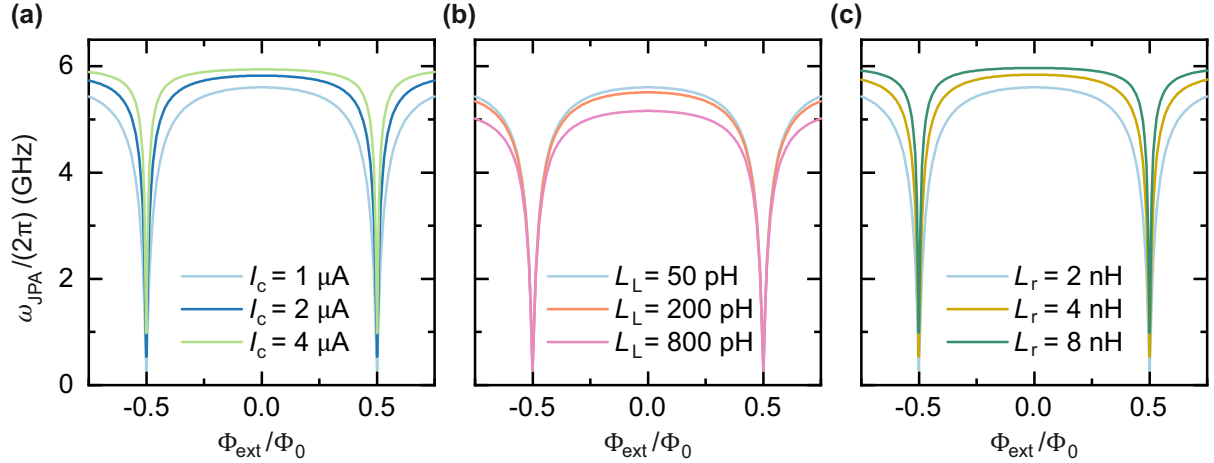$$Q_l^{-1} = Q_{\text{int}}^{-1} + Q_{\text{ext}}^{-1}. \tag{4.21}$$

Figure 4.6: Theoretical resonance frequency ω_{JPA} as a function of the externally applied magnetic flux Φ_{ext} for (a) different critical currents I_{c}, an overall resonator inductance $L_{\mathrm{r}} = 2\,\mathrm{nH}$ and loop inductance $L_{\mathrm{L}} = 50\,\mathrm{pH}$, according to Eq. (4.25). Panel (b) shows the corresponding results for various L_{L}, a fixed value of $I_{\mathrm{c}} = 1\,\mathrm{\mu A}$ and $L_{\mathrm{r}} = 2\,\mathrm{nH}$. In panel (c), we display ω_{JPA} for various values of L_{r} and a fixed $I_{\mathrm{c}} = 1\,\mathrm{\mu A}$, $L_{\mathrm{L}} = 50\,\mathrm{pH}$. Accordingly, the light blue line is identical for all three panels and serves as a reference. The bare resonator frequency is set to $\omega_0/(2\pi) = 6.1\,\mathrm{GHz}$ for all panels.

In experiments, we typically measure these resonators in reflection and can deduce the quality factors from the complex reflection coefficient [221]

$$\Gamma = \frac{(\omega - \omega_0)^2 + \mathrm{i}\kappa_{\mathrm{int}}(\omega - \omega_0) + (\kappa_{\mathrm{ext}}^2 - \kappa_{\mathrm{int}}^2)/4}{[(\omega - \omega_0) + \mathrm{i}(\kappa_{\mathrm{ext}} + \kappa_{\mathrm{int}})/2]^2}, \tag{4.22}$$

from which we can extract the power spectrum [222]

$$|S_{11}(\Delta)|^2 = 1 - \frac{4\,\kappa_{\mathrm{int}}\,\kappa_{\mathrm{ext}}}{\kappa_{\mathrm{tot}}^2 + (2\Delta)^2}, \tag{4.23}$$

where $\Delta = \omega - \omega_0$. The frequency-dependent JPA phase response can be written as

$$\varphi(\Delta) = \mathrm{atan2}\left(\frac{\kappa_{\mathrm{int}}^2 - \kappa_{\mathrm{ext}}^2 + (2\Delta)^2}{(\kappa_{\mathrm{int}} + \kappa_{\mathrm{ext}})^2 + (2\Delta)^2}, \frac{-4\kappa_{\mathrm{ext}}\Delta}{(\kappa_{\mathrm{ext}} - \kappa_{\mathrm{int}})^2 + (2\Delta)^2}\right), \tag{4.24}$$

where atan2 is the 2-argument arctangent function [222, 223]. Note that in experiment, one observes a clear difference between overcoupled ($Q_{\mathrm{ext}} < Q_{\mathrm{int}}$) and undercoupled ($Q_{\mathrm{ext}} > Q_{\mathrm{int}}$) resonators with respect to $\varphi(\Delta)$. Importantly, the phase response shows a phase shift at resonance of approximately 2π for the strongly overcoupled case. In contrast, for strong undercoupling, the phase shift at ω_0 vanishes. For critical coupling, $Q_{\mathrm{ext}} \simeq Q_{\mathrm{int}}$, the observed phase shift amounts to $\pi/2$ [222]. In the magnitude response, the overcoupled and undercoupled regimes are more difficult to distinguish, due to the symmetry of Eq. (4.23) with respect to κ_{int} and κ_{ext}. However, the critical coupling scenario

(a)

(b)
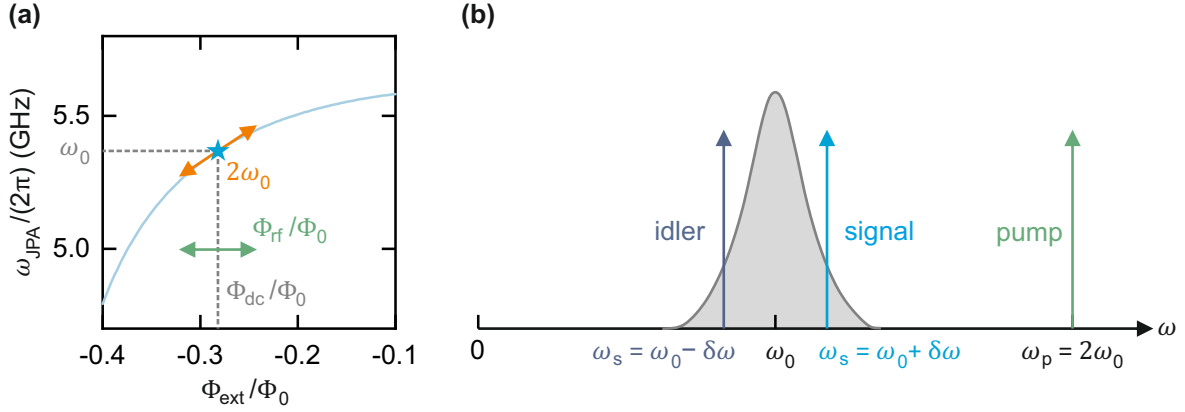
Figure 4.7: (a) Illustration of the distinct roles of the dc-flux bias Φ_{dc} and the rf-flux modulation Φ_{rf} in the flux-driven JPA. (b) Schematic of the frequency space for the JPA, where a pump frequency $\omega_{\mathrm{p}} = 2\omega_0$ results in the amplification of the signal mode $\omega_{\mathrm{s}} = \omega_0 + \delta\omega$ in conjunction with an amplification of the associated idler mode $\omega_{\mathrm{i}} = \omega_0 - \delta\omega$.

is reflected in a strong resonant dip in $|S_{11}|$ due to impedance matching criteria [95, 222]. For more details, see Ref. [222].

Flux-dependent JPA resonance frequency In contrast to the basic CPW resonators introduced in the previous paragraph, the quarter-wavelength resonators in our JPAs are shorted to ground via dc-SQUIDs. The flux-dependent inductance of the dc-SQUID from Eq. (4.17) results in a magnetic-flux dependence of the JPA resonance frequency

$$\omega_{\mathrm{JPA}}(\Phi_{\mathrm{ext}}) = \omega_0 \left(\frac{L_{\mathrm{r}}}{L_{\mathrm{SQ}}(\Phi_{\mathrm{ext}}) + L_{\mathrm{L}}/4 + L_{\mathrm{r}}} \right), \tag{4.25}$$

where L_{r} is the the overall inductance of the bare resonator. Note that Eq. (4.25) is only an approximated, simplified expression for the JPA resonance frequency, assuming that the capacitance of the Josephson junctions is negligible compared to the resonator capacitance, and assuming vanishing transport current through the dc-SQUID. For a detailed study, we refer the reader to Ref. [71]. Figure 4.6 shows the JPA resonance frequency as a function of an externally applied dc flux Φ_{ext}, according to Eq. (4.25), for different values of I_{c}, L_{L}, and L_{r}.

Flux-driven parametric amplification We next investigate the JPA response to a periodic flux modulation through the dc-SQUID. This flux modulation can be implemented by applying a pump tone at the frequency $\omega_{\mathrm{p}} = 2\omega_0$, i.e., at twice the JPA resonance frequency. This pump tone typically couples inductively to the dc-SQUID and causes a periodic modulation of the SQUID inductance, which leads to a periodic modulation of the JPA resonance frequency [81]. The resulting parametric effect is a three-wave mixing process, in which an incident signal with angular frequency $\omega_{\mathrm{s}} = \omega_{\mathrm{p}}/2 + \delta\omega$ is amplified [224, 225].

The amplification is called parametric as it is achieved by the modulation of a system parameter, namely the inductance of the resonator. The quantity $\delta\omega$ denotes the frequency detuning between ω_s and $\omega_p/2$. Due to energy conservation, an idler mode at the frequency $\omega_i = \omega_p/2 - \delta\omega$ additionally appears from the three-wave mixing dynamics [226].

The dynamics of a flux-driven JPA can be well described by the quantum-mechanical treatment of a periodically modulated harmonic oscillator, as introduced by Yamamoto $et\ al.$ [221]. The resulting Hamiltonian can be written as

$$\hat{H}_{\mathrm{JPA}} = \hbar\omega_0 \left[\hat{a}^\dagger \hat{a} + \frac{1}{2} + \epsilon\cos(\alpha\,\omega_0\,t)(\hat{a} + \hat{a}^\dagger)^2 \right], \tag{4.26}$$

where $\epsilon/2$ corresponds to the quasi-classical modulation amplitude and $\alpha\,\omega_0$ is the modulation frequency. The Heisenberg equation of motion, combined with a rotating wave approximation at $\alpha\,\omega_0/2$ results in a closed expression for the JPA output field [108, 221]. Here, it is important to account for the input field coupled to the resonator, as well as for a finite coupling to the environmental bath [221, 222]. Note that we exclusively consider $\alpha = 2$, i.e., $\omega_p = 2\omega_0$. Convergence to a steady-state solution of the Heisenberg equation of motion restricts the modulation amplitude to $\epsilon \leq \epsilon_c = \kappa_{\mathrm{tot}}/(2\omega_0)$, where ϵ_c shows similarities to the critical driving force of a Duffing oscillator and represents the threshold, above which the JPA enters the parametric oscillator regime [218, 227–229]. We restrict our consideration to the operation of the JPA in a steady state and neglect transient dynamics. In the following, we address the two distinct amplification regimes of the JPA, i.e., the frequency-nondegenerate and frequency-degenerate modes.

Frequency-nondegenerate amplification For the case of $\delta\omega \neq 0$, i.e., when the signal frequency $\omega_s = \omega_p/2 + \delta\omega$ is not equal to exactly half the pump frequency, we label the flux-driven JPA operation mode as (frequency-)nondegenerate. The associated signal gain can be written as [221]

$$G_s(\delta\omega) = \frac{\kappa_{\mathrm{int}}^2 \delta\omega^2 + \left[(\kappa_{\mathrm{int}}^2 - \kappa_{\mathrm{ext}}^2)/4 - \epsilon^2\omega_0^2 - \delta\omega^2 \right]^2}{\kappa_{\mathrm{tot}}^2\,\delta\omega^2 + \left[\kappa_{\mathrm{tot}}^2/4 - \epsilon^2\omega_0^2 - \delta\omega^2 \right]^2}, \tag{4.27}$$

whereas the idler gain is given by [221]

$$G_i(\delta\omega) = \frac{\kappa_{\mathrm{ext}}^2\,\epsilon^2\,\omega_0^2}{\kappa_{\mathrm{tot}}^2\,\delta\omega^2 + \left[\kappa_{\mathrm{tot}}^2/4 - \epsilon^2\omega_0^2 - \delta\omega^2 \right]^2}. \tag{4.28}$$

For nondegenerate-gain operation, the JPA is equivalent to a phase-preserving, or phase-insensitive, amplifier. Towards high internal quality factors, or equivalently, vanishing internal losses, $\kappa_{\mathrm{int}} \to 0$, Eqs. (4.27) and (4.28) are linearly related according to $G_s(\delta\omega) - G_i(\delta\omega) = 1$. Equations (4.27) and (4.28) furthermore show that overcoupled JPAs, $\kappa_{\mathrm{int}} \ll \kappa_{\mathrm{ext}}$, generally exhibit amplification characteristics for the entire range of $0 < \epsilon < \epsilon_c$.

Conversely, undercoupled JPAs act as effective attenuators for weak pumping $0 < \epsilon < \epsilon_{\text{th}}$ below a threshold value of $\epsilon_{\text{th}} = \sqrt{\kappa_{\text{int}}^2 - \kappa_{\text{ext}}^2}/(2\omega_0)$, which is applicable for frequencies close to ω_0 [221, 222]. Above this threshold, the undercoupled JPAs act as amplifiers for $\epsilon_{\text{th}} < \epsilon < \epsilon_{\text{c}}$. In this work, we exclusively rely on overcoupled JPAs. The signal and idler gains according to Eqs. (4.27) and (4.28), respectively, are shown in Fig. 4.8(a) for various pump strengths and in Fig. 4.8(b) for different internal quality factors.

Frequency-degenerate amplification   Next, we consider the frequency-degenerate amplification scenario with $\delta\omega = 0$, or equivalently, $\omega_{\text{s}} = \omega_{\text{p}}/2$. Here, the signal and idler modes are frequency-degenerate and can coherently interfere [82, 230]. A resulting constructive or destructive interference directly depends on the phase θ of the the input signal with respect to the phase of the pump signal. As a consequence, selected quadratures of the input field to the JPA can be controllably amplified or attenuated. This phase-dependent, degenerate gain can be written as [221]

$$G_{\text{d}}(\theta) = \frac{\left(\frac{\kappa_{\text{ext}}^2 - \kappa_{\text{int}}^2}{4} + \epsilon^2\omega_0^2\right)^2 + \kappa_{\text{ext}}^2\epsilon^2\omega_0^2 - 2\kappa_{\text{ext}}\epsilon\,\omega_0\left(\frac{\kappa_{\text{ext}}^2 - \kappa_{\text{int}}^2}{4} + \epsilon\,\omega_0^2\right)\sin 2\theta}{\left(\frac{\kappa_{\text{tot}}^2}{4} + \epsilon^2\omega_0^2\right)^2}. \tag{4.29}$$

For strongly overcoupled JPAs, we can simplify Eq. (4.29) and extract the respective maximum and minimum gain according to [108]

$$G_{\text{d}}^{\text{max}} = \left[\frac{\epsilon\,\omega_0 + (\kappa_{\text{ext}} - \kappa_{\text{int}})/2}{\epsilon\,\omega_0 - (\kappa_{\text{ext}} + \kappa_{\text{int}})/2}\right]^2, \tag{4.30}$$

$$G_{\text{d}}^{\text{min}} = \left[\frac{\epsilon\,\omega_0 - (\kappa_{\text{ext}} - \kappa_{\text{int}})/2}{\epsilon\,\omega_0 + (\kappa_{\text{ext}} + \kappa_{\text{int}})/2}\right]^2. \tag{4.31}$$

In phase space, these two extrema are oriented orthogonal to each other, with $\theta^{\text{min}} = \pi/4 + n\,\pi$ and $\theta^{\text{max}} = 3\pi/4 + n\,\pi$ $(n \in \mathbb{N}_0)$. For vanishing internal losses, $\kappa_{\text{int}} = 0$, we obtain

$$G_{\text{d}}^{\text{max}}\,G_{\text{d}}^{\text{min}} = 1. \tag{4.32}$$

This symmetry motivates introducing the squeeze parameter r with $G_{\text{d}}^{\text{max}} = \exp(2r)$ and $G_{\text{d}}^{\text{min}} = \exp(-2r)$ [6, 231]. Similar to the nondegenerate case, the discussed steady-state properties are only valid for $\epsilon < \epsilon_{\text{c}}$.

Standard quantum limit   The noise properties of amplifiers represent an important figure of merit that is usually characterized by the signal-to-noise ratio (SNR). Obviously, a low noise level is useless if the signal level is low too. In the same way a large signal level is useless if the noise level is large. In both cases a small SNR is achieved. It is important to note that in general, deterministic noiseless linear phase-preserving amplification is fundamentally impossible, as dictated by the bosonic commutation relations [226, 232].
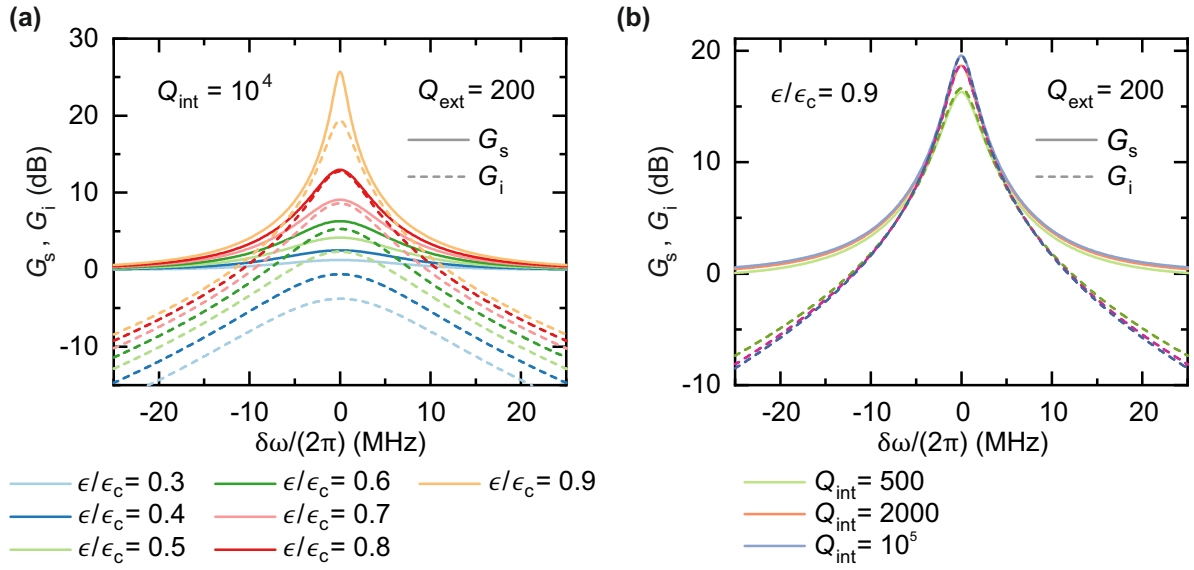
Figure 4.8: Nondegenerate signal and idler gain as a function of detuning $\delta\omega$ for overcoupled JPAs according to Eqs. (4.27) and (4.28). Panel (a) shows the results for various pump powers, an internal quality factor $Q_{int} = 10000$ and an external quality factor $Q_{ext} = 200$. Panel (b) depicts the influence of Q_{int} on the gain spectra for a fixed pump strength $\epsilon/\epsilon_c = 0.9$. The external quality factor is fixed to $Q_{ext} = 200$ and the resonance frequency is set to $\omega_0/(2\pi) = 5.5\,\text{GHz}$ for both panels. Solid lines represent G_s, while dashed line correspond to the associated G_i.

This important principle is formulated in the Haus-Caves theorem [233, 234], which states that these phase-preserving amplifiers add a minimum amount of noise in the amplification process. The quantum efficiency η is one of several established quantities for noise characterization, other common quantifies being the noise temperature or the absolute number of noise photons [95]. The quantum efficiency, in classical electrodynamics similar to the noise figure, is a figure of merit that describes the degradation of the SNR caused by a respective amplifier. Conventionally, the quantum efficiency is defined as

$$\eta = \frac{\text{SNR}_{in}}{\text{SNR}_{out}}, \tag{4.33}$$

where SNR_{in} denotes the SNR at the input of the amplifier and SNR_{out} is the corresponding SNR at the output. The lower limit for the added noise, A_f, expressed in photon units and referred to the input of the amplifier, also known as the standard quantum limit (SQL) for phase-insensitive amplification, can be expressed as [226, 232, 234]

$$A_f \geq \frac{1}{2}\left(1 - \frac{1}{G}\right), \tag{4.34}$$

where G is the amplification gain. Accordingly, phase-preserving amplifiers add a minimum of half a noise photon to the to-be-amplified signal in the limit of large gain, $G \gg 1$ [235].

We can express the quantum efficiency in terms of the SQL according to

$$\eta = \frac{1}{1 + 2A_\mathrm{f}} \leq \frac{G}{2G - 1}, \tag{4.35}$$

which yields $\eta \leq 1/2$ in the limit $G \gg 1$. The operation of JPAs in the phase-sensitive mode grants access to noiseless signal amplification under the condition given in Eq. (4.32). In this case, we can define the phase-averaged gain as $G' = \sqrt{G_\mathrm{d}^\mathrm{max} G_\mathrm{d}^\mathrm{min}} = 1$. For degenerate amplification, we can express the phase-dependent noise contributions by the corresponding geometric mean, $A_\mathrm{f}' = 2\sqrt{A_q A_p}$, where A_q and A_p are the noise contributions to the respective quadratures. Accordingly, we can rewrite Eq. (4.34) as

$$\sqrt{A_q A_p} \geq \frac{1}{4}\left(1 - \frac{1}{\sqrt{G_\mathrm{d}^\mathrm{max} G_\mathrm{d}^\mathrm{min}}}\right), \tag{4.36}$$

which underlines that the lower limit on the added amplification noise, valid for vanishing internal losses, is indeed zero for $G_\mathrm{d}^\mathrm{max} G_\mathrm{d}^\mathrm{min} = 1$. While experimental hurdles and imperfections make it impossible to demonstrate entirely noiseless amplification, various studies have realized phase-sensitive amplification with JPAs exceeding the SQL [73, 75, 82, 236]. The range of applications for this type of amplifier is large and spans from low-noise preamplification of qubit readout signals to effective single-shot homodyne measurements in the microwave regime [90].

Chapter 5

Experimental techniques

Experiments with quantum microwaves at frequencies of several gigahertz are based upon sophisticated experimental techniques. In Sec. 5.1, we introduce fundamental building blocks for conducting advanced quantum microwaves experiments. In this scope, we cover the cryogenic part of the setup, as well as detection and processing of quantum signals at room temperature. Here, the output line calibration represents an important cornerstone for gaining access to information on quantum states at millikelvin temperatures via our detection unit located at ambient conditions. In this work, flux-driven Josephson parametric amplifiers (JPAs) represent a central component for the generation and manipulation of quantum microwave signals. Information on the JPA sample preparation, flux tunability, gain characteristics, and further basic measurement routines is given in Sec. 5.2.

5.1 Quantum microwave experiments at millikelvin temperatures

In this section, we introduce all central tools for conducting experiments with quantum microwaves in the frequency range of several gigahertz. Microwave photons at frequencies around 5 GHz carry an energy which is on the order of 6 magnitudes lower compared to optical photons [1]. These low energies of single microwave quanta make it impossible to operate experiments at the level of a few photons at room temperature. Already a temperature of 600 mK is equivalent to a thermal population of approximately two photons at 5 GHz. At room temperature, the corresponding thermal occupation number already exceeds an average of 1000 photons per mode. In order to generate and manipulate quantum microwave states, we are forced to work at experimental temperatures on the order of 10 mK. Furthermore, finite microwave losses deteriorate the quantum properties of generated states, representing a further experimental hurdle. In order to tackle these challenges, we use state-of-the-art cryogenic setups, which can provide millikelvin

---

[1]An exemplary optical photon with a wavelength of 600 nm, corresponding to approximately 500 THz or 2 eV, versus the microwave photon at 5 GHz characterized by an energy of roughly 3 μeV.
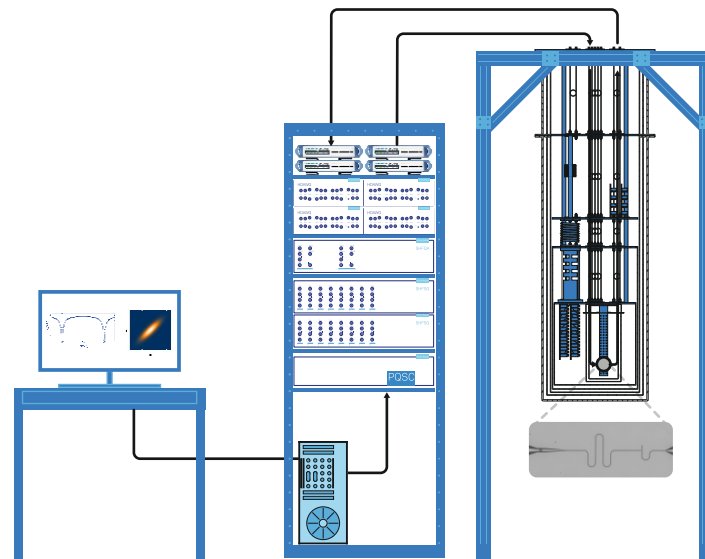
Figure 5.1: Schematic of a cryogenic experimental setup for conducting quantum microwave studies. The cryostat on the right is illustrated in a cross-sectional view, with the sample stage located at its bottom. The cryostat is interfaced to room-temperature test and measurement equipment with rf and dc lines. A CPU with associated graphical user interfaces enables control, readout, and analysis by a user.

temperatures and are (partially) equipped with superconducting low-loss microwave cables to facilitate high-quality quantum information experiments. An exemplary schematic of an experimental setup for conducting quantum microwave studies is shown in Fig. 5.1. Typical experiments, or protocols, are conducted at very low signal levels, which makes direct signal readout challenging. Accordingly, quantum signals are strongly amplified before entering the detection unit at room temperature. The associated added amplification noise drastically blurs the signal and necessitates sophisticated signal detection techniques. A reliable and precise output line calibration allows for correlating the measured classical quantities at room temperature to quantum properties of the signals at the cryogenic sample stage.

5.1.1 Cryogenic setup

Dilution refrigerator   Experiments presented in this work have been either performed in a custom-built wet dilution cryostat [237] or in a commercially available cryogen-free dilution refrigerator[2]. Both cryostats rely on exploiting the spontaneous phase separation in a ^{3}He/^{4}He mixture at around $900\,\mathrm{mK}$, forming a ^{3}He-rich phase, the concentrated phase, and a ^{3}He-poor phase, the dilute phase. In these dilution refrigerators, ^{3}He acts as the circulating working fluid driven by vacuum pumps. Here, ^{3}He is diluted by transitioning across the phase boundary from the concentrated to the diluted phases.

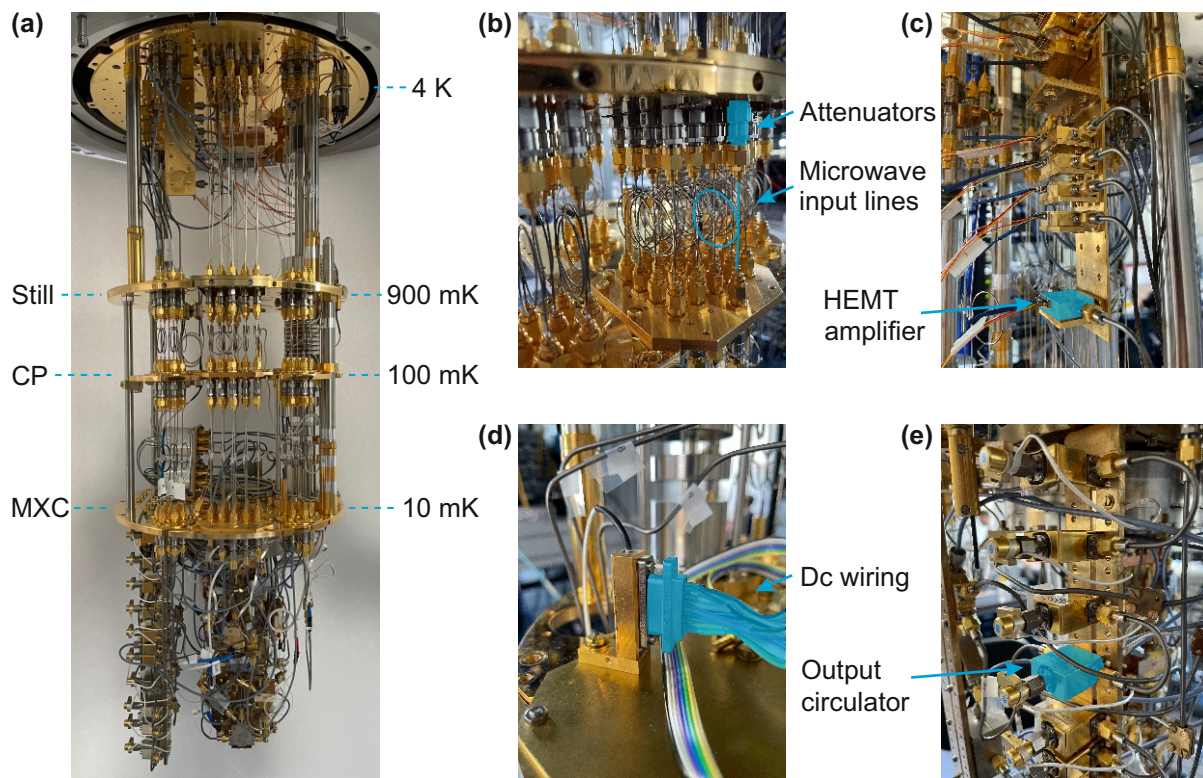[2]LD400 dilution refrigerator measurement system from `Bluefors`.

Figure 5.2: (a) Photograph of the ^{3}He/^{4}He dilution cryostat (LD400 from Bluefors) and its temperature stages. (b) Exemplary microwave input line bundle with corresponding input attenuators. (c) HEMT stack mounted at the 4 K stage. (d) Photograph of the dc wiring at the MXC. (e) Output circulators located between the sample stage and the input to the HEMTs. The respective components are false-colored in blue.

Since this process is endothermic, it removes heat from the ^{3}He/^{4}He mixture and provides an effective cooling power proportional to the amount of ^{3}He crossing the boundary [238]. In this manner, dilution refrigerators can achieve temperatures down to several mK [238–240]. In the following, we exemplarily illustrate the working principle of a commercially available cooling apparatus. Figure 5.2(a) shows the cryostat with several characteristic temperature stages at temperatures of 4 K, 900 mK, 100 mK, and 10 mK, respectively. The latter three are commonly referred to as the still plate, cold plate (CP) and mixing chamber plate (MXC), respectively. Further details on the working principle of ^{3}He/^{4}He dilution refrigerators can be found in Ref. [241]. For a detailed description of the second cryostat that was designed and constructed at the Walther-Meißner-Institut, we refer the reader to Ref. [237].

Dc wiring and thermometry The dilution refrigerator is equipped with thermometry lines to read out the system temperature at various stages. In addition, the system is set up with numerous dc wires in twisted-pair configuration. We use 36 AWG (American Wire Gauge) phosphor-bronze and 35 AWG copper wires between the room temper-

ature interface and the 4 K stage. The lower temperature stages are equipped with either superconducting niobium-titanium (NbTi) filaments embedded in copper-nickel or phosphor-bronze wires. In experiment, these dc wires are used to operate different components, i.e., thermometry, heating, power supply of high-electron-mobility transistor (HEMT) amplifiers, operation of cryogenic microwave switches, and powering of magnetic coils. The different wires are mechanically thermalized at different stages of the cryostat, which is especially important for precise temperature readout. A resistance bridge with closed loop temperature control [3] is used for precise, low-noise four-wire resistance measurements of the thermometers in conjunction with PID-based temperature stabilization. The corresponding preamp/scanner [4] enables readout of 16 independent lines. An additional 8-channel resistance bridge [5] allows for independent temperature readout of further thermometers. Additionally, the wiring is partially low-pass filtered at room temperature in order to suppress high-frequency noise. The power supply for the HEMT amplifiers is custom-built at the Walther-Meißner-Institut.

Microwave lines   The dilution refrigerator is equipped with various $50\,\Omega$ microwave cables, which act as an interface between the sample stage at several mK and the room temperature environment. These cables can be logically divided into input and output cables. Microwave signals can travel into the fridge via these input lines. The presented cryostat is equipped with 28 semi-rigid coaxial lines (0.86 mm SCuNi-CuNi) with SMA connectors leading from the room-temperature interface to the MXC. It is of uttermost importance to minimize the unwanted thermal noise. For that reason, the input cables are sequentially thermalized via microwave attenuators, which are mounted onto the different stages of the cryostat (i.e., the 50 K stage, 4 K stage, still plate, cold plate, and MXC). Via this step-wise approach, the effective noise temperature of the input line is gradually decreased down to millikelvin temperatures, which translates to an average thermal occupation number of $n_{\text{th}} \ll 1$ photons at working frequencies around 5 GHz. Stronger attenuation corresponds to a better thermalization and reduced noise, since the coupling strength to the thermal anchor is proportional to the level of attenuation. Conversely, the overall line attenuation needs to stay low enough to feed the required microwave powers to the designated components. Our quantum microwave experiments at the sample stage are typically conducted at very low signal levels, corresponding to few photons at microwave frequencies. The output lines transmit the information contained in these weak signals towards the HEMT amplifiers, which amplify the signals with a low number of added noise photons, typically on the order of few photons [222]. Superconducting coaxial lines (0.86 mm NbTi between the MXC and still plate and SC-219/50-NbTi-NbTi from the still plate to the HEMTs) ensure minimal transmission losses, $< 0.3\,\text{dB/m}$, before the first

---

[3]Model 370 ac resistance bridge from `Lakeshore`.
[4]Model 3716 from `Lakeshore`.
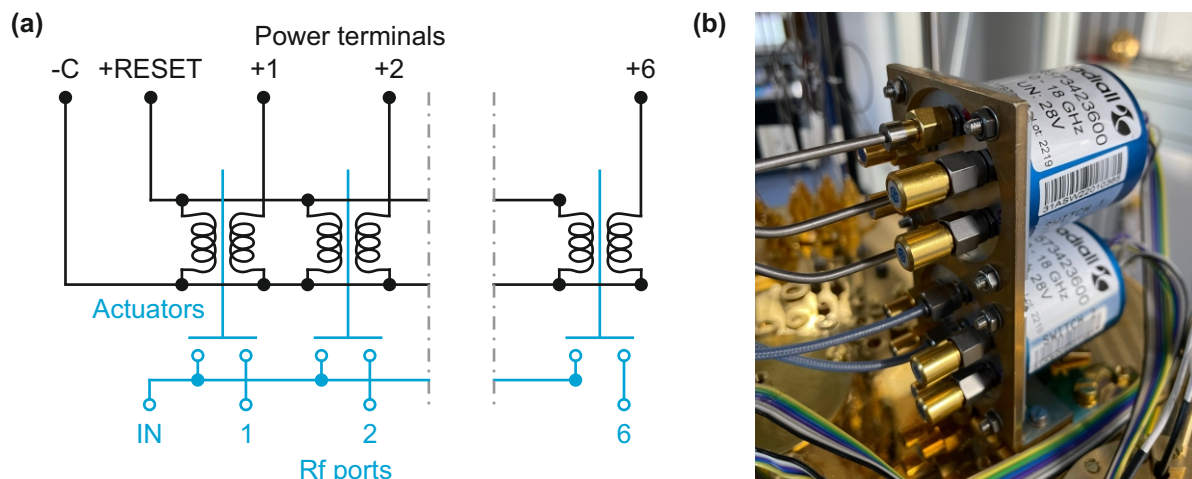[5]Model AVS-47B from `Picowatt`.

Figure 5.3: (a) Schematic diagram of the single-pole-6-throw cryogenic microwave switches. The latch-type actuators can be moved via current pulses applied through the respective power terminals, enabling switching of the rf subsystem, shown in blue. Here, the inner conductor of the rf input port (IN) connects to (disconnects from) the inner conductor of the respective rf output port (1 to 6) for the SET (RESET) operation. (b) Photograph of the two cryogenic microwave switches mounted onto an oxygen-free high thermal conductivity (OFHC) copper holder on top of the MXC. All unused rf ports are terminated by $50\,\Omega$ loads.

amplification stage. We employ cryogenic HEMTs [6] with an average gain of $G_\mathrm{H} = 41\,\mathrm{dB}$ in a bandwidth from $4\,\mathrm{GHz}$ to $8\,\mathrm{GHz}$ and a noise temperature below $2\,\mathrm{K}$. The output lines are partially thermalized to different temperature stages via mechanically pressing one end of annealed silver wires to the outer conductor of the cable and the other end to the respective temperature stages. A sequence of two back-to-back mounted circulators [7] in conjunction with $50\,\Omega$-loads implements effective microwave isolation in order to suppress reflections and noise from the HEMTs, which would affect the sample stage.

Cryogenic microwave switches   The limited number of microwave input and output lines motivates the usage of cryogenic microwave switches, which can significantly expand the complexity and density of a setup. Additionally, these switches enable implementation of basic logic, such as switching between two hypotheses in the quantum radar protocol (see Ch. 3). We employ two cryogenic latching relay microwaves switches with a frequency range from 0 to $18\,\mathrm{GHz}$ [8]. Figure 5.3(a) shows the schematic diagram of the single-pole-6-throw layout. In order to connect the microwave input port to a chosen output port, a current pulse of $125\,\mathrm{mA}$ for a duration of $10\,\mathrm{ms}$ is applied via the power terminals, generating a magnetic field strong enough to drive the designated actuators in a desired latching position. The polarity of the respective current pulse with respect to the common

---

[6]LNF-LNC4-8C cryogenic low noise amplifier from `Low Noise Factory`.
[7]LNF-CIC4-8A single junction double-shielded cryogenic circulator from `Low Noise Factory`.
[8]R573423600 single-pole-6-throw switches with SMA female connectors from `Radiall`.
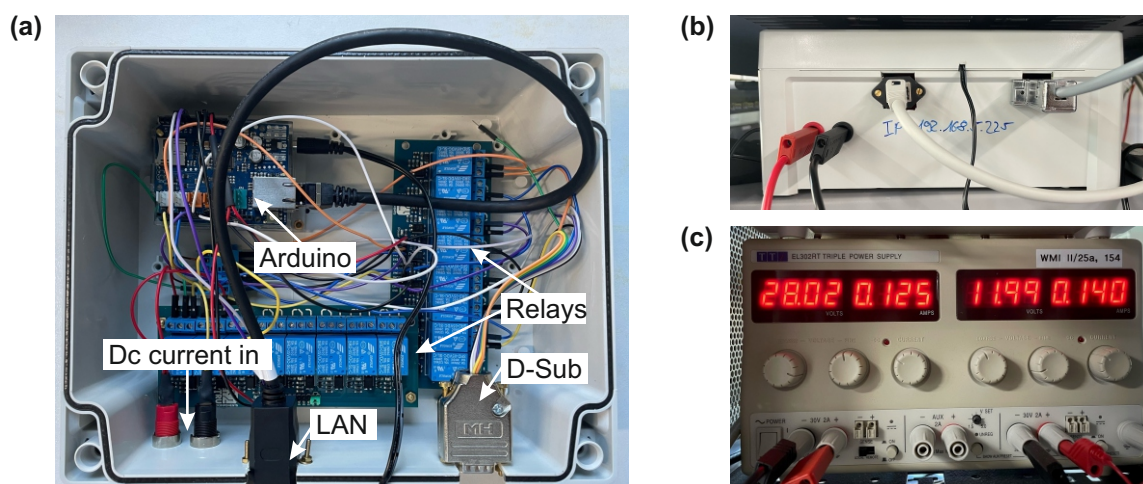
Figure 5.4: Photographs of the custom-built switch driver. (a) and (b) Pulsing module controlled by an Arduino Uno in conjunction with several relays to generate square pulses from a dc current generated by a power supply, depicted in (c).

terminal (C) determines the switching operation: SET or RESET. The SET operation brings the actuators into galvanic contact between the inner conductor of the input port (IN) and the the inner conductor of the respective output port. Similarly, the RESET operation breaks this contact by detaching the actuator. There exists the option of a global SET and RESET of all ports simultaneously, which requires an increased current strength of 750 mA. We typically avoid these global operations to minimize the associated heat load during switching. The latching relay relies on ferromagnetic materials, which can result in stray magnetic fields and, by extension, trapped magnetic flux vortices in the JPA ground planes degrading the internal JPA quality factors [242, 243]. Active switching and the associated magnetic field may additionally distort the dc-flux characteristics of the JPAs. In order to avoid these error sources, we mount the switches outside the cryoperm magnetic shield on top of the MXC, far from all JPAs. Both switches are mounted onto a OFHC copper holder, as depicted in Fig. 5.3(b). A custom-built driver generates suitable current pulses, which can be adjusted in terms of polarity, applied voltage, maximum current and pulse length. This functionality is implemented by a combination of a power source [9] with an adjustable voltage output and a current limiter [cf. Fig. 5.4(c)], combined with an independent pulsing module, shown in Figs. 5.4(a) and (b). The pulsing module consists of an Arduino Uno [10] generating low-voltage (5 V), low-current (20 mA) pulses of adjustable temporal length, combined with several Arduino-compatible relays [11]. The Arduino pulses drive the distinct relay channels to modulate the output signals of the power source and control their polarity via H-bridge logic.

---

[9] `EL302RT` bench power supply from `Aim-TTi`.
[10] `Rev3` in combination with a `Ethernet Shield 2` from `Arduino`.
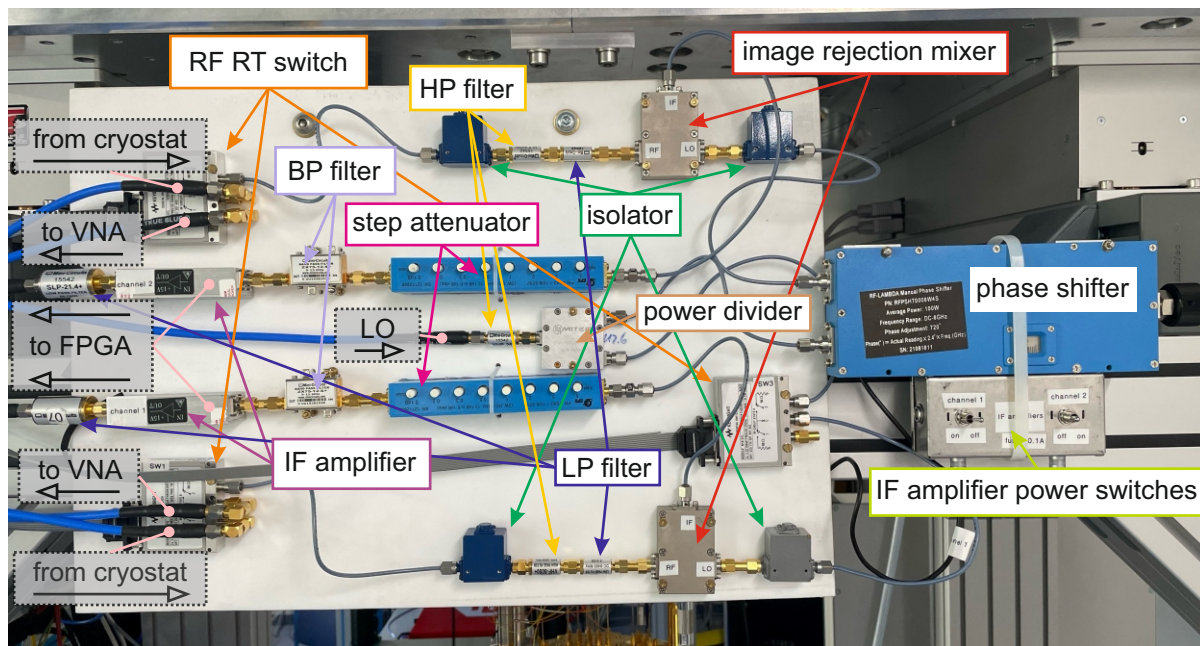[11] `TC-9072496` 8-channel relay module from `TRU COMPONENTS`.

Figure 5.5: Photograph of the dual-path heterodyne microwave receiver.

5.1.2 Quantum microwave detection and processing

In this subsection, we introduce a detection scheme of microwave signals at the cryostat outputs. The discussed detection setup is similar to those presented in Refs. [68, 108, 222]. All microwave devices are referenced to a 10 MHz rubidium frequency standard [12].

Dual-path analog detection unit   First, microwave signals at a working frequency f_{rf} of several gigahertz enter a second amplification stage at room temperature [13], which is temperature-stabilized by a Peltier cooler [14]. Next, these signals are routed to the dual-path heterodyne detection unit depicted in Fig. 5.5. In the following, we illustrate the working principle of the detection unit for a single path due to an underlying symmetric layout with respect to the two paths. Room temperature microwave switches route the incoming signal either to a vector network analyzer (VNA) for frequency-resolved measurements as described in Sec. 5.2, or pass them further to the detection unit. The raw signal passes a microwave isolator [15] and gets subsequently spectrally filtered by a high-pass (HP) filter [16], followed by a low-pass (LP) filter [17]. In a next step, the microwave

---

[12]FS725 atomic clock from `Stanford Research Systems`.

[13]AMT-A0482-EMI 1 GHz to 8 GHz broadband low noise amplifier with EMI shielding from `AgileMWT`.

[14]DA-075-12-02-00-00 Peltier cooler combined with a PT100 thermometer from `Laird`.

[15]IS-18-1 with a frequency range of 3700 to 8200 MHz at insertion loss$< 0.7\,$dB from `MCLI`.

[16]VHF-5050+ with a passband between 5500 and 10 000 MHz with insertion loss$< 2\,$dB and a cutoff frequency of 5050 MHz at a loss of 3 dB from `Mini Circuits`.

[17]VLF-8400+ with a passband between dc and 8400 MHz with insertion loss$< 1.8\,$dB and a cutoff frequency of 9100 MHz at a loss of 3 dB from `Mini Circuits`.

signals are down-converted to an intermediate frequency (IF) of $f_{IF} = 12.5\,\text{MHz}$ in an image-rejection mixer [18] (IRM) with $f_{IF} = f_{rf} - f_{LO}$, where f_{LO} is the frequency of a strong local oscillator (LO) microwave tone. The LO signal is generated by a vector signal generator [19], high-pass filtered [20], and split in a power combiner to supply both IRMs of the two distinct dual detection paths. The relative phase between the two paths is adjustable by usage of a mechanical phase-shifter [21], which is placed directly after the power combiner in one of the two paths. The usage of image-rejection mixers at this stage is crucial especially for measurements of squeezed states, since the reconstructed squeezing level would be inherently limited to 3 dB when using conventional mixers. This is due to the fact that the (in this case red) noisy sideband would also be down-converted to f_{IF}, increasing the variance of the reconstructed signal by the minimum of one quarter of a signal photon, which corresponds to a maximally possible squeezing level of 3 dB [68]. Note that $f_{IF} = 12.5\,\text{MHz}$ is not chosen arbitrarily, but well-detuned from the employed 10 MHz frequency standard to avoid parasitic signals within the spectral bandwidth of the reconstruction, and commensurable with the FPGA sampling frequency of 125 MHz. Furthermore, f_{IF} is well above the spectral range dominated by $1/f$-noise, and clearly below entering aliasing problems associated with the Nyquist-Shannon sampling theorem [107, 222, 244]. After the IRMs, the down-converted signals in both paths are balanced in power using step attenuators [22] and subsequently filtered using band-pass filters [23]. This attenuation and filtering also allows us to prevent compression effects in the subsequent amplification and avoids clipping effects during the analog-to-digital conversion. An IF amplifier [24] in each path combined with another low-pass filter [25] completes the analog part of the dual-path detection unit.

Digital signal processing   Figure 5.6 shows a schematic of the digital signal processing unit with the FPGA [26] image at its core. In a first step, the incoming dual-path analog signals at the IF frequency are analog-to-digital converted (ADC) in a transceiver module [27] at the sampling frequency of 125 MHz. The channel balancing enables correcting for offset mismatches between the two channels, as well as amplitude balancing with a weak coherent signal. Next, the signals are down-converted to zero frequency in a digital down-conversion

---

[18] `IRM4080B` with an LO frequency range of 4000 to 8000 MHz from `Polyphase`.

[19] `SGS100A SGMA` rf source with a frequency range up to 12.75 GHz and a maximal output level of 22 dBm from `Rohde & Schwarz`.

[20] `VHP-26` with a passband between 3000 and 7000 MHz with insertion loss< 1.3 dB and a cutoff frequency of 2570 MHz at a loss of 3 dB from `Mini Circuits`.

[21] `RFPSHT0008W4` high power phase shifter tuner with a phase adjustment of 720°for a frequency range from dc to 8 GHz from `RF-LAMBDA`.

[22] `ESA2-1-10/8-SFSF` attenuators from `EPX microwave inc`.

[23] `ZX75-12-S+` with a passband between 9 and 15 MHz with insertion loss< 3.5 dB from `Mini Circuits`.

[24] `AU-1447-R` with a gain of 60 dB over a frequency range from 0.001 to 400 MHz from `Miteq`.

[25] `SLP-21.4+` with a passband between dc and 22 MHz with insertion loss< 1 dB from `Mini-Circuits`.

[26] `PXIe-7975R` FlexRIO FPGA Module from `National Instruments`.

[27] `NI-5782` Transceiver Adapter Module for FlexRIO from `National Instruments`.
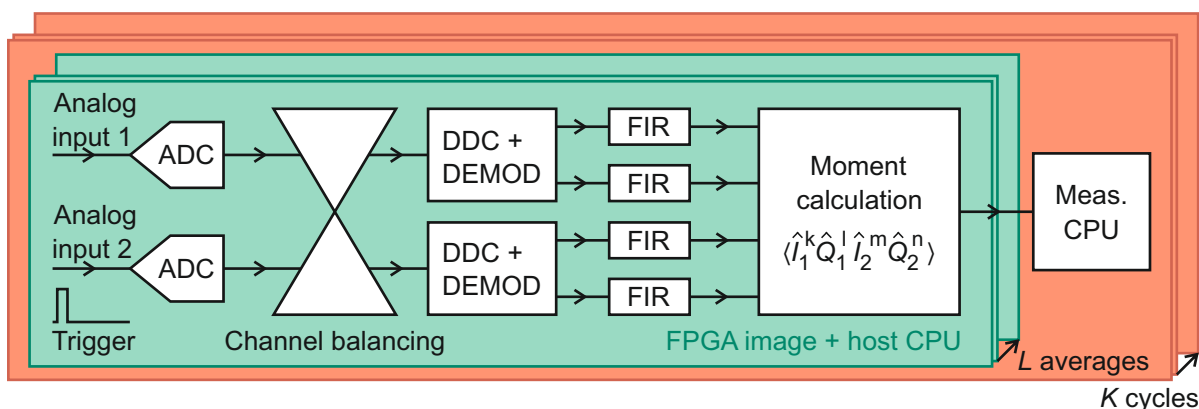
Figure 5.6: Data acquisition and processing scheme based on FPGA logic. The two analog input signal channels are first digitized by an ADC and subsequently balanced with regard to offset and amplitude. In a next step, the two signals are digitally down-converted (DDC) and demodulated (DEMOD). The resulting two pairs of signal components are spectrally filtered (FIR) and finally used for quadrature moment calculation. A number of L averages is accumulated before the data stream is forwarded to the measurement CPU. Each iteration of the FPGA cycle is initiated by means of an external trigger pulse. The scheme repeated K times.

(DDC). This step, combined with signal demodulation, implements digital homodyning and complements the full heterodyne detection sequence. The IQ-demodulation yields the I- and Q-quadratures of each signal path via

$$I_{1,2} = 2 f_{\mathrm{IF}} \int_{t}^{t+f_{\mathrm{IF}}^{-1}} A_{1,2}(\tau) \cos(2\pi f_{\mathrm{IF}} \tau) d\tau, \qquad (5.1)$$

$$Q_{1,2} = 2 f_{\mathrm{IF}} \int_{t}^{t+f_{\mathrm{IF}}^{-1}} A_{1,2}(\tau) \sin(2\pi f_{\mathrm{IF}} \tau) d\tau, \qquad (5.2)$$

where the sine and cosine functions at the IF (or demodulation) frequency are digitally generated, multiplied by the digitized input signals $A_{1,2}(\tau)$, and numerically integrated over a full period of f_{IF}^{-1}. A digital finite-impulse-response (FIR) filter [28] with an adjustable bandwidth precisely selects a narrow frequency window around the signal frequency, further suppressing unwanted noise [245]. Typical full bandwidths of the employed FIR filters are on the order of $400\,\mathrm{kHz}$ [108, 222]. Note that we have to deal with the following trade-off: while decreasing the FIR filter bandwidth is beneficial in terms of SNR, the filter ringing time grows accordingly [245]. An increased filter ringing time implies that longer times are needed to reach a steady-state regime of the system, where we can acquire reliable data. For more details on FIR filter design, we refer the reader to Refs. [108, 222]. In a final step, the FPGA computes the correlation quadrature moments, $\langle \hat{I}_1^n \hat{I}_2^m \hat{Q}_1^k \hat{Q}_2^l \rangle$, with $n + m + k + l \leq 4$ and $n, m, k, l \in \mathbb{N}_0$. This sequence is repeated for L averages and

---

[28]Created via `DSP System Toolbox` in `Matlab`.

afterwards sent to the measurement CPU. Each sequence is prompted by a short square trigger pulse generated by an arbitrary waveform generator [29]. Additionally, the whole scheme can be repeated K times. The data acquisition is split into L averages and K cycles due to memory limitations of the FPGA. The FPGA is referenced by the global $10\,\mathrm{MHz}$ frequency standard. After data acquisition, the FPGA sends the statistical moments data to the host CPU, which continuously runs a LabVIEW program with a graphical user interface (GUI) for data reception and routing [222]. Various measurement parameters, such as the channel balancing and number of averages, are fully controllable via this GUI. The full FPGA image, as well as the measurement code, are written in LabVIEW, facilitating seamless interfaces between FPGA, host CPU and measurement CPU. In operation, the FPGA and host CPU steadily wait for prompts from the measurement CPU, which represents the primary control node for running complex measurement protocols. The transmission of the moment data is established via first-in-first-out (FIFO) buffers at both parties, the FPGA and the host-CPU. As a consequence, the time-resolved information which is contained in the analog signal is preserved in the digital data trace. Post-processing of specific parts of the acquired data, or time traces, in conjunction with pulsed operation of the measurement scheme is a decisive building block of reference-state reconstruction, as described in the next paragraph.

Reference-state reconstruction   In our experiments, we are interested in the evolution of single or few quanta of microwave quantum states. Due to the absence of reliable and versatile signal detectors at cryogenic temperatures, we need to rely on room-temperature components for detection of these low-energy signals. Despite making use of low-noise HEMTs, which dictate the SNR in the amplification chain, we have to use advanced signal recovery methods to reliably reconstruct quantum states at the sample stage. In the following, we introduce techniques on how to perform state tomography of a two-mode quantum state, characterized by the bosonic operators $\hat{a}_k$, with $k = 1, 2$, from a noisy signal with vanishing SNR at room temperature. Throughout this work, we rely on the so-called reference-state reconstruction method to retrieve the signal moments of propagating quantum signals before the action of the amplification chain [67, 68, 108, 246]. As introduced before, the microwave quantum state of interest undergoes a whole amplification chain before detection. As a result, the measured raw signal is not only stronger, but carries a significant noise contribution. According to the Friis law [95], for large HEMT gain the noise of the whole detection chain is governed by the first amplification stage

$$A_{\mathrm{amp}} = A_1 + \frac{A_2}{G_1} + \frac{A_3}{G_1 G_2} + \dots, \tag{5.3}$$

where A_k and G_k ($k = 1, 2, \dots$) are the values of the input noise (in photon units) and gain of the k-th amplifier in the chain, respectively. In the frequency range of 4 to $12\,\mathrm{GHz}$,

---

[29]HDAWG 750 MHz Arbitrary Waveform Generator from Zurich Instruments.

state-of-the-art HEMTs achieve an approximate gain of $G = 40\,\mathrm{dB}$ with around 10 added noise photons, referred to the input. In order to cancel out this noise contribution and account for the overall amplification of the chain, a well-known signal serves as a reference state, allowing for correction of noise and gain [65, 66, 247]. We rely on weak thermal states characterized by a photon number $n_{\mathrm{th}} \ll 1$ per mode at the designated working frequency around $5\,\mathrm{GHz}$, which can be well approximated by the vacuum state. We define dimensionless complex envelope functions

$$S_{1,2} = (I_{1,2} + \mathrm{i}Q_{1,2})/\sqrt{\kappa_{1,2}}, \tag{5.4}$$

where $\kappa_{1,2}$ correspond to the photon number conversion factors introduced in Sec. 5.1.3. The associated envelope operators are given by

$$\hat{S}_{1,2} = (\hat{I}_{1,2} + \mathrm{i}\hat{Q}_{1,2})/\sqrt{\kappa_{1,2}} = \hat{a}_{1,2} + \hat{V}_{1,2}^{\dagger}, \tag{5.5}$$

where $\hat{a}_{1,2}$ are the bosonic operators of the propagating quantum signal in paths 1 and 2. The operators $\hat{V}_{1,2}$ correspond to the added noise from the respective amplification chain. As can be seen from Eq. (5.5), a measurement of the quadrature moments $\langle \hat{I}_1^n \hat{I}_2^m \hat{Q}_1^k \hat{Q}_2^l \rangle$ for a known reference quantum state $\hat{a}_{1,2}$ enables direct evaluation of $\hat{V}_{1,2}$. As stated above, the vacuum state serves as such a reference in our case. Under the assumption of a constant amplification noise, we can reconstruct arbitrary quantum states and their associated signal moments $\langle (\hat{a}_1^{\dagger})^n (\hat{a}_2^{\dagger})^m \hat{a}_1^k \hat{a}_2^l \rangle$ by effectively filtering out the known influence of $\hat{V}_{1,2}$.

Gaussianity   In principle, acquisition of quadrature moments up to the second order is sufficient to reconstruct Gaussian states, which are fully described by the corresponding signal moments. Nonetheless, we typically acquire quadrature moments up to fourth order, which proves to be useful in terms of Gaussianity verification of the measured quantum states. In this framework, we introduce the cumulants

$$\langle\langle (\hat{a}^{\dagger})^k \hat{a}^l \rangle\rangle = \left| \frac{\partial^k}{\partial x^k} \frac{\partial^l}{\partial y^l} \ln \sum_{m,n} \frac{\langle (\hat{a}^{\dagger})^m \hat{a}^n \rangle x^m y^n}{m! n!} \Big|_{x=y=0} \right|. \tag{5.6}$$

of order $(k + l)$, with $k, l \in \mathbb{N}_0$ [247–249]. While cumulants of order $(k + l) \leq 2$ can be non-zero for Gaussian states, higher-order contributions $(k + l) \geq 3$ must theoretically vanish for such states. In experiment, we check whether $\langle\langle (\hat{a}^{\dagger})^k \hat{a}^l \rangle\rangle \to 0$ in terms of skewness, $(k + l) = 3$, and sharpness, $(k + l) = 4$, of the reconstructed states [249]. While the former is a necessary criterion, the latter is a sufficient prerequisite [222, 247]. Since the higher-order cumulants are never strictly zero in experiment, we verify our measured states as Gaussian if cumulants of the third and fourth orders are significantly smaller

than their first and second order counterparts

$$\frac{\langle\langle(\hat{a}^\dagger)^k\hat{a}^l\rangle\rangle}{\langle\langle(\hat{a}^\dagger)^m\hat{a}^n\rangle\rangle} \ll 1 \tag{5.7}$$

for $3 \leq (k + l) \leq 4$ and $(m + n) \leq 2$. Note that this method only grants access to a qualitative analysis of the Gaussianity. Neither the absolute, nor the relative [cf. Eq. (5.7)] magnitude of the higher-order cumulants allows us to determine up to which extent the Gaussian approximation is applicable and how experimental parameters are influenced. Since quantitative approaches exist but are cumbersome to implement in terms of computational effort [250], we rely on the qualitative analysis provided by the cumulant approach.

Physicality check   Apart from Gaussianity, all reconstructed states need to obey the Heisenberg uncertainty principle according to Eq. (2.12). While this principle is universal, the reconstruction of states may suffer from experimental deficiencies, such that the resulting states are nonphysical. For Gaussian states, we formulate the physicality check as

$$\det \boldsymbol{V} \geq \left(\frac{1}{16}\right)^\ell, \tag{5.8}$$

where $\boldsymbol{V}$ is the $2\ell \times 2\ell$ covariance matrix of an ℓ-mode Gaussian state. Accordingly, only states that fulfill this physicality check, or in other words, the Heisenberg relation, are used for further analysis, while all other states are filtered out. Previous experiments with squeezed states have shown that a low number of averages during data acquisition, reflecting a low SNR, tends to produce an increased failure of the physicality check [108]. At the same time, including all measured states in the full analysis can lead to better agreement between experiment and theory in these low-average scenarios, details can be found in Ref. [108].

5.1.3 Output line calibration

Photon number conversion factor   Since the cryostat does not allow for direct access to the signals at the point of interest in our experiment, i.e., at the sample stage, quantitative analysis at room temperature requires a precise relation of the signal powers between these two points. A calibrated photon source at the cryogenic sample stage with well-known and controllable emission characteristics allows for a direct mapping between a voltage amplitude detected at room temperature and the photon number emitted from the calibrated source. This approach can be applied for each output line, such that the detected quadrature moments $\langle\hat{I}_1^k\hat{Q}_1^l\hat{I}_2^m\hat{Q}_2^n\rangle$ provide quantitative insights into the
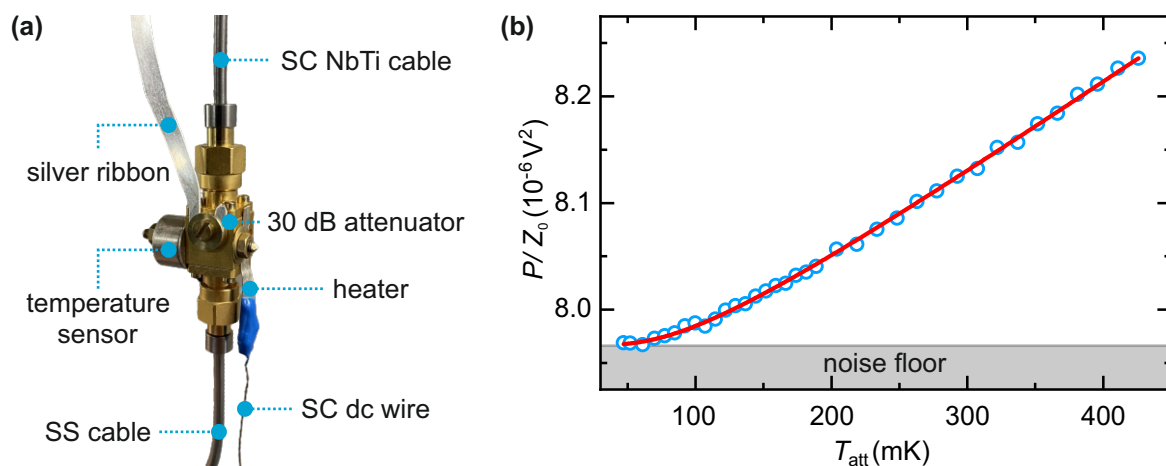
Figure 5.7: (a) Photograph of the calibrated source inside the cryostat. (b) Planck spectroscopy for an exemplary output channel. Blue points are experimental data, the red line corresponds to a fit based on Eq. (5.9). We find a conversion factor $\kappa = (3.64 \pm 0.03)\, 10^{-7}\text{V}^2/\text{photon}$ and an amplification noise $A_\text{H} = 12.82 \pm 0.12$ (in units of photons).

dynamics of the quantum signals at the sample stage. This mapping is conventionally labeled as the photon number conversion factor (PNCF), given in units of V^2/photon, and relates the measured voltages to the photon numbers before amplification. As a calibrated source, we employ a cryogenic 30-dB attenuator as an effective black-body radiator [68]. The temperature of the attenuator is varied between 30 and 450 mK by means of a PID-controlled loop. This loop is realized using a RuO_2 resistive temperature sensor in combination with a heater [30]. The temperature sensor is read out in four-wire configuration with superconducting NbTi twisted pairs. The temperature sensor and heater are clamped to the attenuator on opposite sides in order to reliably control the temperature of the attenuator itself. Furthermore, a thin silver ribbon is clamped to the attenuator at one end, while its other end is thermally anchored at the MXC. This ribbon serves as an additional thermalization channel. The thickness, and thereby, the thermal conductivity of the silver ribbon is designed in a way that the attenuator cools down reasonably fast after active heating, while the MXC temperature stays largely unaffected during heating. Figure 5.7(a) shows a photograph of the 30-dB attenuator that serves as a connecting piece between a stainless steel (SS) input cable and a superconducting NbTi cable. The SS cable serves as an input line. Its other end is connected to the MXC, realizing a weak thermal coupling between the attenuator and the MXC. The superconducting cable leads to the main cryogenic experimental setup, which should remain unaffected by heating effects. Additionally, low losses between the emitted microwave noise and the first amplification stage are beneficial for the output line calibration in terms of reliability

---

[30] $100\,\Omega$ strip resistor soldered to a twisted pair of superconducting NbTi wire. A galvanically decoupled, annealed silver strip, which is glued to the resistor, establishes a good thermal coupling to the 30-dB attenuator.

and robustness [108]. The detected power at the FPGA for a respective output channel is given by [68, 70]

$$P(T_{\text{att}}) = \frac{\kappa}{Z_0} \left[\frac{1}{2} \coth \left(\frac{\hbar\omega_{\text{s}}}{2k_{\text{B}}T_{\text{att}}} \right) + A_{\text{amp}} \right], \tag{5.9}$$

where T_{att} is the varying attenuator temperature, κ in units of V^2/photon is the PNCF that further depends on the full amplification gain G and detection bandwidth B, $Z_0 = 50\,\Omega$ denotes the characteristic line impedance, ω_{s} is the signal frequency, and A_{amp} corresponds to the full amplification noise (in unit of photons) added by our amplification chain. As introduced in Eq. (5.3), this added noise can be well approximated by the HEMT noise, $A_{\text{H}} \simeq A_{\text{amp}}$. Figure 5.7(b) shows a characteristic PNCF measurement with two distinct regimes: a saturation of the signal caused by the quantum fluctuations at temperatures below 60 mK, and the linear Johnson-Nyquist regime above 120 mK. Note that there exists a variety of other self-calibrated microwave sources, such as qubits [251], or tunnel junctions [252]. Similar to our approach, heating the entire MXC and sample stage manifests in well calibrated Johnson-Nyquist noise [253]. This particular approach is, in principle, also implementable in our cryostat. However, the associated heating of all experimental components at the sample stage may affect their characteristics, as it is the case for our JPAs [222]. The local heating approach avoids these potential issues and has proven as a reliable and precise calibration method throughout various experiments [71, 73, 74, 77, 78, 80, 88, 254].

Reconstruction point   By default, the signal reconstruction is conducted with respect to the calibrated source in the setup, i.e., the heatable attenuator. A precise estimation of the losses between the calibrated source and a chosen reconstruction point along the signal path affects the value of κ and enables quantum state reconstruction at arbitrary positions in the setup [68, 108]. Signal reconstruction at variable reference points represents a decisive tool in our experiments, which grants access to, e.g., the statistics of squeezed states right at the output of a respective JPA. The losses, e.g., due to insertion imperfections, must be carefully estimated based on nominal data sheet values of the respective microwave components. Furthermore, microwave cable losses are extracted from room temperature time-domain reflectometry measurements in order to take into account the effects of reflection losses due to impedance mismatch. A beam splitter model, according to which the signal sequentially couples to the environmental bath, allows for including these losses in the PNCF. Additionally, active heating of the 30-dB attenuator locally disturbs this equilibrium bath temperature. The associated losses can be either incorporated by introducing a linear temperature gradient along the following cable [108], or by using the increased attenuator temperature as an effective bath temperature for the first subsequent lossy component, i.e., the SMA connector of the following superconducting cable [222].
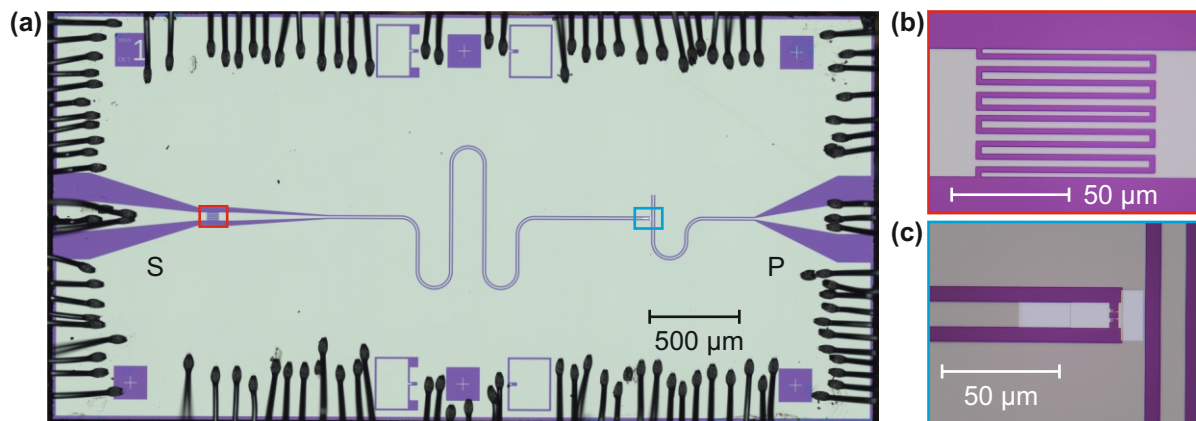
Figure 5.8: (a) Optical microscope image of an NEC JPA chip with the signal and pump ports marked as S and P, respectively. The red rectangle highlights the coupling capacitance between the signal port and the quarter-wavelength resonator, also depicted in panel (b) with larger magnification. Panel (c) shows a close-up of the dc-SQUID and the vertical pump line. The corresponding area is highlighted in blue in panel (a).

5.2 Flux-driven Josephson parametric amplifiers

Device preparation   JPAs represent a versatile tool for the generation of squeezed states and phase-sensitive amplification. Throughout this work, we employ two different JPA batches. For the experiments presented in Ch. 6, we rely on devices fabricated at NEC Smart Energy Research Laboratories, Japan, and RIKEN, Japan [81]. Figure 5.8(a) shows an optical microscope image of a JPA chip from NEC. The results discussed in Ch. 7 are based on JPAs fabricated at the WMI. The architecture of both device types relies on the same fundamental building blocks: a superconducting quarter-wavelength resonator in CPW geometry, which is short-circuited to the ground plane via a dc-SQUID at one end [cf. Fig. 5.8(c)], and capacitively coupled to a signal line at the other end [cf. Fig. 5.8(b)] [71, 81]. In proximity to the dc-SQUID, there is a separate CPW pump line inductively coupled to the dc-SQUID, which allows for parametric driving of the JPA. The NEC devices are patterned onto a silicon substrate of 300 μm thickness with a thermal-oxide top layer. The signal line, resonator, and pump line are realized based on a 50 nm niobium layer that is deposited via magnetron sputtering. The aluminum dc-SQUID with an electrode thickness of 50 nm is fabricated by means of shadow evaporation. Further information about the NEC JPAs can be found in Ref. [81]. The WMI devices rely on the same material stack and are fabricated on silicon substrates with a thickness of 525 μm and a niobium film thickness of 150 nm. The dc-SQUID electrode thickness is 30 nm and 70 nm for the bottom and top electrodes, respectively. The JPA chips are glued in a custom-built sample box that is made of OFHC copper and subsequently gold-plated, as depicted in Fig. 5.9(a). GE varnish [31] glue ensures strong adhesion at low temperatures,

---

[31]GE 7031 from CMR-Direct.

(a)

K-connector   silver glue

alumina substrate   glass bead pin

(b)

superconducting   sample box
coil

silver wire   aluminum
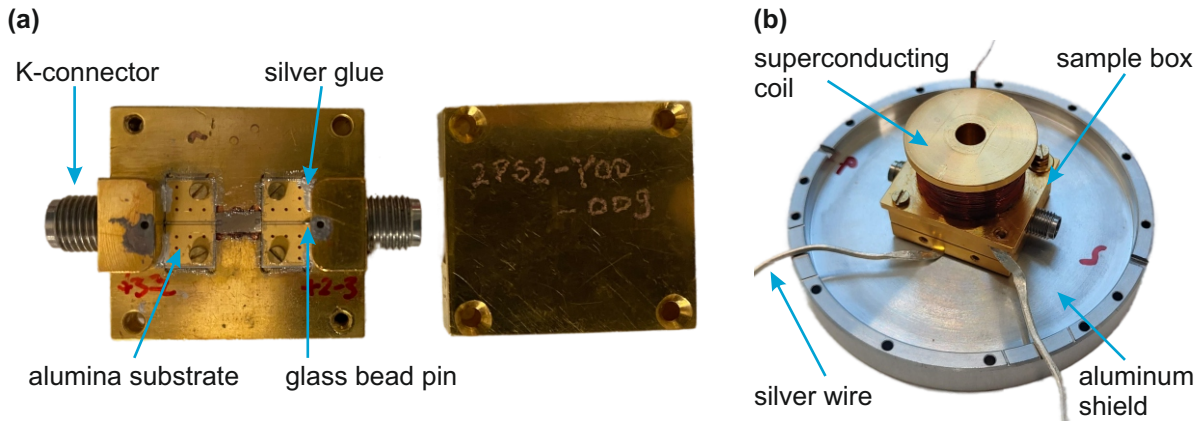   shield

Figure 5.9: (a) Photograph of an assembled sample box with the JPA chip located in the center. The signal and pump lines are connected to the sample box with a K-connector on either side. Aluminum substrates with Au waveguides in CPW geometry serve as an interface between the K-connectors and the JPA chip. (b) Photograph of a closed sample box with a superconducting coil for dc-flux biasing the JPA mounted on top. The sample box is thermalized via two silver wires to the sample rod and mounted into an aluminum box (only the bottom lid is shown) for magnetic shielding.

and provides good thermalization between sample box and chip. The ground plane of the JPA chip is galvanically connected to the sample box via a set of aluminum bonds. The sample box is equipped with two rf K-connectors [32] connecting the respective signal and pump cables. Glass beads serve as an interface between the K-connectors and the inner volume of the sample box. A direct connection between glass beads and respective CPW pads on the chip is challenging to establish. Hence, we make use of an additional interface in the form of a CPW transmission line on a gold-plated printed circuit board (PCB) on an alumina substrate [33]. Similar to the JPA chip, the ground plane of the CPW transmission line is galvanically coupled to the sample box via a set of aluminum bonds. On one side of the alumina substrate, a vertical edge to sample box prevents us from using bonds. Here, we resort to silver glue for establishing a good galvanic connection. The glass bead is soldered to the inner conductor of the PCB transmission line. Aluminum bonds establish a galvanic connection between the other end of the PCB transmission line and the designated signal (or pump) pad of the JPA chip. This assembly technique allows for a typical impedance matching of $50 \pm 3\,\Omega$. For low-loss signal propagation, we connect a superconducting coaxial NbTi cable to the signal port of the sample box. Since microwave losses are not as critical for the pump line, we employ flexible, normal-conducting rf cables [34]. For flux-tuning of the JPAs, we mount a custom-built superconducting coil on top of the respective JPA sample box, as depicted in Fig. 5.9(b). The coil holder is manufactured from OFHC copper and subsequently gold-plated, analogous to the sample

---

[32]K102F-R connector from `Anritsu`.

[33]Fabricated by `Rohde&Schwarz GmbH` with a $50\,\Omega$ impedance matching.

[34]`Minibend` microwave cables from `Huber+Suhner`.

(a)
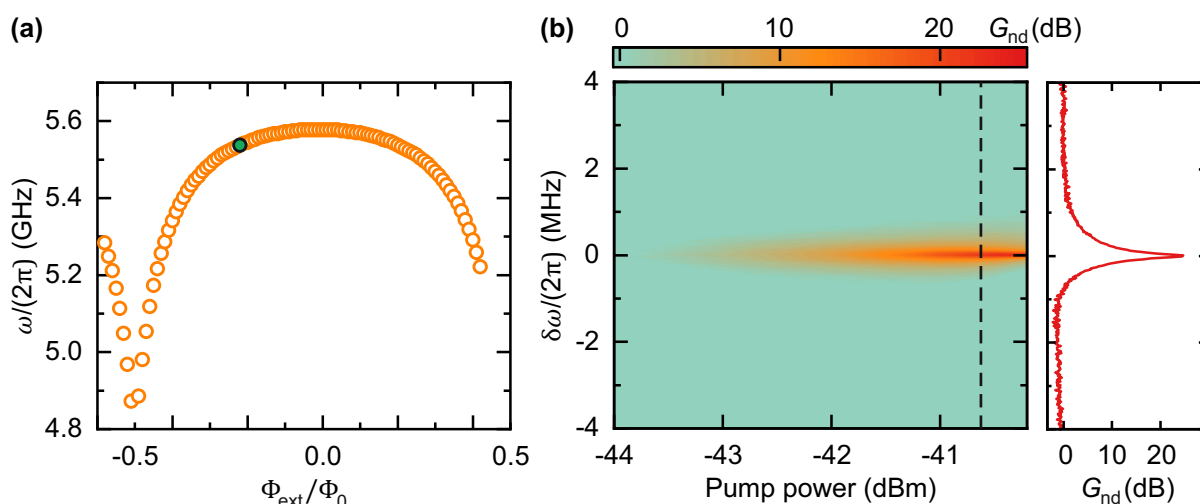
(b)

Figure 5.10: (a) Experimental JPA resonance frequency as a function of the externally applied magnetic flux, Φ_{ext}. (b) Measured nondegenerate gain spectrum G_{nd} as a function of the detuning $\delta\omega$ from the JPA resonance frequency and the JPA pump power referred to the input of the pump port. The working point in (b) coincides with the green data point in (a). The exemplary red spectrum on the right part in panel (b) is a line cut at a pump power of $-40.5\,\mathrm{dBm}$, illustrated by the black-dashed line.

box. For the coil, we employ 300 meters of single-filament NbTi wire[35]. Application of GE varnish to various layers of the coil during winding ensures good mechanical stability and thermalization. In order to confine the applied magnetic field and isolate the JPAs from each other, we place the sample box with coil inside a superconducting aluminum shield. The bottom part of such an aluminum shield is depicted in Fig. 5.9(b). This field confinement is fundamental for avoiding magnetic cross-talk between different JPAs, or other flux-controlled and flux-sensitive devices. For thermalization, two annealed silver wires with a flattened end are clamped between the aluminum shield and the sample box, and between the sample box and the coil holder, respectively. Finally, an input circulator enables measuring the JPA in a reflection-type configuration.

Flux characteristics   The magnetic-flux dependence of the JPA resonance frequency represents an important tool for harmonizing a multitude of JPAs towards one working frequency in advanced experiments [78, 80]. This flexibility is fundamentally important due to a limited reproducibility of system parameters in fabrication, which reflects in a variation of the bare resonance frequencies of the JPAs. We investigate the JPA frequency dependence on the externally applied magnetic field in frequency-resolved measurements, making use of a VNA[36]. The dc current flowing through the superconducting coil, I_{coil}, is applied with a dc current source[37]. Figure 5.10(a) shows a typical flux-dependent JPA res-

---

[35] C510/NbTi wire from `Supercon Inc`.

[36] ZVA24 vector network analyzer from `Rohde & Schwarz`.
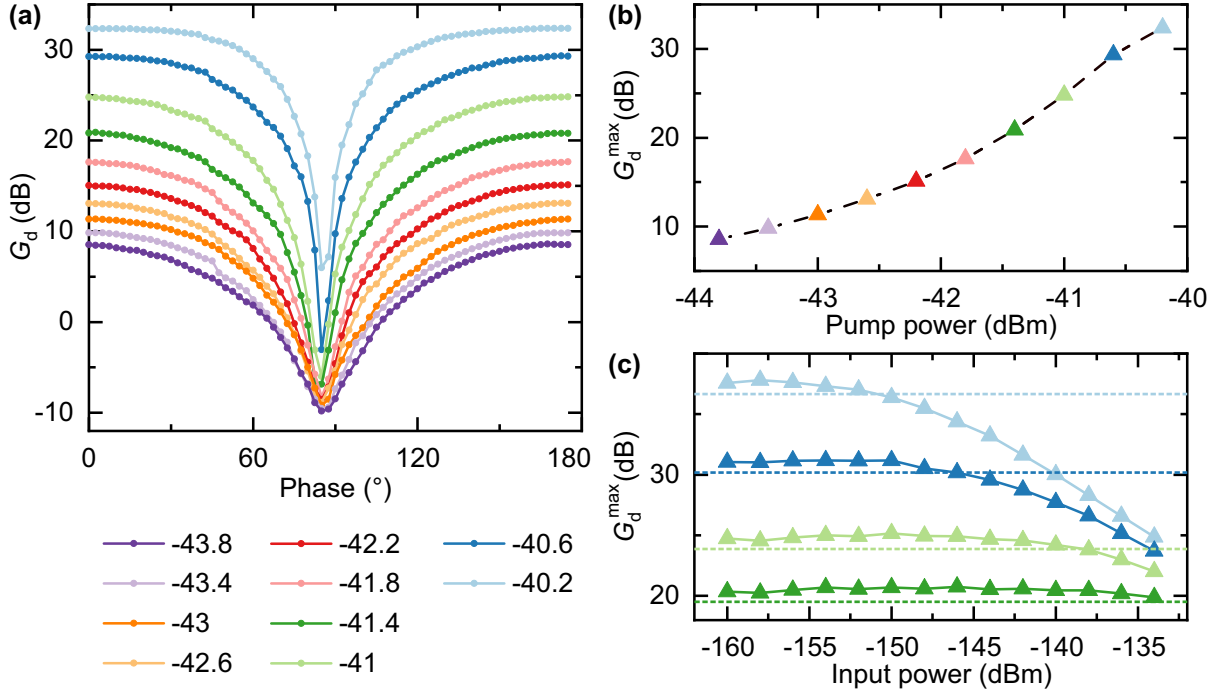
[37] 6241A wide ranging source from `ADCMT`.

Figure 5.11: (a) Experimentally measured phase-dependent degenerate gain G_d as a function of the relative phase between the coherent input signal and the pump tone for various pump powers given in dBm. (b) Maximum degenerate gain values G_d^{max} from (a) as a function of the pump power. (c) Maximum degenerate gain as a function of the coherent input power for different pump powers. The dashed horizontal lines illustrate the corresponding 1 dB compression thresholds. All powers are referred to the JPA pump port. The color code matches between all three panels.

onance response. The JPA resonance frequency follows the expected dependence according to Eq. (4.25). We find the current-flux conversion factor of $I_{coil}/\Phi_{ext} \simeq 0.182 \, \text{mA}/\Phi_0$.

Working frequency Based the measurement shown in Fig. 5.10(a), we fix the dc flux working point to a working frequency of 5.5232 GHz, highlighted as the green data point. While the tunability of the JPA covers a frequency span of approximately 800 MHz, the preferred working regime for our purposes is more narrow. On the one hand, a large slope of the resonance frequency, $\partial \omega_0 / \partial \Phi_{ext}$, makes the JPA sensitive to flux noise. Accordingly, a slight variation of Φ_{ext} results in a stronger shift in JPA resonance frequency in steeper regions [cf. Fig. 5.10(a)], which is why we typically try to avoid these working points. On the other hand, the required pump power to achieve a fixed gain increases with decreasing slope along the flux curve, because the effective pump driving strength is proportional to this slope [222]. As a consequence, pump-induced noise is more pronounced at flat regions of the flux curve for a fixed gain. Hence, we also try to circumvent JPA working points at vanishing slope. Note that this argumentation holds only for pump levels below the onset of higher-order nonlinearities. We use optimized attenuation in the JPA pump microwave

lines, typically, on the order of 30 to 40 dB, which may further limit operation of the JPAs in very flat regimes of the flux curve. This limitation comes from finite dynamic ranges of our room temperature microwave generators. In summary, we face a trade-off in the choice of the JPA working frequencies, which requires careful consideration for each experiment, due to conflicting requirements towards maximizing gain and minimizing noise.

Nondegenerate and degenerate gain In order to generate parametric gain with the JPA, we apply a coherent pump tone at the frequency $\omega_p = 2\omega_0$. Figure 5.10(b) depicts the spectrum of the nondegenerate gain G_{nd} as a function of the applied JPA pump power. The line cut at a pump power of about $-40.5\,\mathrm{dBm}$ in Fig. 5.10(b) shows an exemplary characteristic gain spectrum with a maximal nondegenerate gain $G_{nd} \simeq 25\,\mathrm{dB}$. In a next step, we investigate the phase-sensitive degenerate JPA gain, G_d. In this scope, we apply a weak coherent signal in the single-photon regime at half the pump frequency, $\omega_s = \omega_p/2$, coinciding with the JPA resonance frequency at the chosen working point of $\omega_0/(2\pi) = 5.5232\,\mathrm{GHz}$. For signal readout, we employ the dual-path receiver introduced earlier in Sec. 5.1.2 and determine the power of the amplified coherent tone based on the detected quadrature moments. Figure 5.11(a) shows the phase-dependent gain G_d for different pump powers. Note that the varying phase of the coherent tone is stabilized with respect to the respective pump phase. A calibration measurement with no pump applied provides the reference for calculating G_d. As expected, the JPA acts as a phase-sensitive amplifier, where effectively one quadrature of the incoming signal is amplified, while the orthogonal quadrature is deamplified. Figure 5.11(b) depicts the associated maximum degenerate gain values, G_d^{max}, as a function of the applied pump power. The extracted values of G_d^{max} provide part of the calibration for later studies presented in Ch. 6.

Quantum efficiency The quantum efficiency of JPAs can, in principle, exceed the SQL in the phase-sensitive regime [73, 75, 236]. In the following, we briefly introduce the measurement routine for quantum efficiency determination of flux-tunable JPAs. In a first step, we detune the JPA in frequency by changing the external dc flux, such that the JPA resonance is outside of the measurement bandwidth. Next, we vary the power, P_{in}, of a coherent input tone to calibrate the coherent photon number, $n_c = \langle \hat{n}_c \rangle$, with respect to the JPA input port using the reference-state reconstruction, as introduced earlier in Sec. 5.1.2. These two quantities are related linearly according to [222]

$$n_c(P_{in}) = cP_{in} + o, \tag{5.10}$$

where we treat c and o as free fitting parameters. After this calibration, we tune the JPA to the designated working frequency and apply a time-modulated measurement routine. We fix the JPA phase in a parallel configuration with respect to the coherent displacement

angle, $\gamma = \theta$, as defined in Ch. 2. Without loss of generality, we choose to amplify the q-quadrature. During one pulse of our time sequence, the coherent and pump tones are both applied. We extract the detected power, P_{on}, for the amplified q-quadrature from the first-order signal moment according to

$$P_{\mathrm{on}} = \frac{\kappa}{Z_0} \langle \hat{q} \rangle^2, \tag{5.11}$$

where κ is the PNCF. During a second pulse of our sequence, we record the power, P_{off}, associated with the q-quadrature without the pump tone. This reference enables a direct estimation of the degenerate JPA gain

$$G_{\mathrm{d}} = \frac{P_{\mathrm{on}}}{P_{\mathrm{off}}}. \tag{5.12}$$

With the reference point located directly after the JPA, we can additionally reconstruct the signal variance of the amplified quadrature while the JPA pump is on, given by

$$\sigma_{\mathrm{on}}^2 = \left[G_{\mathrm{d}}(\sigma_{\mathrm{in}}^2 + \sigma_\chi^2) \right] = \left[G_{\mathrm{d}}(\frac{1}{4} + \sigma_\chi^2) \right], \tag{5.13}$$

where $\sigma_{\mathrm{in}}^2 = \frac{1}{4}$ is the vacuum variance of our coherent input signal and σ_χ^2 denotes the added amplification noise, reflected in an enhanced variance associated with the q-quadrature. From Eq. (5.13), we can directly evaluate the unknown variance σ_χ^2 and use it for analysis of the quadrature quantum efficiency according to

$$\eta = \frac{1}{1 + 2\sigma_\chi^2}, \tag{5.14}$$

where $\sigma_\chi^2 \simeq n_{\mathrm{JPA}}/2 + A_{\mathrm{H}}/(2G_{\mathrm{d}})$. The quantity n_{JPA} is the noise added by the JPA, referred to its input. This noise depends on the JPA gain according to [73]

$$n_{\mathrm{JPA}}(G_{\mathrm{d}}) = \lambda(G_{\mathrm{d}} - 1)^\beta, \tag{5.15}$$

where λ and β are fitting parameters. Figure 5.12 depicts the measured JPA quantum efficiency η as a function of the degenerate gain, G_{d}. In agreement with the Friis formula, we account for the JPA noise and the HEMT noise, while neglecting further noise added by the remaining amplification chain. The displayed fit relies on Eqs. (5.14) and (5.15).

Compression   In realistic scenarios, JPAs operate as linear amplifiers only up to a finite signal input power due to compression effects caused by higher-order nonlinearities and pump depletion effects [163, 255, 256]. We introduce the 1 dB compression point as the

---

[38]Note that, without loss of generality, the displayed data in this figure is acquired with displaced squeezed states as an input to the JPA.

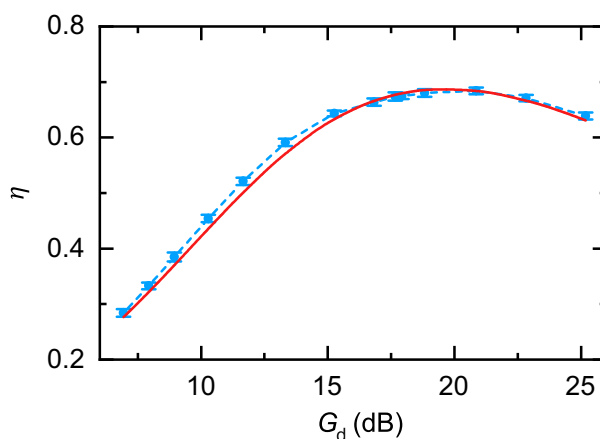**Figure 5.12:** Experimental JPA quantum efficiency, η, as a function of the degenerate gain, G_d. The blue symbols with associated error bars correspond to measured data, the blue dashed line is a guide to the eye. The red solid line is a fit to the data according to Eq. (5.14) and Eq. (5.15). The corresponding fit parameters are $\lambda = 0.048$ and $\beta = 0.42$.[38]

signal input level at which the maximum gain of the amplifier is decreased by $1\,\text{dB}$ with respect to its low power value [95]. Figure 5.11(c) shows the maximum degenerate gain as a function of the coherent signal power. Each data point is extracted from a measurement as shown in Figs. 5.11(a) and (b) for varying signal levels. We repeat the measurement for four different pump powers with a matching color code between Figs. 5.11(c) and (a). The flat plateaus represent the linear amplification regime. As expected, we observe compression effects appearing at progressively lower input powers with increasing pump powers.

Squeezing   Apart from amplification purposes, the generation of squeezed states is another key application of JPAs. The measurement routine for squeezed vacuum states is similar to the phase-sensitive gain scheme, but without a coherent input tone. Instead, the JPA phase-sensitively amplifies the incident weak thermal state, which can be well approximated by vacuum fluctuations. For these states, the squeeze level S can be calculated from the second-order moments [6]. Squeezing along the q- or p-quadrature, without loss of generality, enables extraction of the corresponding variances from the reconstructed signal moments according to [79]

$$\sigma_q^2 = \frac{1}{4}\left(\langle \hat{a}^2 \rangle + \langle (\hat{a}^\dagger)^2 \rangle + 2\langle \hat{a}^\dagger \hat{a} \rangle + 1\right), \tag{5.16}$$

$$\sigma_p^2 = \frac{1}{4}\left(\langle \hat{a}^2 \rangle + \langle (\hat{a}^\dagger)^2 \rangle - 2\langle \hat{a}^\dagger \hat{a} \rangle + 1\right). \tag{5.17}$$

The squeezed and anti-squeezed quadratures can be evaluated as $\sigma_s^2 = \min(\sigma_q^2, \sigma_p^2)$ and $\sigma_a^2 = \max(\sigma_q^2, \sigma_p^2)$, respectively. Figure 5.13(a) shows the reconstructed S as a function of the applied pump power. We observe a steady increase in S up to $S_{\text{max}} \simeq 8\,\text{dB}$. Beyond
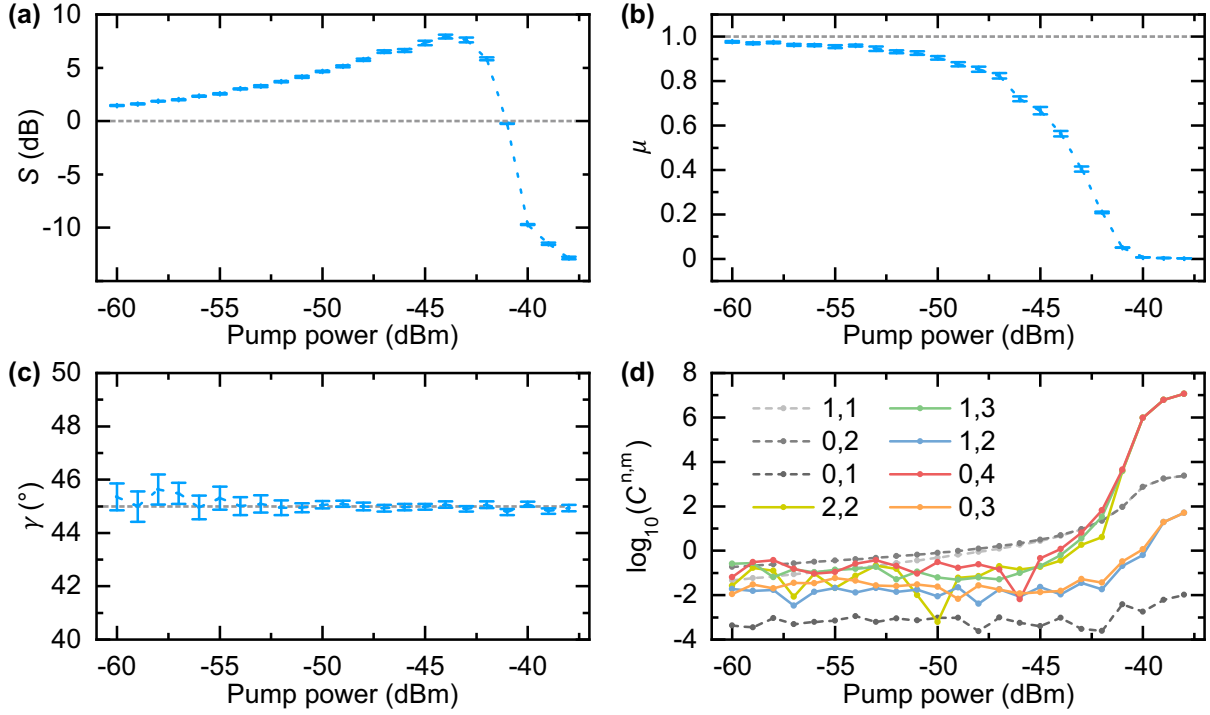
Figure 5.13: (a) Squeezing level S with associated statistical error bars as a function of the applied pump power referred to the JPA pump port. The gray-dashed line illustrates the vacuum limit, above which the reconstructed states are categorized as squeezed. (b) Corresponding reconstructed purity μ with associated statistical error bars, the upper bound of unity is depicted as the gray-dashed line. (c) Experimental squeeze angle γ for the target squeeze angle of 45°. (d) Absolute values of the cumulants $C^{n,m} = \langle\langle(\hat{a}^\dagger)^n\hat{a}^m\rangle\rangle$. The lines connecting the data points in panels (a) to (d) are a guide to the eye.

the associated pump power of approximately $-44\,\mathrm{dBm}$, the squeezing level abruptly decreases and exceeds the vacuum fluctuations, characterized by $S = 0\,\mathrm{dB}$. Figure 5.13(b) depicts the purity μ according to Eq. (2.26) of the investigated states. The purity steadily decreases with increasing pump power, and remains $\mu > 0.9$, close to unity, for pump powers up to $-50\,\mathrm{dBm}$. At this power, the corresponding squeezing level is $S \simeq 5\,\mathrm{dB}$. The monotonic decrease of μ potentially stems from higher-order nonlinearities, pump-induced noise, and gain-dependent environmental noise [73, 108, 163, 221, 222]. The squeezing angle is stabilized to 45° in the phase-locked loop, the reconstructed squeezing angle γ is shown in Fig. 5.13(c). The precision and variance of the phase stabilization increases with increasing pump power, due to larger powers of the generated output states and, thus, better SNRs in the phase estimation. Figure 5.13(d) depicts the corresponding absolute values of the cumulants. The cumulants the first two orders steadily increase and dominate at low pump powers, while the higher-order cumulants $n + m \geq 3$ stay constant at lower values. The fourth-order cumulants start rising at pump powers around $-45\,\mathrm{dBm}$ and surpass the second order cumulants at around $-43\,\mathrm{dBm}$. Beyond this threshold, the reconstructed states cannot be considered Gaussian anymore [108].

To conclude, the experimental techniques described in this chapter are the cornerstone for performing advanced quantum microwave experiments, such as the experimental study discussed in the next chapter. While the cryogenic part of the setup is the core of such experiments, the associated room temperature counterpart is of central importance for data detection and processing. Sophisticated measurement techniques, such as the output line calibration and a precise control of the JPAs, complement our tool set for conducting studies with quantum microwaves at frequencies of several gigahertz.

Chapter 6

Quantum microwave parametric interferometer
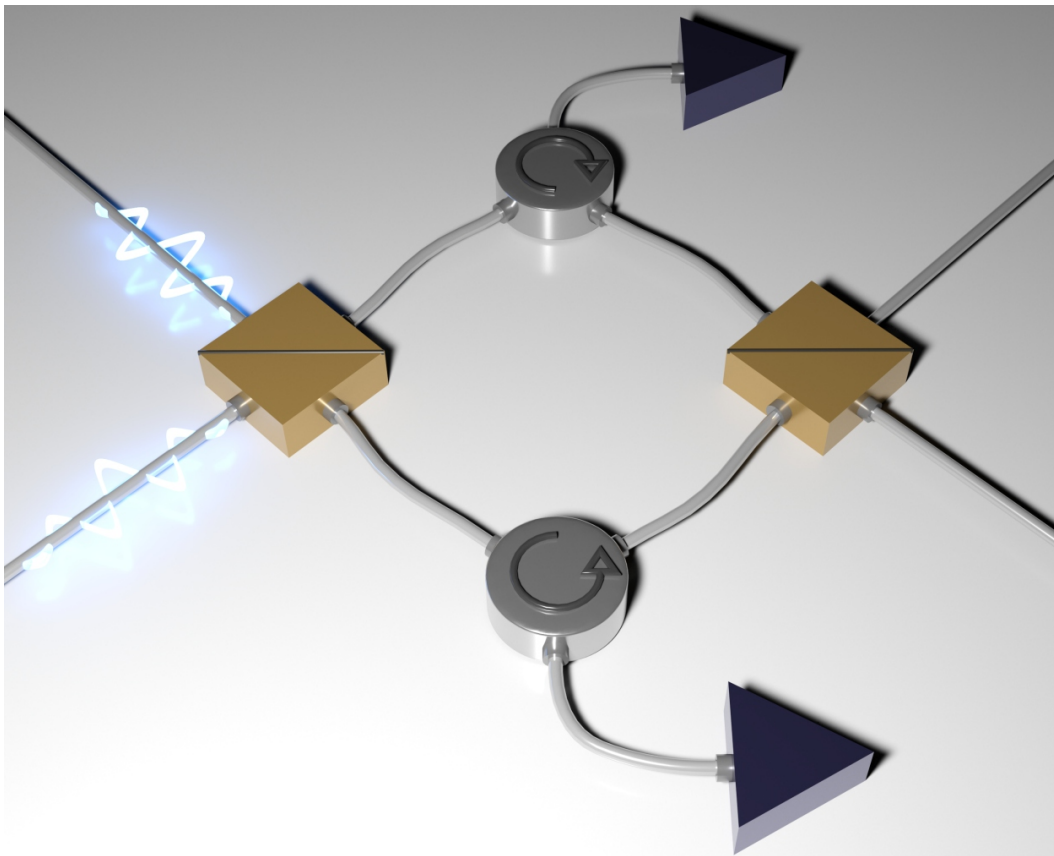
Interferometry is a fundamental technique of high precision measurements and metrology. In the broadest sense, coherent-wave interference can provide precise information on a variety of physical quantities, such as magnetic fields and gravitational waves, which directly or indirectly cause phase differences between the associated waves propagating along the two interferometer arms (one only can measure phase differences but not phases) [257]. The immense sensitivity of interferometers is based on the fact that tiny changes of the phase difference can be detected: for example, in the approach of gravitational-wave detection in the Laser Interferometer Gravitational Wave Observatory
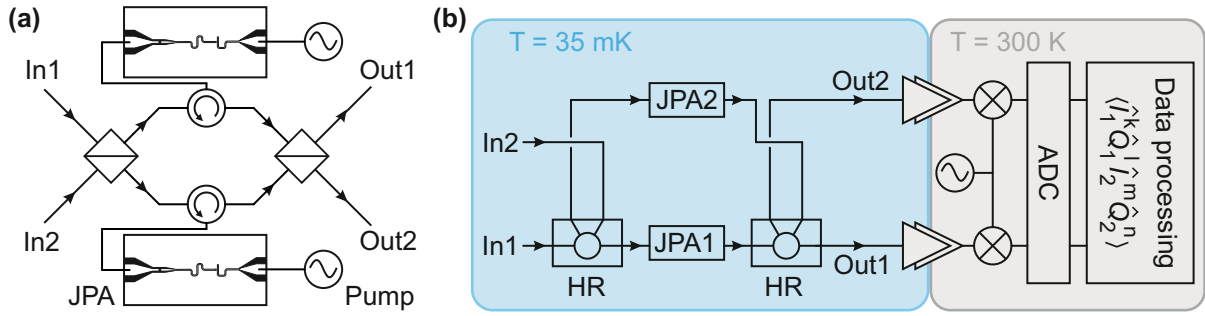
Figure 6.1: (a) General scheme of the QUMPI. Here, a circulator separates the incoming and outgoing signals for each JPA. (b) Details of the experimental setup consisting of a 180° hybrid ring (HR), which splits and symmetrically superimposes two incoming signals from ports In1 and In2, two JPAs for phase-sensitive amplification, and a second 180° HR, which completes the nonlinear interferometer. Output two-mode signals are detected with a heterodyne microwave receiver and digitally processed to extract statistical signal moments. The latter enable a full state tomography.

(LIGO), a gravitational wave passing over one arm of an interferometer changes its length, which affects the interference pattern and a resulting readout signal [258]. Classical interferometers, such as the Mach-Zehnder interferometer, typically rely on the injection of a coherent state into one port of a beam splitter, while only vacuum fluctuations enter the second port [259]. Their phase sensitivity is limited by the shot noise of the coherent signal, also known as the standard quantum limit (SQL). As the uncertainty in the photon number of a coherent state is $\sqrt{N}$, the one of the phase is $1/\sqrt{N}$ according to the Heisenberg uncertainty relation, leading to a signal-to-noise ratio (SNR) of $N/\sqrt{N}$. As a consequence, the SQL reflects in a $\sqrt{N}$ scaling of the SNR [40, 257]. This linear interferometer sensitivity can be improved by coupling quantum states, such as squeezed states, into the second beam splitter port [257, 260]. The use of squeezed states allows to reduce the detection noise below the SQL, which is equivalent to an augmented phase sensitivity [261]. Alternatively, the SQL can be overcome by using nonlinear elements, such as parametric amplifiers, leading to interactions between photons [262–265]. In principle, exploiting quantum correlations between photons in these states allows one to achieve the Heisenberg limit (HL) with a linear scaling of the SNR with respect to N [257, 266]. While nonlinear interferometers have been investigated at optical frequencies, the microwave domain, so far, remained largely unexplored due to relatively small energies of microwave photons with frequencies in the 1–10 GHz regime and the associated difficulty of single-photon detection [257, 265, 267, 268]. Meanwhile, quantum microwave sensing and communication represent novel and rapidly growing fields, which promise groundbreaking fundamental experiments and applications [52, 55, 78, 269]. The results presented in this chapter have been published in Ref. [80]. Parts of the text and figures are adapted from this reference.

In this chapter, we present an experimental realization of a nonlinear microwave interferometer making use of Josephson-junction-based superconducting quantum circuits,

illustrated in Fig. 6.1. This quantum microwave parametric interferometer (QUMPI) consists of two linear balanced microwave beam splitters and two nonlinear quantum devices in the form of flux-driven JPAs. Low-loss microwave cryogenic circulators are used to separate the incoming and outgoing signals of the JPAs. In Fig. 6.1(a), we present the idea of the QUMPI. Input signals at ports In1 and In2 are split and subsequently fed into JPA1 and JPA2. Then, the nonlinearly amplified signals from the JPAs interfere and leave the circuit at ports Out1 and Out2. Figure 6.1(b) shows a detailed circuit layout of our experiment. We employ two symmetric hybrid rings (HRs) as microwave beam splitters and two superconducting flux-driven JPAs. In Sec. 6.1 we perform a network analysis of the interferometer, which highlights the extreme phase-sensitivity of the circuit and the associated need for a precise geometric design of the interferometer building blocks. An understanding of measured data requires a detailed theoretical model of the QUMPI, which we introduce in Sec. 6.2. Details on the experimental setup are provided in Sec. 6.3. Finally, in Sec. 6.4, we present results of an in-depth experimental study of the QUMPI.

6.1 Frequency-resolved network analysis

Interferometric devices rely on a superposition of waves, such that the resulting interference effects directly reflect properties of the underlying electromagnetic waves. Apart from the amplitudes of these incoming waves, their respective phases and a resulting phase difference play a decisive role in interferometry. While the design of interferometers aims at a specific transformation of the incoming waves, realistic implementations always suffer from finite imperfections in the arm length or in the form of intrinsic losses. In superconducting circuits, losses are typically small and well known. Conversely, the macroscopic design of the QUMPI and the employed custom-built superconducting cables introduce finite length offsets in the interferometer arms. In the following, we perform a full network analysis of the QUMPI in order to investigate the robustness of the circuit towards relative length variations in the interferometer arms, and equivalently, variations of the phase difference. In this analysis, we focus on the passive part of the interferometer and assume the JPAs to be detuned in frequency. The remaining passive interferometer can be decomposed into two 180° HRs and various transmission lines. We use the even & odd mode approach [270] for this analysis, which is convenient for decomposing multi-port devices into a cascaded series of two-port networks [95]. The individual two-port devices can be straightforwardly described by the corresponding $ABCD$ matrices. In contrast to scattering matrices, these $ABCD$ matrices can be cascaded since they act as effective transfer matrices. For an intuitive understanding, consider the scattering matrix $\boldsymbol{\mathcal{S}}$ of a two-port device, defined as [95]

$$\begin{pmatrix} V_1^- \\ V_2^- \end{pmatrix} = \boldsymbol{\mathcal{S}} \begin{pmatrix} V_1^+ \\ V_2^+ \end{pmatrix} = \begin{pmatrix} S_{11} & S_{12} \\ S_{21} & S_{22} \end{pmatrix} \begin{pmatrix} V_1^+ \\ V_2^+ \end{pmatrix}, \tag{6.1}$$
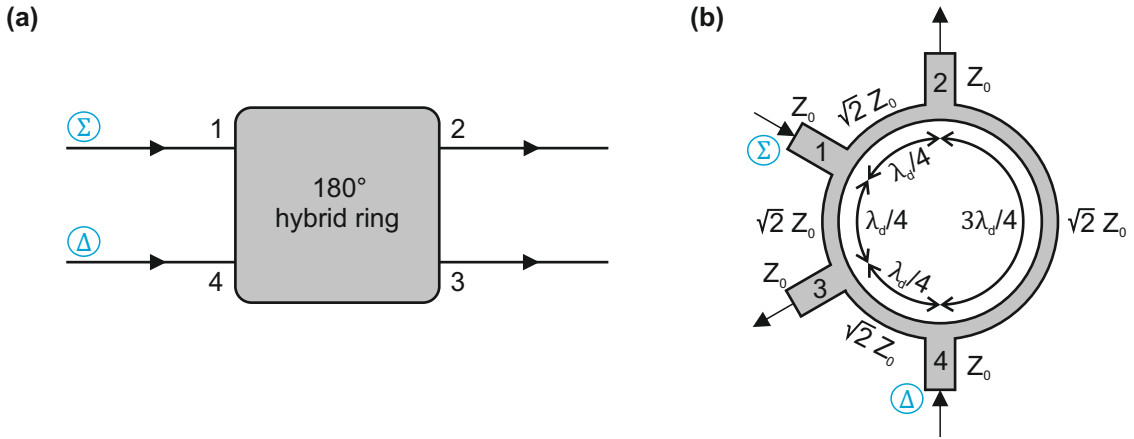
Figure 6.2: (a) Illustration of a 180° HR as a four-port device with two nominal input ports and two nominal output ports. (b) Geometric configuration and impedance specifications of the 180° HR depicted in (a).

relating the complex voltage amplitudes of the reflected waves, V_1^- and V_2^-, of a device under test to the incident wave amplitudes V_1^+ and V_2^+, where the subscripts denote the corresponding port. The associated two-port transfer matrix $\mathcal{T}$ is defined as

$$\begin{pmatrix} V_2^- \\ V_2^+ \end{pmatrix} = \mathcal{T} \begin{pmatrix} V_1^+ \\ V_1^- \end{pmatrix} = \begin{pmatrix} T_{11} & T_{12} \\ T_{21} & T_{22} \end{pmatrix} \begin{pmatrix} V_1^+ \\ V_1^- \end{pmatrix}, \tag{6.2}$$

connecting the voltages at the output port 2, incident (V_2^+) as well as reflected (V_2^-), to the voltages V_1^+ and V_1^- at the input port 1. As a result, transfer matrices can be easily cascaded, which is useful for modeling a sequence of devices that are connected back-to-back. Based on such 2×2 transfer matrices, we derive the full scattering matrix of the interferometer. For details on microwave network analysis, we refer the reader to Ref. [95].

180° hybrid ring　　The 180° HR represents a central building block of the QUMPI and corresponds to a four-port network with a 180° phase shift between the two output ports, schematically depicted in Fig. 6.2. The device has one symmetric input, denoted by the $\sum$ symbol, and an asymmetric input port, illustrated by the Δ symbol. With respect to the port labeling according to Fig. 6.2, a signal applied to port 1 is split in a balanced manner and couples to ports 2 and 3 with an identical phase, while port 4 is isolated. An input signal applied to port 4 is also evenly split and leaves the HR at ports 2 and 3, with port 1 being isolated. In this case, the signal leaving the HR at port 2 acquires a phase difference of 180° with respect to the signal leaving at port 3. The ideal scattering matrix

for the 180° HR is given by [95]

$$\boldsymbol{S}_{\text{HR}} = \frac{-i}{\sqrt{2}} \begin{pmatrix} 0 & 1 & 1 & 0 \\ 1 & 0 & 0 & -1 \\ 1 & 0 & 0 & 1 \\ 0 & -1 & 1 & 0 \end{pmatrix}. \tag{6.3}$$

The basic design criteria for a 180° HR are shown in Fig. 6.2(b). The design wavelength λ_{d} determines the respective lengths of the ring segments, while the impedance of the transmission lines forming the ring is a factor of $\sqrt{2}$ larger than the characteristic input impedance Z_0.

Geometric symmetries in a circuit result in well-defined relationships between arbitrary waves that symmetrically enter the circuit, which simplifies a corresponding circuit analysis. In the following, we perform such a symmetry-based approach called the even-odd analysis [270] of the 180° HR. The even-odd analysis technique [270] allows for decomposing the system along its symmetry plane into a superposition of one even excitation and one odd excitation with a respective wave amplitude of 1/2, as illustrated in Figs. 6.3(a) and (b), respectively. We start by analyzing an incident wave at port 1 of unit amplitude. Based on the design, the wave splits into two components that can constructively interfere at ports 2 and 3. At port 4, the divided wave components arrive 180° out of phase and destructively interfere. Here, the even case corresponds to an even polarity (++) of the respective 1/2 excitations at ports 1 and 3, while odd refers to a corresponding odd polarity (+-). The result of the even-odd decomposition is a 2-port network that we can describe via cascading the known transfer matrices of the respective sub-components, i.e., open stubs, shorted stubs, and transmission lines, shown in Fig. 6.4. The transfer matrices of an open stub [Fig. 6.4(a)] and a shorted stub [Fig. 6.4(b)] as a function of the signal wavelength λ, segment length l, and impedance Z, are

$$\begin{pmatrix} A & B \\ C & D \end{pmatrix}_{\text{O}} = \begin{pmatrix} 1 & 0 \\ \frac{i}{Z} \tan\left(\frac{2\pi l}{\lambda}\right) & 1 \end{pmatrix} \quad \text{and} \quad \begin{pmatrix} A & B \\ C & D \end{pmatrix}_{\text{S}} = \begin{pmatrix} 1 & 0 \\ -\frac{i}{Z} \cot\left(\frac{2\pi l}{\lambda}\right) & 1 \end{pmatrix}, \tag{6.4}$$

respectively. The transfer matrix of a transmission line [Fig. 6.4(c)] can be expressed as

$$\begin{pmatrix} A & B \\ C & D \end{pmatrix}_{\text{TL}} = \begin{pmatrix} \cos\left(\frac{2\pi l}{\lambda}\right) & iZ\sin\left(\frac{2\pi l}{\lambda}\right) \\ \frac{i}{Z}\sin\left(\frac{2\pi l}{\lambda}\right) & \cos\left(\frac{2\pi l}{\lambda}\right) \end{pmatrix}. \tag{6.5}$$

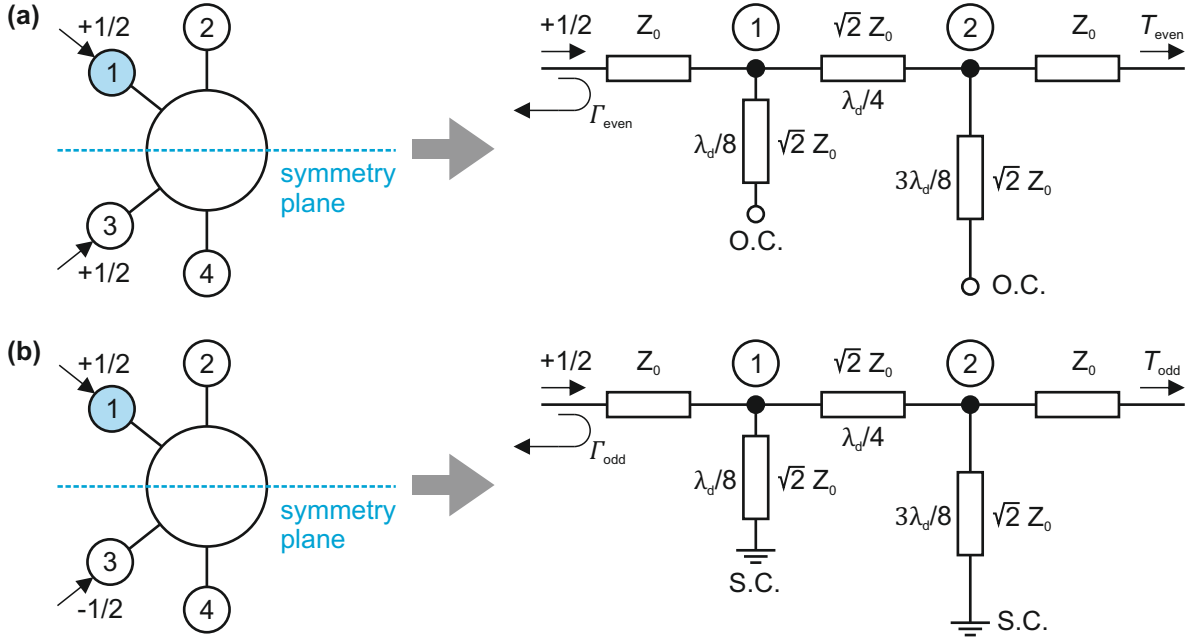The resulting transfer matrix for the even case and excitation via port one (denoted by

Figure 6.3: Even-odd decomposition of the HR for unit amplitude excitation at port 1. (a) The even-mode case yields an effective open circuit (O.C.) along the symmetry plane. (b) The circuit equivalent for the odd case corresponds to a shorted circuit (S.C.) along the symmetry plane. The O.C. in (a) and S.C. in (b) stem from interference effects of the respective excitations due to the system symmetry.

the superscript) is given by

$$
\begin{pmatrix} A & B \\ C & D \end{pmatrix}^1_{\text{even}} = \begin{pmatrix} A & B \\ C & D \end{pmatrix}_{\text{O}} \cdot \begin{pmatrix} A & B \\ C & D \end{pmatrix}_{\text{TL}} \cdot \begin{pmatrix} A & B \\ C & D \end{pmatrix}_{\text{O}} =
$$
$$
= \begin{pmatrix} 1 & 0 \\ \frac{i}{\sqrt{2}Z_0} \tan\left(\frac{2\pi}{\lambda}\frac{\lambda_d}{8}\right) & 1 \end{pmatrix} \begin{pmatrix} \cos\left(\frac{2\pi}{\lambda}\frac{\lambda_d}{4}\right) & i\sqrt{2}Z_0 \sin\left(\frac{2\pi}{\lambda}\frac{\lambda_d}{4}\right) \\ \frac{i}{\sqrt{2}Z_0} \sin\left(\frac{2\pi}{\lambda}\frac{\lambda_d}{4}\right) & \cos\left(\frac{2\pi}{\lambda}\frac{\lambda_d}{4}\right) \end{pmatrix} \begin{pmatrix} 1 & 0 \\ \frac{i}{\sqrt{2}Z_0} \tan\left(\frac{2\pi}{\lambda}\frac{3\lambda_d}{8}\right) & 1 \end{pmatrix},
$$
(6.6)

where we set $Z = \sqrt{2}Z_0$ and inserted the corresponding segment lengths from Fig. 6.3 according to the HR design from Fig. 6.2 into Eqs. (6.4) and (6.5). Similarly, the odd decomposition yields

$$
\begin{pmatrix} A & B \\ C & D \end{pmatrix}^1_{\text{odd}} = \begin{pmatrix} A & B \\ C & D \end{pmatrix}_{\text{S}} \cdot \begin{pmatrix} A & B \\ C & D \end{pmatrix}_{\text{TL}} \cdot \begin{pmatrix} A & B \\ C & D \end{pmatrix}_{\text{S}} =
$$
$$
= \begin{pmatrix} 1 & 0 \\ \frac{-i}{\sqrt{2}Z_0} \cot\left(\frac{2\pi}{\lambda}\frac{\lambda_d}{8}\right) & 1 \end{pmatrix} \begin{pmatrix} \cos\left(\frac{2\pi}{\lambda}\frac{\lambda_d}{4}\right) & i\sqrt{2}Z_0 \sin\left(\frac{2\pi}{\lambda}\frac{\lambda_d}{4}\right) \\ \frac{i}{\sqrt{2}Z_0} \sin\left(\frac{2\pi}{\lambda}\frac{\lambda_d}{4}\right) & \cos\left(\frac{2\pi}{\lambda}\frac{\lambda_d}{4}\right) \end{pmatrix} \begin{pmatrix} 1 & 0 \\ \frac{-i}{\sqrt{2}Z_0} \cot\left(\frac{2\pi}{\lambda}\frac{3\lambda_d}{8}\right) & 1 \end{pmatrix}.
$$
(6.7)

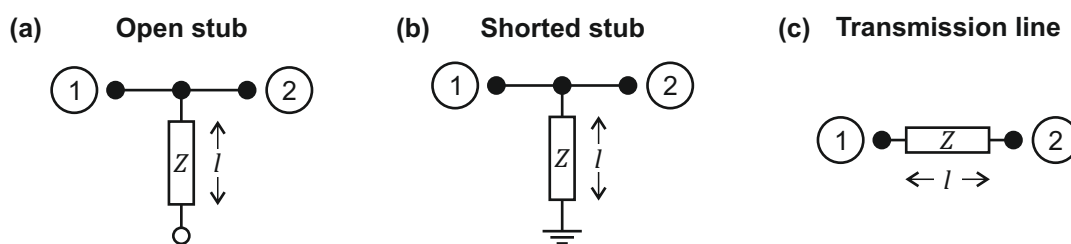**Figure 6.4:** Decomposed circuit sub-components with known $ABCD$ matrices.

In a next step, we transform the even and odd transfer matrices into 2×2 scattering matrices according to

$$S_{11} = \frac{A + \frac{B}{Z_0} - CZ_0 - D}{A + \frac{B}{Z_0} + CZ_0 + D},$$

(6.8)

$$S_{12} = S_{21} = \frac{2}{A + \frac{B}{Z_0} + CZ_0 + D},$$

(6.9)

$$S_{22} = \frac{-A + \frac{B}{Z_0} - CZ_0 + D}{A + \frac{B}{Z_0} + CZ_0 + D}.$$

(6.10)

For arbitrary waves, the transmission coefficients T and reflection coefficients Γ are related to the scattering matrices via

$$T = S_{21} \quad \text{and} \quad \Gamma = S_{11}.$$

(6.11)

Accordingly, we can evaluate the even coefficients, T_{even} and Γ_{even}, as well as the odd coefficients, T_{odd} and Γ_{odd}. In a superposition, the sum of the even case and the odd case corresponds to a single, unit-amplitude incoming signal at port 1. Similarly, the output signals are formed by a superposition of the even mode and odd mode results. The resulting vector amplitudes of the output signals at the four ports are given by [95]

$$B_1^1 = \frac{1}{2}\Gamma_{\text{even}} + \frac{1}{2}\Gamma_{\text{odd}},$$

(6.12)

$$B_2^1 = \frac{1}{2}T_{\text{even}} + \frac{1}{2}T_{\text{odd}},$$

(6.13)

$$B_3^1 = \frac{1}{2}\Gamma_{\text{even}} - \frac{1}{2}\Gamma_{\text{odd}},$$

(6.14)

$$B_4^1 = \frac{1}{2}T_{\text{even}} - \frac{1}{2}T_{\text{odd}}.$$

(6.15)

where the superscript denotes the incident wave at port one. These B-entries coincide with the final scattering matrix entries, since the input wave amplitude is unity [95]. To this end, we can calculate the first and third columns of the final 4×4 scattering matrix
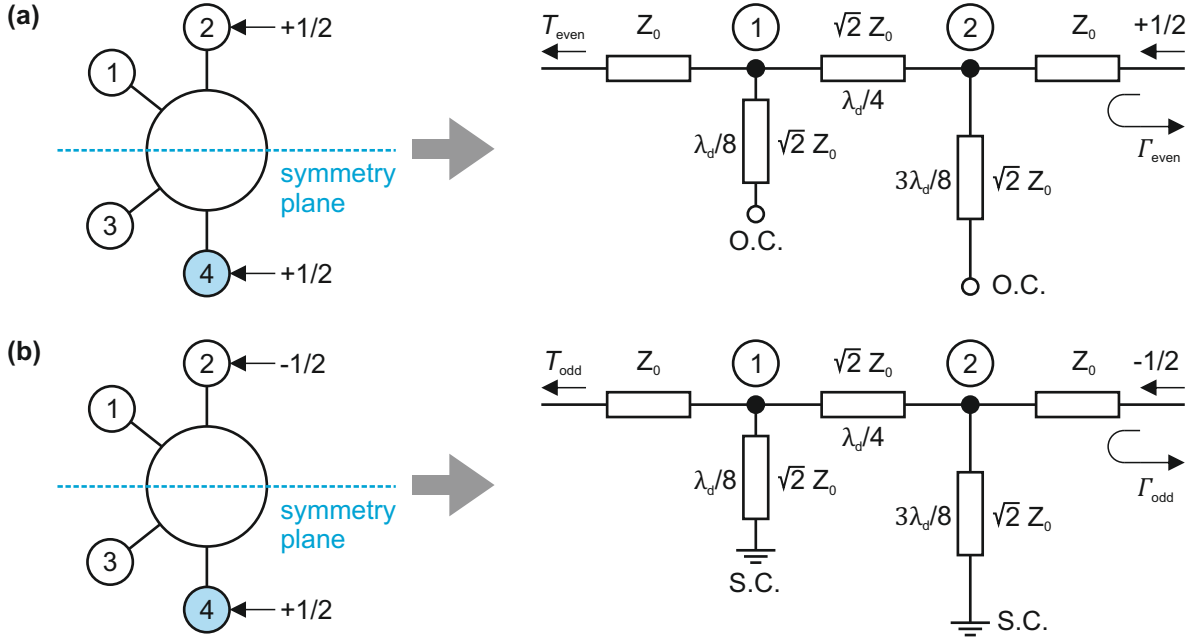
Figure 6.5: Even-odd decomposition of the HR for unit amplitude excitation at port 4. (a) The even-mode case yields an effective open circuit along the symmetry plane. (b) The circuit equivalent for the odd case corresponds to a shorted circuit along the symmetry plane.

of the 180° HR

$$\boldsymbol{\mathcal{S}}_{\text{HR}} = \begin{pmatrix} B_1^1 & B_2^4 & B_3^1 & B_4^4 \\ B_2^1 & B_1^4 & B_4^1 & B_3^4 \\ B_3^1 & B_4^4 & B_1^1 & B_2^4 \\ B_4^1 & B_3^4 & B_2^1 & B_1^4 \end{pmatrix}, \tag{6.16}$$

where the superscripts denote the incident wave at ports one and four. Note that the scattering matrix in Eq. (6.16) simplifies to the ideal case [cf. Eq. (6.3)] for an incoming excitation at the design wavelength $\lambda = \lambda_{\text{d}}$. The second and fourth columns of $\boldsymbol{\mathcal{S}}_{\text{HR}}$ can be calculated by repetition of the even-odd analysis with port four as an active port, shown in Figs. 6.5(a) and (b). For an incoming wave at port 4, the two divided wave components travel along the ring and arrive in phase at ports 2 and 3 to interfere constructively. Note that there is a 180° phase difference between the output of the two ports. At port 1, the wave components interfere in a destructive manner and cancel each other. For the sake of conciseness, we do not show each step in the analysis of port 4, which can be conducted in a straightforward manner analogous to the wave excitation at port 1. Figure 6.6 shows the complex frequency-dependent scattering parameters according to Eq. (6.16) for an incoming wave at port 1 and a design frequency $\omega_{\text{d}}/(2\pi) = 5.75\,\text{GHz}$ of the 180° HR. Strong signal suppression can be observed for the reflection (S_{11}) and isolation (S_{41}) magnitudes in Fig. 6.6(a). The signal is evenly split ($-3\,\text{dB}$) between port 2 (S_{21}) and port 3 (S_{31}) at $\omega_{\text{d}}/(2\pi) = 5.75\,\text{GHz}$ over a flat bandwidth of roughly 750 MHz. With port 1 as the symmetric input port, the signals leave ports 2 and 3 in phase, shown
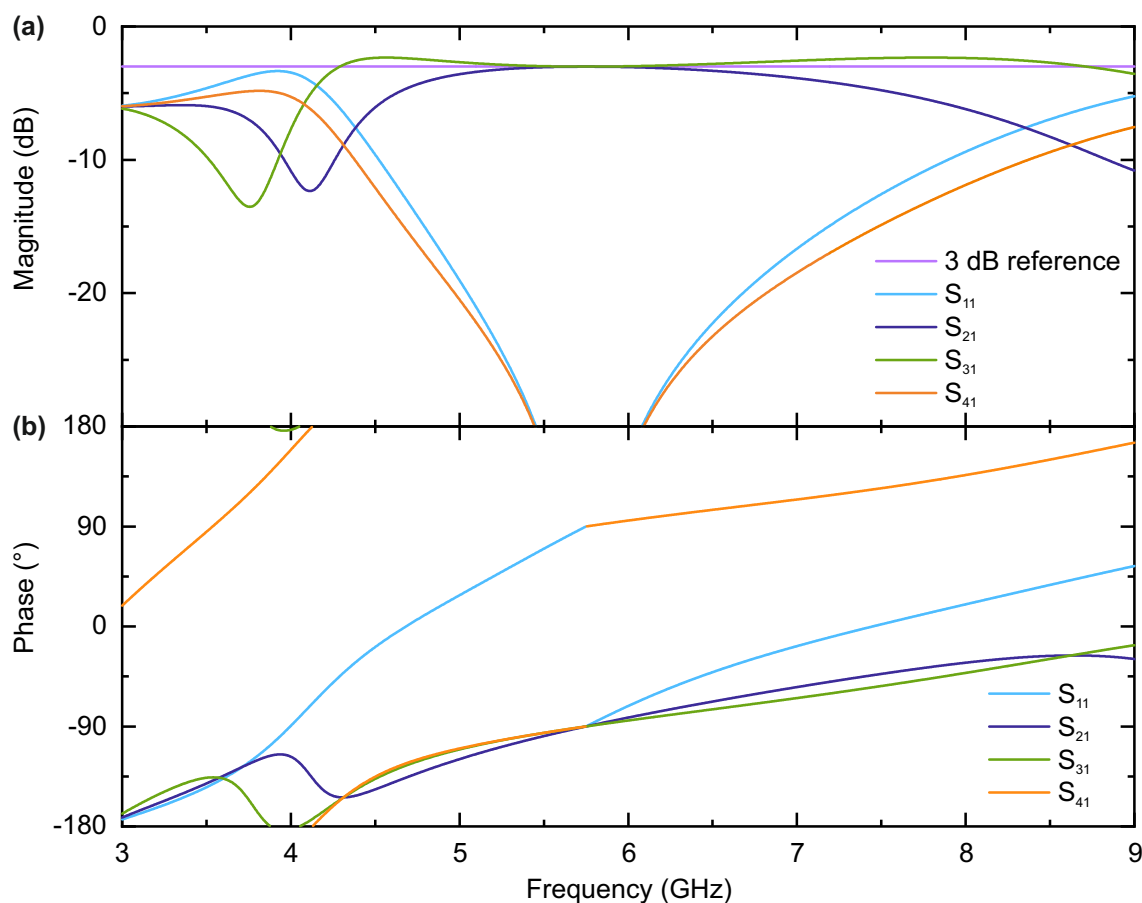
Figure 6.6: Theoretical (a) magnitude and (b) phase of the complex scattering parameters of a 180°
HR with design frequency $\omega_d/(2\pi) = 5.75\,\text{GHz}$ for an excitation at the symmetric port 1
according to the scattering matrix derived in Eq. (6.16).

in Fig. 6.6(b). For comparison, we plot the calculated scattering spectrum for an incoming
wave at the asymmetric port 4 in Fig. 6.7. Analogous to Fig. 6.6(a), we observe a strong
signal damping in reflection (S_{44}) and isolation (S_{14}) combined with an even splitting
of the incoming wave at ports 2 and 3, as depicted in Fig. 6.7(a). The associated phase
response shown in Fig. 6.7(b) illustrates the 180° phase difference between port 2 and port
3 at the design frequency.

Scattering parameters of the interferometer   A full network analysis of the passive
interferometer can be conducted by cascading the transfer matrices of its building blocks
according to

$$\mathcal{T}_{\text{QUMPI}} = \mathcal{T}_{\text{HR}} \cdot \mathcal{T}_{\text{TL}} \cdot \mathcal{T}_{\text{HR}}, \tag{6.17}$$

where $\mathcal{T}_{\text{QUMPI}}$, $\mathcal{T}_{\text{HR}}$, and $\mathcal{T}_{\text{TL}}$ are the 4×4 transfer matrices of the QUMPI, the
180° HR, and the transmission lines connecting the two HRs, respectively. In a first step,
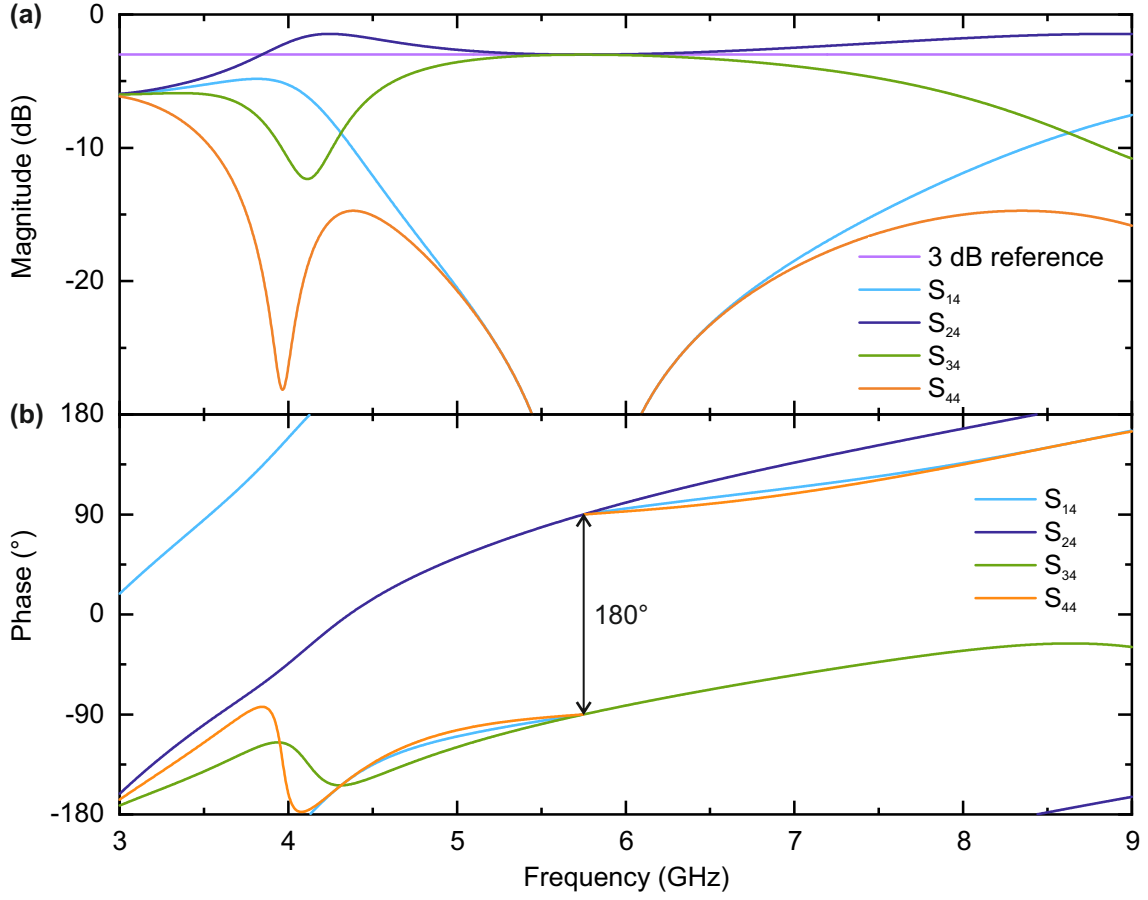we transform the 4×4 HR scattering matrix $\boldsymbol{\mathcal{S}}_{\text{HR}}$ from Eq. (6.16) into the corresponding

Figure 6.7: Theoretical (a) magnitude and (b) phase of the complex scattering parameters of a 180°
HR with design frequency $\omega_{\mathrm{d}}/(2\pi) = 5.75\,\mathrm{GHz}$ for an excitation at the asymmetric port 4
according to the scattering matrix derived in Eq. (6.16).

transfer matrix

$$
\boldsymbol{\mathcal{T}}_{\mathrm{HR}} = \begin{pmatrix} \mathcal{T}_{11} & \mathcal{T}_{12} & \mathcal{T}_{13} & \mathcal{T}_{14} \\ \mathcal{T}_{21} & \mathcal{T}_{22} & \mathcal{T}_{23} & \mathcal{T}_{24} \\ \mathcal{T}_{31} & \mathcal{T}_{32} & \mathcal{T}_{33} & \mathcal{T}_{34} \\ \mathcal{T}_{41} & \mathcal{T}_{42} & \mathcal{T}_{43} & \mathcal{T}_{44} \end{pmatrix}. \tag{6.18}
$$

The explicit expressions for calculating an arbitrary transfer matrix based on a known
scattering matrix of dimension 4×4 are provided in Appendix B. The two interferometer
arms can be straightforwardly modeled by the transfer matrix

$$
\boldsymbol{\mathcal{T}}_{\mathrm{TL}} = \begin{pmatrix} \exp(-\mathrm{i}\,2\pi l_1/\lambda) & 0 & 0 & 0 \\ 0 & \exp(-\mathrm{i}\,2\pi l_1/\lambda) & 0 & 0 \\ 0 & 0 & \exp(-\mathrm{i}\,2\pi l_2/\lambda) & 0 \\ 0 & 0 & 0 & \exp(-\mathrm{i}\,2\pi l_2/\lambda) \end{pmatrix}, \tag{6.19}
$$

where l_1 and l_2 are the two interferometer arm lengths, respectively. Here, we assume

lossless signal propagation along the interferometer arms, which is appropriate based on the low losses $< 0.3\,\mathrm{dB/m}$ of our employed superconducting cables (cf. Sec. 5.1.1) and geometric arm lengths $\simeq 0.5\,\mathrm{m}$. Finally, we obtain the full scattering matrix of the entire circuit by inverting the linear system given in Appendix B.

Figures 6.8(a) to (c) show the theoretical magnitude of the scattering parameters of the 4×4 network for an excitation at port 1 of the interferometer for different arm length differences $\Delta l = l_2 - l_1$, where l_1 and l_2 are the respective interferometer arm lengths. We observe constructive interference of the incoming signal at output port 3 (S_{31}) with approximately $0\,\mathrm{dB}$ attenuation over a flat bandwidth of more than $2\,\mathrm{GHz}$ around the center frequency of $5.75\,\mathrm{GHz}$ for a balanced configuration with $\Delta l = 0$, shown in Fig. 6.8(a). This case corresponds to the ideal design. Signal transmission through port 2 is strongly attenuated by more than $20\,\mathrm{dB}$ over this bandwidth. Similarly, reflection (S_{11}) and isolation (S_{41}) are heavily suppressed. Already a small arm length asymmetry, $\Delta l = \lambda/4$, which corresponds to a length of approximately $9.5\,\mathrm{mm}$ in our superconducting cable at the carrier frequency of around $5.5\,\mathrm{GHz}$, results in a drastically different setting, depicted in Fig. 6.8(b). In this configuration, the two output ports are balanced with around $3\,\mathrm{dB}$ of attenuation at the design frequency, which can decisively affect the functionality of the interferometer. For the configuration of $\Delta l = 0.45\lambda$, shown in Fig. 6.8(c), we observe an inverted scenario with respect to Fig. 6.8(a). Here, the incoming signal constructively interferes at the interferometer output port 2, while being strongly suppressed at port 3. Additionally, we observe a strong frequency dependence of the scattering parameters, where S_{21} and S_{31} are almost balanced at $-3\,\mathrm{dB}$ at $5.5\,\mathrm{GHz}$. The observed strong dependence of the interferometer response as a function of the arm length difference is exactly what we expect from such a device, since we effectively vary the overall phase difference between the two arms, which coincides with the operation of a classical Mach-Zehnder interferometer. However, the QUMPI additionally encompasses active components in the form of JPAs, which we intend to operate at a fixed frequency. Accordingly, we aim towards a well-defined circuit design of the interferometer with $\Delta l = 0$, corresponding to Fig. 6.8(a).

6.2 Frequency-degenerate theory model

After the frequency-resolved analysis in the previous section, we investigate the expected characteristics of the QUMPI at the designated working frequency of $\omega/2\pi = 5.48\,\mathrm{GHz}$ based on the input-output formalism. The nonlinear interferometer is modeled in a step-wise approach as a sequence of different operations, as depicted in Fig. 6.9. Since the thermal population of our states at the carrier frequency of $\omega/2\pi = 5.48\,\mathrm{GHz}$ and with the effective temperature of $T \simeq 50\,\mathrm{mK}$ is small, $n_{\mathrm{th}} = 1/(\exp(\hbar\omega/k_{\mathrm{B}}T) - 1) \simeq 5 \cdot 10^{-3} \ll 1$, we assume vacuum states as both signal inputs, as discussed in Sec. 5.1.2. The initial coherent states $\hat{a}_k$ ($k = 1, 2$) with complex displacement amplitudes α_k are modeled by
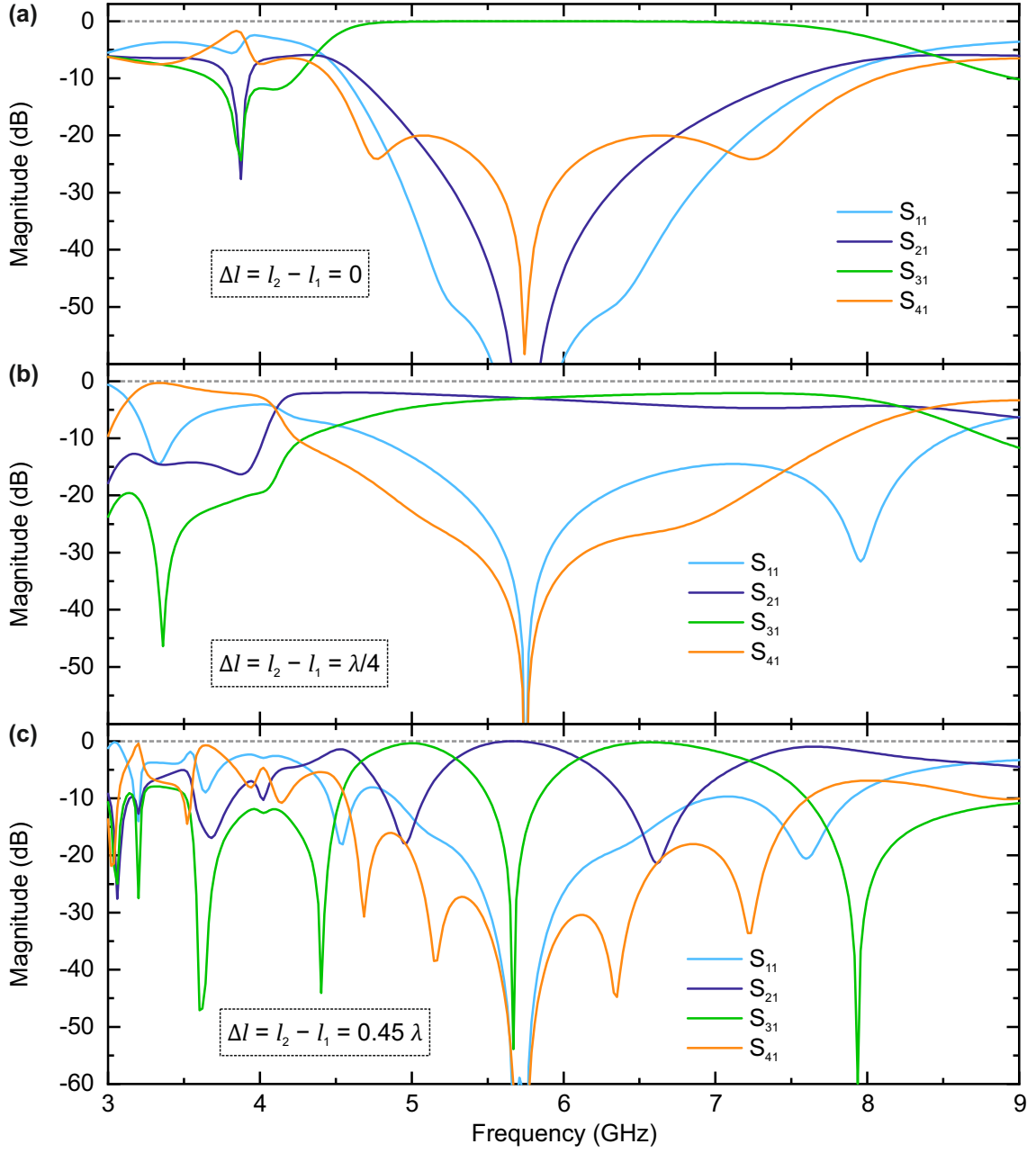
Figure 6.8: Theoretical magnitude of the complex scattering parameters of the passive part of the
QUMPI as a function of the signal frequency for an excitation at port 1 and (a) identical arm
lengths with $\Delta l = l_2 - l_1 = 0$, where l_1 and l_2 are the respective interferometer arm lengths.
Panel (b) depicts the associated scattering parameters for an arm length offset corresponding
to $\Delta l = \lambda/4$ at the frequency of $5.5\,\text{GHz}$. Panel (c) shows the results of the network analysis
for $\Delta l = 0.45\,\lambda$ at $5.5\,\text{GHz}$. The shown curves are evaluated based on Eq. (6.17).

applying the displacement operator $\hat{D}(\alpha_k)$ to vacuum, $\hat{v}_k$,

$$\hat{a}_k = \hat{v}_k + \alpha_k. \tag{6.20}$$

First, the signals of the two input lines are superimposed at an ideal 180° HR, which we model as

$$\hat{B}_k^\dagger \begin{pmatrix} \hat{a}_1 \\ \hat{a}_2 \end{pmatrix} \hat{B}_k = \frac{1}{\sqrt{2}} \begin{pmatrix} -1 & 1 \\ 1 & 1 \end{pmatrix} \begin{pmatrix} \hat{a}_1 \\ \hat{a}_2 \end{pmatrix}, \tag{6.21}$$

with $k \in \{1, 2\}$. The expression used in Eq. (6.21) corresponds to the ideal scattering matrix in Eq. (6.3), which is an appropriate assumption based on our working frequency $\omega/2\pi = 5.48\,\text{GHz}$ being well within the bandwidth $\simeq 750\,\text{MHz}$ of the HR with a design frequency $\omega_\text{d}/2\pi = 5.75\,\text{GHz}$. The losses due to insertion, connectors, and cable attenuation are modeled with a non-unitary loss operator according to

$$\hat{L}_j^\dagger \begin{pmatrix} \hat{a}_1 \\ \hat{a}_2 \end{pmatrix} \hat{L}_j = \begin{pmatrix} \sqrt{1 - \varepsilon_j}\,\hat{a}_1 + \sqrt{\varepsilon_j}\,\hat{v}_1 \\ \sqrt{1 - \varepsilon_j}\,\hat{a}_2 + \sqrt{\varepsilon_j}\,\hat{v}_2 \end{pmatrix}, \tag{6.22}$$

with $j \in \{1, 2, 3\}$. The phases ϕ_k that are acquired by the signals traveling along each interferometer arm are modeled as

$$\hat{P}^\dagger \begin{pmatrix} \hat{a}_1 \\ \hat{a}_2 \end{pmatrix} \hat{P} = \begin{pmatrix} e^{\text{i}\phi_1} & 0 \\ 0 & e^{\text{i}\phi_2} \end{pmatrix} \begin{pmatrix} \hat{a}_1 \\ \hat{a}_2 \end{pmatrix}, \tag{6.23}$$

which are connected to the interferometer arm lengths via $\phi_k = 2\pi l_k/\lambda$ [cf. Eq. (6.19)]. Next, the two JPAs perform a phase-sensitive amplification which we model by a squeezing operator according to

$$\hat{S}^\dagger \begin{pmatrix} \hat{a}_1 \\ \hat{a}_2 \end{pmatrix} \hat{S} = \begin{pmatrix} (\hat{a}_1 + \zeta_1) \cosh r_1 - \left(\hat{a}_1^\dagger + \zeta_1^* \right) e^{-2\text{i}\gamma_1} \sinh r_1 \\ (\hat{a}_2 + \zeta_2) \cosh r_2 - \left(\hat{a}_2^\dagger + \zeta_2^* \right) e^{-2\text{i}\gamma_2} \sinh r_2 \end{pmatrix}, \tag{6.24}$$

where the JPA gain G_k is related to the squeezing parameter r_k via $G_k = e^{2r_k}$. The respective squeezing angle is denoted by γ_k. Note the difference between the pure squeeze operator introduced in Eq. (2.47) and Eq. (6.24). The noise added by the two JPAs is taken into account by introducing a random classical variable ζ_k, which fulfills $\langle \zeta_k \zeta_k^* \rangle = n_k(G_k)$ and $\langle \text{Re}\,(\zeta)^2 \rangle = \langle \text{Im}\,(\zeta)^2 \rangle = n_k(G_k)/2$. Note that this noise number depends on the respective gain [73]. For a reliable analysis of G_k and n_k, we reconstruct the corresponding quantum states at the output of the second HR, when exclusively JPA1 (JPA2) is driven, as depicted in Fig. 6.11. The full transformation of the circuit is given by the combined operator

$$\hat{F} = \hat{L}_3 \hat{B}_2 \hat{L}_2 \hat{S} \hat{P} \hat{L}_1 \hat{B}_1. \tag{6.25}$$

Consequently, the final state $|\Psi\rangle$ can be expressed as [1]

---

[1]Note that this is only a symbolic notation for better clarity. For a full description, the environment enters via two additional modes. Since we do not care further about the environment, we drop these modes.
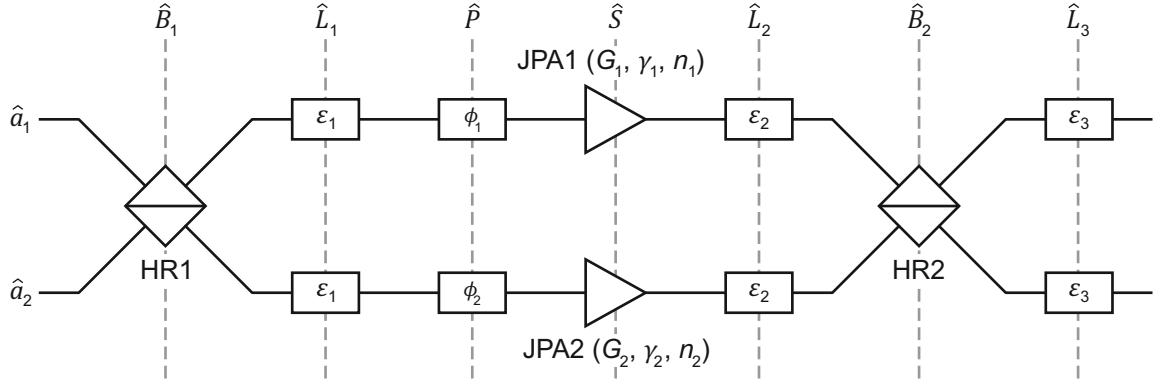
Figure 6.9: Scheme of the theoretical model of the interferometer circuit. The incoming modes $\hat{a}_1$ and $\hat{a}_2$ sequentially undergo various transformations, as indicated by the vertical dashed lines. The final states are reconstructed after the operation $\hat{L}_3$.

$$|\Psi\rangle = \hat{F}|\alpha_1;\alpha_2\rangle. \tag{6.26}$$

The signal moments of the circuit outputs $\hat{b}_k$ are given by

$$\begin{pmatrix} \langle(\hat{b}^\dagger)^n\hat{b}^m\rangle_1 \\ \langle(\hat{b}^\dagger)^n\hat{b}^m\rangle_2 \end{pmatrix} = \langle\Psi| \begin{pmatrix} \langle(\hat{a}^\dagger)^n\hat{a}^m\rangle_1 \\ \langle(\hat{a}^\dagger)^n\hat{a}^m\rangle_2 \end{pmatrix} |\Psi\rangle. \tag{6.27}$$

As introduced in Sec. 5.1.2, we exclusively consider Gaussian states and restrict ourselves to signal moments up to the second order [6]. They are obtained by applying the operator of Eq. (6.25) to the initial signal moments with $m + n \leq 2$. Based on the complementary quadrature operators given in Eqs. (2.7) and (2.8), we further rely on the first and second statistical moments according to Eqs. (2.24) and (2.25).

All quantities discussed in Sec. 6.4 are either evaluated directly with the signal moments, the associated first and second statistical moments, or by using the second-order correlation function [131] and interferometric power (IP) [271]. For two-mode fields, the respective second-order auto-correlation functions, $g_k^{(2)}(0)$, can be written as [cf. Eq. (2.77) in Sec. 2.4]

$$g_k^{(2)}(0) = \frac{\langle\hat{a}_k^\dagger\hat{a}_k^\dagger\hat{a}_k\hat{a}_k\rangle}{\langle\hat{a}_k^\dagger\hat{a}_k\rangle^2}, \tag{6.28}$$

where $k = 1, 2$. The associated second-order cross-correlation function, $g_C^{(2)}(0)$, can be expressed as [cf. Eq. (2.84) in Sec. 2.4]

$$g_C^{(2)}(0) = \frac{\langle\hat{a}_1^\dagger\hat{a}_1^\dagger\hat{a}_1\hat{a}_1\rangle + \langle\hat{a}_2^\dagger\hat{a}_2^\dagger\hat{a}_2\hat{a}_2\rangle + 2\langle\hat{a}_1^\dagger\hat{a}_1\hat{a}_2^\dagger\hat{a}_2\rangle}{\left(\langle\hat{a}_1^\dagger\hat{a}_1\rangle + \langle\hat{a}_2^\dagger\hat{a}_2\rangle\right)^2}. \tag{6.29}$$

For more details on the second-order correlation function, see Sec. 2.4. We combine our model with the approach from Ref. [131] to express second-order correlation functions for

arbitrary Gaussian states based on their respective covariance matrices and displacement vectors. The explicit expressions for the different Gaussian second-order correlation functions are provided in Appendix C.

The IP is defined as [271]

$$
\mathcal{P}\left(\rho_{\mathrm{AB}}\right) = \frac{1}{4} \inf_{\hat{U}_{\mathrm{A}}} \mathcal{F}\left(\rho_{\mathrm{AB}}^{\Phi, \hat{U}_{\mathrm{A}}}\right),
\tag{6.30}
$$

where ρ_{AB} is the two-mode probe state, $\hat{U}_{\mathrm{A}}$ is an arbitrary unitary transformation of the subsystem A, $\mathcal{F}$ is the quantum Fisher information, and Φ is the corresponding estimator [271, 272]. For Gaussian states, the IP can be expressed as [271]

$$
\mathcal{P} = \frac{\left(X + \sqrt{X^2 + YZ}\right)}{2Y},
\tag{6.31}
$$

where

$$
X = (D + F) \cdot (1 + E + F - G) - G^2,
\tag{6.32}
$$

$$
Y = (G - 1) \cdot (1 + D + E + 2F + G),
\tag{6.33}
$$

$$
Z = (D + G) \cdot (D \cdot E - G) + F(2D + F) \cdot (1 + E),
\tag{6.34}
$$

and

$$
D = 4(V_{11}V_{22} - V_{12}V_{21}),
\tag{6.35}
$$

$$
E = 4(V_{33}V_{44} - V_{34}V_{43}),
\tag{6.36}
$$

$$
F = 4(V_{13}V_{24} - V_{14}V_{23}),
\tag{6.37}
$$

$$
G = \det(4\boldsymbol{V}).
\tag{6.38}
$$

The theoretical concepts introduced in this section combined with the theoretical foundations of Ch. 2 provide us with all necessary tools to conduct a profound experimental investigation of the QUMPI.

6.3   Experimental setup

In Fig. 6.10, we show a photograph of the custom-built wet dilution cryostat, in which the experiment has been conducted. A detailed scheme of the setup is shown in Fig. 6.11. An arbitrary waveform generator [2] provides modulation pulses to rf sources [3] and for synchronizing the FPGA [4]. The rf sources are referenced to each other in a daisy-chain

---

[2] `HDAWG` 750 MHz from `Zurich Instruments`.
[3] `SGS100A SGMA` rf source from `Rohde & Schwarz`.
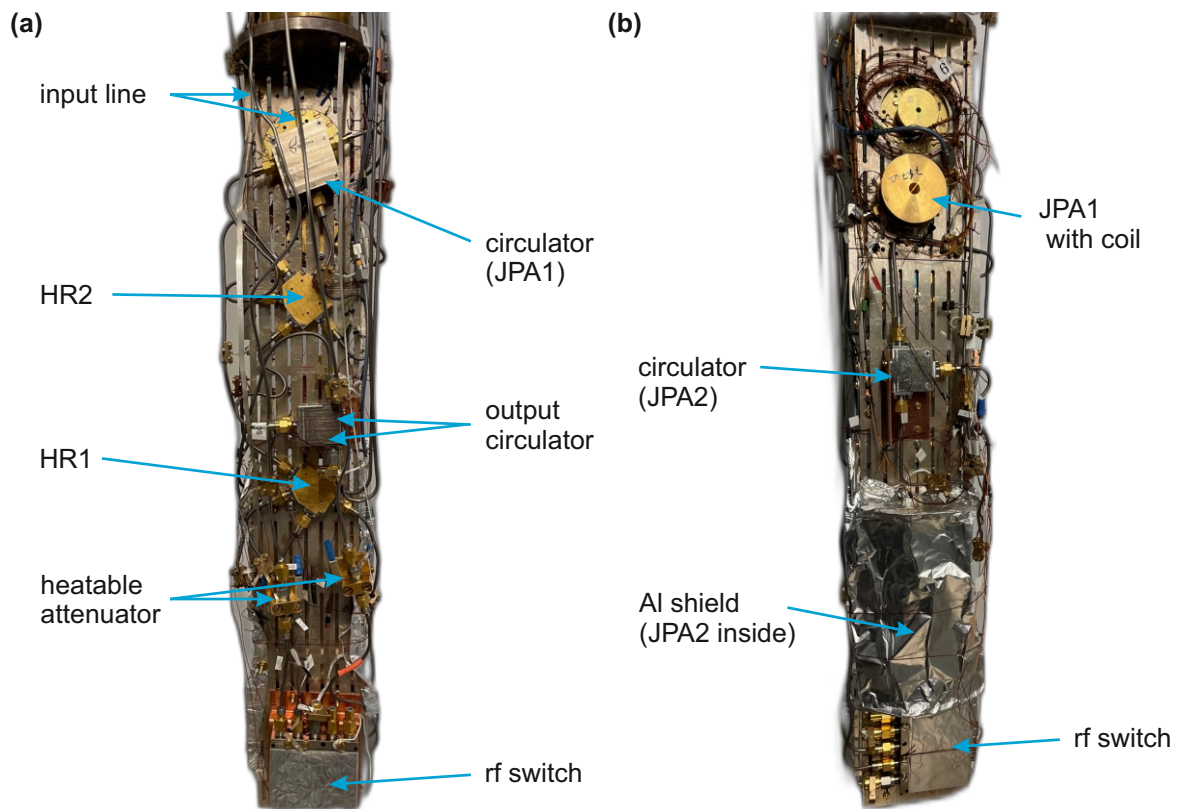[4] `PXIe 7972` from `National Instruments`.

Figure 6.10: Photographs of the cryogenic experimental setup. Panel (a) shows the front of the sample rod with two microwave input lines, which are connected to a heatable attenuator, respectively. Next, the two lines lead to a first hybrid ring (HR1). The two output ports of HR1 are connected to the two JPAs, located on the back of the sample rod, shown in panel (b), via respective circulators. JPA2 is enclosed in an aluminum (Al) shield in order to avoid crosstalk to JPA1. The second hybrid ring, HR2, completes the interferometer. The output circulators suppress unwanted back scattered noise from the HEMTs. The depicted rf switches are not used in the presented experiment.

configuration at a frequency of 1000 MHz starting with the rf source connected to In2. This source, the AWG and the FPGA are synchronized at a frequency of 10 MHz by means of a rubidium frequency standard [5]. The different input lines (In1, In2, P1, P2) are sequentially attenuated at various temperature stages. The coldest attenuator of the line associated with In1 (In2) is thermally coupled to a 100-Ω heater and a RuO_2 temperature sensor. At the same time, the attenuator is only weakly coupled to the mixing chamber plate of the dilution refrigerator. This allows for a precise PID temperature control of the coldest attenuators, while all other components can remain stable at a base temperature of $T = 35$ mK. The photon numbers in the reconstructed states are calibrated using Planck spectroscopy, as introduced in Sec. 5.1.3 [70]. For that, we vary the temperature of a heatable 30-dB attenuator in the range between 50 mK and 430 mK. The sample stage

---

[5] FS725 atomic clock from `Stanford Research Systems`.

is surrounded by a cryoperm shield to protect it from magnetic stray fields. In addition, JPA2 is enclosed in a superconducting aluminum shield in order to avoid cross-talk between individual JPAs. Due to the low signal level, both signals at the output of the cryogenic sample stage require amplification with a cryogenic high-electron-mobility transistor (HEMT) amplifier and subsequent additional room-temperature amplifiers. Frequency-resolved measurements are performed using a vector network analyzer (VNA, not shown). The tomography of quantum microwave states is performed using a heterodyne receiver setup and data processing as described in Sec. 5.1.2, similar to previous experiments described in Refs. [72, 74, 78, 88]. Output signals at the operating frequency of 5.48 GHz are down-converted to an intermediate frequency of 11 MHz using image rejection mixers in combination with a local oscillator (LO) operating at 5.491 GHz. We employ a digital FIR filter with a full bandwidth of 400 kHz. The JPA squeezing angles are set via a phase-locked loop, where in each measurement cycle the actual squeezing orientation, γ_k^{exp} ($k = 1, 2$), is extracted from the quadrature moments of the signals emitted from the respective JPA. Next, the phase of the corresponding JPA pump signal is adjusted by $2\Delta\gamma_k$, where $\Delta\gamma_k$ is the difference between the actual angle γ_k^{exp} and the target angle $\gamma_k^{\mathrm{target}}$. The respective phases of the coherent input tones are stabilized in a similar way by computing $\Delta\theta_k = \theta_k^{\mathrm{exp}} - \theta_k^{\mathrm{target}}$ and corrected by $\Delta\theta_k$. For independent adjustment of each rf source, the AWG produces a pulse-modulation sequence which activates each source twice per sequence for a fixed duration: first for individual phase adjustment and the second time for data acquisition. A general scheme of the AWG modulation sequence is depicted in the inset of Fig. 6.11. For details on the phase stabilization and pump modulation, we refer the reader to Ref. [108].

6.4 Results and discussion

The experimental results presented in this section can be divided into two categories. The first part covers the circuit calibration, which is a non-trivial task due to the active interferometer elements, i.e., the JPAs. This important basic prerequisite enables advanced circuit analysis in active operation of the QUMPI, which constitutes the second part of this section. For well-calibrated coherent input tones, we investigate various output quantities of interest, i.e., photon numbers, interferometric power, and second-order correlation functions.

A systematic study of the QUMPI requires careful circuit calibration and a precise control of the JPAs. The latter are operated at a frequency of $\omega_0/2\pi = 5.48$ GHz. Experimental bandwidths of JPA1 and JPA2 are 2 MHz and 10 MHz, respectively. We operate both JPAs in the phase-sensitive amplification regime by pumping them at twice the resonance frequency, $\omega_{\mathrm{p}} = 2\omega_0$ [81, 82]. The microwave interferometer arms are tailored to have identical lengths within an accuracy of less than 1 mm. At the carrier frequency of around 5.5 GHz, the associated wavelength in our superconducting cables
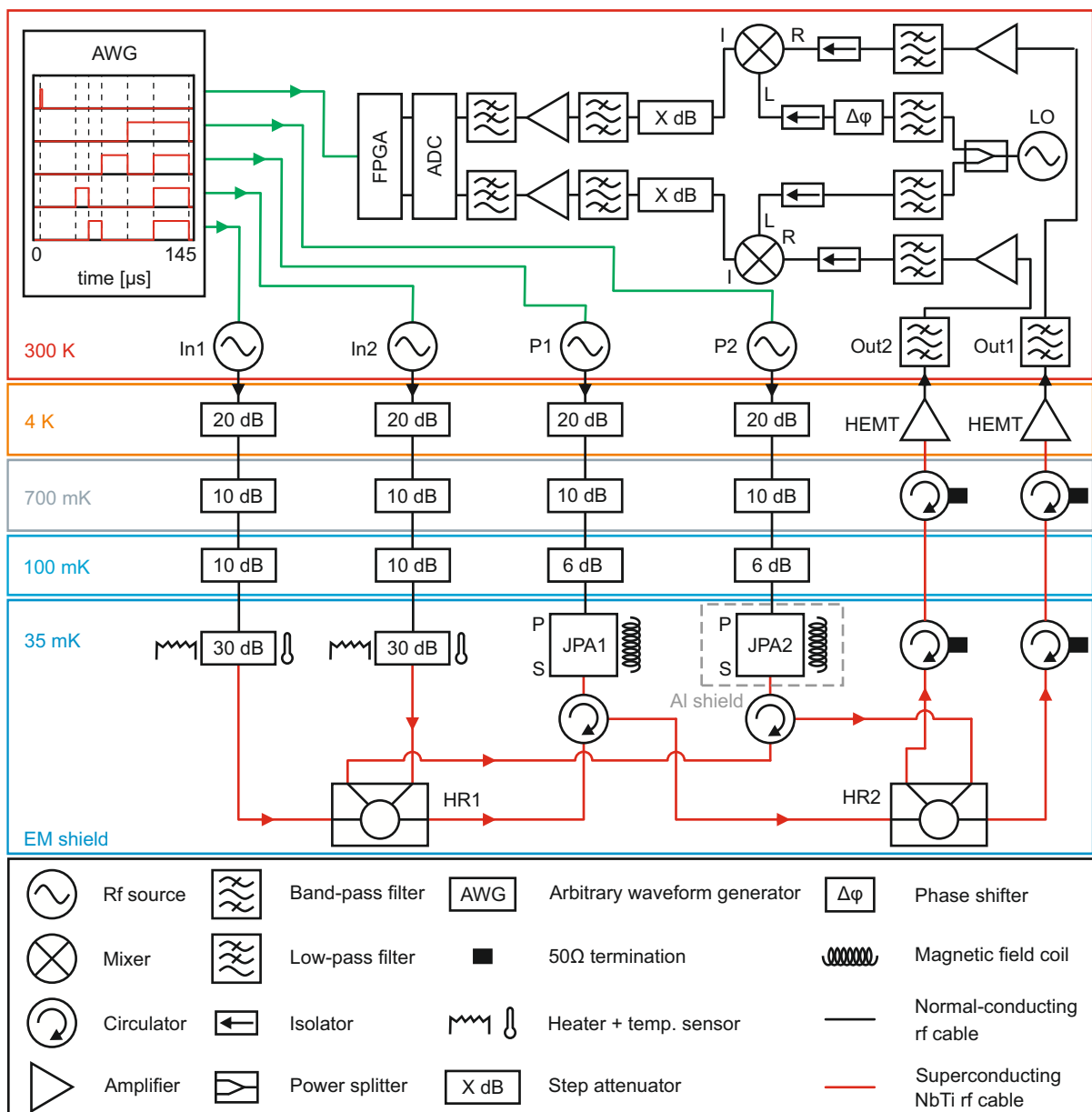
Figure 6.11: Schematic of the measurement setup. The output signals are amplified and filtered in subsequent steps, down-converted, and digitized. An arbitrary waveform generator (AWG) creates a pulse-modulation sequence for the individual rf sources and the FPGA, which is required for the sequential reference-state reconstruction [65].

is approximately $38\,\text{mm}$, which corresponds to signal propagation at around $70\,\%$ of the speed of light in vacuum. Given the interferometer arm accuracy in comparison with the signal wavelength, microwave signals traveling along different interferometer paths do not acquire a significant relative, path-induced phase shift. This geometric precision is decisive for achieving the intended functionality of the QUMPI, as evaluated in Sec. 6.1. However, the overall phase difference also depends on JPA-induced phase shifts, which
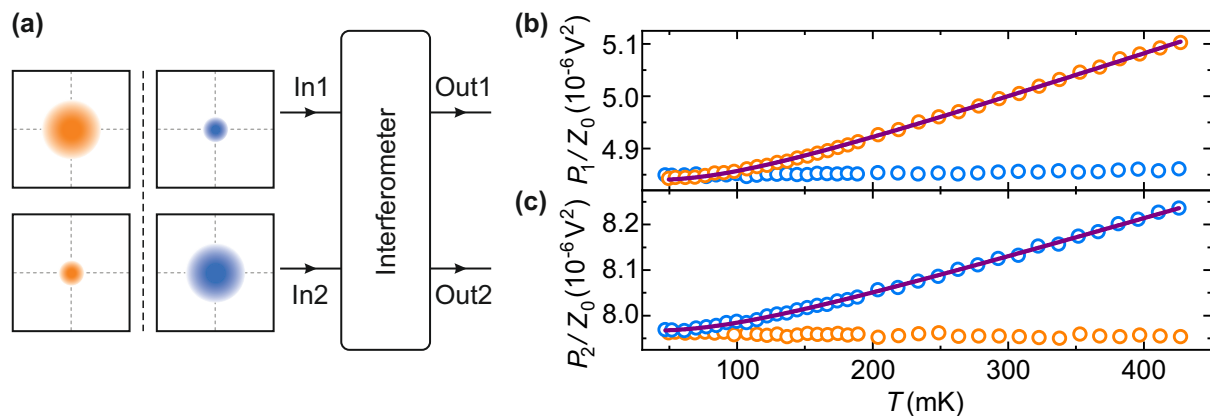
Figure 6.12: Planck spectroscopy of the interferometer in the linear regime for output channel powers (b) P_1 at Out1 and (c) P_2 at Out2. Orange points correspond to injection of thermal states at In1 and vacuum at In2, blue points correspond to the inverted case of thermal-state injection at In2 and vacuum at In1, as depicted schematically in the quadrature planes in (a). The temperature dependence of P_1 (P_2) for orange (blue) data points yields the photon number calibration for the interferometer and verifies its functionality. The corresponding error bars are smaller than the symbol size. The solid purple lines represent fits based on Eq. (5.9). We find PNCF values of $\kappa_1 = (3.64 \pm 0.03)\,10^{-7}\,\mathrm{V}^2/\mathrm{photon}$, $A_{\mathrm{H},1} = 12.78 \pm 0.28$, $\kappa_2 = (3.74 \pm 0.05)\,10^{-7}\,\mathrm{V}^2/\mathrm{photon}$, and $A_{\mathrm{H},2} = 20.80 \pm 0.29$, where the noise contributions, $A_{\mathrm{H},1}$ and $A_{\mathrm{H},2}$, are given in photon units.

can be adjusted by fine-tuning the JPA operation frequency with an external magnetic flux [81]. The output state tomography relies on heterodyne measurements with the FPGA-based setup described in Ch. 5. After digital down-conversion and filtering, we use the reference-state reconstruction method to extract statistical field quadrature moments and recover a covariance matrix of the quantum states at a certain reference point, also introduced in Ch. 5.

In a first step, we detune both JPAs from the intended operation frequency and switch our interferometer into a linear regime. Then, we perform Planck spectroscopy of our system by injecting thermal states generated by a heatable attenuator at one input and vacuum at the other, as illustrated in Fig. 6.12(a) [273]. Figures 6.12(b) and 6.12(c) show the corresponding experimental results. We observe both constructive and destructive interference of the broadband thermal signals, as expected in a symmetric linear interferometer. Thermal-signal injection at In1 (orange points) results in the temperature dependence of P_1, while P_2 remains independent of T due to destructive interference. The inverted case of thermal-signal injection at In2 (blue points) provides clear evidence for the symmetry of the system, which is reflected in a $P_2(T)$-dependence and a T-independent response of P_1. These experimental results underline that we are indeed in the configuration associated with a symmetric interferometer, see Fig. 6.8(a).

As a second part of the calibration routine, we tune both JPAs to the same resonance frequency of $\omega_0/2\pi = 5.48\,\mathrm{GHz}$. This step converts the QUMPI into the nonlinear

(a) $W(q_1,p_1)$

0.01   0.18

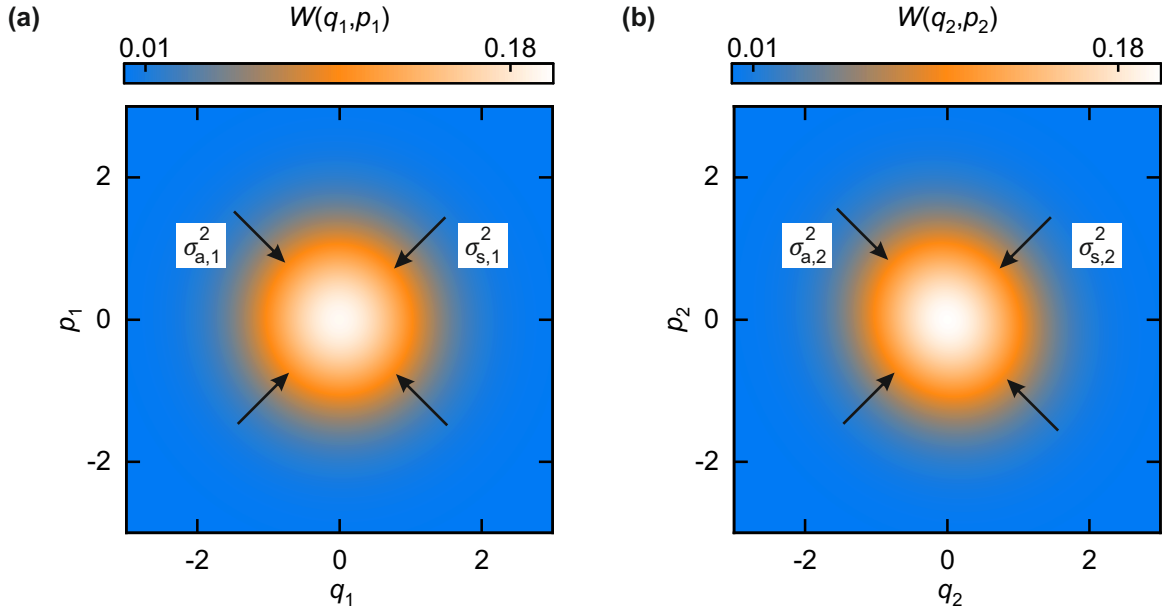**(b)** $W(q_2,p_2)$

0.01   0.18

Figure 6.13: Interferometer calibration. The squashed variances $\sigma^2_{s,k}$ and amplified variances $\sigma^2_{a,k}$ ($k = 1, 2$) of the reconstructed Wigner functions $W(q_k, p_k)$ of the output fields in (a) Out1 and (b) Out2 are used to define a balancing parameter $\mathcal{B} = \left(\sigma^2_{s,1}/\sigma^2_{a,1}\right) \cdot \left(\sigma^2_{s,2}/\sigma^2_{a,2}\right)$.

regime. The JPA responses are controlled via magnitude and phase of the coherent pump tones. Since we expect the best interferometric performance for a balanced gain of $G_1 = G_2$ [257], we inject vacuum states at both circuit inputs and pump the JPAs with varying magnitude and phase [65]. We balance the produced two-mode states at the interferometer output by minimizing asymmetries of the local output modes. These asymmetries result in squashed variances $\sigma^2_{s,k}$ and amplified variances $\sigma^2_{a,k}$ ($k = 1, 2$ denotes path 1 and path 2, respectively) of the local phase space distributions. We define a balancing criterion as $\mathcal{B} = \left(\sigma^2_{s,1}/\sigma^2_{a,1}\right) \cdot \left(\sigma^2_{s,2}/\sigma^2_{a,2}\right)$. For our system, we observe $\mathcal{B}$ reaching values of around 0.91, close to the optimum value of $\mathcal{B} = 1$. Finite asymmetries and insertion losses of the HRs, as well as the nonidentical noise properties of the JPAs, limit the balancing. Figure 6.13 illustrates the concept behind the balancing parameter $\mathcal{B} = \left(\sigma^2_{s,1}/\sigma^2_{a,1}\right) \cdot \left(\sigma^2_{s,2}/\sigma^2_{a,2}\right)$. Figure 6.13(a) shows the reconstructed Wigner function of the local output Out1 of the interferometer during calibration. We analyze remaining variance asymmetries between two orthogonal quadratures, $\sigma^2_{a,1}$ and $\sigma^2_{s,1}$, and try to minimize them. Similarly, as shown in Fig. 6.13(b), we optimize $\sigma^2_{a,2}$ versus $\sigma^2_{s,2}$. For a fixed $\Delta\gamma_{JPA} = \pi/2$, we investigate $\mathcal{B}$ as a function of the pump powers, P_{P1} and P_{P2}, entering the respective JPA pump ports [see Fig. 6.14(a)]. Note that $\mathcal{B}$ is unity for an ideal balanced state and decreases with increasing imbalance between the local variances. As can be seen in Fig. 6.14(b), the balancing is best for amplification along orthogonal orientations in phase space, i.e., $\Delta\gamma_{JPA} = |\gamma_2 - \gamma_1| = \pi/2$, as expected from theory [6].

After the calibration, we investigate the nonlinear interferometer response to coherent signals applied to both input ports, In1 and In2, with a photon number of $|\alpha_1|^2 = |\alpha_2|^2 =$
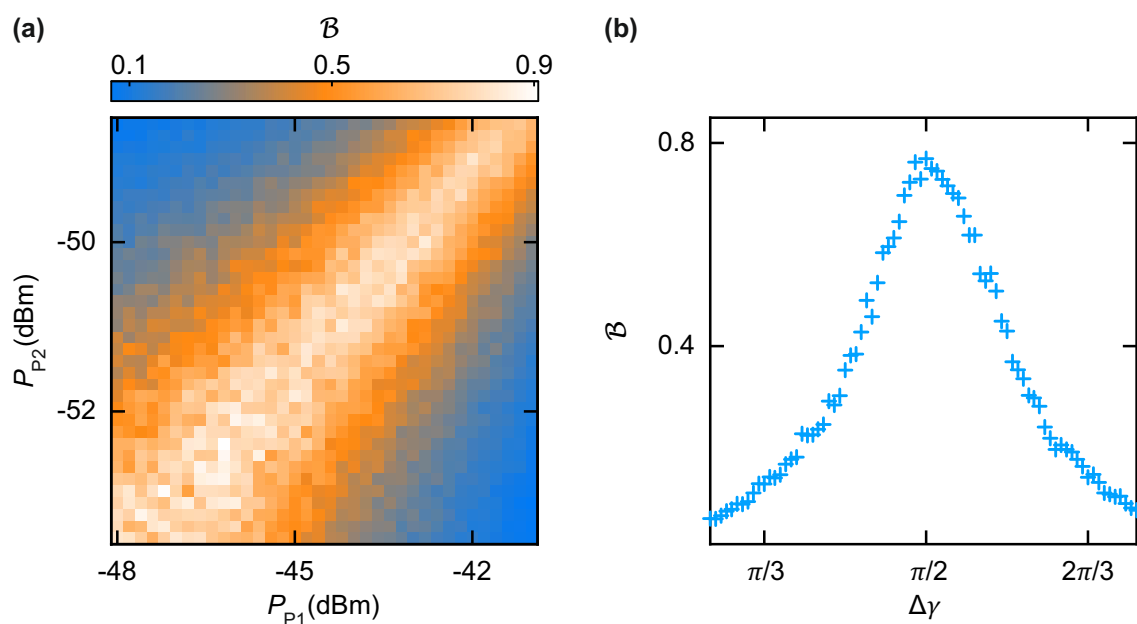
(a)

(b)

Figure 6.14: Interferometer calibration. The balancing parameter $\mathcal{B}$ enables optimization of the (c) JPA pump powers P_{P1} and P_{P2} (referred to the JPA pump ports) and the (d) relative JPA amplification orientation, $\Delta\gamma = |\gamma_1 - \gamma_2|$.

0.69(7), where $|\alpha_k|$ ($k = 1, 2$) are the respective displacement amplitudes [274]. We fix one coherent displacement angle, $\theta_1 = 0.64\pi$, while varying the other, θ_2. Both JPAs are operated with an average gain $\overline{G}_{1,2} = 7.73\,\mathrm{dB}$ and an average number $\overline{n}_{1,2} = 0.238$ of added noise photons referred to the JPA inputs. The JPA2 squeezing angle, γ_2, is fixed to 0 and we vary γ_1. We compare the acquired data with a theoretical model of our system based on the input–output formalism introduced in Sec. 6.2. Figures 6.15(a) and 6.15(b) show the photon numbers $N_k = \langle \hat{a}_k^\dagger \hat{a}_k \rangle$ at the respective outputs Out1 and Out2. Here, $\hat{a}_k^\dagger$ ($\hat{a}_k$) is the photon creation (annihilation) operator. The bottom row of Fig. 6.15 shows the model prediction. The common color bars for each column underline a good quantitative agreement between experiment and theory. As a model quality metric, we introduce the normalized distance, $d(x) \equiv \sum_{k=1}^{M} \sum_{l=1}^{N} |a_{kl} - b_{kl}|/|a_{kl}|$, between the respective data matrices a_{kl} and model matrices b_{kl} of dimension $M \times N$ with respect to a quantity x. The corresponding distances are $d(N_1) = 7.6\,\%$ and $d(N_2) = 6.5\,\%$. Since our model intrinsically corresponds to a nonlinear interferometer, this agreement confirms that our experimental system acts as such. The asymmetry in the patterns between Fig. 6.15(a) and 6.15(b) stems from the nonlinear character of our interferometer.

Next, we evaluate the interferometric power (IP) of the QUMPI. For a bipartite quantum probe state, the IP defines the worst-case precision of a parameter estimation, where the corresponding parameter experiences unitary dynamics in one of the two subsystems (e.g., a phase shift of the signal in one interferometer arm) [271]. Remarkably, the IP provides a measure of bipartite discord-type correlations for Gaussian states beyond pure
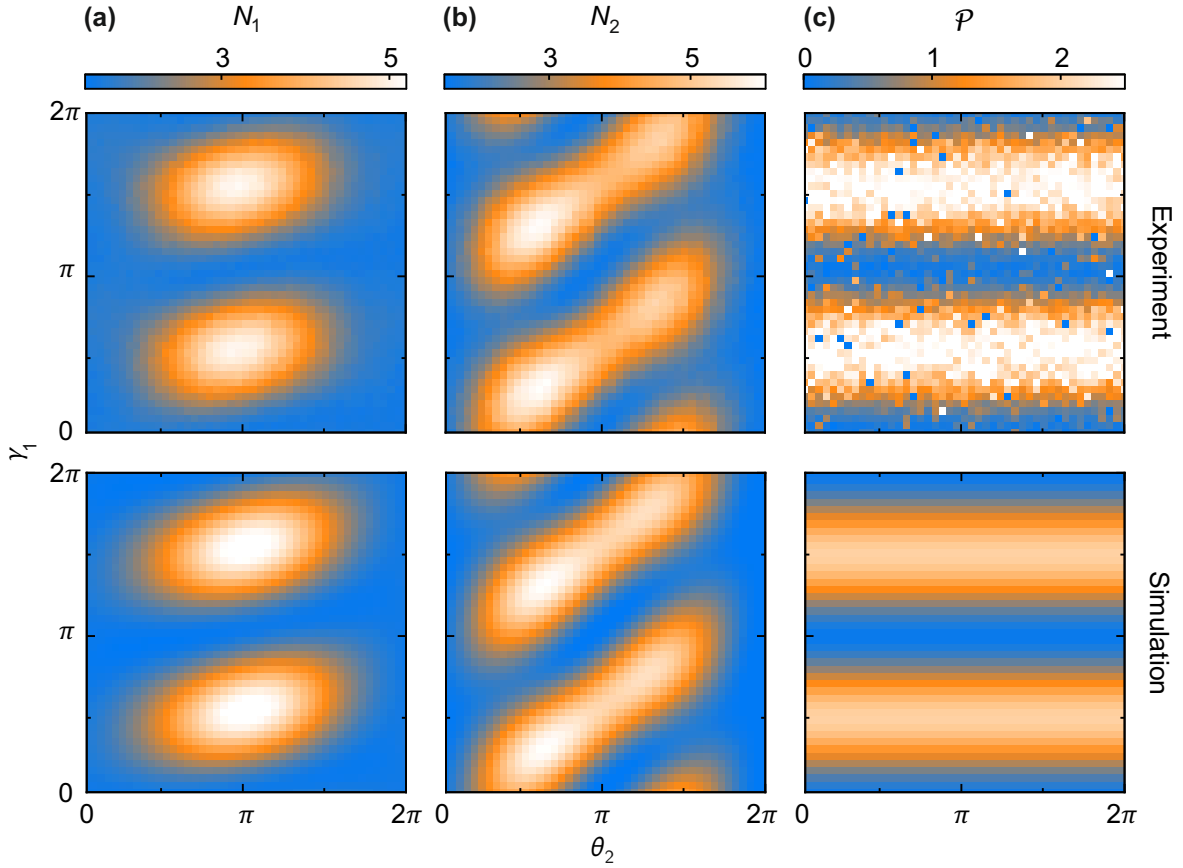
Figure 6.15: Interferometer measurements with coherent signals applied to In1 and In2. The corresponding displacement amplitudes are $|\alpha_1| = |\alpha_2| = 0.83(5)$, and the displacement angle θ_1 is fixed to 0.64π, while θ_2 varies from 0 to 2π. Both JPAs are operated as squeezers with the average gain $\overline{G}_{1,2} = 7.73\,\mathrm{dB}$ and squeezing angle γ_1 varying from 0 to 2π, while $\gamma_2 = 0$. Top row shows the experimentally reconstructed photon numbers (a) N_1 and (b) N_2 at the ports Out1 and Out2, respectively, as a function of θ_2 and γ_1. (c) Interferometric power $\mathcal{P}$ of the QUMPI illustrating the two-mode state probe capabilities. The bottom row depicts the model predictions according to Eqs. (6.27) and (6.31).

entanglement [271, 275]. We apply the expressions according to Eqs. (6.31) to (6.35) to our theory model, as well as to the reconstructed experimental covariance matrices, in order to extract the IP of the QUMPI [271]. Figure 6.15(c) depicts both the experimental and theoretical IP as a function of θ_2 and γ_1. The data in Fig. 6.15(c) is independent of θ_2, since $\mathcal{P}$ is invariant under local unitary operations [271]. Furthermore, $\mathcal{P}$ goes to zero for parallel amplification angles, $\gamma_1 = \gamma_2 + n\pi$ $(n = 1, 2, ...)$, where output states become separable, and is maximal for orthogonal amplification, where the states are entangled. In this context, the SQL sets an upper bound, $\mathcal{P}_{\mathrm{SQL}} = N$, for separable two-mode probe states, where N is the mean photon number in the probing subsystem. For pure two-mode squeezed states $\mathcal{P}$ saturates at the HL with $\mathcal{P}_{\mathrm{HL}} = N(N + 1)$ [271]. The simulated IP reproduces the experimental data, however with a noticeably smaller maximum value, as it
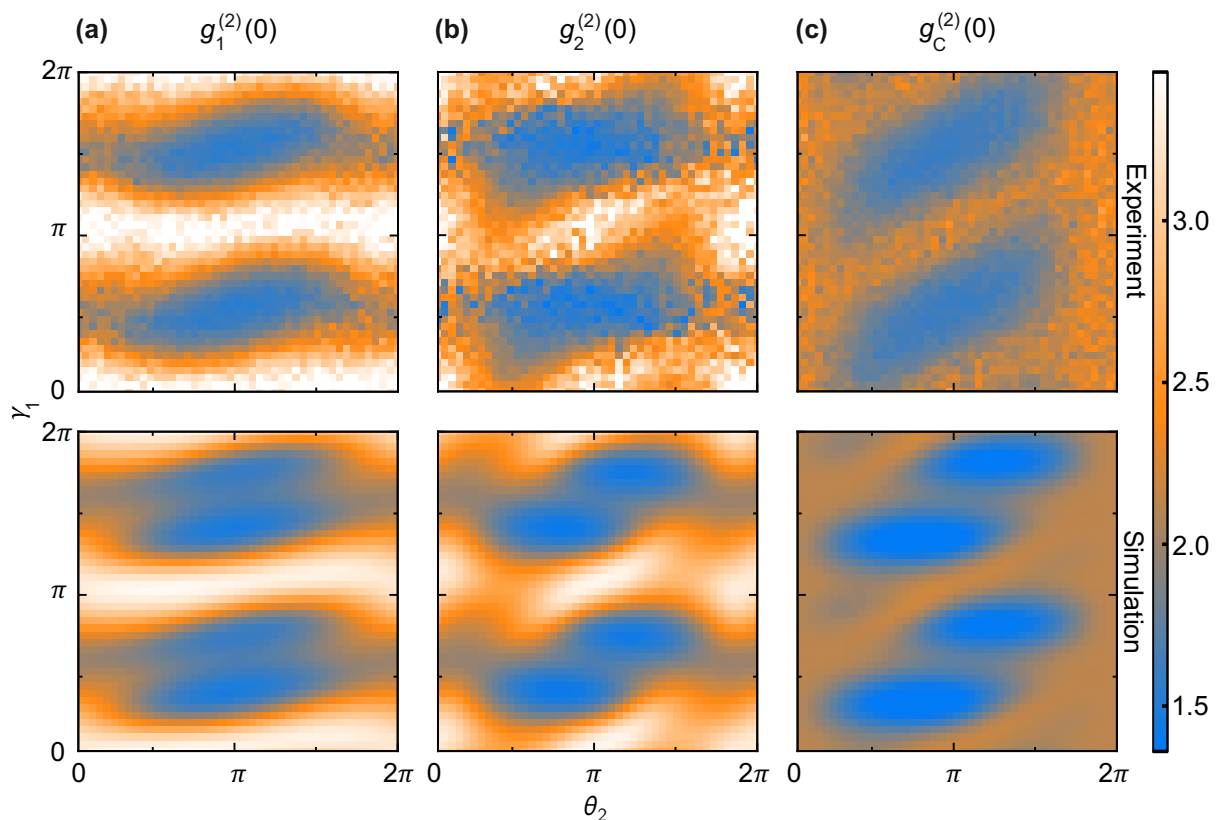
Figure 6.16: Second-order correlation analysis of the QUMPI. Single-mode second-order correlation functions, $g_1^{(2)}(0)$ and $g_2^{(2)}(0)$, at the interferometer ports (a) Out1 and (b) Out2. (c) Second-order cross-correlation function, $g_C^{(2)}(0)$, between ports Out1 and Out2. Experimental results are shown in the top row, model predictions according to Eqs. (C.1) to (C.3) are depicted in the bottom row. The experimental parameters are identical to those in Fig. 6.15.

can be seen from Fig. 6.15(c) and $d(\mathcal{P}) = 47.0\,\%$. We attribute this deviation to possible misestimates of losses in the underlying photon number calibration. Both, maximum theoretical ($\mathcal{P}_{\text{theory}}/\mathcal{P}_{\text{SQL}} = 1.38$) and experimental ($\mathcal{P}_{\text{exp}}/\mathcal{P}_{\text{SQL}} = 1.70$) values exceed the SQL but do not reach the HL ($\mathcal{P}_{\text{theory}}/\mathcal{P}_{\text{HL}} = 0.58$, $\mathcal{P}_{\text{exp}}/\mathcal{P}_{\text{HL}} = 0.65$). The presence of finite noise in the system prevents reaching an IP closer to the HL. We note, however, that $\mathcal{P}_{\text{exp}} > \mathcal{P}_{\text{SQL}}$ provides direct evidence that the QUMPI exceeds the $\sqrt{N}$ scaling of the SNR, since SNR $\propto \sqrt{\mathcal{P}}$. Here, we use the theoretical (reconstructed) photon number of the local mode at Out1 of our circuit to compute $\mathcal{P}_{\text{SQL}} = N = \left(2(\sigma_q^2 + \sigma_p^2) - 1\right)/2$ and $\mathcal{P}_{\text{HL}}$. The parameters used in the theoretical model are summarized in Tables 6.1 and 6.2. The parameters ε_1, ε_2, and ε_3 are estimated from the data sheets of the respective passive microwave components. The displacement amplitudes, $|\alpha_1|$ and $|\alpha_2|$, are adjusted via the photon number calibration factor in combination with an individual two-step modulation power sweep of the two rf sources connected to In1 and In2. The displacement angles, θ_1 and θ_2, in Table 6.1 (Table 6.2) are reconstructed and adjusted in real time using $6.248 \cdot 10^8$ ($9.372 \cdot 10^8$) raw data points before demodulation. The squeezing angles, γ_1

and γ_2, in Table 6.1 (Table 6.2) are processed similarly using $1.2496 \cdot 10^9$ $(1.8744 \cdot 10^9)$ raw data points before demodulation. The reconstructed JPA squeezing factors, r_1 and r_2, are obtained in post-processing, where the averaged demodulated data is taken into account for 46 independent measurements of $1.2496 \cdot 10^9$ $(1.8744 \cdot 10^9)$ raw data points before demodulation, respectively. The theory model introduced in Sec. 6.2 relies on ϕ_k as a free parameter, representing the phase acquired by signals in paths 1 and 2 of the interferometer, respectively.

$\lvert\alpha_1\rvert^2$	θ_1	$\lvert\alpha_2\rvert^2$	θ_2	$\varepsilon_1\,(\mathrm{dB})$	ϕ_1	ϕ_2	r_1
0.723	0.639π	0.670	0 to 2π	0.63	1.31π	1.36π	1.01(4)
γ_1	n_1	r_2	γ_2	n_2	$\varepsilon_2\,(\mathrm{dB})$	$\varepsilon_3\,(\mathrm{dB})$	
0 to 2π	0.034(5)	0.723(2)	0	0.441(9)	0.31	0.3	

Table 6.1: Model parameters used for the simulated results of Figs. 6.15 and 6.16. Each point in Figs. 6.15 and 6.16 is obtained using $1.4 \cdot 10^9$ raw data points before demodulation. The loss values ε_j are estimated based on the respective data sheet values. The complex displacement amplitudes, $\alpha_k = \lvert\alpha_k\rvert\exp[\mathrm{i}(\pi/2 - \theta_k)]$, and the respective JPA parameters (r_k, n_k, γ_k) are reconstructed.

In order to study correlation properties and related intensity fluctuation statistics of the QUMPI, we analyze the second-order correlation function at zero delay time, $g^{(2)}(0)$, for the single-mode fields at the interferometer outputs, as well as the cross-correlations between the outputs, as introduced in Eqs. (6.28) and (6.29) and adapted for Gaussian states in Appendix C [88]. The experimentally obtained data for $g_1^{(2)}(0)$, $g_2^{(2)}(0)$, and $g_C^{(2)}(0)$ as a function of θ_2 and γ_1 are depicted in Fig. 6.16. The bottom row shows the respective theoretical predictions [131]. Our model sufficiently well reproduces the experimental observations with $d[g_1^{(2)}(0)] = 8.6\,\%$, $d[g_2^{(2)}(0)] = 10.4\,\%$ and $d[g_C^{(2)}(0)] = 7.8\,\%$, although some fine features are not resolved in the experimental data. In accordance with the model, the local output modes show correlation functions indicating photon bunching, $g_1^{(2)}(0)$, $g_2^{(2)}(0)$, $g_C^{(2)}(0) > 1$.

To further explore the QUMPI, we experimentally investigate $g_C^{(2)}(0)$ as a function of the displacement amplitude of the incident coherent states. We observe that for sufficiently large displacement amplitudes, $\lvert\alpha_1\rvert$ and $\lvert\alpha_2\rvert$, and equal displacement angles, $\theta_1 = \theta_2$, $g_C^{(2)}(0)$ indicates anti-bunching between the interferometer outputs, providing evidence for nonclassical correlations between them [131]. In Fig. 6.17(a), we show $g_C^{(2)}(0)$ predicted by our theoretical model. For the experimentally relevant model parameters, most importantly the adapted average JPA gain $\overline{G}_{1,2} = 4.06\,\mathrm{dB}$, Fig. 6.17(a) shows that $\lvert\alpha_1\rvert^2, \lvert\alpha_2\rvert^2 > 5$ is required to realize nonlocal photon anti-bunching, $g_C^{(2)}(0) < 1$. Figure 6.17(b) shows the experimental data of $g_C^{(2)}(0)$ as a function of $\lvert\alpha\rvert^2 = \lvert\alpha_1\rvert^2 = \lvert\alpha_2\rvert^2$. The blue line is a cut along the main diagonal of Fig. 6.17(a). The inset shows an expanded view of the
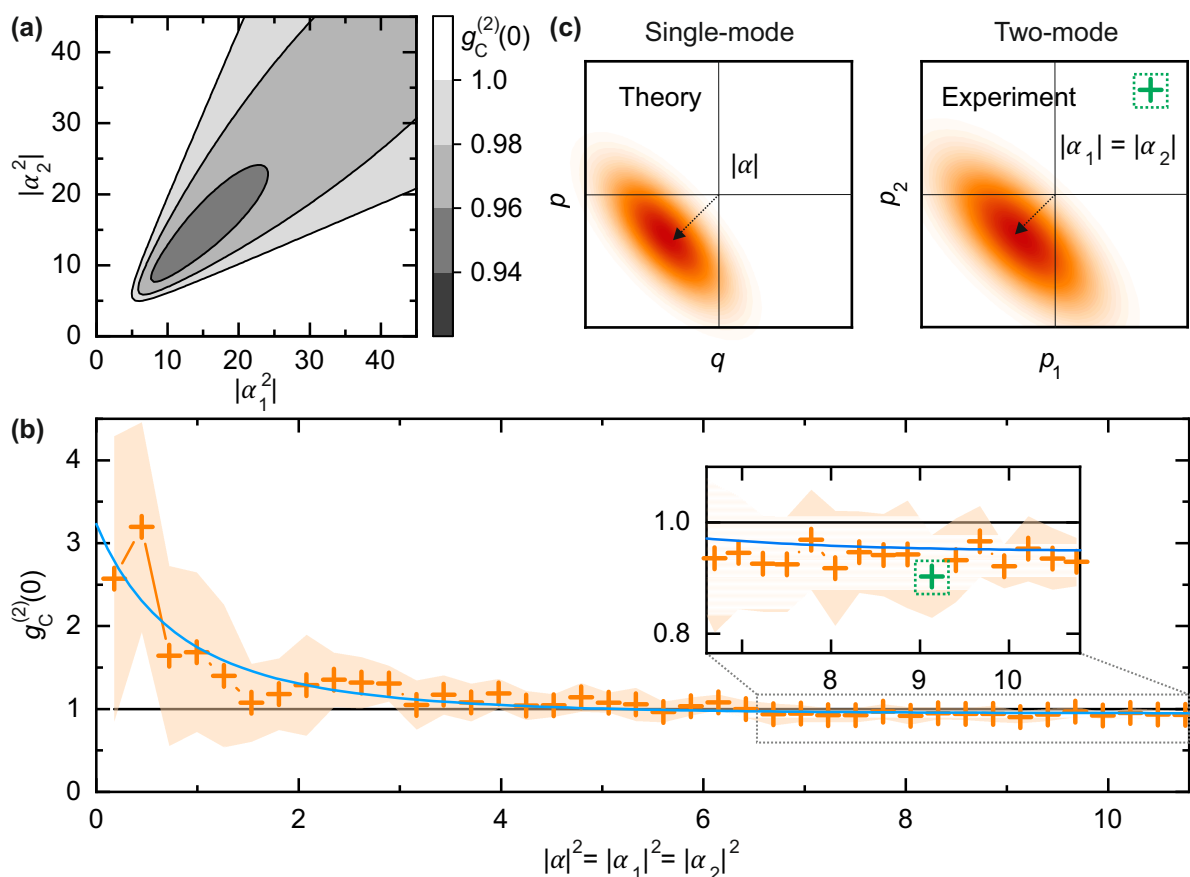
Figure 6.17: Intensity cross-correlations, $g_\mathrm{C}^{(2)}(0)$, of the interferometer output fields for variable displacement amplitudes of coherent input signals. (a) Model predictions as a function of the number of coherent photons $|\alpha_1|^2$ and $|\alpha_2|^2$ ($\theta_1 = \theta_2 = 0.81\pi$) entering the circuit at In1 and In2, respectively. (b) Experimental results for $g_\mathrm{C}^{(2)}(0)$ (orange crosses with standard deviation shown in shaded orange) as a function of the symmetrically varied displacement amplitudes. The blue line depicts the theoretical prediction. The horizontal black line illustrates the classical limit of $g_\mathrm{C}^{(2)}(0) = 1$. (c) Analogy between Wigner functions of single-mode (theory) and two-mode [experiment, green cross from (b)] displaced squeezed states exhibiting $g^{(2)}(0) < 1$ ($g_\mathrm{C}^{(2)}(0) < 1$).

region where the data points for $g_\mathrm{C}^{(2)}(0)$ drop below the classical limit. Our theory model suggests that the minimal coherent photon number $|\alpha|^2 = |\alpha_1|^2 = |\alpha_2|^2$ required to achieve $g_\mathrm{C}^{(2)}(0) < 1$ increases with increasing JPA gain, while $g_{\mathrm{C,min}}^{(2)}(0)$ converges towards unity for large JPA gain. At the same time, $g_\mathrm{C}^{(2)}(0)$ becomes more robust towards noise with increasing JPA gain.

Summary and discussion   We have realized and systematically analyzed a quantum microwave parametric interferometer. We have studied the frequency-dependent circuit response in an even-odd analysis. We have performed a detailed investigation of the input-output relations of our QUMPI device with coherent and thermal input states. Our

$\lvert\alpha_1\rvert^2$	θ_1	$\lvert\alpha_2\rvert^2$	θ_2	$\varepsilon_1\,(\mathrm{dB})$	ϕ_1	ϕ_2
0.177 to 10.76	0.806π	0.177 to 10.76	0.806π	0.63	1.03π	1.36π
r_1	γ_1	n_1	r_2	γ_2	n_2	$\varepsilon_2\,(\mathrm{dB})$
0.508(5)	$\pi/2$	0.0004(6)	0.422(5)	π	0.124(4)	0.31
$\varepsilon_3\,(\mathrm{dB})$						
0.3						

Table 6.2: Model parameters used for the simulated results of Fig. 6.17. Each point in Fig. 6.17 is obtained using $2.1 \cdot 10^9$ raw data points before demodulation per independent measurement. The listed values are derived in the same way as in Table 6.1 and averaged over 16 independent measurements.

experimental results can be well explained by using a theoretical model based on the input–output quantum formalism. As part of this study, we have demonstrated non-local photon anti-bunching at the QUMPI outputs, characterized by $g_{\mathrm{C}}^{(2)}(0) < 1$ for coherent input states. Remarkably, for the specific operating point of the JPAs with equal gain values and orthogonal amplification angles, the input–output relations of the QUMPI simplify to

$$\begin{aligned}
\hat{b}_1 &= \sqrt{G_{\mathrm{eff}}}\,\hat{a}_1 + \sqrt{G_{\mathrm{eff}}-1}\,\hat{a}_2^\dagger, \\
\hat{b}_2 &= \sqrt{G_{\mathrm{eff}}}\,\hat{a}_2 + \sqrt{G_{\mathrm{eff}}-1}\,\hat{a}_1^\dagger,
\end{aligned} \tag{6.39}$$

with the effective gain $\sqrt{G_{\mathrm{eff}}} = \cosh(r)$ and the JPA squeezing factors $r = r_1 = r_2$ according to the JPA gain $G = \exp(2r)$. The input and output modes are described by bosonic operators $\hat{a}_1, \hat{a}_2$ and $\hat{b}_1, \hat{b}_2$, respectively. The relations in Eq. (6.39) coincide with those describing the so-called Josephson mixer, which can be utilized for producing microwave EPR states [78, 269]. For low effective gain values, $G_{\mathrm{eff}} \simeq 1$, our interferometer can be applied in a quantum illumination detection scheme for achieving the 3-dB quantum advantage in the error exponent over the ideal classical counterpart, as introduced in Ch. 3 [47, 145, 155]. The application of the QUMPI in an experimental quantum radar scheme is further discussed in Ch. 7. Interestingly, the input–output relations in Eq. (6.39) also coincide with those of a SU(1,1) interferometer, with the exception that the coefficients, G_{eff} and $(G_{\mathrm{eff}}-1)$, enter linearly in the SU(1,1) implementation [257]. This difference is related to the fact that the parametric amplifiers are connected in series for the conventional SU(1,1) implementation, whereas the JPAs in the QUMPI are arranged in a parallel configuration. Furthermore, our findings open a new avenue towards quantum-enhanced nonlinear interferometers in the fast-evolving field of superconducting circuits operating in the microwave regime. Remarkably, current dark matter axion search experiments focus on the frequency range from 1 GHz to 25 GHz and rely on read-out by quantum-limited amplifiers [276]. To this end, the QUMPI could find applications in related dark matter

axion search experiments [277]. As such, the investigated circuit is expected to be useful in many applications ranging from quantum-enhanced interferometry to mode-mixing as part of a joint quantum receiver in quantum sensing experiments [155, 278].

Chapter 7

Conclusion and outlook

Conclusion In this thesis, we have developed fundamental concepts and techniques for the experimental realization of microwave quantum illumination. As a prerequisite, we have introduced and motivated continuous variables in quantum information processing, which offer a powerful alternative to discrete variables in terms of control and measurement, efficiency, and seamless interfacing with classical platforms. Gaussian states represent a versatile class of continuous-variable states that can be fully described in a comprehensive manner. Throughout this work, we also have introduced a basic tool set for the generation, manipulation, and characterization of Gaussian microwave states.

As one of the key results of this thesis we have provided a comprehensive theoretical framework for the description of microwave quantum illumination (QI). To this end, we have shed light on the fundamental concepts of classical radar systems to provide the performance limits of classical systems that QI aims to overcome. We have tackled important topics in this realm, such as the ideal decision strategy for object detection and the basics of hypothesis testing. In general, the quantum illumination protocol promises a quantum advantage (QA) up to $6\,\mathrm{dB}$ in the error exponent with respect to the ideal classical radar. We have shown that a simple scheme, saturating the ideal classical bound, is the coherent-state transmitter combined with homodyne detection, which naturally motivates the use of Gaussian states. In our analysis we have evaluated the restrictions on specific parameters required to enter the regime of a genuine QA: bright thermal background, low signal powers, low object reflectivity, and large time-bandwidth product. The required bright thermal background makes QI suboptimal at optical frequencies where the thermal photon population per mode is negligibly small at room temperature. In contrast, at microwave frequencies one observes a strong thermal background radiation with over 1000 photons per mode at room temperature, making this frequency regime ideal for QI. The unprecedented potential of QI relies on quantum-entangled probe states that are characterized by the presence of quantum correlations exceeding classical limits. The initial entanglement is quickly lost due to the interaction with the bright thermal background. However, residual nonclassical correlations persist and enable the performance enhancement in QI. These residual correlations are non-local, which renders local homodyne or heterodyne detection schemes useless.

There have been vivid research activities proposing various detection schemes which may benefit from the non-local correlations and hence allow for a finite QA. Although some of these proposals, in theory, can exploit the full 6 dB QA, their experimental realization is extremely challenging with state-of-the-art technology. Fortunately, there also exist various simplified schemes that are more straightforward in implementation and can achieve a reduced, but still useful 3 dB QA. As of today, the only successful experimental implementation of a microwave quantum radar relies on the parametric-mixer (PM) receiver [55]. In this approach, the return and idler modes first interact nonlinearly in a parametric mixer, followed by single-photon counting (PC1) at one of the mixer outputs. However, the potential impact of photon counting at the other mixer output (PC2) on the resulting QA has not been investigated yet. We have bridged this gap and found a strong asymmetry in the photon number expectation values at the outputs of the mixer, with $N_1 \ll 1$ and $N_2 \simeq N_\mathrm{B} \gg 1$, where N_B is the number of thermal background photons coupled to the signal. This asymmetry leads to the underperformance of the detection scheme based on PC2 alone, which is clearly inferior to the classical scheme, while detection exclusively with PC1 converges to the 3 dB QA in the asymptotic regime of a large number of transmitted modes.

We have additionally investigated an adapted scheme of the PM receiver, where we have studied a correlated photon counting (CPC) scheme that simultaneously exploits both mixer outputs. From an intuitive point of view, these outputs are highly correlated due to their interaction in the mixer and have the potential of outperforming individual detection with PC1. We have observed such a performance enhancement and have identified an optimal analytical weighting of the individual outputs for PC1 and PC2, which is of central importance in CPC. In addition, we have investigated the robustness of the associated QA against various imperfections in the QI protocol. First, we have shown that the purity requirements for the two-mode squeezed vacuum resource state are stringent, which is caused by a high fragility of the retained idler mode against noise. This fragility is reflected in a required two-mode purity of at least 98 %, for a conventionally considered photon number of $N = 0.01$ per mode, to reach a QA. We have thoroughly discussed the influence of realistic detection parameters in terms of single-photon detection efficiencies and dark count probabilities, which are subject to a design trade-off in realistic devices based on superconducting quantum circuits. We have unveiled strongly asymmetric photon-number resolution requirements for detecting the two mixer outputs, caused by the largely different mean photon numbers. While a binary single-photon detector without any photon-number resolution capabilities is close to the ideal performance for PC1, the second photon counter PC2 requires a resolution of $K \gg 1$ to become practically useful, which is out of reach with currently available technology. Hence, we have shown that individual detection with PC1 represents a practically optimal way towards achieving the genuine 3 dB QA. The discussed results have been published as Ref. [54].

In the next step, we have turned to experimental aspects of microwave QI. We have

introduced superconducting quantum technology and the associated fundamental concepts and and devices, such as superconductivity, Josephson junctions, dc-SQUIDs, and Josephson parametric amplifiers (JPAs). Here, JPAs represent the main microwave quantum building block of our experimental work and serve as versatile tools for producing propagating squeezed states in the microwave regime. We have introduced the experimental techniques for conducting quantum microwave experiments at millikelvin temperatures with carrier frequencies of several gigahertz. Furthermore, we have presented concepts for quantum microwave detection and processing at room temperature. Here, the reference-state reconstruction represents a central tool for experimental tomography of propagating quantum states. In this context, we have presented various important aspects of our experiments, such as a photon-number calibration routine for output lines and characterization measurements of superconducting JPAs.

We have exploited the phase-sensitive amplification regime of JPAs in order to experimentally realize a nonlinear Josephson interferometer operating in the microwave regime. The successful realization of such an interferometer is the second main result of this thesis. The main building blocks of our quantum microwave parametric interferometer (QUMPI) are two flux-driven JPAs in combination with linear microwave hybrid rings (HRs). While the sensitivity of classical interferometers is intrinsically limited by shot noise, one can exceed this fundamental bound and reach the ultimate Heisenberg limit by using quantum input states or nonlinear quantum elements. We have conducted a frequency-resolved network analysis of the QUMPI circuit in order to understand its experimental requirements. Here, we have theoretically investigated the sensitivity of the QUMPI against geometrical asymmetries in the interferometer arms, which is of central importance for the design of our experimental setup. In addition, we have developed a quantum model to describe the QUMPI input-output relations for the injection of microwave coherent states with various parameters. We have found excellent agreement between the model predictions and our experimental results for the photon numbers N_1 and N_2 at the two outputs of the interferometer, which is quantified by the normalized distances $d(N_1) = 7.6\%$ and $d(N_2) = 6.5\%$ between the experimental data and theory model. We have found that the interferometric power $\mathcal{P}$ of the QUMPI clearly exceeds the shot-noise limit in both theory ($\mathcal{P}_{\text{theory}}/\mathcal{P}_{\text{SQL}} = 1.38$) and experiment ($\mathcal{P}_{\text{exp}}/\mathcal{P}_{\text{SQL}} = 1.70$). Furthermore, we have analyzed the single-mode second-order correlation functions at the interferometer outputs and have found a good agreement between our model and the experimental results with normalized distances on the order of 10%. We have experimentally demonstrated non-local photon antibunching in the output modes for coherent amplitudes $|\alpha|^2 > 5$ of the input states and low JPA squeeze factors $r \simeq 0.5$ by means of a second-order cross-correlation function $g_{\text{C}}^{(2)}(0) < 1$. Finally, we have identified a low-gain operation regime of the QUMPI, where its input-output relations coincide with those of the PM-type receiver in QI, enabling its application in microwave quantum illumination schemes. These experimental results have been published as Ref. [80].
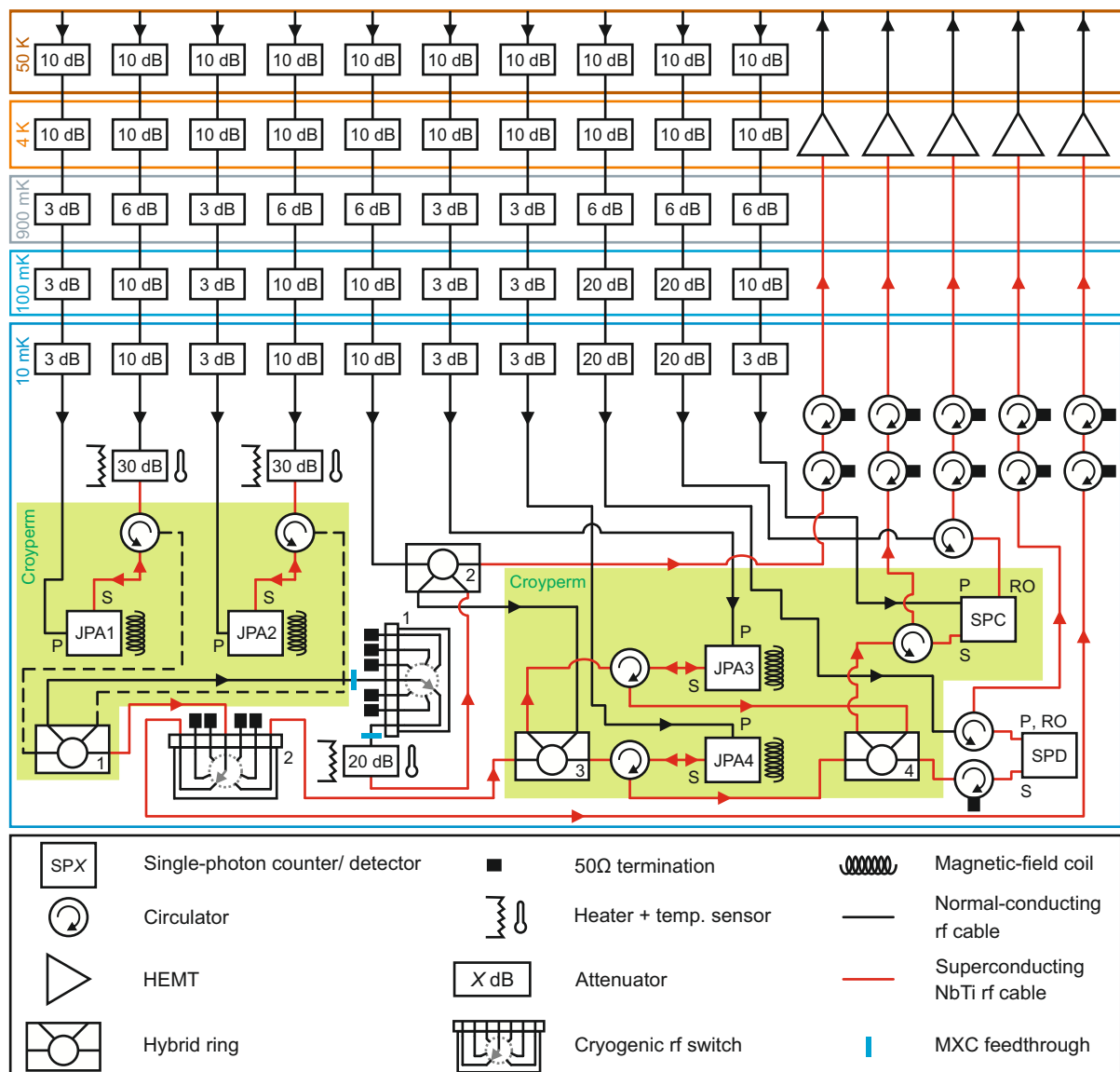
SP*X*	Single-photon counter/ detector	■	50Ω termination	〰〰	Magnetic-field coil
Circulator		Heater + temp. sensor		Normal-conducting rf cable
HEMT		*X* dB	Attenuator	Superconducting NbTi rf cable
Hybrid ring		Cryogenic rf switch		MXC feedthrough

Figure 7.1: Schematic of the cryogenic quantum illumination setup. The output signals are amplified and filtered in subsequent steps, down-converted and digitized in a room temperature setup (not shown), similar to the one illustrated in Fig. 6.11.

Outlook The theoretical studies and experimental work conducted in this thesis directly aim toward an experimental study of quantum illumination in the microwave regime. For the realization of the latter, we consider the experimental layout shown in Fig. 7.1. Here, JPAs 1 and 2, in conjunction with the associated HR 1, are employed for the generation of two-mode squeezed vacuum (TMSV) states that constitute the resource states of the protocol. The cryogenic rf switch 1 implements a central logical component, i.e., switching between hypotheses H_0 (object absent) and H_1 (object present). To implement H_0, the incoming signal is terminated with a $50\,\Omega$ load. Under H_1, the switch position changes in a way to allow the incoming signal to propagate to a 20-dB attenuator, which models the

strong signal attenuation condition, $\kappa \ll 1$. This (heatable) 20-dB attenuator can also serve as a thermal-noise source for calibration purposes. Next, the signals enter a second HR 2, where we can feed in microwave noise signals generated at room temperature to fulfill the important condition, $N_{\mathrm{B}} \gg 1$. One of the two outputs is directly connected to an output line, e.g., for calibration of the coupled noise. The second HR output serves as an input to the parametric mixer, or QUMPI. The idler part of the resource state first propagates to a second rf switch 2, which we can toggle between two positions. The first position is connected directly to an output line for calibration and stabilization of the TMSV states. The second position allows the idler to propagate to the QUMPI. One of the two QUMPI outputs is connected to a single-photon counter (SPC), which relies on a working principle described in Ref. [185]. The second QUMPI output leads to a single-photon detector (SPD) based on our novel 3D-cavity architecture [279]. This parallel access to both the SPC and SPD devices allows to directly compare their performance in terms of the associated QA in the full quantum illumination protocol. Figure 7.2 shows
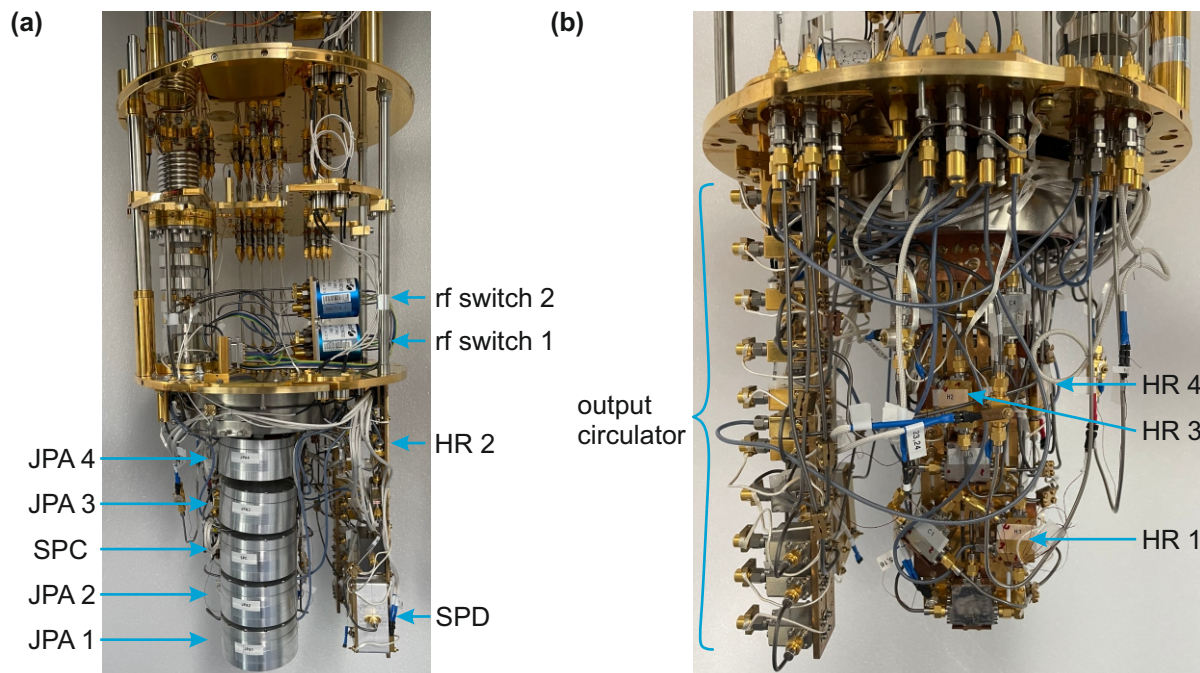
Figure 7.2: Photograph of the cryogenic quantum illumination setup. Panels (a) and (b) show different perspectives on the cryogenic sample stage. The JPAs and the SPC are enclosed in aluminum cylinders for magnetic shielding. The central sample rod is later additionally enclosed in a double-layered cryoperm shield (not shown here) for extra protection from stray magnetic fields.

a photograph of the assembled cryogenic setup according to the layout illustrated in Fig. 7.1.Based on our studies, we expect a performance of the setup around a quantum advantage of 1 dB. Such a proof-of-principle demonstration will lay a foundation for more practical schemes, such as coupling the signal mode directly into free space by means of

an antenna structure, and, eventually, may lead to field-deployable quantum radars.

The field of quantum sensing and metrology is advancing at an excitingly rapid pace along with the neighboring disciplines of quantum computing and quantum communication [36]. The immediate and broad application potential in sensing and metrology is arguably a unique selling point compared to the other fields. Highly sensitive magnetic field detectors are already available today in the form of quantum magnetometers based on SQUIDs and atomic vapor cells. Based on the impact of these quantum devices in their application segment, it can be extrapolated that future solutions in quantum sensing and metrology will decisively shape the technology landscape of the coming decades.

Appendix A

Hypothesis-dependent covariances in the CPC scheme

The covariance between $\hat{N}_1$ and $\hat{N}_2$ in Eqs. (3.36) and (3.37) is given by

$$\text{Cov}\left(\hat{N}_1, \hat{N}_2\right) = \text{Cov}\left(\hat{b}_1^\dagger \hat{b}_1, \hat{b}_2^\dagger \hat{b}_2\right) = \langle \hat{b}_1^\dagger \hat{b}_1 \hat{b}_2^\dagger \hat{b}_2 \rangle - \langle \hat{b}_1^\dagger \hat{b}_1 \rangle \langle \hat{b}_2^\dagger \hat{b}_2 \rangle. \tag{A.1}$$

For a complex random vector $X = (X^1, \ldots, X^n)$, we introduce the moment notation

$$m^i = \langle X^i \rangle, \; m^{ij} = \langle X^i X^j \rangle, \; \ldots \tag{A.2}$$

The fourth-order moments can be expressed as

$$m^{ijkl} = c^{ijkl} + c^i c^{jkl}[4] + c^{ij} c^{kl}[3] + c^i c^j c^{kl}[6] + c^i c^j c^k c^l, \tag{A.3}$$

where $c^i, \ldots, c^{ijkl}$ denote the cumulants of order one to four and the numbers in the square brackets indicate the number of terms contained in each expression as the indices rotate, i.e., $i \to j, j \to k$ etc. For Gaussian states, cumulants of order ≥ 3 vanish and the fourth-order moment simplifies to

$$m_{\text{Gauss}}^{ijkl} = c^{ij} c^{kl}[3] + c^i c^j c^{kl}[6] + c^i c^j c^k c^l. \tag{A.4}$$

The remaining first and second order cumulants are connected to the moments via

$$c^i = m^i \quad \text{and} \quad c^{ij} = m^{ij} - m^i m^j. \tag{A.5}$$

Since the first-order signal moments and the corresponding first-order cumulants vanish for $\hat{b}_1$ and $\hat{b}_2$, the fourth-order signal moment from Eq. (A.1) simplifies to

$$\langle \hat{b}_1^\dagger \hat{b}_1 \hat{b}_2^\dagger \hat{b}_2 \rangle = \langle \hat{b}_1^\dagger \hat{b}_1 \rangle \langle \hat{b}_2^\dagger \hat{b}_2 \rangle + \langle \hat{b}_1^\dagger \hat{b}_2^\dagger \rangle \langle \hat{b}_1 \hat{b}_2 \rangle + \langle \hat{b}_1^\dagger \hat{b}_2 \rangle \langle \hat{b}_1 \hat{b}_2^\dagger \rangle, \tag{A.6}$$

where we used the expressions from Eq. (A.5). The covariance between $\hat{N}_1$ and $\hat{N}_2$ reduces to

$$\mathrm{Cov}\left(\hat{N}_1, \hat{N}_2\right) = \langle \hat{b}_1^\dagger \hat{b}_2^\dagger \rangle \langle \hat{b}_1 \hat{b}_2 \rangle + \langle \hat{b}_1^\dagger \hat{b}_2 \rangle \langle \hat{b}_1 \hat{b}_2^\dagger \rangle. \tag{A.7}$$

The expressions from Eqs. (3.45) and (3.46) can be straightforwardly derived by insertion of Eqs. (3.23), (3.24), and (6.39) into Eq. (A.7).

Appendix B

Conversion of a scattering matrix into a transfer matrix

Here, we provide the explicit expressions to calculate a 4×4 transfer matrix $\mathcal{T}$ [see Eq. (6.18)] based on a known 4×4 scattering matrix $\mathcal{S}$ according to [95]

$$\mathcal{T}_{11} = \mathcal{S}_{21} + \frac{\mathcal{S}_{22}\mathcal{S}_{13} - \mathcal{S}_{23}\mathcal{S}_{12}}{\mathcal{S}_{42}\mathcal{S}_{13} - \mathcal{S}_{43}\mathcal{S}_{12}} \left(-\mathcal{S}_{41} + \frac{\mathcal{S}_{43}\mathcal{S}_{11}}{\mathcal{S}_{13}} \right) - \frac{\mathcal{S}_{23}\mathcal{S}_{11}}{\mathcal{S}_{13}}, \tag{B.1}$$

$$\mathcal{T}_{12} = \frac{\mathcal{S}_{22}\mathcal{S}_{13} - \mathcal{S}_{23}\mathcal{S}_{12}}{\mathcal{S}_{42}\mathcal{S}_{13} - \mathcal{S}_{43}\mathcal{S}_{12}} \frac{-\mathcal{S}_{43}}{\mathcal{S}_{13}} + \frac{\mathcal{S}_{23}}{\mathcal{S}_{13}}, \tag{B.2}$$

$$\mathcal{T}_{13} = \frac{\mathcal{S}_{22}\mathcal{S}_{13} - \mathcal{S}_{23}\mathcal{S}_{12}}{\mathcal{S}_{42}\mathcal{S}_{13} - \mathcal{S}_{43}\mathcal{S}_{12}} \left(\frac{\mathcal{S}_{43}\mathcal{S}_{14}}{\mathcal{S}_{13}} - \mathcal{S}_{44} \right) + \frac{\mathcal{S}_{23}\mathcal{S}_{14}}{\mathcal{S}_{13}} + \mathcal{S}_{24}, \tag{B.3}$$

$$\mathcal{T}_{14} = \frac{\mathcal{S}_{22}\mathcal{S}_{13} - \mathcal{S}_{23}\mathcal{S}_{12}}{\mathcal{S}_{42}\mathcal{S}_{13} - \mathcal{S}_{43}\mathcal{S}_{12}}, \tag{B.4}$$

$$\mathcal{T}_{21} = \frac{\mathcal{S}_{13}}{\mathcal{S}_{42}\mathcal{S}_{13} - \mathcal{S}_{43}\mathcal{S}_{12}} \left(-\mathcal{S}_{41} + \frac{\mathcal{S}_{43}\mathcal{S}_{11}}{\mathcal{S}_{13}} \right), \tag{B.5}$$

$$\mathcal{T}_{22} = \frac{\mathcal{S}_{13}}{\mathcal{S}_{42}\mathcal{S}_{13} - \mathcal{S}_{43}\mathcal{S}_{12}} \left(-\frac{\mathcal{S}_{43}}{\mathcal{S}_{13}} \right), \tag{B.6}$$

$$\mathcal{T}_{23} = \frac{\mathcal{S}_{13}}{\mathcal{S}_{42}\mathcal{S}_{13} - \mathcal{S}_{43}\mathcal{S}_{12}} \left(-\mathcal{S}_{44} + \frac{\mathcal{S}_{43}\mathcal{S}_{14}}{\mathcal{S}_{13}} \right), \tag{B.7}$$

$$\mathcal{T}_{24} = \frac{\mathcal{S}_{13}}{\mathcal{S}_{42}\mathcal{S}_{13} - \mathcal{S}_{43}\mathcal{S}_{12}}, \tag{B.8}$$

$$\mathcal{T}_{31} = \frac{\mathcal{S}_{32}\mathcal{S}_{13} - \mathcal{S}_{33}\mathcal{S}_{12}}{\mathcal{S}_{42}\mathcal{S}_{13} - \mathcal{S}_{43}\mathcal{S}_{12}} \left(-\mathcal{S}_{41} + \frac{\mathcal{S}_{43}\mathcal{S}_{11}}{\mathcal{S}_{13}} \right) + \mathcal{S}_{31} - \frac{\mathcal{S}_{33}\mathcal{S}_{11}}{\mathcal{S}_{13}}, \tag{B.9}$$

$$\mathcal{T}_{32} = \frac{\mathcal{S}_{32}\mathcal{S}_{13} - \mathcal{S}_{33}\mathcal{S}_{12}}{\mathcal{S}_{42}\mathcal{S}_{13} - \mathcal{S}_{43}\mathcal{S}_{12}} \left(-\frac{\mathcal{S}_{43}}{\mathcal{S}_{13}} \right) + \frac{\mathcal{S}_{33}}{\mathcal{S}_{13}}, \tag{B.10}$$

$$\mathcal{T}_{33} = \frac{\mathcal{S}_{32}\mathcal{S}_{13} - \mathcal{S}_{33}\mathcal{S}_{12}}{\mathcal{S}_{42}\mathcal{S}_{13} - \mathcal{S}_{43}\mathcal{S}_{12}} \left(-\mathcal{S}_{44} + \frac{\mathcal{S}_{43}\mathcal{S}_{14}}{\mathcal{S}_{13}} \right) + \mathcal{S}_{34} - \frac{\mathcal{S}_{33}\mathcal{S}_{14}}{\mathcal{S}_{13}}, \tag{B.11}$$

$$\mathcal{T}_{34} = \frac{\mathcal{S}_{32}\mathcal{S}_{13} - \mathcal{S}_{33}\mathcal{S}_{12}}{\mathcal{S}_{42}\mathcal{S}_{13} - \mathcal{S}_{43}\mathcal{S}_{12}}, \tag{B.12}$$

$$\mathcal{T}_{41} = \frac{-\mathcal{S}_{12}}{\mathcal{S}_{42}\mathcal{S}_{13} - \mathcal{S}_{43}\mathcal{S}_{12}} \left(-\mathcal{S}_{41} + \frac{\mathcal{S}_{43}\mathcal{S}_{11}}{\mathcal{S}_{13}} \right) - \frac{\mathcal{S}_{11}}{\mathcal{S}_{13}}, \tag{B.13}$$

$$\mathcal{T}_{42} = \frac{-\mathcal{S}_{12}}{\mathcal{S}_{42}\mathcal{S}_{13} - \mathcal{S}_{43}\mathcal{S}_{12}} \left(-\frac{\mathcal{S}_{43}}{\mathcal{S}_{13}} \right) + \frac{1}{\mathcal{S}_{13}}, \tag{B.14}$$

$$\mathcal{T}_{43} = \frac{-\mathcal{S}_{12}}{\mathcal{S}_{42}\mathcal{S}_{13} - \mathcal{S}_{43}\mathcal{S}_{12}} \left(-\mathcal{S}_{44} + \frac{\mathcal{S}_{43}\mathcal{S}_{14}}{\mathcal{S}_{13}} \right) - \frac{\mathcal{S}_{14}}{\mathcal{S}_{13}}, \tag{B.15}$$

$$\mathcal{T}_{44} = \frac{-\mathcal{S}_{12}}{\mathcal{S}_{42}\mathcal{S}_{13} - \mathcal{S}_{43}\mathcal{S}_{12}}. \tag{B.16}$$

Appendix C

Gaussian second-order correlation functions

The second-order auto-correlation functions $g_1^{(2)}(0)$ and $g_2^{(2)}(0)$, as well as the second-order cross-correlation function $g_C^{(2)}(0)$ for Gaussian states are given by [131]

$$
g_1^{(2)}(0) = 2 \left[2 \left(2 \left(V_{11} + V_{22} \right)^2 + 4 \left(V_{11} + V_{22} \right) \left(\frac{|d_1 + \mathrm{i}\, d_2|}{\sqrt{2}} \right)^2 \right. \right.
$$
$$
+ \left. \left(\left| (V_{11} - V_{22} - 2\mathrm{i}\, V_{12}) + \left(\frac{|d_1 + \mathrm{i}\, d_2|}{\sqrt{2}} \right)^2 \right| \right)^2 \right) - 4 \left(V_{11} + V_{22} + \left(\frac{|d_1 + \mathrm{i}\, d_2|}{\sqrt{2}} \right)^2 \right) + 1 \right]
$$
$$
\left/ \left[\left(2 \left(V_{11} + V_{22} + \left(\frac{|d_1 + \mathrm{i}\, d_2|}{\sqrt{2}} \right)^2 \right) - 1 \right)^2 \right] \right. , \quad \text{(C.1)}
$$

$$
g_2^{(2)}(0) = 2 \left[2 \left(2 \left(V_{33} + V_{44} \right)^2 + 4 \left(V_{33} + V_{44} \right) \left(\frac{|d_3 + \mathrm{i}\, d_4|}{\sqrt{2}} \right)^2 \right. \right.
$$
$$
+ \left. \left(\left| (V_{33} - V_{44} - 2\mathrm{i}\, V_{34}) + \left(\frac{|d_3 + \mathrm{i}\, d_4|}{\sqrt{2}} \right)^2 \right| \right)^2 \right) - 4 \left(V_{33} + V_{44} + \left(\frac{|d_3 + \mathrm{i}\, d_4|}{\sqrt{2}} \right)^2 \right) + 1 \right]
$$
$$
\left/ \left[\left(2 \left(V_{33} + V_{44} + \left(\frac{|d_3 + \mathrm{i}\, d_4|}{\sqrt{2}} \right)^2 \right) - 1 \right)^2 \right] \right. , \quad \text{(C.2)}
$$

$$g_C^{(2)}(0) = \left[2\left(A+B\right)^2 - 3B - 3a - 3b + \left| A - B - 2\mathrm{i}\,C + \frac{(x_2 + \mathrm{i}\,y_2)^2}{2} \right|^2 \right.$$

$$+ \frac{|x_1 + \mathrm{i}\,y_1|^2\,|x_2 + \mathrm{i}\,y_2|^2}{2} - 3A + 2\left(a+b\right)\left(A+B\right) - \frac{3\,|x_1 + \mathrm{i}\,y_1|^2}{2}$$

$$- \frac{3\,|x_2 + \mathrm{i}\,y_2|^2}{2} + \frac{|x_2 + \mathrm{i}\,y_2|^2\,(4A + 4B)}{2} + \left| a - b - 2\mathrm{i}\,c + \frac{(x_1 + \mathrm{i}\,y_1)^2}{2} \right|^2$$

$$+ 2\,|e + h + \mathrm{i}\,f - \mathrm{i}\,g|^2 + 2\left(a+b\right)^2 + \frac{|x_1 + \mathrm{i}\,y_1|^2\,(4a + 4b)}{2} + |x_1 + \mathrm{i}\,y_1|^2\,(A+B)$$

$$+ 2\,|h - e + \mathrm{i}\,f + \mathrm{i}\,g|^2 + |x_2 + \mathrm{i}\,y_2|^2\,(a+b) + (x_1 - \mathrm{i}\,y_1)\,(x_2 + \mathrm{i}\,y_2)\,(e + h - \mathrm{i}\,f + \mathrm{i}\,g)$$

$$+ (x_1 + \mathrm{i}\,y_1)\,(x_2 - \mathrm{i}\,y_2)\,(e + h + \mathrm{i}\,f - \mathrm{i}\,g) - (x_1 - \mathrm{i}\,y_1)\,(x_2 - \mathrm{i}\,y_2)\,(h - e + \mathrm{i}\,f + \mathrm{i}\,g)$$

$$\left. + (x_1 + \mathrm{i}\,y_1)\,(x_2 + \mathrm{i}\,y_2)\,(e - h + \mathrm{i}\,f + \mathrm{i}\,g) + \frac{3}{2} \right]$$

$$\Big/ \left[\frac{|x_1 + \mathrm{i}\,y_1|^2}{2} + \frac{|x_2 + \mathrm{i}\,y_2|^2}{2} + A + B + a + b - 1 \right]^2, \quad \text{(C.3)}$$

where

$$a = V_{11}, \qquad b = V_{22}, \qquad c = V_{12}, \qquad e = V_{13}, \qquad f = V_{14}, \qquad g = V_{23},$$
$$h = V_{24}, \qquad A = V_{33}, \qquad B = V_{44}, \qquad C = V_{34}, \tag{C.4}$$

and

$$x_1 = d_1, \qquad y_1 = d_2, \qquad x_2 = d_3, \qquad y_2 = d_4. \tag{C.5}$$

Bibliography

[1] M. A. Nielsen and I. L. Chuang, *Quantum Computation and Quantum Information* (Cambridge University Press, Cambridge, 2010), URL https://doi.org/10.1017/CBO9780511976667.

[2] N. Meher and S. Sivakumar, "A review on quantum information processing in cavities", The European Physical Journal Plus **137**, 985 (2022).

[3] M. H. Devoret and R. J. Schoelkopf, "Superconducting Circuits for Quantum Information: An Outlook", Science **339**, 1169 (2013).

[4] A. Blais, S. M. Girvin, and W. D. Oliver, "Quantum information processing and quantum optics with circuit quantum electrodynamics", Nature Physics **16**, 247 (2020).

[5] F. Flamini, N. Spagnolo, and F. Sciarrino, "Photonic quantum information processing: a review", Reports on Progress in Physics **82**, 016001 (2018).

[6] S. L. Braunstein and P. van Loock, "Quantum information with continuous variables", Rev. Mod. Phys. **77**, 513 (2005).

[7] C. Weedbrook, S. Pirandola, R. García-Patrón, N. J. Cerf, T. C. Ralph, J. H. Shapiro, and S. Lloyd, "Gaussian quantum information", Rev. Mod. Phys. **84**, 621 (2012).

[8] J. P. Dowling and G. J. Milburn, "Quantum technology: the second quantum revolution", Philosophical transactions. Series A, Mathematical, physical, and engineering sciences **361**, 1655 (2003).

[9] Y. Aharonov and D. Bohm, "Significance of Electromagnetic Potentials in the Quantum Theory", Phys. Rev. **115**, 485 (1959).

[10] B. Misra and E. C. G. Sudarshan, "The Zeno's paradox in quantum theory", Journal of Mathematical Physics **18**, 756 (1977).

[11] H. B. G. Casimir and D. Polder, "The Influence of Retardation on the London-van der Waals Forces", Phys. Rev. **73**, 360 (1948).

[12] S. P. Walborn, M. O. Terra Cunha, S. Pádua, and C. H. Monken, "Double-slit quantum eraser", Phys. Rev. A **65**, 033818 (2002).

[13] R. Feynman, R. Leighton, and M. Sands, *The Feynman Lectures on Physics, Vol. III: The New Millennium Edition: Quantum Mechanics*, The Feynman Lectures on Physics (Basic Books, 2011), ISBN 9780465025015, URL https://books.google.de/books?id=KsnbNL_rh04C.

[14] L. D. Landau and L. M. Lifshitz, *Quantum Mechanics Non-Relativistic Theory, Third Edition: Volume 3* (Butterworth-Heinemann, 1981), 3rd ed., ISBN 0750635398, URL http://www.worldcat.org/isbn/0750635398.

[15] D. Griffiths and P. Griffiths, *Introduction to Quantum Mechanics*, Pearson international edition (Pearson Prentice Hall, 2005), ISBN 9780131118928, URL https://books.google.de/books?id=z4fwAAAAMAAJ.

[16] J. S. Bell, "On the Einstein Podolsky Rosen paradox", Physics Physique Fizika **1**, 195 (1964).

[17] A. Einstein, B. Podolsky, and N. Rosen, "Can Quantum-Mechanical Description of Physical Reality Be Considered Complete?", Phys. Rev. **47**, 777 (1935).

[18] E. Knill, R. Laflamme, and G. J. Milburn, "A scheme for efficient quantum computation with linear optics", Nature **409**, 46 (2001).

[19] R. Raussendorf and H. J. Briegel, "A One-Way Quantum Computer", Phys. Rev. Lett. **86**, 5188 (2001).

[20] M. N. Leuenberger and D. Loss, "Quantum computing in molecular magnets", Nature **410**, 789 (2001).

[21] D. Gottesman and I. L. Chuang, "Demonstrating the viability of universal quantum computation using teleportation and single-qubit operations", Nature **402**, 390 (1999).

[22] A. Kitaev, "Fault-tolerant quantum computation by anyons", Annals of Physics **303**, 2 (2003).

[23] A. Blais, R.-S. Huang, A. Wallraff, S. M. Girvin, and R. J. Schoelkopf, "Cavity quantum electrodynamics for superconducting electrical circuits: An architecture for quantum computation", Phys. Rev. A **69**, 062320 (2004).

[24] D. P. DiVincenzo, "The Physical Implementation of Quantum Computation", Fortschritte der Physik **48**, 771 (2000).

[25] F. Arute et al., "Quantum supremacy using a programmable superconducting processor", Nature **574**, 505 (2019).

[26] P. W. Shor, "Algorithms for quantum computation: discrete logarithms and factoring", Proceedings 35th Annual Symposium on Foundations of Computer Science pp. 124–134 (1994).

[27] L. K. Grover, "A Fast Quantum Mechanical Algorithm for Database Search", in *Proceedings of the Twenty-Eighth Annual ACM Symposium on Theory of Computing* (Association for Computing Machinery, New York, NY, USA, 1996), STOC '96, p. 212, ISBN 0897917855, URL https://doi.org/10.1145/237814.237866.

[28] D. Deutsch and R. Jozsa, "Rapid solution of problems by quantum computation", Proceedings of the Royal Society of London. Series A: Mathematical and Physical Sciences **439**, 553 (1992).

[29] S. Pirandola, U. L. Andersen, L. Banchi, M. Berta, D. Bunandar, R. Colbeck, D. Englund, T. Gehring, C. Lupo, C. Ottaviani, J. L. Pereira, M. Razavi, J. S. Shaari, M. Tomamichel, V. C. Usenko, G. Vallone, P. Villoresi, and P. Wallden, "Advances in quantum cryptography", Adv. Opt. Photon. **12**, 1012 (2020).

[30] C. H. Bennett, G. Brassard, and A. K. Ekert, *Quantum Cryptography*, 4 (Scientific American, a division of Nature America, Inc., 1992), URL http://www.jstor.org/stable/24939253.

[31] C. H. Bennett, F. Bessette, G. Brassard, L. Salvail, and J. Smolin, "Experimental quantum cryptography", Journal of Cryptology **5**, 3 (1992).

[32] N. Gisin, G. Ribordy, W. Tittel, and H. Zbinden, "Quantum cryptography", Rev. Mod. Phys. **74**, 145 (2002).

[33] C. Portmann and R. Renner, "Security in quantum cryptography", Rev. Mod. Phys. **94**, 025008 (2022).

[34] M. Dušek, N. Lütkenhaus, and M. Hendrych, "Quantum cryptography", Progress in optics **49**, 381 (2006).

[35] S. Pirandola, B. R. Bardhan, T. Gehring, C. Weedbrook, and S. Lloyd, "Advances in photonic quantum sensing", Nature Photonics **12**, 724 (2018).

[36] C. L. Degen, F. Reinhard, and P. Cappellaro, "Quantum sensing", Rev. Mod. Phys. **89**, 035002 (2017).

[37] Z. Zhang and Q. Zhuang, "Distributed quantum sensing", Quantum Science and Technology **6**, 043001 (2021).

[38] B. J. Lawrie, P. D. Lett, A. M. Marino, and R. C. Pooser, "Quantum Sensing with Squeezed Light", ACS Photonics **6**, 1307 (2019).

[39] J. M. Boss, K. S. Cujia, J. Zopes, and C. L. Degen, "Quantum sensing with arbitrary frequency resolution", Science **356**, 837 (2017).

[40] C. M. Caves, "Quantum-mechanical noise in an interferometer", Physical Review D **23**, 1693 (1981).

[41] R. E. Slusher, L. W. Hollberg, B. Yurke, J. C. Mertz, and J. F. Valley, "Observation of Squeezed States Generated by Four-Wave Mixing in an Optical Cavity", Phys. Rev. Lett. **55**, 2409 (1985).

[42] P. A. M. Dirac, *The Principles of Quantum Mechanics* (Clarendon Press, 1947), 2nd ed., URL https://digbib.bibliothek.kit.edu/volltexte/wasbleibt/57355817/57355817.pdf.

[43] R. G. Torrome, "Quantum Illumination with Non-Gaussian Three Photons States", arXiv:2305.10458 (2023).

[44] M. Skolnik, *Introduction to Radar Systems*, Electrical engineering series (McGraw-Hill, 2001), ISBN 9780071181891, URL https://books.google.de/books?id=Y6-APwAACAAJ.

[45] G. Slepyan, S. Vlasenko, D. Mogilevtsev, and A. Boag, "Quantum Radars and Lidars: Concepts, realizations, and perspectives", IEEE Antennas and Propagation Magazine **64**, 16 (2022).

[46] W. Wai-Lok Lai, X. Derobert, and P. Annan, "A review of Ground Penetrating Radar application in civil engineering: A 30-year journey from Locating and Testing to Imaging and Diagnosis", NDT & E International **96**, 58 (2018).

[47] S. Lloyd, "Enhanced Sensitivity of Photodetection via Quantum Illumination", Science **321**, 1463 (2008).

[48] S.-H. Tan, B. I. Erkmen, V. Giovannetti, S. Guha, S. Lloyd, L. Maccone, S. Pirandola, and J. H. Shapiro, "Quantum Illumination with Gaussian States", Physical Review Letters **101**, 253601 (2008).

[49] A. Karsa, A. Fletcher, G. Spedalieri, and S. Pirandola, "Quantum Illumination and Quantum Radar: A Brief Overview", arXiv:2310.06049 (2023).

[50] J. H. Shapiro and S. Lloyd, "Quantum illumination versus coherent-state target detection", New Journal of Physics **11**, 063045 (2009).

[51] E. D. Lopaeva, I. Ruo Berchera, I. P. Degiovanni, S. Olivares, G. Brida, and M. Genovese, "Experimental Realization of Quantum Illumination", Physical Review Letters **110**, 153603 (2013).

[52] S. Barzanjeh, S. Guha, C. Weedbrook, D. Vitali, J. H. Shapiro, and S. Pirandola, "Microwave Quantum Illumination", Physical Review Letters **114**, 080503 (2015).

[53] A. Karsa and S. Pirandola, "Noisy Receivers for Quantum Illumination", IEEE Aerospace and Electronic Systems Magazine **35**, 22 (2020).

[54] F. Kronowetter, M. Würth, W. Utschick, R. Gross, and K. Fedorov, "Imperfect photon detection in quantum illumination", Phys. Rev. Appl. **21**, 014007 (2024).

[55] R. Assouly, R. Dassonneville, T. Peronnin, A. Bienfait, and B. Huard, "Quantum advantage in microwave quantum radar", Nature Physics **19**, 1418 (2023).

[56] G. Sorelli, N. Treps, F. Grosshans, and F. Boust, "Detecting a Target With Quantum Entanglement", IEEE Aerospace and Electronic Systems Magazine **37**, 68 (2022).

[57] M. Reichert, Q. Zhuang, J. H. Shapiro, and R. Di Candia, "Quantum Illumination with a Hetero-Homodyne Receiver and Sequential Detection", Phys. Rev. Appl. **20**, 014030 (2023).

[58] H. Shi, B. Zhang, and Q. Zhuang, "Fulfilling entanglement's optimal advantage via converting correlation to coherence", arXiv:2207.06609 (2022).

[59] Z. Zhang, S. Mouradian, F. N. C. Wong, and J. H. Shapiro, "Entanglement-Enhanced Sensing in a Lossy and Noisy Environment", Physical Review Letters **114**, 110506 (2015).

[60] D. Luong, S. Rajan, and B. Balaji, "Quantum Two-Mode Squeezing Radar and Noise Radar: Correlation Coefficients for Target Detection", IEEE Sensors Journal **20**, 5221 (2020).

[61] D. Luong, C. W. S. Chang, A. M. Vadiraj, A. Damini, C. M. Wilson, and B. Balaji, "Receiver Operating Characteristics for a Prototype Quantum Two-Mode Squeezing Radar", IEEE Transactions on Aerospace and Electronic Systems **56**, 2041 (2020).

[62] D. G. England, B. Balaji, and B. J. Sussman, "Quantum-enhanced standoff detection using correlated photon pairs", Phys. Rev. A **99**, 023828 (2019).

[63] C. W. S. Chang, A. M. Vadiraj, J. Bourassa, B. Balaji, and C. M. Wilson, "Quantum-enhanced noise radar", Applied Physics Letters **114**, 112601 (2019).

[64] R. G. Torrome and S. Barzanjeh, "Advances in Quantum Radar and Quantum LiDAR", arXiv:2310.07198 (2023).

[65] E. P. Menzel, R. Di Candia, F. Deppe, P. Eder, L. Zhong, M. Ihmig, M. Haeberlein, A. Baust, E. Hoffmann, D. Ballester, K. Inomata, T. Yamamoto, Y. Nakamura, E. Solano, A. Marx, and R. Gross, "Path Entanglement of Continuous-Variable Quantum Microwaves", Phys. Rev. Lett. **109**, 250502 (2012).

[66] C. Eichler, D. Bozyigit, C. Lang, L. Steffen, J. Fink, and A. Wallraff, "Experimental State Tomography of Itinerant Single Microwave Photons", Phys. Rev. Lett. **106**, 220503 (2011).

[67] E. P. Menzel, F. Deppe, M. Mariantoni, M. A. Araque Caballero, A. Baust, T. Niemczyk, E. Hoffmann, A. Marx, E. Solano, and R. Gross, "Dual-Path State Reconstruction Scheme for Propagating Quantum Microwaves and Detector Noise Tomography", Phys. Rev. Lett. **105**, 100401 (2010).

[68] E. P. Menzel, "Propagating quantum microwaves: dual-path state reconstruction and path entanglement", Phd thesis, Technische Universität München (2013), URL https://mediatum.ub.tum.de/1177178.

[69] M. Mariantoni, "New trends in superconducting circuit quantum electrodynamics: two amplifiers, two resonators, and two photons: a not so short introduction to quantum circuits and signals", Ph.D. thesis, Tech. U., Munich (main) (2009), URL https://www.wmi.badw.de/fileadmin/WMI/Publications/Mariantoni_Doktorarbeit_2009.pdf.

[70] M. Mariantoni, E. P. Menzel, F. Deppe, M. A. Araque Caballero, A. Baust, T. Niemczyk, E. Hoffmann, E. Solano, A. Marx, and R. Gross, "Planck Spectroscopy and Quantum Noise of Microwave Beam Splitters", Phys. Rev. Lett. **105**, 133601 (2010).

[71] S. Pogorzalek, K. G. Fedorov, L. Zhong, J. Goetz, F. Wulschner, M. Fischer, P. Eder, E. Xie, K. Inomata, T. Yamamoto, Y. Nakamura, A. Marx, F. Deppe, and R. Gross, "Hysteretic Flux Response and Nondegenerate Gain of Flux-Driven Josephson Parametric Amplifiers", Phys. Rev. Applied **8**, 024012 (2017).

[72] S. Pogorzalek, K. G. Fedorov, M. Xu, A. Parra-Rodriguez, M. Sanz, M. Fischer, E. Xie, K. Inomata, Y. Nakamura, E. Solano, A. Marx, F. Deppe, and R. Gross, "Secure quantum remote state preparation of squeezed microwave states", Nature Communications **10**, 2604 (2019).

[73] M. Renger, S. Pogorzalek, Q. Chen, Y. Nojiri, K. Inomata, Y. Nakamura, M. Partanen, A. Marx, R. Gross, F. Deppe, and K. G. Fedorov, "Beyond the standard quantum limit for parametric amplification of broadband signals", npj Quantum Inf. **7**, 160 (2021).

[74] M. Renger, S. Pogorzalek, F. Fesquet, K. Honasoge, F. Kronowetter, Q. Chen, Y. Nojiri, K. Inomata, Y. Nakamura, A. Marx, F. Deppe, R. Gross, and K. G. Fedorov, "Flow of quantum correlations in noisy two-mode squeezed microwave states", Phys. Rev. A **106**, 052415 (2022).

[75] L. Zhong, E. P. Menzel, R. D. Candia, P. Eder, M. Ihmig, A. Baust, M. Haeberlein, E. Hoffmann, K. Inomata, T. Yamamoto, Y. Nakamura, E. Solano, F. Deppe, A. Marx, and R. Gross, "Squeezing with a flux-driven Josephson parametric amplifier", New J. Phys. **15**, 125013 (2013).

[76] K. G. Fedorov, L. Zhong, S. Pogorzalek, P. Eder, M. Fischer, J. Goetz, E. Xie, F. Wulschner, K. Inomata, T. Yamamoto, Y. Nakamura, R. Di Candia, U. Las Heras, M. Sanz, E. Solano, E. P. Menzel, F. Deppe, A. Marx, and R. Gross, "Displacement of Propagating Squeezed Microwave States", Phys. Rev. Lett. **117**, 020502 (2016).

[77] S. Pogorzalek, K. G. Fedorov, M. Xu, A. Parra-Rodriguez, M. Sanz, M. Fischer, E. Xie, K. Inomata, Y. Nakamura, E. Solano, A. Marx, F. Deppe, and R. Gross, "Secure quantum remote state preparation of squeezed microwave states", Nat. Commun. **10**, 2604 (2019).

[78] K. G. Fedorov, M. Renger, S. Pogorzalek, R. D. Candia, Q. Chen, Y. Nojiri, K. Inomata, Y. Nakamura, M. Partanen, A. Marx, R. Gross, and F. Deppe, "Experimental quantum teleportation of propagating microwaves", Sci. Adv. **7**, eabk0891 (2021).

[79] F. Fesquet, F. Kronowetter, M. Renger, W. K. Yam, S. Gandorfer, K. Inomata, Y. Nakamura, A. Marx, R. Gross, and K. G. Fedorov, "Demonstration of microwave single-shot quantum key distribution", arXiv:2311.11069 (2023).

[80] F. Kronowetter, F. Fesquet, M. Renger, K. Honasoge, Y. Nojiri, K. Inomata, Y. Nakamura, A. Marx, R. Gross, and K. Fedorov, "Quantum Microwave Parametric Interferometer", Phys. Rev. Appl. **20**, 024049 (2023).

[81] T. Yamamoto, K. Inomata, M. Watanabe, K. Matsuba, T. Miyazaki, W. D. Oliver, Y. Nakamura, and J. S. Tsai, "Flux-driven Josephson parametric amplifier", Appl. Phys. Lett. **93**, 042510 (2008).

[82] B. Yurke, L. R. Corruccini, P. G. Kaminsky, L. W. Rupp, A. D. Smith, A. H. Silver, R. W. Simon, and E. A. Whittaker, "Observation of parametric amplification and deamplification in a Josephson parametric amplifier", Phys. Rev. A **39**, 2519 (1989).

[83] J. Y. Mutus, T. C. White, R. Barends, Y. Chen, Z. Chen, B. Chiaro, A. Dunsworth, E. Jeffrey, J. Kelly, A. Megrant, C. Neill, P. J. J. O'Malley, P. Roushan, D. Sank, A. Vainsencher, J. Wenner, K. M. Sundqvist, A. N. Cleland, and J. M. Martinis,

"Strong environmental coupling in a Josephson parametric amplifier", Applied Physics Letters **104**, 263513 (2014).

[84] J. B. Clark, F. Lecocq, R. W. Simmonds, J. Aumentado, and J. D. Teufel, "Sideband cooling beyond the quantum backaction limit with squeezed light", Nature **541**, 191 (2017).

[85] A. Bienfait, P. Campagne-Ibarcq, A. H. Kiilerich, X. Zhou, S. Probst, J. J. Pla, T. Schenkel, D. Vion, D. Esteve, J. J. L. Morton, K. Moelmer, and P. Bertet, "Magnetic Resonance with Squeezed Microwaves", Phys. Rev. X **7**, 041011 (2017).

[86] A. Eddins, S. Schreppler, D. M. Toyli, L. S. Martin, S. Hacohen-Gourgy, L. C. G. Govia, H. Ribeiro, A. A. Clerk, and I. Siddiqi, "Stroboscopic Qubit Measurement with Squeezed Illumination", Phys. Rev. Lett. **120**, 040505 (2018).

[87] R. Vijay, D. H. Slichter, and I. Siddiqi, "Observation of Quantum Jumps in a Superconducting Artificial Atom", Phys. Rev. Lett. **106**, 110502 (2011).

[88] K. G. Fedorov, S. Pogorzalek, U. Las Heras, M. Sanz, P. Yard, P. Eder, M. Fischer, J. Goetz, E. Xie, K. Inomata, Y. Nakamura, R. Di Candia, E. Solano, A. Marx, F. Deppe, and R. Gross, "Finite-time quantum entanglement in propagating squeezed microwaves", Scientific Reports **8**, 6416 (2018).

[89] C. H. Bennett, G. Brassard, C. Crépeau, R. Jozsa, A. Peres, and W. K. Wootters, "Teleporting an unknown quantum state via dual classical and Einstein-Podolsky-Rosen channels", Phys. Rev. Lett. **70**, 1895 (1993).

[90] F. Fesquet, F. Kronowetter, M. Renger, Q. Chen, K. Honasoge, O. Gargiulo, Y. Nojiri, A. Marx, F. Deppe, R. Gross, and K. G. Fedorov, "Perspectives of microwave quantum key distribution in the open air", Phys. Rev. A **108**, 032607 (2023).

[91] A. Furusawa, J. L. Sørensen, S. L. Braunstein, C. A. Fuchs, H. J. Kimble, and E. S. Polzik, "Unconditional Quantum Teleportation", Science **282**, 706 (1998).

[92] U. Leonhardt and H. Paul, "Measuring the quantum state of light", Progress in Quantum Electronics **19**, 89 (1995).

[93] R. Loudon, *The quantum theory of light*, Oxford science publications (Oxford University Press, Oxford, 2000), 3rd ed., ISBN 9780198501770, URL https://books.google.de/books?id=guHRngEACAAJ.

[94] W. Heisenberg, "Über den anschaulichen Inhalt der quantentheoretischen Kinematik und Mechanik", Zeitschrift für Physik **43**, 172 (1927).

[95] D. M. Pozar, *Microwave Engineering* (Wiley, 2011), ISBN 9780470631553, URL https://books.google.de/books?id=_YEbGAXCcAMC.

[96] G. Adesso, S. Ragy, and A. R. Lee, "Continuous Variable Quantum Information: Gaussian States and Beyond", Open Systems & Information Dynamics **21**, 1440001 (2014).

[97] D. F. Walls and G. J. Milburn, *Quantum Optics* (Springer, Berlin, 2008), URL https://books.google.de/books?id=o6nrCAAAQBAJ.

[98] E. Wigner, "On the Quantum Correction For Thermodynamic Equilibrium", Phys. Rev. **40**, 749 (1932).

[99] R. J. Glauber, "Coherent and Incoherent States of the Radiation Field", Phys. Rev. **131**, 2766 (1963).

[100] E. C. G. Sudarshan, "Equivalence of Semiclassical and Quantum Mechanical Descriptions of Statistical Light Beams", Phys. Rev. Lett. **10**, 277 (1963).

[101] K. Husimi, "Some Formal Properties of the Density Matrix", Proceedings of the Physico-Mathematical Society of Japan. 3rd Series **22**, 264 (1940).

[102] A. Wunsche, "Reconstruction of operators from their normally ordered moments for a single boson mode", Quantum Optics: Journal of the European Optical Society Part B **2**, 453 (1990).

[103] V. Bužek, G. Adam, and G. Drobný, "Quantum state reconstruction and detection of quantum coherences on different observation levels", Phys. Rev. A **54**, 804 (1996).

[104] M. O. Scully and M. S. Zubairy, *Quantum Optics* (Cambridge University Press, 1997), ISBN 9780521435956, URL https://books.google.de/books?id=20ISsQCKKmQC.

[105] M. G. A. Paris, F. Illuminati, A. Serafini, and S. De Siena, "Purity of Gaussian states: Measurement schemes and time evolution in noisy channels", Phys. Rev. A **68**, 012314 (2003).

[106] M. Ghasemkhani, A. A. Varshovi, and R. Bufalo, "Perturbative effective action for the photon in noncommutative QED_2 and exactness of the Schwinger mass", Phys. Rev. D **97**, 065005 (2018).

[107] H. Nyquist, "Certain Topics in Telegraph Transmission Theory", Transactions of the American Institute of Electrical Engineers **47**, 617 (1928).

[108] S. Pogorzalek, "Remote State Preparation of Squeezed Microwave States", Phd thesis, Technische Universität München (2020), URL https://mediatum.ub.tum.de/1540503.

[109] N. Bloembergen, *Nonlinear Optics* (WORLD SCIENTIFIC, 1996), 4th ed., URL https://www.worldscientific.com/doi/abs/10.1142/3046.

[110] M. Schubert and B. Wilhelmi, *Nonlinear Optics and Quantum Electronics* (Wiley, 1986), ISBN 9780471088073, URL https://books.google.de/books?id=e8vvAAAAMAAJ.

[111] R. Di Candia, K. G. Fedorov, L. Zhong, S. Felicetti, E. P. Menzel, M. Sanz, F. Deppe, A. Marx, R. Gross, and E. Solano, "Quantum teleportation of propagating quantum microwaves", EPJ Quantum Technology **2**, 25 (2015).

[112] V. Giovannetti, S. Lloyd, and L. Maccone, "Quantum-Enhanced Measurements: Beating the Standard Quantum Limit", Science **306**, 1330 (2004).

[113] A. K. Ekert, "Quantum cryptography based on Bell's theorem", Phys. Rev. Lett. **67**, 661 (1991).

[114] C. Gerry, P. Knight, and P. Knight, *Introductory Quantum Optics* (Cambridge University Press, 2005), ISBN 9780521527354, URL https://books.google.de/books?id=CgByyoBJJwgC.

[115] P. Yard, "Noncommutation and finite-time correlations with propagating quantum microwave states", Master's thesis, Technische Universität München (2016), URL https://www.wmi.badw.de/fileadmin/WMI/Publications/Yard%2CPatrick_Masterarbeit_2016.pdf.

[116] M. Esposito, A. Ranadive, L. Planat, S. Leger, D. Fraudet, V. Jouanny, O. Buisson, W. Guichard, C. Naud, J. Aumentado, F. Lecocq, and N. Roch, "Observation of Two-Mode Squeezing in a Traveling Wave Parametric Amplifier", Phys. Rev. Lett. **128**, 153603 (2022).

[117] A. Serafini, F. Illuminati, and S. D. Siena, "Symplectic invariants, entropic measures and correlations of Gaussian states", Journal of Physics B: Atomic, Molecular and Optical Physics **37**, L21 (2003).

[118] G. Adesso, A. Serafini, and F. Illuminati, "Determination of Continuous Variable Entanglement by Purity Measurements", Phys. Rev. Lett. **92**, 087901 (2004).

[119] G. Adesso and F. Illuminati, "Gaussian measures of entanglement versus negativities: Ordering of two-mode Gaussian states", Phys. Rev. A **72**, 032334 (2005).

[120] H. Ollivier and W. H. Zurek, "Quantum Discord: A Measure of the Quantumness of Correlations", Phys. Rev. Lett. **88**, 017901 (2001).

[121] K. Modi, A. Brodutch, H. Cable, T. Paterek, and V. Vedral, "The classical-quantum boundary for correlations: Discord and related measures", Rev. Mod. Phys. **84**, 1655 (2012).

[122] P. Giorda and M. G. A. Paris, "Gaussian Quantum Discord", Phys. Rev. Lett. **105**, 020503 (2010).

[123] G. Adesso, T. R. Bromley, and M. Cianciaruso, "Measures and applications of quantum correlations", Journal of Physics A: Mathematical and Theoretical **49**, 473001 (2016).

[124] G. Adesso, M. Cianciaruso, and T. R. Bromley, "An introduction to quantum discord and non-classical correlations beyond entanglement", arXiv:1611.01959 (2016).

[125] G. Adesso and A. Datta, "Quantum versus Classical Correlations in Gaussian States", Phys. Rev. Lett. **105**, 030501 (2010).

[126] S. Pirandola, G. Spedalieri, S. L. Braunstein, N. J. Cerf, and S. Lloyd, "Optimality of Gaussian Discord", Phys. Rev. Lett. **113**, 140405 (2014).

[127] M. Gessner, E.-M. Laine, H.-P. Breuer, and J. Piilo, "Correlations in quantum states and the local creation of quantum discord", Phys. Rev. A **85**, 052122 (2012).

[128] R. H. BROWN and R. Q. TWISS, "Correlation between Photons in two Coherent Beams of Light", Nature **177**, 27 (1956).

[129] N. B. Grosse, T. Symul, M. Stobińska, T. C. Ralph, and P. K. Lam, "Measuring Photon Antibunching from Continuous Variable Sideband Squeezing", Phys. Rev. Lett. **98**, 153603 (2007).

[130] M. Alexanian, "Temporal second-order coherence function for displaced-squeezed thermal states", Journal of Modern Optics **63**, 961 (2016).

[131] S. Olivares, S. Cialdi, and M. G. Paris, "Homodyning the g(2)(0) of Gaussian states", Optics Communications **426**, 547 (2018).

[132] H. Corporation, *Quantum sensors program*, Final Technical Report (Harris Corporation, 2009), ISBN AFRLRI-RS-TR-2009-208, URL https://apps.dtic.mil/sti/pdfs/ADA506209.pdf.

[133] M. Richards, *Fundamentals of Radar Signal Processing*, Professional Engineering (McGraw-Hill Education, 2005), ISBN 9780071776486, URL https://books.google.de/books?id=j91oJ22ldoQC.

[134] F. Daum, "Radar Handbook, 3rd Edition (M.I. Skolnik, Ed; 2008) [Book Review]", IEEE Aerospace and Electronic Systems Magazine **23**, 41 (2008).

[135] D. Jenn, *Radar and Laser Cross Section Engineering*, AIAA education series (American Institute of Aeronautics and Astronautics, 2005), ISBN 9781563475061, URL https://books.google.de/books?id=SDMfAQAAIAAJ.

[136] H. L. van Trees, K. L. Bell, and Z. Tian, *Detection estimation and modulation theory* (John Wiley & Sons, Inc., Hoboken, N.J, 2013), 2nd ed., ISBN 9780470542965, URL https://books.google.de/books?id=CePNHWd8S4oC.

[137] R. Miller, "Fundamentals of Radar Signal Processing (Richards, M.A.; 2005) [Book review]", IEEE Signal Processing Magazine **26**, 100 (2009).

[138] E. L. Lehmann and J. P. Romano, *Testing Statistical Hypotheses* (Springer, 2022), 4th ed., ISBN 978-3-030-70577-0, URL https://books.google.de/books?id=K6t5qn-SEp8C.

[139] F. Nielsen, "An Information-Geometric Characterization of Chernoff Information", IEEE Signal Processing Letters **20**, 269 (2013).

[140] C. W. Helstrom, ed., *Quantum Detection and Estimation Theory*, vol. 123 of *Mathematics in Science and Engineering* (Elsevier, 1976), URL https://www.sciencedirect.com/science/article/pii/S0076539208602477.

[141] K. M. R. Audenaert, J. Calsamiglia, R. Muñoz Tapia, E. Bagan, L. Masanes, A. Acin, and F. Verstraete, "Discriminating States: The Quantum Chernoff Bound", Phys. Rev. Lett. **98**, 160501 (2007).

[142] J. Audretsch, *Verschränkte Systeme: Die Quantenphysik auf neuen Wegen*, Lehrbuch Physik (Wiley, 2008), ISBN 9783527618590, URL https://books.google.de/books?id=B_uFblp3tkYC.

[143] A. Serafini, *Quantum Continuous Variables: A Primer of Theoretical Methods* (CRC Press, 2017), ISBN 9781351645003, URL https://books.google.de/books?id=bMItDwAAQBAJ.

[144] R. Nair, "Discriminating quantum-optical beam-splitter channels with number-diagonal signal states: Applications to quantum reading and target detection", Phys. Rev. A **84**, 032312 (2011).

[145] S. Guha and B. I. Erkmen, "Gaussian-state quantum-illumination receivers for target detection", Physical Review A **80**, 052310 (2009).

[146] R. Di Candia, H. Yigitler, G. Paraoanu, and R. Jäntti, "Two-Way Covert Quantum Communication in the Microwave Regime", PRX Quantum **2**, 020316 (2021).

[147] M. Sanz, U. Las Heras, J. J. García-Ripoll, E. Solano, and R. Di Candia, "Quantum Estimation Methods for Quantum Illumination", Phys. Rev. Lett. **118**, 070803 (2017).

[148] A. Ly, M. Marsman, J. Verhagen, R. Grasman, and E.-J. Wagenmakers, "A Tutorial on Fisher Information", arXiv:1705.01064 (2017).

[149] D. Petz and C. Ghinea, *Introduction to quantum Fisher information* (World Scientific, 2011), URL https://www.worldscientific.com/doi/abs/10.1142/9789814338745_0015.

[150] L. Rigovacca, A. Farace, L. A. M. Souza, A. De Pasquale, V. Giovannetti, and G. Adesso, "Versatile Gaussian probes for squeezing estimation", Phys. Rev. A **95**, 052331 (2017).

[151] O. Pinel, P. Jian, N. Treps, C. Fabre, and D. Braun, "Quantum parameter estimation using general single-mode Gaussian states", Phys. Rev. A **88**, 040102 (2013).

[152] D. Safranek, A. R. Lee, and I. Fuentes, "Quantum parameter estimation using multi-mode Gaussian states", New Journal of Physics **17**, 073016 (2015).

[153] D. Bures, "An extension of Kakutani's theorem on infinite product measures to the tensor product of semifinite w*-algebras", Transactions of the American Mathematical Society **135**, 199 (1969).

[154] W. Zhong, W.-Y. Zhu, Y. Li, L. Zhou, M.-M. Du, and Y.-B. Sheng, "Relation between quantum illumination and quantum parameter estimation", arXiv:2308.07150 (2023).

[155] U. Las Heras, R. Di Candia, K. G. Fedorov, F. Deppe, M. Sanz, and E. Solano, "Quantum illumination reveals phase-shift inducing cloaking", Scientific Reports **7**, 9333 (2017).

[156] S. Kay, *Fundamentals of Statistical Signal Processing*, Detection Theory (Prentice-Hall PTR, 1998), ISBN 9780133457117, URL https://books.google.de/books?id=vA9LAQAAIAAJ.

[157] J. Calsamiglia, J. I. de Vicente, R. Muñoz Tapia, and E. Bagan, "Local Discrimination of Mixed States", Phys. Rev. Lett. **105**, 080504 (2010).

[158] S. Bandyopadhyay, "More Nonlocality with Less Purity", Phys. Rev. Lett. **106**, 210402 (2011).

[159] Q. Zhuang, Z. Zhang, and J. H. Shapiro, "Optimum Mixed-State Discrimination for Noisy Entanglement-Enhanced Sensing", Physical Review Letters **118**, 040801 (2017).

[160] J. H. Shapiro, "First-photon target detection: Beating Nair's pure-loss performance limit", Phys. Rev. A **106**, 032415 (2022).

[161] B. Kraus and J. I. Cirac, "Discrete Entanglement Distribution with Squeezed Light", Phys. Rev. Lett. **92**, 013602 (2004).

[162] C. W. Sandbo Chang, M. Simoen, J. Aumentado, C. Sabín, P. Forn-Díaz, A. M. Vadiraj, F. Quijandría, G. Johansson, I. Fuentes, and C. M. Wilson, "Generating Multimode Entangled Microwaves with a Superconducting Parametric Cavity", Phys. Rev. Appl. **10**, 044019 (2018).

[163] S. Boutin, D. M. Toyli, A. V. Venkatramani, A. W. Eddins, I. Siddiqi, and A. Blais, "Effect of Higher-Order Nonlinearities on Amplification and Squeezing in Josephson Parametric Amplifiers", Phys. Rev. Appl. **8**, 054030 (2017).

[164] M. Pompili, S. L. N. Hermans, S. Baier, H. K. C. Beukers, P. C. Humphreys, R. N. Schouten, R. F. L. Vermeulen, M. J. Tiggelman, L. dos Santos Martins, B. Dirkse, S. Wehner, and R. Hanson, "Realization of a multinode quantum network of remote solid-state qubits", Science **372**, 259 (2021).

[165] J. J. L. Morton, A. M. Tyryshkin, R. M. Brown, S. Shankar, B. W. Lovett, A. Ardavan, T. Schenkel, E. E. Haller, J. W. Ager, and S. A. Lyon, "Solid-state quantum memory using the 31P nuclear spin", Nature **455**, 1085 (2008).

[166] C. Grezes, Y. Kubo, B. Julsgaard, T. Umeda, J. Isoya, H. Sumiya, H. Abe, S. Onoda, T. Ohshima, K. Nakamura, I. Diniz, A. Auffeves, V. Jacques, J.-F. Roch, D. Vion, D. Esteve, K. Moelmer, and P. Bertet, "Towards a spin-ensemble quantum memory for superconducting qubits", Comptes Rendus Physique **17**, 693 (2016).

[167] J. O'Sullivan, O. W. Kennedy, K. Debnath, J. Alexander, C. W. Zollitsch, M. Šimėnas, A. Hashim, C. N. Thomas, S. Withington, I. Siddiqi, K. Mølmer, and J. J. L. Morton, "Random-Access Quantum Memory Using Chirped Pulse Phase Encoding", Phys. Rev. X **12**, 041014 (2022).

[168] G. Romero, J. J. Garcia-Ripoll, and E. Solano, "Microwave Photon Detector in Circuit QED", Physical Review Letters **102**, 173602 (2009).

[169] F. Helmer, M. Mariantoni, E. Solano, and F. Marquardt, "Quantum nondemolition photon detection in circuit QED and the quantum Zeno effect", Physical Review A **79**, 052115 (2009).

[170] K. Koshino, K. Inomata, T. Yamamoto, and Y. Nakamura, "Implementation of an Impedance-Matched Λ System by Dressed-State Engineering", Physical Review Letters **111**, 153601 (2013).

[171] S. R. Sathyamoorthy, L. Tornberg, A. F. Kockum, B. Q. Baragiola, J. Combes, C. M. Wilson, T. M. Stace, and G. Johansson, "Quantum Nondemolition Detection of a Propagating Microwave Photon", Physical Review Letters **112**, 093601 (2014).

[172] H. Fan, Y.-N. Wang, L. Jing, J.-D. Yue, H.-D. Shi, Y.-L. Zhang, and L.-Z. Mu, "Quantum cloning machines and the applications", Physics Reports **544**, 241 (2014).

[173] O. Kyriienko and A. S. Sorensen, "Continuous-Wave Single-Photon Transistor Based on a Superconducting Circuit", Physical Review Letters **117**, 140503 (2016).

[174] Sankar Raman Sathyamoorthy, Thomas M. Stace, and Göran Johansson, "Detecting itinerant single microwave photons", Comptes Rendus Physique **17**, 756 (2016).

[175] Xiu Gu, Anton Frisk Kockum, Adam Miranowicz, Yu-xi Liu, and Franco Nori, "Microwave photonics with superconducting quantum circuits", Physics Reports **718-719**, 1 (2017).

[176] C. H. Wong and M. G. Vavilov, "Quantum efficiency of a single microwave photon detector based on a semiconductor double quantum dot", Physical Review A **95**, 012325 (2017).

[177] J. Leppäkangas, M. Marthaler, D. Hazra, S. Jebari, R. Albert, F. Blanchet, G. Johansson, and M. Hofheinz, "Multiplying and detecting propagating microwave photons using inelastic Cooper-pair tunneling", Physical Review A **97**, 013855 (2018).

[178] B. Royer, A. L. Grimsmo, A. Choquette-Poitevin, and A. Blais, "Itinerant Microwave Photon Detector", Physical Review Letters **120**, 203602 (2018).

[179] Y.-F. Chen, D. Hover, S. Sendelbach, L. Maurer, S. T. Merkel, E. J. Pritchett, F. K. Wilhelm, and R. McDermott, "Microwave Photon Counter Based on Josephson Junctions", Physical Review Letters **107**, 217401 (2011).

[180] K. Inomata, Z. Lin, K. Koshino, W. D. Oliver, J.-S. Tsai, T. Yamamoto, and Y. Nakamura, "Single microwave-photon detector using an artificial Λ-type three-level system", Nature Communications **7**, 12303 (2016).

[181] J.-C. Besse, S. Gasparinetti, M. C. Collodo, T. Walter, P. Kurpiers, M. Pechal, C. Eichler, and A. Wallraff, "Single-Shot Quantum Nondemolition Detection of Individual Itinerant Microwave Photons", Phys. Rev. X **8**, 021003 (2018).

[182] S. Kono, K. Koshino, Y. Tabuchi, A. Noguchi, and Y. Nakamura, "Quantum nondemolition detection of an itinerant microwave photon", Nature Physics **14**, 546 (2018).

[183] A. Narla, S. Shankar, M. Hatridge, Z. Leghtas, K. M. Sliwa, E. Zalys-Geller, S. O. Mundhada, W. Pfaff, L. Frunzio, R. J. Schoelkopf, and M. H. Devoret, "Robust Concurrent Remote Entanglement Between Two Superconducting Qubits", Phys. Rev. X **6**, 031036 (2016).

[184] R. Lescanne, S. Deléglise, E. Albertinale, U. Réglade, T. Capelle, E. Ivanov, T. Jacqmin, Z. Leghtas, and E. Flurin, "Irreversible Qubit-Photon Coupling for the Detection of Itinerant Microwave Photons", Phys. Rev. X **10**, 021038 (2020).

[185] R. Dassonneville, R. Assouly, T. Peronnin, P. Rouchon, and B. Huard, "Number-Resolved Photocounter for Propagating Microwave Mode", Phys. Rev. Appl. **14**, 044022 (2020).

[186] H. Yang, N. Samantaray, and J. Jeffers, "Quantum Illumination with Multiplexed Photodetection", Phys. Rev. Appl. **18**, 034021 (2022).

[187] L. Balembois, J. Travesedo, L. Pallegoix, A. May, E. Billaud, M. Villiers, D. Esteve, D. Vion, P. Bertet, and E. Flurin, "Practical Single Microwave Photon Counter with 10^{-22} W/$\sqrt{Hz}$ sensitivity", arXiv:2307.03614 (2023).

[188] A. Karsa and S. Pirandola, "Energetic Considerations in Quantum Target Ranging", 2021 IEEE Radar Conference (RadarConf21) **1**, 1 (2021).

[189] Q. Zhuang and J. H. Shapiro, "Ultimate Accuracy Limit of Quantum Pulse-Compression Ranging", Phys. Rev. Lett. **128**, 010501 (2022).

[190] M. Reichert, R. Di Candia, M. Z. Win, and M. Sanz, "Quantum-enhanced Doppler lidar", npj Quantum Information **8**, 147 (2022).

[191] Z. Huang, C. Lupo, and P. Kok, "Quantum-Limited Estimation of Range and Velocity", PRX Quantum **2**, 030303 (2021).

[192] L. Maccone and C. Ren, "Quantum Radar", Phys. Rev. Lett. **124**, 200503 (2020).

[193] R. Gallego Torrome, "Quantum Illumination with Multiple Entangled Photons", Advanced Quantum Technologies **4**, 2100101 (2021).

[194] E. Jung and D. Park, "Quantum illumination with three-mode Gaussian state", Quantum Information Processing **21**, 71 (2022).

[195] S. Zhang, J. Guo, W. Bao, J. Shi, C. Jin, X. Zou, and G. Guo, "Quantum illumination with photon-subtracted continuous-variable entanglement", Phys. Rev. A **89**, 062309 (2014).

[196] L. Fan and M. S. Zubairy, "Quantum illumination using non-Gaussian states generated by photon subtraction and photon addition", Phys. Rev. A **98**, 012319 (2018).

[197] S. Barzanjeh, S. Pirandola, D. Vitali, and J. M. Fink, "Microwave quantum illumination using a digital receiver", Science Advances **6**, eabb0451 (2020).

[198] S. Pirandola, "Composable security for continuous variable quantum key distribution: Trust levels and practical key rates in wired and wireless networks", Phys. Rev. Research **3**, 043014 (2021).

[199] M. Zhang, S. Pirandola, and K. Delfanazari, "Millimetre-waves to Terahertz SISO and MIMO Continuous Variable Quantum Key Distribution", arXiv:2301.04723 (2023).

[200] W. Buckel and R. Kleiner, *Superconductivity: Fundamentals and Applications*, Physics textbook (Wiley, 2008), ISBN 9783527618514, URL https://books.google.de/books?id=v_k3EyDe4OIC.

[201] R. Gross and A. Marx, *Festkörperphysik* (De Gruyter, 2012), ISBN 9783486714869, URL https://books.google.de/books?id=IaVJAAAAQBAJ.

[202] K. Gavroglu, H. Onnes, and Y. Goudaroulis, *Through Measurement to Knowledge: The Selected Papers of Heike Kamerlingh Onnes 1853–1926*, Boston Studies in the Philosophy and History of Science (Springer Netherlands, 2012), ISBN 9789400920798, URL https://books.google.de/books?id=XnoFCAAAQBAJ.

[203] D. van Delft and P. Kes, "The discovery of superconductivity", Physics Today **63**, 38 (2010).

[204] H. Kamerlingh Onnes, "Nobel lecture", Commun. Leiden Suppl. **34b**, 133 (1913).

[205] W. Meissner and R. Ochsenfeld, "Ein neuer Effekt bei Eintritt der Supraleitfähigkeit", Naturwissenschaften **21**, 787 (1933).

[206] R. Doll and M. Näbauer, "Experimental Proof of Magnetic Flux Quantization in a Superconducting Ring", Phys. Rev. Lett. **7**, 51 (1961).

[207] B. S. Deaver and W. M. Fairbank, "Experimental Evidence for Quantized Flux in Superconducting Cylinders", Phys. Rev. Lett. **7**, 43 (1961).

[208] F. London and H. London, "The electromagnetic equations of the supraconductor", Proceedings of the Royal Society of London. Series A - Mathematical and Physical Sciences **149**, 71 (1935).

[209] V. L. Ginzburg and L. D. Landau, "On the Theory of superconductivity", Zh. Eksp. Teor. Fiz. **20**, 1064 (1950).

[210] J. Bardeen, L. N. Cooper, and J. R. Schrieffer, "Theory of Superconductivity", Phys. Rev. **108**, 1175 (1957).

[211] J. Bardeen, L. N. Cooper, and J. R. Schrieffer, "Microscopic Theory of Superconductivity", Phys. Rev. **106**, 162 (1957).

[212] Mercereau, J.E., "Superconducting magnetometers", Rev. Phys. Appl. **5**, 13 (1970).

[213] J. E. Zimmerman, P. Thiene, and J. T. Harding, "Design and Operation of Stable rf Biased Superconducting Point Contact Quantum Devices, and a Note on the Properties of Perfectly Clean Metal Contacts", Journal of Applied Physics **41**, 1572 (2003).

[214] J. Clarke and A. Braginski, *The SQUID Handbook: Fundamentals and Technology of SQUIDs and SQUID Systems* (Wiley, 2006), ISBN 9783527604586, URL https://books.google.de/books?id=BsTTM-nU-JkC.

[215] J. Clarke, "A superconducting galvanometer employing Josephson tunnelling", The Philosophical Magazine: A Journal of Theoretical Experimental and Applied Physics **13**, 115 (1966).

[216] R. C. Jaklevic, J. Lambe, A. H. Silver, and J. E. Mercereau, "Quantum Interference Effects in Josephson Tunneling", Phys. Rev. Lett. **12**, 159 (1964).

[217] M. Sandberg, C. M. Wilson, F. Persson, T. Bauch, G. Johansson, V. Shumeiko, T. Duty, and P. Delsing, "Tuning the field in a microwave resonator faster than the photon lifetime", Applied Physics Letters **92**, 203501 (2008).

[218] M. Göppl, A. Fragner, M. Baur, R. Bianchetti, S. Filipp, J. M. Fink, P. J. Leek, G. Puebla, L. Steffen, and A. Wallraff, "Coplanar waveguide resonators for circuit quantum electrodynamics", J. Appl. Phys. **104**, 113904 (2008).

[219] J. Goetz, F. Deppe, M. Haeberlein, F. Wulschner, C. W. Zollitsch, S. Meier, M. Fischer, P. Eder, E. Xie, K. G. Fedorov, E. P. Menzel, A. Marx, and R. Gross, "Loss mechanisms in superconducting thin film microwave resonators", Journal of Applied Physics **119**, 015304 (2016).

[220] D. S. Wisbey, J. Gao, M. R. Vissers, F. C. S. da Silva, J. S. Kline, L. Vale, and D. P. Pappas, "Effect of metal/substrate interfaces on radio-frequency loss in superconducting coplanar waveguides", Journal of Applied Physics **108**, 093918 (2010).

[221] T. Yamamoto, K. Koshino, and Y. Nakamura, *Parametric Amplifier and Oscillator Based on Josephson Junction Circuitry* (Springer Japan, Tokyo, 2016), URL https://books.google.de/books?id=RLlPCwAAQBAJ.

[222] M. Renger, "Inter-Lab Quantum Microwave Teleportation", Phd thesis, Technische Universität München (2023), URL https://mediatum.ub.tum.de/1540503.

[223] E. Organick, *A Fortran IV Primer*, Addison-Wesley series in computer science and information processing (Addison-Wesley, 1966), URL https://books.google.de/books?id=36tQAAAAMAAJ.

[224] W. H. Louisell, A. Yariv, and A. E. Siegman, "Quantum Fluctuations and Noise in Parametric Processes. I.", Phys. Rev. **124**, 1646 (1961).

[225] J. P. Gordon, W. H. Louisell, and L. R. Walker, "Quantum Fluctuations and Noise in Parametric Processes. II", Phys. Rev. **129**, 481 (1963).

[226] A. A. Clerk, M. H. Devoret, S. M. Girvin, F. Marquardt, and R. J. Schoelkopf, "Introduction to quantum noise, measurement, and amplification", Rev. Mod. Phys. **82**, 1155 (2010).

[227] W. Wustmann and V. Shumeiko, "Parametric resonance in tunable superconducting cavities", Phys. Rev. B **87**, 184501 (2013).

[228] P. Krantz, A. Bengtsson, M. Simoen, S. Gustavsson, V. Shumeiko, W. D. Oliver, C. M. Wilson, P. Delsing, and J. Bylander, "Single-shot read-out of a superconducting qubit using a Josephson parametric oscillator", Nature Communications **7**, 11417 (2016).

[229] C. M. Wilson, T. Duty, M. Sandberg, F. Persson, V. Shumeiko, and P. Delsing, "Photon Generation in an Electromagnetic Cavity with a Time-Dependent Boundary", Phys. Rev. Lett. **105**, 233907 (2010).

[230] D. J. Parker, M. Savytskyi, W. Vine, A. Laucht, T. Duty, A. Morello, A. L. Grimsmo, and J. J. Pla, "Degenerate Parametric Amplification via Three-Wave Mixing Using Kinetic Inductance", Phys. Rev. Applied **17**, 034064 (2022).

[231] D. F. Walls, "Squeezed states of light", Nature **306**, 141 (1983).

[232] C. M. Caves, J. Combes, Z. Jiang, and S. Pandey, "Quantum limits on phase-preserving linear amplifiers", Phys. Rev. A **86**, 063802 (2012).

[233] H. A. Haus and J. A. Mullen, "Quantum Noise in Linear Amplifiers", Phys. Rev. **128**, 2407 (1962).

[234] C. M. Caves, "Quantum limits on noise in linear amplifiers", Phys. Rev. D **26**, 1817 (1982).

[235] D. Kouznetsov, R. Ortega-Martínez, and D. Rohrlich, "Quantum noise limits for nonlinear, phase-invariant amplifiers", Phys. Rev. A **52**, 1665 (1995).

[236] R. Movshovich, B. Yurke, P. G. Kaminsky, A. D. Smith, A. H. Silver, R. W. Simon, and M. V. Schneider, "Observation of zero-point noise squeezing via a Josephson-parametric amplifier", Phys. Rev. Lett. **65**, 1419 (1990).

[237] M. A. A. Caballero, "A Setup for Quantum Signal Detection in a Circuit QED Architecture", Master's thesis, Technische Universität München (2008), URL https://www.wmi.badw.de/fileadmin/WMI/Publications/Araque%20Caballero_Diplomarbeit_2008.pdf.

[238] A. T. A. M. de Waele, "Basic Operation of Cryocoolers and Related Thermal Machines", Journal of Low Temperature Physics **164**, 179 (2011).

[239] C. Enss and S. Hunklinger, *Low-Temperature Physics*, SpringerLink: Springer e-Books (Springer Berlin Heidelberg, 2005), ISBN 9783540266198, URL https://books.google.de/books?id=ufM7sPMTGdAC.

[240] C. R. Lawson, A. T. Jones, W. Kockelmann, S. J. Horney, and O. Kirichek, "Neutron imaging of an operational dilution refrigerator", Scientific Reports **12**, 1130 (2022).

[241] F. Pobell, *Matter and Methods at Low Temperatures* (Springer Berlin Heidelberg, 2007), ISBN 9783540463603, URL https://books.google.de/books?id=mRZOuPfiWTQC.

[242] A. Abrikosov, "The magnetic properties of superconducting alloys", Journal of Physics and Chemistry of Solids **2**, 199 (1957).

[243] B. Chiaro, A. Megrant, A. Dunsworth, Z. Chen, R. Barends, B. Campbell, Y. Chen, A. Fowler, I. C. Hoi, E. Jeffrey, J. Kelly, J. Mutus, C. Neill, P. J. J. O'Malley, C. Quintana, P. Roushan, D. Sank, A. Vainsencher, J. Wenner, T. C. White, and J. M. Martinis, "Dielectric surface loss in superconducting resonators with flux-trapping holes", Superconductor Science and Technology **29**, 104006 (2016).

[244] C. Shannon, "Communication in the Presence of Noise", Proceedings of the IRE **37**, 10 (1949).

[245] B. Shenoi, *Introduction to Digital Signal Processing and Filter Design* (Wiley, 2005), ISBN 9780471656388, URL https://books.google.de/books?id=37g8oUqaS_AC.

[246] R. D. Candia, E. P. Menzel, L. Zhong, F. Deppe, A. Marx, R. Gross, and E. Solano, "Dual-path methods for propagating quantum microwaves", New Journal of Physics **16**, 015001 (2014).

[247] C. Eichler, Y. Salathe, J. Mlynek, S. Schmidt, and A. Wallraff, "Quantum-Limited Amplification and Entanglement in Coupled Nonlinear Resonators", Phys. Rev. Lett. **113**, 110502 (2014).

[248] R. Schack and A. Schenzle, "Moment hierarchies and cumulants in quantum optics", Phys. Rev. A **41**, 3847 (1990).

[249] S.-H. Xiang, W. Wen, Y.-J. Zhao, and K.-H. Song, "Evaluation of the non-Gaussianity of two-mode entangled states over a bosonic memory channel via cumulant theory and quadrature detection", Phys. Rev. A **97**, 042303 (2018).

[250] S. N. Filippov and V. I. Man'ko, "Evolution of microwave quantum states in terms of measurable ordered moments of creation and annihilation operators", Optics and Spectroscopy **112**, 365 (2012).

[251] C. Macklin, K. O'Brien, D. Hover, M. E. Schwartz, V. Bolkhovsky, X. Zhang, W. D. Oliver, and I. Siddiqi, "A near quantum-limited Josephson traveling-wave parametric amplifier", Science **350**, 307 (2015).

[252] L. Spietz, K. W. Lehnert, I. Siddiqi, and R. J. Schoelkopf, "Primary Electronic Thermometry Using the Shot Noise of a Tunnel Junction", Science **300**, 1929 (2003).

[253] S. Gandorfer, M. Renger, W. K. Yam, F. Fesquet, A. Marx, R. Gross, and K. G. Fedorov, "Two-Dimensional Planck Spectroscopy", arXiv:2308.02389 (2023).

[254] M. Renger, K. G. Fedorov, S. Pogorzalek, Y. Nojiri, Q. Chen, M. Partanen, A. Marx, F. Deppe, and R. Gross, "Chained Josephson Parametric Amplifiers", in *Annual Report 2019* (Walther-Meißner-Institut, 2019), pp. 67–68, URL https://www.wmi.badw.de/fileadmin/WMI/Publications/Annual_Reports/2019.pdf.

[255] C. Eichler and A. Wallraff, "Controlling the dynamic range of a Josephson parametric amplifier", EPJ Quantum Technol. **1**, 2 (2014).

[256] D. Arweiler, "Multi-SQUID Josephson Parametric Amplifiers", Master's thesis, Technische Universität München (2018), URL http://www.wmi.badw.de/publications/theses/Arweiler,Daniel_Masterarbeit_2018.pdf.

[257] Z. Y. Ou and X. Li, "Quantum SU(1,1) interferometers: Basic principles and applications", APL Photonics **5**, 080902 (2020).

[258] B. P. Abbott, R. Abbott, F. Acernese, R. Adhikari, P. Ajith, B. Allen, G. Allen, M. Alshourbagy, R. S. Amin, and S. B. Anderson *et al.*, "An upper limit on the stochastic gravitational-wave background of cosmological origin", Nature **460**, 990 (2009).

[259] M. Born, E. Wolf, A. B. Bhatia, P. C. Clemmow, D. Gabor, A. R. Stokes, A. M. Taylor, P. A. Wayman, and W. L. Wilcock, *Principles of Optics* (Cambridge University Press, 2013), ISBN 9780521642224, URL https://books.google.de/books?id=HY-GDAAAQBAJ.

[260] P. Grangier, R. E. Slusher, B. Yurke, and A. LaPorta, "Squeezed-light-enhanced polarization interferometer", Physical Review Letters **59**, 2153 (1987).

[261] R. Schnabel, "Squeezed states of light and their applications in laser interferometers", Physics Reports **684**, 1 (2017).

[262] V. Giovannetti, S. Lloyd, and L. Maccone, "Quantum Metrology", Physical Review Letters **96**, 010401 (2006).

[263] V. Giovannetti, S. Lloyd, and L. Maccone, "Advances in quantum metrology", Nature Photonics **5**, 222 (2011).

[264] M. Napolitano, M. Koschorreck, B. Dubost, N. Behbood, R. J. Sewell, and M. W. Mitchell, "Interaction-based quantum metrology showing scaling beyond the Heisenberg limit", Nature **471**, 486 (2011).

[265] B. Yurke, S. L. McCall, and J. R. Klauder, "SU(2) and SU(1,1) interferometers", Physical Review A **33**, 4033 (1986).

[266] Z. Y. Ou, "Fundamental quantum limit in precision phase measurement", Physical Review A **55**, 2598 (1997).

[267] Z. Y. Ou, "Enhancement of the phase-measurement sensitivity beyond the standard quantum limit by a nonlinear interferometer", Physical Review A **85**, 023815 (2012).

[268] F. Hudelist, J. Kong, C. Liu, J. Jing, Z. Y. Ou, and W. Zhang, "Quantum metrology with parametric amplifier-based photon correlation interferometers", Nature Communications **5**, 3049 (2014).

[269] E. Flurin, N. Roch, F. Mallet, M. H. Devoret, and B. Huard, "Generating Entangled Microwave Radiation Over Two Transmission Lines", Physical Review Letters **109**, 183901 (2012).

[270] J. Reed and G. Wheeler, "A Method of Analysis of Symmetrical Four-Port Networks", IRE Transactions on Microwave Theory and Techniques **4**, 246 (1956).

[271] G. Adesso, "Gaussian interferometric power", Physical Review A **90**, 022321 (2014).

[272] D. Girolami, A. M. Souza, V. Giovannetti, T. Tufarelli, J. G. Filgueiras, R. S. Sarthour, D. O. Soares-Pinto, I. S. Oliveira, and G. Adesso, "Quantum Discord Determines the Interferometric Power of Quantum States", Physical Review Letters **112**, 210401 (2014).

[273] M. Mariantoni, E. P. Menzel, F. Deppe, M. A. Araque Caballero, A. Baust, T. Niemczyk, E. Hoffmann, E. Solano, A. Marx, and R. Gross, "Planck Spectroscopy and Quantum Noise of Microwave Beam Splitters", Physical Review Letters **105**, 133601 (2010).

[274] K. G. Fedorov, L. Zhong, S. Pogorzalek, P. Eder, M. Fischer, J. Goetz, E. Xie, F. Wulschner, K. Inomata, T. Yamamoto, Y. Nakamura, R. Di Candia, U. Las Heras, M. Sanz, E. Solano, E. P. Menzel, F. Deppe, A. Marx, and R. Gross, "Displacement of Propagating Squeezed Microwave States", Physical Review Letters **117**, 020502 (2016).

[275] K. Modi, A. Brodutch, H. Cable, T. Paterek, and V. Vedral, "The classical-quantum boundary for correlations: Discord and related measures", Reviews of Modern Physics **84**, 1655 (2012).

[276] Y. K. Semertzidis and S. Youn, "Axion dark matter: How to see it?", Science Advances **8**, eabm9928 (2022).

[277] C. M. Adair, K. Altenmüller, V. Anastassopoulos, S. Arguedas Cuendis, J. Baier, K. Barth, A. Belov, D. Bozicevic, and H. Bräuninger *et al.*, "Search for Dark Matter Axions with CAST-CAPP", Nature Communications **13**, 6180 (2022).

[278] Z. Gong, N. Rodriguez, C. N. Gagatsos, S. Guha, and B. A. Bash, "Quantum-Enhanced Transmittance Sensing", IEEE Journal of Selected Topics in Signal Processing pp. 1–17 (2022).

[279] Y. Nojiri, K. E. Honasoge, A. Marx, K. G. Fedorov, and R. Gross, "Onset of transmon ionization in microwave single-photon detection", arXiv:2402.01884 (2024).

List of publications

1. <u>F. Kronowetter</u>, M. Würth, W. Utschick, R. Gross, K. G. Fedorov, "Imperfect photon detection in quantum illumination", Phys. Rev. Appl. **21**, 014007 (2024).

2. <u>F. Kronowetter</u>, F. Fesquet, M. Renger, K. Honasoge, Y. Nojiri, K. Inomata, Y. Nakamura, A. Marx, R. Gross, K. G. Fedorov, "Quantum microwave parametric interferometer", Phys. Rev. Appl. **20**, 024049 (2023).

3. <u>F. Kronowetter</u>, "Quantenkorrelation verbessert Radartechnik", R&S NEUES **226**, 024 (2023).

4. F. Fesquet, <u>F. Kronowetter</u>, M. Renger, W. Yam, S. Gandorfer, K. Inomata, Y. Nakamura, A. Marx, R. Gross, K. G. Fedorov, "Demonstration of microwave single-shot quantum key distribution", arXiv:2311.11069 (2023).

5. F. Fesquet, <u>F. Kronowetter</u>, M. Renger, Q. Chen, K. E. Honasoge, O. Gargiulo, Y. Nojiri, A. Marx, F. Deppe, R. Gross, K. G. Fedorov, "Perspectives of microwave quantum key distribution in open-air", Phys. Rev. A **108**, 032607 (2023).

6. R. Gross, <u>F. Kronowetter</u>, "Quantensensorik und Quantenmetrologie machen gewaltige Fortschritte", R&S NEUES **226**, 020 (2023).

7. M. Renger, S. Gandorfer, W. Yam, F. Fesquet, M. Handschuh, K. E. Honasoge, <u>F. Kronowetter</u>, Y. Nojiri, M. Partanen, A. Marx, K. G. Fedorov, R. Gross, F. Deppe, "Cryogenic microwave link for quantum local area networks", arXiv:2308.12398 (2023).

8. M. Renger, S. Pogorzalek, F. Fesquet, K. E. Honasoge, <u>F. Kronowetter</u>, Q. Chen, Y. Nojiri, K. Inomata, Y. Nakamura, A. Marx, F. Deppe, R. Gross, K. G. Fedorov, "Flow of quantum correlations in noisy two-mode squeezed microwave states", Phys. Rev. A **106**, 052415 (2022).

9. Q. Chen, <u>F. Kronowetter</u>, F. Fesquet, K. E. Honasoge, Y. Nojiri, S. Pogorzalek, , Y. Nojiri, M. Renger, K. G. Fedorov, A. Marx, F. Deppe, R. Gross, "Tuning and amplifying the interactions in superconducting quantum circuits with subradiant qubits", Phys. Rev. A **105**, 012405 (2022).

10. Q. Chen, M. Partanen, F. Fesquet, K. E. Honasoge, <u>F. Kronowetter</u>, Y. Nojiri, M. Renger, K. G. Fedorov, A. Marx, F. Deppe, R. Gross, "Scattering coefficients

of superconducting microwave resonators. II. System-bath approach", Phys. Rev. B **106**, 214506 (2022).

11. Q. Chen, M. Pfeiffer, M. Partanen, F. Fesquet, K. E. Honasoge, <u>F. Kronowetter</u>, Y. Nojiri, M. Renger, K. G. Fedorov, A. Marx, F. Deppe, R. Gross, "Scattering coefficients of superconducting microwave resonators. I. Transfer matrix approach", Phys. Rev. B **106**, 214505 (2022).

Acknowledgments

Over the past three years, I have had the pleasure of diving deep into quantum physics and learning about fascinating phenomena that have the potential to change the world as we know it. This journey has been supported by many different people whom I would like to thank:

First, my doctoral advisor *Prof. Dr. Rudolf Gross* for supervising my efforts at the WMI as part of my doctorate. I enjoyed our regular discussions and learned many things from your experienced perspective on a variety of topics.

Dr. Kirill G. Fedorov for your daily guidance throughout the doctorate. We had many fruitful discussions on the nontrivial topic of quantum illumination and I was able to acquire quite some knowledge about quantum physics as part of your team. A special appreciation for your agile feedback when it comes to manuscripts, these efficient feedback loops facilitated my academic life a lot, from scientific papers to this thesis.

Florian Fesquet for the many hours we spent together in the lab. Thank you for the numerous discussions that helped me to somewhat understand quantum physics. I appreciate these frequent exchanges and am proud of what we have achieved together!

My colleagues at Rohde & Schwarz for their constant support throughout this journey, as part of and beyond this project. First of all, I would like to thank *Dr. Gerd Hechtfischer* for mentoring my journey at R&S and for the various quantum physics related discussions from an industrial point of view, I am always impressed by your broad technological overview combined with a deep understanding of the underlying physics. Next, I would like to thank *Dr. Christian Pinta* for your great help with all the organizational challenges and the seamless integration into your team. I am very impressed by your leadership style, which is a unique combination of fun, know-how, calmness and focus, resulting in a great team dynamic. I would also like to thank *Dr. Melvyn Ho* for coordinating the quantum activities at R&S in a very structured and friendly manner. I appreciate your proactive efforts to involve me in many exciting tasks beyond the scope of the quantum radar research project. Many thanks also to *Dr. Baris Güzelarslan* for coordinating the Quantum Radar team in the early stages of the project. In addition, I thank *Dr. Thomas Ruster* for coordinating the project in its second phase.

All other members of the QUARATE project. Thank you, *Prof. Dr. Wolfgang Utschick*, for initiating the project and for your strong efforts to bridge the conceptual gap between